



Virginia Commonwealth University  
VCU Scholars Compass

---

Theses and Dissertations

Graduate School

---

2010

## Core-Shell Nanoparticles: Synthesis, Design, and Characterization

Kyler Carroll

*Virginia Commonwealth University*

Follow this and additional works at: <https://scholarscompass.vcu.edu/etd>

Part of the Chemistry Commons

---

© The Author

---

Downloaded from

<https://scholarscompass.vcu.edu/etd/2204>

This Dissertation is brought to you for free and open access by the Graduate School at VCU Scholars Compass. It has been accepted for inclusion in Theses and Dissertations by an authorized administrator of VCU Scholars Compass. For more information, please contact [libcompass@vcu.edu](mailto:libcompass@vcu.edu).

© Kyler J. Carroll 2010  
All Rights Reserved

# Core-shell Nanoparticles: Synthesis, Design, and Characterization

A dissertation submitted in partial fulfillment of the requirements for the degree of  
Doctor of Philosophy at Virginia Commonwealth University.

by

Kyler James Carroll  
B.S., Aquinas College, 2007

Director: Everett E. Carpenter,  
Associate Professor of Chemistry

Virginia Commonwealth University  
Richmond, Virginia  
July, 2010

## Acknowledgments

In completion of this dissertation, there are many people to thank. Without these individuals, this work would have never become possible. First, I would like to thank my wife Jeanne for not only encouraging me to pursue chemistry further, but for the love, support, and guidance that keeps me going every day of my life. This truly would not have been achievable without you. I would also like to thank my friends and family, who never became too worried and disappointed with the weeks of no communication, forgotten birthdays, and missed holidays and weddings. I would like to specifically thank my grandparents, without whom I truly would have never been able to afford college and pursue my education. I would also like to thank my parents who worked so hard to provide me with the opportunities to excel. I would like to thank Dr. Jensen, who first encouraged me to pursue chemistry as a major. I would have never been introduced to my beautiful wife and a wonderful career path were it not for you. I would like to thank Dr. Carpenter, my advisor, who provided me with direction and encouragement throughout my research. Many thanks are due to Dr. Glaspell, who also provided me with continuous direction and motivation throughout my research. Both of you have taught me that applications drive inspiration. Thanks must also go to my many contributors from University of Delaware, Northeastern University, Brookhaven National Laboratory, and William and Mary. Without your collaborations, my research would not have been as successful. I also must thank my labmates for the many hours of conversation, relaxation, and inspiration. Lastly, I would like to thank my committee members and other VCU staff that have provided me with a wonderful program in which to study.

## Table of Contents

List of Figures .....	viii
List of Tables .....	xvii
Chapter 1: Introduction .....	1
1.1 Introduction.....	2
1.2 Overview.....	2
1.3 Nucleation and Growth.....	5
1.4 Electronic properties .....	7
1.5 Optical properties.....	8
1.6 Magnetic properties .....	9
1.6.1 Introduction to Magnetism.....	10
1.6.2 Diamagnetism .....	10
1.6.3 Paramagnetism.....	11
1.6.4 Cooperative magnetism .....	11
1.7 Design and Synthesis of Monodisperse Nanoparticles.....	13
1.7.1 Polyol Process.....	14
1.7.2 Aqueous Reduction by borohydride .....	15
1.7.3 Design of Core/Shell nanoparticles .....	17
1.8 Summary of Objectives: .....	19

Chapter 2: Characterization Techniques .....	20
2.1 Introduction.....	21
2.2 X-ray Diffraction (XRD) .....	22
2.2.1 Bragg's Law.....	24
2.2.2 X-ray diffractometer .....	26
2.3 Transmission Electron Microscopy (TEM) .....	27
2.4 X-ray Photoelectron Microscopy (XPS).....	28
2.4.1 Notation.....	30
2.4.2 Charge Compensation.....	31
2.4.3 Depth Profiling.....	32
2.4.4 Peak Fitting .....	33
2.5 Vibrating Sample Magnetometry (VSM) .....	35
2.6 X-ray Absorption Spectroscopy (XAS) .....	35
2.6.1 Experimental.....	38
2.7 Thermal Analysis .....	38
2.8 Ultraviolet-Visible Spectroscopy (UV-vis) .....	39
Section 1: Aqueous Reduction.....	41
Chapter 3: Non-classical Crystallization of Fe Nanoparticles .....	42
3.1 Introduction.....	43
3.2 Experimental Section .....	43
3.2.1 RF Exposure.....	44
3.3 Results and Discussion .....	44
3.4 Conclusion .....	51
Chapter 4: Design of $\text{Fe}_x\text{Co}_{100-x}$ Nanoparticles.....	52

4.1 Introduction.....	53
4.2 Experimental .....	53
4.3. Results and Discussion .....	56
4.4 Conclusion .....	64
Chapter 5: Design of Fe and Ag core/shell Nanoparticles.....	66
5.1 Introduction.....	67
5.2 Experimental Section .....	68
5.2.1 Preparation of Fe nanoparticles .....	68
5.2.2 Preparation of Fe/Ag and Ag/Fe core/shell nanoparticles. ....	69
5.3 Characterization .....	69
5.4 Results.....	71
5.5 Discussion.....	79
5.6 Surface Enhanced Raman Scattering .....	81
5.7 Conclusion .....	85
Chapter 6: Design of Fe/SiO <sub>2</sub> /Au Nanoparticles .....	87
6.1 Introduction.....	88
6.2 Synthesis of Fe/SiO <sub>2</sub> NPs .....	88
6.3 Synthesis of Fe/SiO <sub>2</sub> /Au NPs.....	88
6.4 Heat Treatment.....	88
6.5 Results and Discussion .....	89
6.6 Conclusion .....	96
Section 2: Polyol Method.....	97
Chapter 7: Design of Cu and Ni nanoparticles .....	98
7.1 Introduction.....	99

7.2 History of the Polyol Process.....	101
7.3 Experimental .....	104
7.3.1 Sample Preparation .....	104
7.3.2 Characterization .....	104
7.3.3 Theoretical Investigation .....	105
7.4 Results and Discussion .....	105
7.4.1 X-ray and Morphological Characterization .....	105
7.4.2 XPS Results .....	115
7.4.3 Crystal Growth.....	117
7.5 Crystallization of Copper-glycolate.....	119
7.5.1 Refinement Details.....	125
7.6 Mechanism Study.....	126
7.7 Conclusion .....	131
Chapter 8: Design of Cu/Ni core/Shell Nanoparticles .....	133
8.1 Introduction.....	134
8.2 Synthesis .....	136
8.2.1 Materials. ....	136
8.2.2 Synthesis of Cu-Ni CSNPs. ....	136
8.2.3 Synthesis of Ni-Cu CSNPs. ....	137
8.3 Results and discussion .....	137
8.4 Conclusions.....	142
Chapter 9: Design of Aqueous Based Ferrofluids .....	144
9.1 Design of Fe-FeOx Nanoparticles .....	145
9.2 Synthesis .....	147

9.3. Results and Discussion .....	149
9.3.1 MRI Contrast Agent.....	153
9.3.2 Magnetic/RE luminescent Core/Shell Design .....	155
9.4 Conclusions.....	162
Chapter 10: Design of Cobalt Carbide Nanoparticles.....	163
10.1 Introduction.....	164
10.2 Synthesis Techniques.....	165
10.3 Results and Discussion .....	167
10.4 Conclusions.....	173
Chapter 11: Summary .....	174
References.....	178
Vita.....	202

## List of Figures

### **Chapter 1**

<b>Figure 1.1.</b> Calculated surface to bulk ratios for solid metal particles versus size. <sup>39</sup> The % of surface atoms increases while the % of bulk atoms decrease when going to nanometer scales.....	5
<b>Figure 1.2.</b> LaMer crystallization model. 3-step crystallization model for homogeneous nucleation and growth: I. Pre-nucleation period; II. Nucleation; III. Growth .....	6
<b>Figure 1.3.</b> Fluorescence emission of CdSe(ZnS) quantum dots of various sizes(image is adapted from reference). <sup>46</sup> .....	8
<b>Figure 1.4.</b> The types of magnetism seen in materials. Blue Arrows signify the direction of the applied field. Blue arrows in the black circle signify the direction of the electron spin.....	12
<b>Figure 1.5.</b> Various polyols used for the reduction of metal salt precursors. Varying the hydroxyl sites has an effect on the overall reduction potential of the polyol along with a boiling point change.....	15

### **Chapter 2**

<b>Figure 2.1.</b> Typical techniques used to characterize nanomaterials.....	21
<b>Figure 2.2.</b> Schematic illustrating the process of an ejection of a core electron and the resulting x-ray emissions by electrons filling the ejected electron hole. ....	22
<b>Figure 2.3.</b> Figure illustrates that each energy level emits a characteristic x-ray by the relaxation process.....	23
<b>Figure 2.4.</b> Diffraction of x-rays by planes of atoms. ....	25
<b>Figure 2.5.</b> Schematic of the ESCAlab 250 spectrometer used at Virginia Commonwealth University. ....	29

<b>Figure 2.6.</b> A schematic diagram of a typical XPS spectrometer using a monochromatized single anode X-ray source. The key components of the spectrometer are identified. ....	30
<b>Figure 2.7.</b> Common polyethylene terephthalate (PET) polymer C 1s spectra with peak fitting.....	33
<b>Figure 2.8.</b> Mn 2p <sub>3/2</sub> spectrum of the same sample displayed using background subtracted data, where four different background types are used to model the background. ....	34
<b>Figure 2.9.</b> Typical Spectrum obtained from XAS.....	36
<b>Figure 2.10.</b> Linear combination fit of the XANES data of mixed Fe/FeOx nanoparticles. ....	37
<b>Figure 2.11.</b> Schematic of a typical XAS setup at a synchrotron light source.....	38
<b>Figure 2.12.</b> Effect of size and shape on Plasmon resonance spectrum for silver nanowires and nanodiscs(image adapted and altered from reference). <sup>96</sup> .....	40
<b>Chapter 3</b>	
<b>Figure 3.1.</b> TEM image of the as-prepared amorphous nanoparticles. The particle size is about 200 nm. The bottom inset shows the histogram of the particles size distribution. .	44
<b>Figure 3.2.</b> (A) Depth profile of the Fe2p XPS region spectra. (B) Atomic percentage versus etch level which shows a decrease in Fe <sup>2+</sup> and an increase in elemental Fe as the etch level increases. This suggests that a layer of Fe <sup>2+</sup> is present at the surface and not in the bulk.....	46
<b>Figure 3.3.</b> Representative C1s region scan of the as-prepared nanoparticles. The region scan shows 3 peaks which correspond to C-O (blue), C=O (green), and C-C (red). The analysis is representative of a citrate ion. ....	46
<b>Figure 3.4.</b> X-ray diffraction patterns of the resulting particles. As the RF exposure increase from 0s to 45s an increase in the crystallinity is seen.....	48
<b>Figure 3.5.</b> Graph of crystallite size (nm) versus RF exposure time (s) for Fe nanoparticles. ....	48
<b>Figure 3.6.</b> Transmission electron microscopy images of the nanoparticles at various RF annealing times. ....	49

**Figure 3.7.** Magnetization saturation values as a function of RF exposure times. The inset shows how the temperature of the Fe/ethanol solution is affected by the RF exposure time. The solid line is meant as merely a guide for the eye..... 49

**Figure 3.8.** Room temperature hysteresis loops with various RF exposure times. ..... 50

## Chapter 4

**Figure 4.1.** Graphical representation of the color changes seen during the synthesis of FeCo nanoparticles synthesized by aqueous reduction..... 54

**Figure 4.2.** Differential Scanning Calorimetry patterns of 4 different ratios of nanoparticles. ..... 55

**Figure 4.3.** SQUID data of the as-prepared 50 at. % Co content nanoparticles. ..... 56

**Figure 4.4.** Plot of Magnetization and Coercivity versus Fe/Co ratio. ..... 58

**Figure 4.5.** Magnetization hysteresis loops of  $\text{Fe}_{50}\text{Co}_{50}$  content nanoparticles at various annealing temperatures. ..... 59

**Figure 4.6.** Powder x-ray diffraction patterns of  $\text{Fe}_{30}\text{Co}_{70}$  content nanoparticles at various annealing temperatures. ..... 59

**Figure 4.7.** Transmission electron micrographs of various as-prepared nanoparticles.... 61

**Figure 4.8.** Representative XPS survey scan of FeCo nanoparticles. .... 62

**Figure 4.9.** Representative Co and Fe region scans. .... 63

## Chapter 5

**Figure 5.1.** High resolution TEM image of (a) as-synthesized Fe nanoparticles,(b) Fe/Ag nanoparticles showing a clear distinction between the core (Ag) and shell ( $\text{FeB}/\text{Fe}_2\text{B}$ ) (c) Ag/Fe nanoparticles, and (d) Fe nanoparticles with islanding of Ag. .... 71

**Figure 5.2.** XANES spectra of the sample plotted with spectra collected from Fe metal foil and  $\text{Fe}_3\text{C}$  standards. .... 72

**Figure 5.3.** a) Comparison of Fourier Transform EXAFS spectra of Fe foil and Ag/Fe; b) Fourier Transform magnitude of the data and the fit plotted with the contributions of Fe and B signals. .... 74

<b>Figure 5.4.</b> (a) High-resolution XPS survey scan of a representative Fe/Ag core/shell nanoparticle (b) Atomic percentage of Fe2p and Ag3d as a function of AgNO <sub>3</sub> addition time determined by survey scans and standard sensitivity factors. ....	75
<b>Figure 5.5.</b> Fe2p region scans at with different AgNO <sub>3</sub> addition times which produced various core/shell nanoparticles with various Fe environments. ....	77
<b>Figure 5.6.</b> UV-vis absorption spectra of the Fe/Ag (solid blue line), Ag/Fe (solid green line), pure Ag (dotted black line), and pure Fe (solid red line) nanoparticles. ....	78
<b>Figure 5.7.</b> The proposed reaction scheme for the reduction of sodium citrate, FeCl <sub>2</sub> *7H <sub>2</sub> O and NaBH <sub>4</sub> . Addition of AgNO <sub>3</sub> at various times after the addition of NaBH <sub>4</sub> produced various core/shell morphologies.....	79
<b>Figure 5.8.</b> Room temperature VSM data showing how the magnetization is affected by the addition time of AgNO <sub>3</sub> compared to as-synthesized iron nanoparticles. ....	80
<b>Figure 5.9.</b> Representative XRD patterns of synthesized Fe, Ag, and Ag/Fe core/shell nanoparticles with their associated miller indices from JCPDS reference. ....	81
<b>Figure 5.10.</b> Utilizing magnetic core shell particles to pre-concentrate the target analyte for improved sensitivity. ....	83
<b>Figure 5.11.</b> The SERS is dominated by two intense bands at about 1,008 and 1,036 cm <sup>-1</sup> , corresponding to the ring breathing and to the triangular-deformation modes, respectively. The enhancement is seen only with the Fe core Ag shell nanoparticles. ....	84
<b>Chapter 6</b>	
<b>Figure 6.1.</b> TEM images of (A) Fe/SiO <sub>2</sub> nanoparticles and (B) Fe/SiO <sub>2</sub> /Au nanoparticles. ....	89
<b>Figure 6.2.</b> XRD patterns of (A) as-synthesized Fe/SiO <sub>2</sub> nanoparticles and (B) as-synthesized Fe/SiO <sub>2</sub> /Au nanoparticles. ....	90
<b>Figure 6.3.</b> Room temperature Hysteresis loops for (A) as-synthesized Fe nanoparticles and (B) as-synthesized Fe/SiO <sub>2</sub> /Au nanoparticles. ....	91
<b>Figure 6.4.</b> TGA analysis of Fe, FeSiO <sub>2</sub> , and Fe/SiO <sub>2</sub> /Au nanoparticles. ....	91
<b>Figure 6.5.</b> XPS spectra before (A) and after (B) annealing of Fe/SiO <sub>2</sub> /Au nanoparticles. ....	92

**Figure 6.6.** (A) Utilizing magnetic core/shell particles to pre-concentrate the target analyte for improved sensitivity. (B) SERS of the pyridine reference and Fe/SiO<sub>2</sub>/Au core/shell nanoparticles before and after heat treatment. The SERS is dominated by two intense bands at about 1,008 and 1,036 cm<sup>-1</sup>, corresponding to the ring breathing and to the triangular-deformation modes, respectively. ..... 94

## Chapter 7

**Figure 7.1.** Graph depicting the number of publications involving the polyol process as a medium for the reduction of metals, oxides, and mixed metal oxide nanoparticles. The polyol process became highly published after 2001. The results are from a combined search for “polyol process”, “polyol method”, and “metal reduction by Polyol” in the Web of Science and Scifinder databases. ..... 101

**Figure 7.2.** Proposed mechanism by Fievet. et.al. Ethylene glycol dehydrates to acetaldehyde followed by the formation of diacetyl. X represents anions such as: Cl or SO<sub>4</sub>.<sup>171</sup> ..... 102

**Figure 7.3.** Mechanism showing duplicative oxidation of ethylene glycol proposed by Patrice et al. ..... 103

**Figure 7.4.** Proposed mechanism for the formation of Metal nanoparticles from metal oxide precursors. The reaction assumes that a complete oxidation of ethylene glycol produces gaseous carbon dioxide and water. ..... 103

**Figure 7.5.** X-ray diffraction patterns of Cu salt precursors in ethylene glycol under refluxing and distillation conditions. In each case, the result is elemental Cu. ..... 106

**Figure 7.6.** TEM images of elemental Cu nanoparticles synthesized using Cu Chloride with EG and DEG under either refluxing(-R) or distillation(-D) conditions..... 108

**Figure 7.7.** The synthesis of the polyol reaction can yield various elemental Cu morphologies by simply varying the reaction medium. In the case of these 6 nanoparticles, the solvents varied from A) EG under reflux, B) EG under distillation, C) PG under reflux, D) DEG under reflux, E) DEG under distillation, and F) TEG under distillation to TEG. It is thought that the morphology is dependent on the chain length of the polyol. ..... 110

<b>Figure 7.8.</b> (1) XRD patterns of Ni nanoparticles reduced with various polyols under distillation. (2) The results of Ni chloride under refluxing conditions. A Ni-LHS forms instead of elemental Ni.....	112
<b>Figure 7.9.</b> TEM images of Ni nanoparticles reduced under various glycol environments. ....	114
<b>Figure 7.10.</b> XRD graphs of (left) Ni salts reduced under refluxing conditions and (right) Ni salts reduced under distillation conditions using EG.....	114
<b>Figure 7.11.</b> (A) Cu 2p and Ni 2p region scans and (b) reference Cu 2p and Ni 2p.....	115
<b>Figure 7.12.</b> XPS data of the C 1s region scans using different glycals.....	116
<b>Figure 7.13.</b> Representation of the crystallized counterions forming the copper-glycolate superstructure.....	120
<b>Figure 7.14.</b> The molecular structure of (I), showing the atom-numbering scheme. Displacement ellipsoids are drawn at the 40% probability level. The disordered atom O8b and methylene H atoms have been omitted for clarity. [symmetry codes: (i) -x; -y; -z (ii) -x; -y; 1-z].....	122
<b>Figure 7.15.</b> A packing diagram of (I) viewed approximately down the a axis showing the hydrogen-bonding interactions between the anionic and cationic units. H atoms not involved in hydrogen bonding and the disordered atom O8B have been omitted for clarity. [Symmetry codes: (ii) -x, -y, -z; (iii) -x, -y, 1-z; (v) 1-x, 1-7, -z; (vi) 1-x, 1-y, 1-z; (vii) x, y, 1+z.] .....	124
<b>Figure 7.16.</b> Optimized geometries for the successive binding of EG to CuCl <sub>2</sub> , a), and NiCl <sub>2</sub> , b). The incremental binding energies (IBE) in units of kcal/mol are also given. 128	
<b>Figure 7.17.</b> Plot of the calculated change in energy ( $\Delta E$ ) for each step of the proposed reaction mechanism of the Cu <sup>2+</sup> reduction pathway by the polyol process using ethylene glycol (EG) in a basic medium. ....	129
<b>Figure 7.18.</b> Plot of the calculated change in energy ( $\Delta E$ ) for each step of the proposed reaction mechanism of the Ni <sup>2+</sup> reduction pathway by the polyol process using ethylene glycol (EG) in a basic medium. ....	129
<b>Figure.7.19</b> Proposed Mechanism for (a) the reduction of CuCl <sub>2</sub> to Cu-metal and (b) the reduction of NiCl <sub>2</sub> to Ni-metal.....	130

## Chapter 8

**Figure 8.1.** TEM images and composition maps (red and blue corresponding to Cu and Ni, respectively) of typical of A,B) Cu/Ni and C,D) Ni/Cu CSNPs. The uncolored coating on the composition maps corresponds to residual organic material. .... 137

**Figure 8.2.** XRD patterns of elemental Cu, Cu/Ni, Ni/Cu, and elemental Ni. The elemental metals were prepared using the respective metal chlorides (see the Supporting Information). .... 138

**Figure 8.3.** Fourier transforms of the EXAFS signals from the Ni/Cu CSNPs, the pure metal reference foils, and their respective fits. The foil and foil fit are presented to show the expected differences in the transform. .... 139

**Figure 8.4.** EXAFS spectra of Ni/Cu CSNPs and the corresponding pure metal reference foils. .... 140

**Figure 8.5.** Room temperature hysteresis loops for the Cu/Ni (blue) and Ni/Cu (red) CSNPs. The magnetization axis has been scaled based on the ICP-OES measured composition to indicate the magnetization per gram of Ni in the sample. .... 141

## Chapter 9

**Figure 9.1.** Synthesis scheme for the design of an aqueous based Fe/FeOx ferrofluid. 147

**Figure 9.2.** (A) TEM image of magnetite/α-Fe particles prepared by the polyol process in 1,2 propanediol. The TEM shows that the particle size distribution is relatively monodispersed. (B) A histogram of the particle size from the TEM with an average particle size of 14.5 nm. .... 149

**Figure 9.3.** XRD pattern showing a two-phase system of iron oxide and α-iron. .... 150

**Figure 9.4.** XANES spectra for the ferrofluid material, iron foil, and iron oxide standards. .... 151

**Figure 9.5.** Room temperature VSM data of the as-prepared ferrofluid material plotted as magnetization (emu/g) versus applied field (Oe)..... 152

**Figure 9.6.** T<sub>2</sub>W images of a tumor-bearing rat infused with aqueous ferrofluid (0.34 mM iron concentration, 18 μL) at different time points. The infusate appears dark within the

implanted T9 tumor (right side of the tumor). Note that at 6-days post infusion, some of the iron/iron oxide particles have migrated in the tumor periphery (dark ring). ..... 154

**Figure 9.7.** (a) Proposed structure of magnetic core luminescent shell particles, (b) XRD pattern of the as synthesized particles, and (c) TEM micrograph. The scale bar is 50 nm. ..... 157

**Figure 9.8.** (a) Temperature dependence of the magnetic susceptibility  $\chi$ , (b) M vs H variations measured at 5 and 300 K for magnetic 5% Eu:YVO<sub>4</sub>, and (c) photograph indicative of the magnetic and luminescent properties of the as-prepared nanoparticles. ..... 158

**Figure 9.9.** Emission spectra of (a) conventional and magnetic core luminescent nanoparticles prepared hydrothermally, (b) the effect of varying amounts of ferrofluid, (c) the effects of varing the RE dopants, and (d) the unique signatures can be created by combining various dopants. ..... 160

## Chapter 10

**Figure 10.1.** Energy products versus coercivity of cobalt carbide nanoparticle powders compared with powders of AlNiCo and ceramic ferrites systems..... 165

**Figure 10.2.** A representative XRD scan obtained from powders processed using the polyol reduction reaction. Vertical lines corresponding to the position and amplitude of diffraction peaks from JCPDS reference powder diffraction files Co<sub>2</sub>C (65-1457) and Co<sub>3</sub>C (26-0450) are also presented. ..... 167

**Figures 10.3.** (A-C). High-resolution transmission electron microscopy images of a representative cobalt carbide sample. The insert to (A) shows an agglomerated particle cluster about 300-500 nm in diameter. Panels (A) and (B) are TEM images of rod-like Co-carbide crystals surrounded by a thin 1 to 4 nm graphite-like layer (denoted by arrows). (C) is an HRTEM image of a rod-like Co-carbide nanoparticle with an aspect ratio near 5:1. ..... 168

**Figure 10.4.** (A-C) HRTEM image of Co<sub>3</sub>C nanoparticles with orientation close to the [010] zone axis. The FFT was indexed to the Co<sub>3</sub>C phase. A simulated diffraction pattern of Co<sub>3</sub>C along the same zone axis is provided for comparison. ..... 170

**Figure 10.5.** (A-C) HRTEM images of a Co<sub>2</sub>C rich area of a nanoparticle. The FFT and a simulated FFT Co<sub>2</sub>C images are shown for comparison. ..... 171

**Figure 10.6.** Room temperature hysteresis loop of representative sample having  $M_s$  of 73 emu/g and an  $H_c$  of 3.1 kOe. The  $(BH)_{max}^3$  is 20.7 kJ/m<sup>3</sup> ..... 171

**Figure 10.7.** A plot of magnetic properties versus the phase volume ratio illustrating the interrelationship between saturation magnetization and coercivity to the volume fraction of  $\text{Co}_2\text{C}$  to  $\text{Co}_3\text{C}$  measured by X-ray diffraction. The plotted lines are intended as a guide to the eye. Error bars reflect the uncertainty in measured values. ..... 173

## List of Tables

Table 1.1. The table shows examples in the literature regarding the unique properties of particles at the nanoscale dimension.....	4
Table 2.1. Characteristic Wavelength values (in Å) for common anode materials. ....	24
Table 2.2. The correlation between quantum numbers and the notations used for spectroscopists' and x-ray.....	31
Table 4.1. Magnetization saturation ( $M_s$ ) and coercivity ( $H_c$ ) values of the various annealed alloy nanoparticles and the composition differences.....	58
Table 5.1. Fitting with Fe and B paths.....	75
Table 5.2.XPS binding energies of FeB, Fe <sub>2</sub> B, and elemental Fe core levels. ....	77
Table 7.1. Results from the analysis of the Cu XRD patterns showing the mean crystallite size, lattice strain, and lattice parameters.....	109
Table 7.2. Results from the analysis of the Ni XRD patterns showing the mean crystallite size, lattice strain, and lattice parameters.....	113
Table 7.3. Selected bond lengths(Å) for the copper glycolate structure.....	121
Table 7.4. Comparison of known ethylene glycolate and ethylene glycol complexes... ..	123
Table 7.5. Hydrogen bond geometry (Å,°) .....	125
Table 8.1. EXAFS fitting parameters for the copper and nickel edges of the Ni/Cu CSNPs and the pure metal reference foils. ....	142

## Abstract

# CORE-SHELL NANOPARTICLES: SYNTHESIS, DESIGN, AND CHARACTERIZATION

By Kyler J. Carroll, Ph.D.

A dissertation submitted in partial fulfillment of the requirements for the degree of Doctor of Philosophy at Virginia Commonwealth University.

Virginia Commonwealth University, 2010

Director: Dr. Everett E. Carpenter  
Associate Professor of Chemistry

The design of core/shell nanoparticles is of great interest for a wide range of applications. The primary focus of this dissertation is on the design and optimization of two synthetic routes. The first one is an aqueous reduction method using sodium borohydride and sodium citrate. This method was extended to design two types of core/shell nanoparticles, both of which have many applications in bio-sensing, magnetic resonance imaging, and magnetically guided SERS for the identification of environmental threats. The first, Fe/Ag core/shell nanoparticles were designed using a novel one-pot method by varying the AgNO<sub>3</sub> addition time in the system. For example, if

$\text{AgNO}_3$  is added five minutes after the start of the reaction, the already formed Fe nanoparticles serve as seeds for heterogeneous nucleation and growth of Ag nanoparticles. The result of the synthesis was 50 nanometer spherical particles with a narrow size distribution. The second type,  $\text{Fe/SiO}_2/\text{Au}$  core/shell nanoparticles were designed using a two-step method. First, 150 nanometer spherical Fe nanoparticles were synthesized followed by the addition of tetraethylorthosilicate (TEOS). This created a  $\text{Fe/SiO}_2$  core/shell nanoparticle to which  $\text{HAuCl}_3$  was added. In both cases,  $\text{Fe/Ag}$  and  $\text{Fe/SiO}_2/\text{Au}$ , the formed nanoparticles were characterized and tested for the application as SERS active materials.

The second part of this dissertation work was focused on using the polyol method to design bimetallic  $\text{Cu/Ni}$ ,  $\text{Fe/FeO}_x$ , and  $\text{Co/C}$  core/shell nanoparticles. In each case, the polyol method provided an easy one-pot reaction to synthesize these novel nanomaterials. The design of the  $\text{Cu/Ni}$  nanoparticles allowed for further insight into the polyol mechanism by independently investigating the factors that govern the formation of elemental Cu and Ni nanoparticles. By understanding the ability of the polyols to easily prepare metal and metal oxide nanoparticles, we were able to manipulate a one-pot reaction to design an aqueous ferrofluid consisting of  $\text{Fe/FeO}_x$  nanoparticles. These spherical 15 nanometer particles were studied for their potential application as MRI contrast agents. In addition, the aqueous ferrofluid served as a precursor for the design of magnetic/luminescent core/shell nanoparticles. Finally, the polyol method was extended to create  $\text{Co/C}$  nanoparticles for permanent magnet applications.

## **Chapter 1: Introduction**

## 1.1 Introduction

This dissertation work aims at the fundamental understanding of the properties of materials at the nanoscale dimension for the design and fabrication of functional nanomaterials. Such an understanding is essential for the exploitation of these properties for a range of applications such as sensors, catalysts, and renewable energy and storage devices. In this chapter, an overview of some of the recent advances in nanostructured materials and applications will be discussed. This overview is followed by a discussion of recent advances in the design of monodisperse nanoparticles through the understanding of the nucleation and growth process. Finally, a discussion on how properties are affected in the nanoscale dimension will be given.

## 1.2 Overview

The fundamental understanding of chemical, optical, electronic, and magnetic properties of materials at the nanoscale dimension has been of significant importance over the past decade. By understanding these properties, researchers have been able to design and fabricate functional nanomaterials for a wide range of technological applications such as sensors and catalysts. Significant research has demonstrated that several properties are affected by the size of the particles at the nanoscale (table 1.1).<sup>1-3</sup> For example, it has been shown that band gaps can be altered, magnetic properties can be manipulated, melting points of metals can be decreased, surfaces become more reactive, and the mechanical hardness increases dramatically with respect to their bulk counterparts. All of the properties mentioned exhibit the strongest behavior when the dimensions are less than 100 nm and decrease as the particle gets larger.<sup>1</sup> The term

nanomaterial covers various types of nanostructured materials that have at least one dimension in the range of 1-500 nm. Examples of these include metallic, semiconducting, and ceramic nanoparticles, nanowires, nanotubes, nanorods, etc. A major distinction of the nanoscale materials from their bulk counterparts is the presence of unique or improved electrical, optical, magnetic, and other physical properties, which have made them attractive components in many new and improved devices. Among many unique physical and chemical properties at the nanoscale, one basic physical property for nanomaterials is the large surface area to volume ratio. For example, in bulk materials only a relatively small percentage of atoms can be at or near the surface. When the dimensions continue to shrink to the nanoscale, the percentage of bulk atoms decreases while the surface atoms increase (Figure 1.1).<sup>2</sup> The exact proportion of atoms at the surface will depend upon the shape and surface roughness of the material as well as its composition. The enhanced surface structure and properties are important in many applications such as catalysis. It is therefore important when designing nanoparticles for applications that the size and particle morphology be uniform throughout the sample. This monodispersity has been a goal of many material syntheses over the past decade. For the purpose of simplicity, monodisperse will be defined as having a narrow size distribution with a standard deviation under 15%. Much of the current research to date is striving to produce nanoparticles with a monodisperse size distribution by controlling the nucleation and growth steps.<sup>3</sup>

**Table 1.1.** The table shows examples in the literature regarding the unique properties of particles at the nanoscale dimension.

Property	Description	References
Magnetism	Magnetic properties of nanoparticles	4-5
	Oxide-metal core/shell particles	6-7
Optical	Band gap changes in semiconductors	8-11
	Plasma resonances in metals	12-25
Melting points	Photoluminescence in indirect band gap semiconductors	26
	Sodium gas phase clusters	27
Surface chemistry	Gold particles	28
	Metals and molecular crystals	29-30
Mechanical	Semiconductor crystals	31
	Destructive adsorption of $\text{CCl}_4$	32
Metallic behavior	Adsorption of acid gases	33
	Reaction with $\text{AlEt}_3$ , pyridine	34
Mechanical	Increased hardness of metals	35
	Increased ductility of ceramics	36-37
Metallic behavior	One electron energy gaps	38

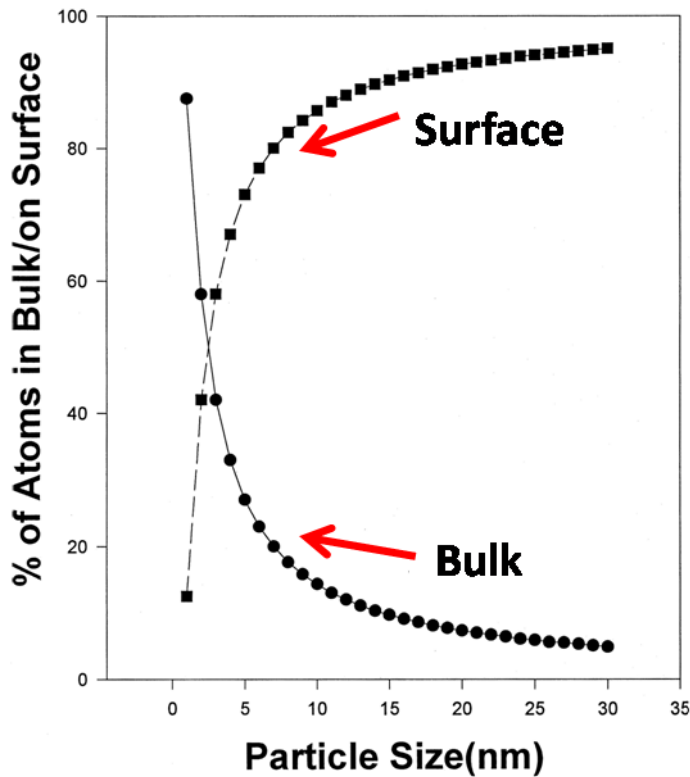


**Figure 1.1.** Calculated surface to bulk ratios for solid metal particles versus size.<sup>39</sup> The % of surface atoms increases while the % of bulk atoms decrease when going to nanometer scales.

### 1.3 Nucleation and Growth

Simultaneous nucleation and growth results in a relatively large size distribution and non-uniform nanoparticles, thus separating these two steps is an important aspect to the uniform growth of nanometer size crystals. Nanoparticles have been used for many years; however, it was not until Ostwald and LaMer that we could understand how and why particles form. The study of the crystallization process, by Friedrich Wilhelm Ostwald in 1897, led to the popular explanation called the Ostwald rule of stages. It states that the formation of crystals occurs in stages and in general the first product is usually not the most thermodynamically stable product but rather a kinetic metastable product that

closely resembles that of the solvent.<sup>40</sup> Eventually, the product grows into a more thermodynamically stable form.

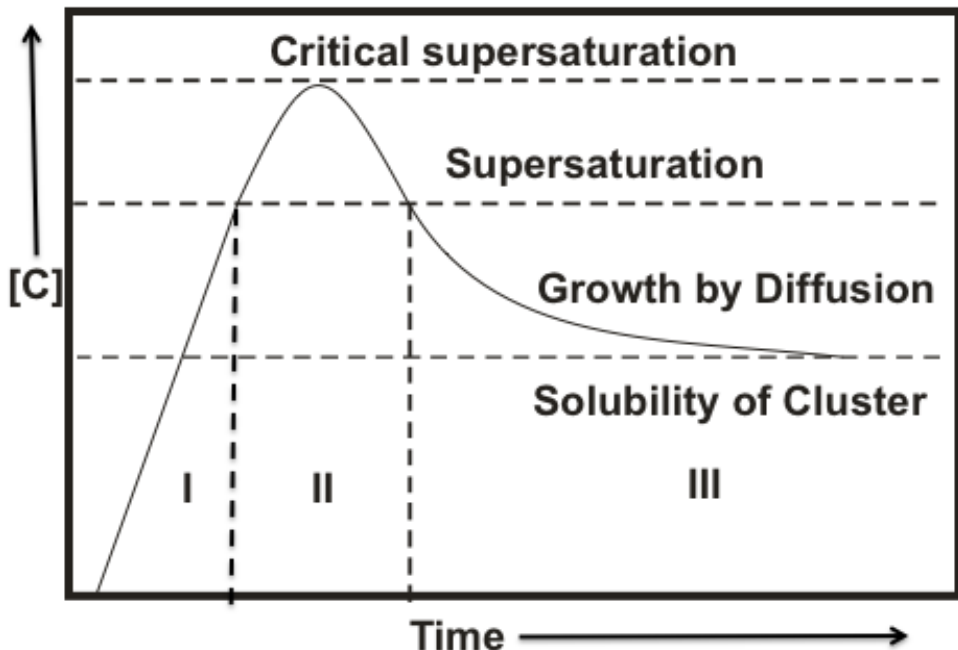


**Figure 1.2.** LaMer crystallization model. 3-step crystallization model for homogeneous nucleation and growth: I. Pre-nucleation period; II. Nucleation; III. Growth .

In 1952, Victor Kuhn LaMer proposed that crystallization was a diffusion-driven process.<sup>40</sup> He also introduced a very useful graph that allows for a visual inspection of crystal growth by homogeneous nucleation (Figure 1.2).<sup>41</sup> The model is divided into three steps. Initially, the reactive material in solution builds until a critical concentration, termed supersaturation. Once this point is reached, the materials begin to collide and form clusters. As the clusters become stable, they allow nucleation to occur, which creates the first stable nuclei. A critical supersaturation is reached when the concentration of free material no longer increases and eventually starts to decrease. This point is termed the critical supersaturation point. The suppression of the supersaturation occurs when

there is no longer any free material and the stable nuclei begin to grow. The growth follows diffusion kinetics and Ostwald ripening.<sup>40</sup> Separation of the nucleation step from the growth step will enable increased control of particle size, shape, and morphology. However, the separation of these two steps has been complicated and is not a routine factor to control.

#### 1.4 Electronic properties

The understanding of the electronic properties of nanomaterials has attracted a great deal of interest over the past decade. While the electronic structures of atoms, molecules and single crystalline bulk materials have been well established, there was limited knowledge regarding the electronic structures of nanoscale counterparts until recently. It is predicted, in both theoretical and experimental papers, that metal semiconducting nanoparticles in the size range of 1-10 nm can display unique quantum effects, leading to properties that are different from those of bulk metals.<sup>42</sup> As the particle size decreases below the Bohr radius of the semiconductor material, the electron becomes more confined in the particle. This leads to an increase in the band gap energy and the valence and conduction bands break into quantized energy levels. For example, Figure 1.3 shows the effect of changing the particle size of CdSe nanoparticles. The band gap emission shown is observed to shift through the entire visible region, from red emission for the largest particles, to blue emission for the smallest clusters. The significance of nanoscale quantum confinement of the electrons provides visualization of the shift in the characteristics of the material depending on the size of the nanoparticles. These effects

have been reported to create novel applications that have been used over the past decade.<sup>43-45</sup>

## Quantum Dot Nanoparticles



**Figure 1.3.** Fluorescence emission of CdSe(ZnS) quantum dots of various sizes(image is adapted from reference).<sup>46</sup>

### 1.5 Optical properties

As with the electronic properties, the optical properties of nanomaterials differ remarkably from bulk materials. This difference can be mainly attributed to the quantum confinement effects, unique surface phenomena, and efficient energy and charge transfer over nanoscale distances within nanomaterials. These phenomena result from localized surface plasmons, where the finite volume given by the geometry of the nanoparticle binds the plasma oscillations of free electrons in the metal. Surface plasmon excitation occurs when a photon is absorbed and transfers energy into the collective oscillations of conduction electrons that are coupled in-phase with incident radiation. For Au and Ag nanoparticles, these resonant frequencies occur in the visible wavelengths, giving rise to the brilliant colors associated with their colloidal solutions. One of the most popular examples demonstrating the unique optical properties of nanoscale materials is the Lycurgus Cup from the 4<sup>th</sup> century AD.<sup>47</sup> The origin of the color difference in the cup is

attributed to the optical response of colloidal nanoparticles of gold dispersed in the glass. The current ability to exploit similar optical properties of nanomaterials has sparked interest in exploring application in sensing, biomedical imaging, and photonic devices. These explorations have been facilitated by the establishment of many synthetic methods for constructing different nanomaterials with controlled sizes and shapes.<sup>13,21,48-55</sup> The optical properties can be tailored by controlling the nanocrystal dimensions in terms of size, shape, and surface properties. The shape of the nanocrystal determines surface plasmon frequency, amplitude, and polarity.

### **1.6 Magnetic properties**

The study of magnetic properties of materials at the nanoscale is an important area for the advancement of nanoscience and nanotechnology. Part of the motivation can be attributed to the fact that the nanoscale magnetic properties differ from their bulk counterparts. Magnetic nanoparticles in the size range of 1-100 nm have attracted a great deal of interest due to their technological importance. The research has evolved to develop nanoparticles in applications such as magnetic resonance imaging (MRI) for medical diagnosis, high-density magnetic recording, magneto-optical switches, and controlled drug delivery.<sup>56-59</sup> In a basic sense, all materials can be divided into three categories according to their interaction with an external magnetic field: diamagnetism, paramagnetism, and cooperative magnetism. The last category, cooperative magnetism, involves several sub-subcategories: ferromagnetism, ferrimagnetism, and antiferromagnetism.

### 1.6.1 Introduction to Magnetism

In an atom, the electron possesses a spin that is equivalent to the strength of the magnetic field (magnetic moment) of the electron itself. Electrons are arranged in energy states of successive order, and for each energy state there can only be two electrons of opposite spins as established by Pauli's principle. The orbital motion of an unpaired electron around the nucleus and the spin of the electron about its own axis can generate magnetic moments. The magnetic moment of each electron pair in an energy level is opposed and consequently, whenever an energy level is completely full there is no net magnetic moment. Based on this reasoning, we expect any atom of an element with an odd atomic number to have a net magnetic moment from the unpaired electron. In most of the elements, the unpaired electron is in the valence shell and can interact with other valence electrons leading to the cancellation of the net magnetic moment in the material. However, certain elements such as cobalt and nickel have an inner energy level that is not completely filled, i.e., each atom in the metal has a permanent magnetic moment, equal in strength to the number of unpaired electrons.

### 1.6.2 Diamagnetism

**Diamagnetism** refers to a material that exhibits a negative magnetism. Even though the substance is composed of atoms that have no net magnetic moment (paired electrons), it reacts in a particular way to an applied field. Wilhelm Weber and Paul Langevin theorized that an applied field acts on a single electron orbit to reduce the effective current of the orbit, in turn producing a magnetic moment that opposes an

applied field.<sup>4</sup> Common diamagnetic materials are water, wood, most organic compounds and in the case of this work copper.

### 1.6.3 Paramagnetism

In other cases, atoms whose shells contain electrons with spins that are not compensated by another electron of an opposing spin will have a resultant magnetic moment; this is due to the unpaired electrons. These moments tend to align (positively) with the applied field; however, they are kept from total alignment by thermal energy. This scenario is referred to as **paramagnetism**.

### 1.6.4 Cooperative magnetism

Lastly, if the atoms are in close enough contact with each other so that the electrons can be exchanged between neighboring atoms, a cooperative magnetization may occur which spontaneously aligns all atoms in a lattice and creates a synergistic and strong magnetic moment. When the spins between neighboring atoms are aligned parallel, the material is said to be **ferromagnetic**. In some cases, the spins between neighboring atoms are anti-parallel and are referred to as **antiferromagnetic**. In antiferromagnetic materials, the resultant magnetization is small because the opposite spins cancel each other out. Lastly, if two atoms have anti-parallel magnetization of unequal magnitude a resultant magnetization remains in the direction of the stronger magnetic moment and applied field. This is referred to as **ferrimagnetism**. Figure 1.4 summarized the above-described behavior of materials when a magnetic field is applied.

Type of Magnetism	Applied Magnetic Field
Diamagnetism	
Paramagnetism	
Ferromagnetism	
antiferromagnetism	
Ferrimagnetism	

**Figure 1.4.** The types of magnetism seen in materials. Blue Arrows signify the direction of the applied field. Blue arrows in the black circle signify the direction of the electron spin.

## 1.7 Design and Synthesis of Monodisperse Nanoparticles

As mentioned in a previous section, the complete separation of nucleation and growth is critical for the successful production of monodisperse nanoparticles. These nanoparticles, in which a large fraction of atoms are on the surface, have an increased surface energy due to lattice strain, surface vacancies, and coordination deficiency. These surface effects and large surface area have proven to result in the high reactivity required for increased catalytic performance.<sup>60-68</sup> However, in applications where the magnetic and optical properties are exploited, a key challenge is minimizing the oxidation of nanoparticles. Oxidation occurs rapidly when the nanoparticles are exposed to an oxygen rich environment because of oxygen's ability to coordinate with metals and minimize the overall surface energy. In the last decade, significant progress has been made to provide different synthetic techniques for the design of monodisperse monometallic, bimetallic, and core/shell nanoparticles.

Several research groups, such as Park et al. and Sun et al., have shown novel procedures for the synthesis of monodisperse nanoparticles of metals and metal oxides.<sup>69-73</sup> In some cases, to produce stable nanoparticles it is necessary to terminate the particle growth and to stabilize the surface. To accomplish stability, researchers are able to control the nucleation and growth process by introducing surfactants and capping agents such as sodium oleate, oleic acid, trioctylphosphine (TOP), and polyvinylpyrrolidone (PVP). For example, Park et al. has shown that by using a metal chloride precursor with sodium oleate, an intermediate metal-oleate complex is formed.<sup>74</sup> When this complex is heated, using thermal decomposition techniques, the resulting products are monodisperse

nanoparticles. While the production of monometallic nanoparticles is useful for catalytic activity, it has been shown that bimetallic nanoparticles offer greater reactivity. Sun et al. highlighted the synthesis of monodisperse FePt nanoparticles by also using thermal decomposition and utilizing both oleic acid and oleyl amine as surfactants.<sup>75</sup> In their process, they also found that the surfactants prevented the particles from oxidation.

### 1.7.1 Polyol Process

The polyol process refers to a polyalcohol that acts not only as a solvent, but also as a mild reducing agent and when coupled with a base, it serves as a perfect medium for the reduction of metal salt precursors. In this process, a solid inorganic precursor is suspended in a liquid polyol. The suspension is stirred and heated to a given temperature, which can reach the boiling point of the polyol for less easily reducible metals. The starting materials can range from hydroxides (eg: Cu(OH)<sub>2</sub>), nitrates (eg: AgNO<sub>3</sub>), oxides (eg: Cu<sub>2</sub>O), chlorides (eg: FeCl<sub>2</sub>), to acetates (eg: Ni(CH<sub>3</sub>COO)). The reduction to metal can be achieved in various polyols such as ethylene glycol, propylene glycol, diethylene glycol, trimethylene glycol, butylene glycol, and trimethylene glycol (Figure 1.5).

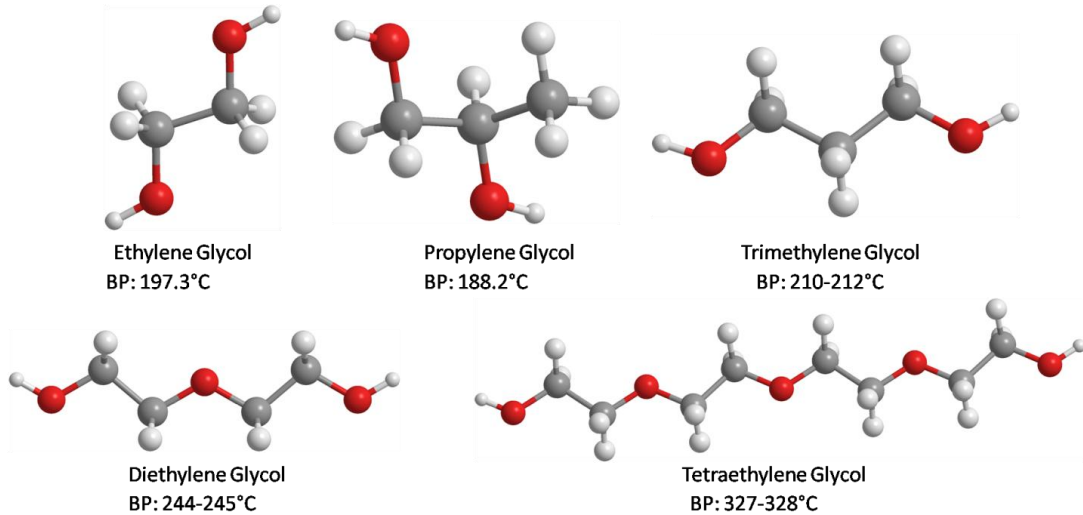


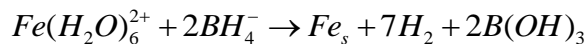
**Figure 1.5.** Various polyols used for the reduction of metal salt precursors. Varying the hydroxyl sites has an effect on the overall reduction potential of the polyol along with a boiling point change.

Different polyols are chosen depending on the reduction potential of the metals; easily reducible metals which do not require high heat can be reduced in butylene glycol, while less easily reducible metals require higher temperatures and tetraethylene glycol is required. Fievet et. al. proposed that the reduction of metals in a liquid polyol medium occurs by dissolution of the metal salt precursor, reduction by the polyol of the dissolved species, and nucleation and growth of the metal particles from the solution. This dissertation work aims to exploit the previous synthetic methods for the preparation of Cu, Ni, Co, Fe, and Fe oxide, nanoparticles for the preparation of novel core/shell nanoparticles for the investigation in magnetic and bio-sensing applications.

### 1.7.2 Aqueous Reduction by borohydride

Aqueous reduction of transition metals, specifically Fe, Cu, and Ni, using sodium borohydride has been used as a simple method for producing amorphous nanoparticles

over the past decade.<sup>76-83</sup> Glavee et al. in 1992 first presented the synthesis for the preparation of Cu metal nanoparticles and studied the kinetic effects of the aqueous method. More importantly however, in 1995, they reported on the facile synthesis of Fe nanoparticles by the aqueous method; this has been one of the simplest methods for producing Fe nanoparticles. Specifically, iron(II) sulfate or iron(II) chloride are dissolved in distilled water, where it dissociates into  $\text{Fe}^{2+}$  and  $\text{SO}_4^{2-}$  or  $\text{Cl}^-$  ions. The  $\text{Fe}^{2+}$  ions then form an aqua complex with six water molecules. The  $\text{Fe}^{2+}$  is reduced to  $\text{Fe}^0$  by the use of a reducing agent, sodium borohydride, which dissociates into  $\text{Na}^+$  and  $\text{BH}_4^-$  ions. The borohydride ion is then oxidized and forms  $\text{B(OH)}_3$  and the iron is reduced to elemental Fe by the reaction:



The resulting Fe atoms undergo nucleation and growth, as described in a previous section, and eventually grows into clusters of various morphologies. In addition, depending on the acidity and oxygen content of the water, the particles will oxidize forming  $\text{Fe}_2\text{O}_3$ . Glavee et al. have also shown that in some cases, where the amount of water was varied in the reaction, FeB and  $\text{Fe}_2\text{B}$  was formed by an alternate mechanism<sup>80</sup>:



While a simple synthesis was reported, protecting the particles from eventual oxidation has been a challenge. The particles can be protected from significant oxidation by performing the reaction carefully in de-oxygenated water. However, the oxidation and agglomeration has been still a significant problem associated with the borohydride

reduction. As with the previously mentioned reactions, surfactants may help by stabilizing the particles from oxidation and growth. Recently, Ekeirt et al. reported on the synthesis of elemental Fe nanoparticles by using sodium citrate as a surfactant.<sup>84</sup> Through several trials, they found that the optimum Citrate to Fe ratio ( $[{\text{Cit}}]/[{\text{Fe}}^{2+}]$ ) of 10/1 produced 100 nm clusters of 5 nm alpha-Fe nanoparticles. They also have hypothesized that the 100 nm clusters were protected from oxidation by a citrate shell formed around the particle, even in highly oxygen-rich environments. This dissertation work aims to utilize the synthesis of Fe nanoparticles by the reduction of  $\text{FeSO}_4$  described by Ekeirt and Glavee et al. for the preparation of various bimetallic, and core/shell nanoparticles to study their magnetic and optical properties.

### 1.7.3 Design of Core/Shell nanoparticles

As described above, the surface chemistry and reactivity of materials at the nanoscale becomes important and can govern their magnetic, electronic, and optical properties. It is therefore very critical to develop new techniques to control the surface chemistry of the resulting nanomaterials. The study of the reaction of these nanoparticles with a variety of functionalized alkanes including alcohols, thiols, and silanes along with other metals and metal oxides to produce particles with core/shell structures has been an important area of research. Several reports in the last decade have reported on the synthesis of  $\text{Fe}/\text{Fe}_3\text{O}_4$ , gold and silver-coated iron oxide ( $\text{Fe}_2\text{O}_3$  or partially oxidized  $\text{Fe}_3\text{O}_4$ ), and  $\text{Fe}_3\text{O}_4/\text{SiO}_2$  core/shell nanoparticles.<sup>85-87</sup> Also, others have reported on the synthesis of magnetic core  $\text{Ag}/\text{Ni}$  and  $\text{Au}/\text{Ni}$  for the investigation of the magnetic tunability by manipulating the size of core and shell.<sup>88</sup>

The motivation of this work involving the design and synthesis of core/shell nanoparticles of Cu/Ni, Co/C, Fe/Fe<sub>3</sub>O<sub>4</sub>, Fe/Fe<sub>3</sub>O<sub>4</sub>/Eu:YVO<sub>4</sub>, Fe/Ag, and Fe/SiO<sub>2</sub>/Au largely stems from the realization of some of the important properties. These properties include enhancement of chemical stability by protecting the magnetic core from oxidation and corrosion, biocompatibility, and recyclable SERS active and luminescent materials for CBRNE detection. In an effort to address these challenges, through the design and modification of well-established synthetic techniques, this dissertation work aims to investigate the mechanistic processes involved in the formation of the core/shell nanoparticles.

There are many applications of core/shell nanoparticles with a magnetic component. In these applications, the shell component exploits unique electronic, magnetic, catalytic, and chemical or biological sensing properties. When exploring the magnetic properties, recent studies include the formation of magnetic core/shell nanoparticles with controllable self-assembly for achieving enhanced stability and construction of ordered arrays for information storage.<sup>75</sup> In the recent exploration of the unique catalytic properties of nanoscale Au and Ag, it was reported that nanoparticles supported on iron oxide exhibit excellent catalytic properties for water-gas shift reactions.<sup>89</sup> Also, in the area exploring applications of magnetic nanoparticles in biology and medicine, the use of magnetic nanoparticles for magnetic resonance imaging offer the ability to alter the contrast of certain cell types by several orders of magnitude.<sup>56,90</sup> All of these applications have indicated that the ability to control the surface and interparticle spatial properties (monodispersity) of magnetic nanoparticles are important for the

advancement of many applications. The advancement of these and related technological applications can be facilitated by the development of new synthetic strategies for the control of particle size, composition, and surface chemistry of single component and core/shell magnetic nanoparticles.

### **1.8 Summary of Objectives:**

The overall goal of this dissertation work is to develop and design novel synthesis strategies for the fabrication and characterization of nanomaterials for various applications. Such applications for the materials synthesized in this dissertation include chemical sensing, MRI contrast agents, catalysis, and permanent magnets. Some key objectives of this dissertation work are:

- 1) Develop new strategies for the synthesis and assembly of magnetic core/shell nanoparticles of elemental Cu and Ni nanoparticles. Also, combine our experimental measurements and computational modeling to gain insight into the mechanism of the polyol method.
- 2) Develop new strategies for the synthesis of core/shell nanoparticles of Fe/Fe<sub>3</sub>O<sub>4</sub> for the use as MRI contrast agents and the design of magnetic/luminescent core/shell nanoparticles for environmental applications.
- 3) Develop new high performance permanent magnet nanoparticles using the polyol method.
- 4) Develop new strategies for the synthesis and assembly of core/shell nanoparticles with both magnetic and optical properties for applications in SERS.

## **Chapter 2: Characterization Techniques**

## 2.1 Introduction

The characterization of nanomaterials is extremely important to all researchers. From developing a new synthetic technique to testing the quality control of an existing technique, characterization aids in the correct identification of phases, impurities, and surface chemistry effects. Because of its importance to the advancement of quality scientific research, the following chapter will review some basic principles of the characterization techniques used in this research. Some sections, because of the ubiquity of the technique, have been described in less detail. If the reader finds the need for more description, the referenced material from this chapter is located at the end of the dissertation and can provide additional information.

Technique	Details	Cost and Data Analysis
X-ray Absorption Spectroscopy (XAS)	XANES- Oxidation state EXAFS-Nearest neighbor interactions/bonding, Crystallite size (tends to be smaller)	Expensive, not easily available, tedious data refinement
X-ray Photoelectron Spectroscopy (XPS)	Surface Chemistry Oxidation state information	In house(relatively inexpensive), High energy (Expensive, not easily available), data analysis easy and cheap
X-ray Diffraction (XRD)	Crystal structure, grain size (Scherer equation)	In house (Inexpensive), easy to refine
Neutron Diffraction (ND)	More information on bonding and crystal structures	Expensive, hard refinement
Infrared Spectroscopy (IR)	Ligands and mechanistic information	Cheap, easy to refine
Ultra-violet visible Spectroscopy (UV-VIS)	Ligands	Cheap, easy to refine
Microscopy (TEM,SEM,AFM)	Particle morphology and size	In house (relatively expensive), easy

**Figure 2.1.** Typical techniques used to characterize nanomaterials.

## 2.2 X-ray Diffraction (XRD)

During the course of this research, powder XRD was used for phase identification, identifying the purity of samples, and determining the crystallinity of products. It was used for compositional analysis and as a probe into the structural properties of crystals, amorphous samples, and layered systems. By comparing the position of the peaks in the diffracted beam to the standards provided by the Joint Committee on Powder Diffraction Standards (JCPDS) and the International Center for Diffraction Data (ICDD) the unknown phases present in each sample were identified.

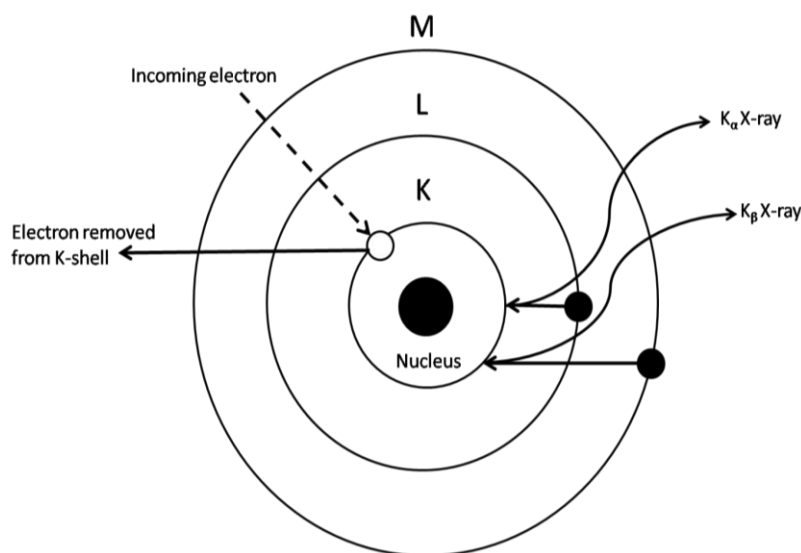


**Figure 2.2.** Schematic illustrating the process of an ejection of a core electron and the resulting x-ray emissions by electrons filling the ejected electron hole.

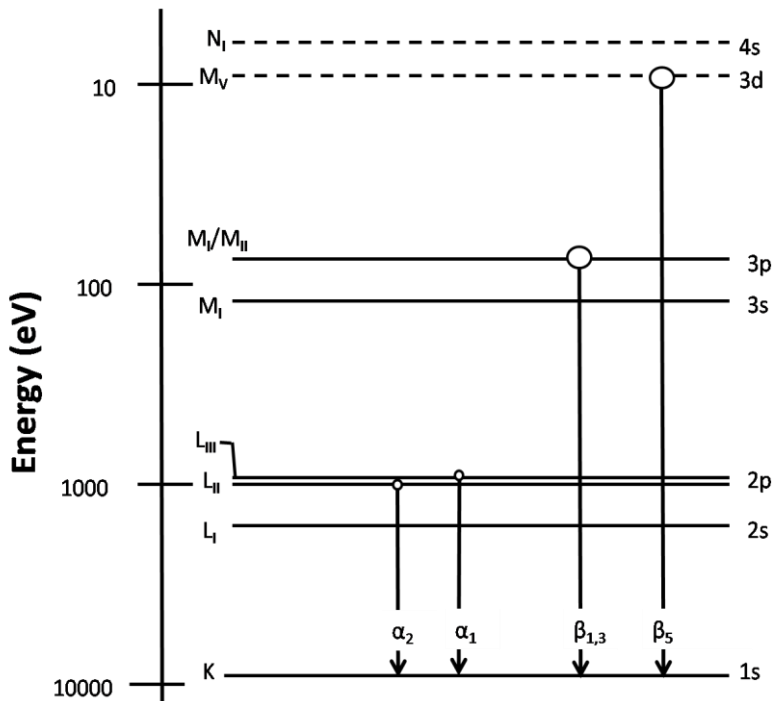


**Figure 2.3.** Figure illustrates that each energy level emits a characteristic x-ray by the relaxation process.

X-rays are produced by a beam of fast electrons bombarding a metal target in an evacuated tube. The energetic electrons excite the target atoms, which subsequently emit high frequency electromagnetic radiation as they decay back to their ground states. The emitted x-rays are characteristic for the target material and usually consist of a few strong lines. Cu and Mo are the most widely used target metals; however, other anodes are also used. Table 1 shows characteristic wavelength values for common anode materials. The resulting beam is then filtered by using a monochromating crystal, which allows the passage of the  $K_{\alpha 1}$  and  $K_{\alpha 2}$  x-rays with wavelengths of 1.5405 Å and 1.544 Å respectively. The intensity ratio for the  $K_{\alpha 1}$  and  $K_{\alpha 2}$  x-rays is approximately 2:1 and the weighted average of the radiation is 1.5418 Å.<sup>91</sup>

**Table 2.1.** Characteristic Wavelength values (in Å) for common anode materials.

Anode	$K_{\alpha 1}$	$K_{\alpha 2}$	$K_{\beta}$
Cu	1.5406	1.54439	1.3922
Mo	0.7093	0.71359	0.63229
Cr	2.2897	2.29361	2.08487
Co	1.78897	1.79285	1.62079
Fe	1.93604	1.93998	1.75661

### 2.2.1 Bragg's Law

X-rays are a form of electromagnetic radiation that have high energies and short wavelengths. When a beam of x-rays hit a material, a portion of the beam will be scattered in all directions from the material and constructively interfere in distinct directions based upon the symmetry of the repeating crystal structure associated with the material (Figure 2.3). The angles where the peaks in the x-ray diffraction spectrum occur obey Bragg's law:

$$n\lambda = 2d_{(hkl)} \sin \theta$$

Where  $\lambda$  is the wavelength of the x-ray beam,  $d_{(hkl)}$  is the spacing between the  $(hkl)$  crystallographic plane contributing to the diffraction peak,  $\theta$  is the angle of diffraction, and  $n$  is an integer. The Bragg condition indicates the angular positions at which only constructive interference can be found. If Bragg conditions are not satisfied, then the interference will be nonconstructive and will yield a very low intensity diffracted beam. In a typical x-ray diffraction study, a range of  $\theta$  is scanned to find the Bragg reflection angles and determine the lattice spacing (Figure 2.4).

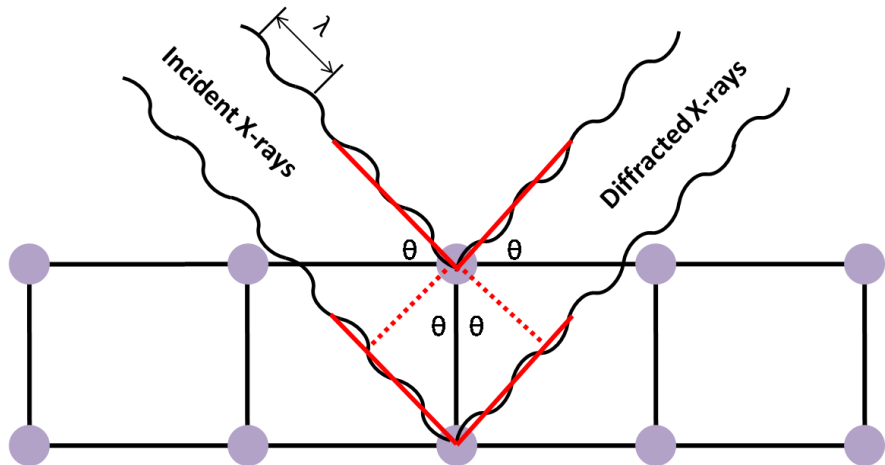


**Figure 2.4.** Diffraction of x-rays by planes of atoms.

After the phase of the material was determined, the XRD patterns were then used to investigate the structural nature of the material, for example, the size and crystallinity of the particles. A material's structural nature can be either crystalline or amorphous. Crystalline materials have sharp constructive diffraction lines in their XRD patterns and have minimal microstrain associated with the peaks, while amorphous materials have more diffuse diffraction lines due to a lack of atom-to-atom long range ordering. There are also many factors that may contribute to the broadening of diffraction lines, which makes the analysis of XRD patterns difficult. For example, instrumental broadening, microstrain (lattice strain), powder inhomogeneity, and temperature are a few contributions that can convolute a diffraction pattern. Broadening in the diffraction pattern can also occur with a reduction in particle or crystallite size. Peak width due to crystallite size varies inversely with crystallite size. So as the crystallite size gets smaller, the peaks get broader. Paul Scherrer, who is most famous for his equation for crystallite broadening, first realized this in 1918.

$$B(2\theta) = \frac{K\lambda}{L \cos \theta}$$

In his equation, B refers to the peak width, typically referred to as the full width at half maximum (FWHM) of the diffraction peak. B is inversely proportional to the crystallite size L, K is the Scherrer constant, typically 0.94 for spherical particles with cubic symmetry,  $\lambda$  is the wavelength of irradiation, and  $\theta$  is half the diffraction angle. Crystallite broadening is most pronounced at large angles of  $2\theta$ ; however, lattice strain and instrumental broadening is largest at a larger  $2\theta$ . In addition, to make this more difficult, peak intensity is usually the weakest at these larger angles. Typically, to get the best calculation of crystallite size, peaks between 30 and 50  $2\theta$  are analyzed.

### 2.2.2 X-ray diffractometer

The diffractometer used to obtain x-ray diffraction patterns for this work was a Panalytical X'pert pro. A copper anode was used as the source of x-rays with a current of 45 mA at an accelerating voltage of 40 kV. As described previously, the copper source emits x-rays with  $K\alpha 1$  and  $K\alpha 2$  wavelengths of 1.5405 Å and 1.544 Å respectively. A continuous scan mode is employed, in which the x-ray source and the x-ray detector continuously repeat the  $2\theta$  range, utilizing a Bragg-Brentano scattering geometry. The dried powder samples were gently ground using a mortar and pestle and then pressed onto a low background, low volume holder using a Fisherbrand pre-cleaned microscope slide. The sample holder was then placed in the instrument for XRD analysis. Upon completion of the run, the data were analyzed in the Highscore plus program, which has a

built-in diffraction library to compare the sample's diffraction pattern to the diffraction patterns in the JCPDS-ICDD database.

### **2.3 Transmission Electron Microscopy (TEM)**

Transmission electron microscopy (TEM) was used in this work to determine the size, shape, and arrangement of the particles produced from the reactions. The TEM analysis done for this work was performed at various institutions. For routine TEM analysis, the work was performed at the VCU Department of Anatomy and Neurobiology Microscopy Facility, which was supported in part, with funding from NIH-NINDS center core grant (5P30NSD47463-02). To obtain TEM images, a JEOL CM120 Transmission Electron Microscope (TEM) fitted with a Gatan digital camera was utilized. Samples were mounted on a 300 mesh lacey carbon TEM grid. The particles were first ultrasonicated in solution for about 10 minutes. After sonication, a small pipette was used to transfer a drop ( $7\mu\text{L}$ ) of each nanoparticle solution onto a grid. After drying, the grid was mounted in the instrument.

When analyzing the TEM image, both light and dark areas will be visible. The lighter areas are where the material is less dense and more electrons have passed through. The darker areas are where the material has greater electron density and fewer electrons have been transmitted. The materials the electrons are passing through in this work are both organic and inorganic in nature and have low and high electron densities, respectively. From the TEM images, one can determine the size, shape, and arrangement of the inorganic nanoparticles in the sample.

## 2.4 X-ray Photoelectron Microscopy (XPS)

X-ray photoelectron spectroscopy (XPS) was used in this work to analyze chemical state information for the resulting nanoparticles. All XPS analysis done for this work was performed at the VCU Nanomaterials Characterization Center (NCC).

X-ray photoelectron spectroscopy (XPS) was performed on a Thermo Scientific ESCALAB 250 microprobe with a focused monochromatic Al K $\alpha$  x-ray (1486.6 eV) source and a 180° hemispherical analyzer with a 6-element multichannel detector (Figure 2.5). The incident x-ray beam is 45° off normal to the sample while the x-ray photoelectron detector is normal to the sample. Charge compensation is employed during data collection by using an internal flood gun (2 eV electrons) and a low energy Ar $^+$  external flood gun. Depth profiling experiments were conducted with a high energy Ar $^+$  EX05 ion gun. Binding energies of the photoelectron are corrected to either the aliphatic hydrocarbon C 1s peak at 284.6 eV or the Ag3d<sub>5/2</sub> peak at 368.3 eV, depending on the sample composition. A large area XL magnetic lens with a 500  $\mu\text{m}$  spot size in constant analyzer energy (CAE) mode is typically utilized with a pass energy of 20 eV. Thirty scans per region are taken with a step size of 0.100 eV. Powdered samples are pressed onto a strip of indium foil and mounted onto a sample holder using double-sided adhesive carbon tape.

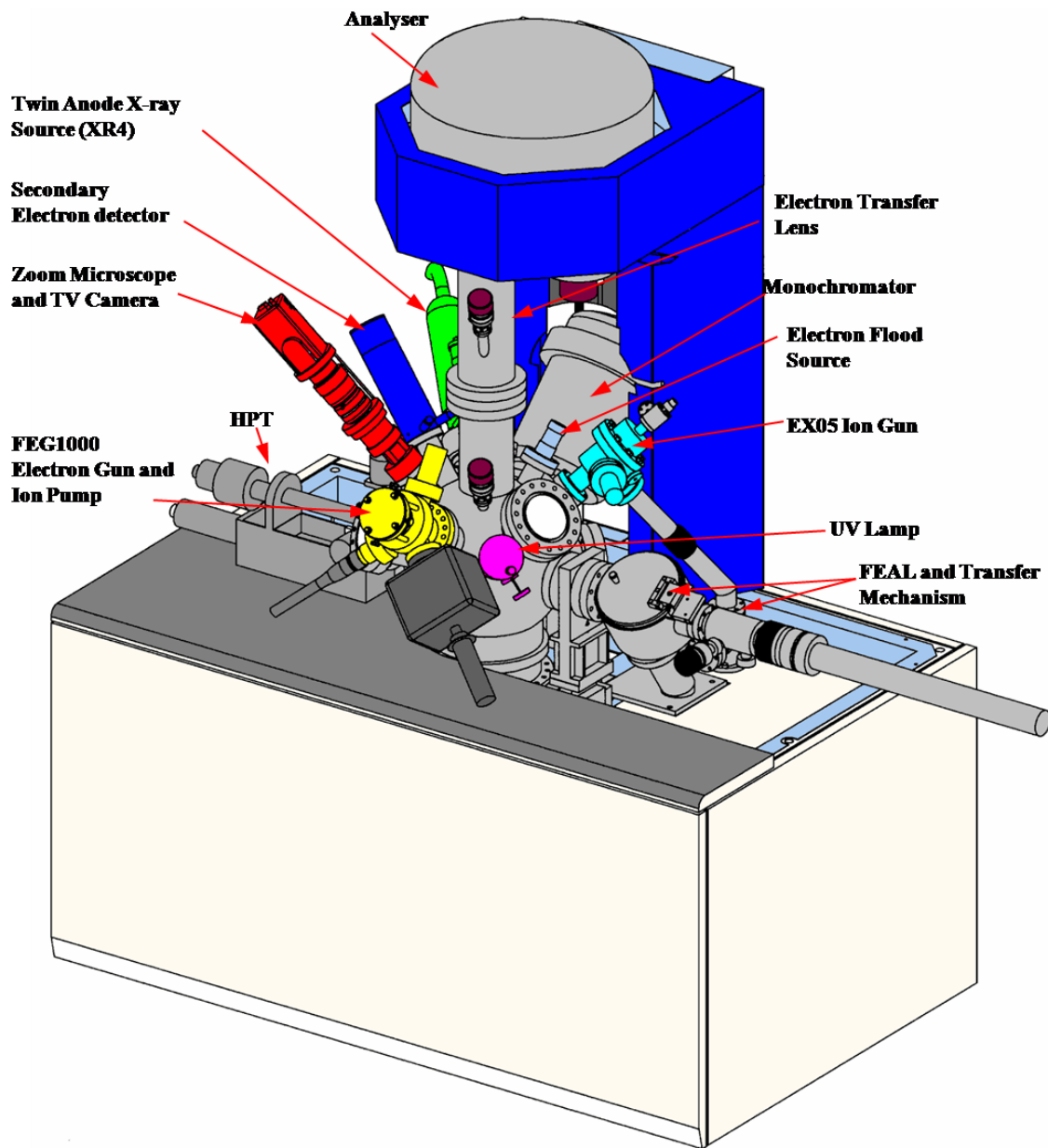


**Figure 2.5.** Schematic of the ESCAlab 250 spectrometer used at Virginia Commonwealth University.

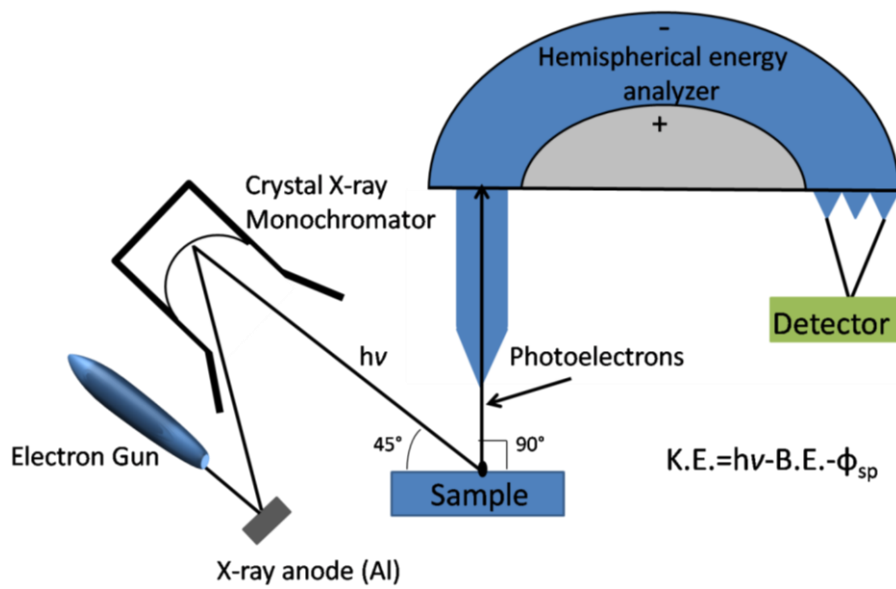


**Figure 2.6.** A schematic diagram of a typical XPS spectrometer using a monochromatized single anode X-ray source. The key components of the spectrometer are identified.

#### 2.4.1 Notation

In XPS analysis, it is important to identify the photoelectrons that are emitted from a sample. In order to do this, it is necessary to have some idea about how to describe which electrons are involved with each transition; XPS users commonly use the spectroscopists' notation.

In this notation, the photoelectrons observed are described by means of their quantum numbers. Transitions are typically labeled according to the scheme  $nl_j$ . The first part of this notation is the principle quantum number,  $n$ . The second part,  $l$ , is the orbital angular momentum of the electron. The third part,  $j$ , is the added vector product of the two angular momenta using the expression,  $j = |l + s|$ .

**Table 2.2.** The correlation between quantum numbers and the notations used for spectroscopists' and x-ray.

quantum numbers				Spectroscopists' notation	X-ray notation
<i>n</i>	<i>l</i>	<i>s</i>	<i>j</i>		
1	0	+1/2,-1/2	1/2	1s <sub>1/2</sub>	K
2	0	+1/2,-1/2	1/2	2s <sub>1/2</sub>	L <sub>1</sub>
2	1	+1/2	1/2	2p <sub>1/2</sub>	L <sub>2</sub>
2	1	-1/2	3/2	2p <sub>3/2</sub>	L <sub>3</sub>
3	0	+1/2,-1/2	1/2	3s <sub>1/2</sub>	M <sub>1</sub>
3	1	+1/2	1/2	3p <sub>1/2</sub>	M <sub>2</sub>
3	1	-1/2	3/2	3p <sub>3/2</sub>	M <sub>3</sub>
3	2	+1/2	3/2	3d <sub>3/2</sub>	M <sub>4</sub>
3	2	-1/2	5/2	3d <sub>5/2</sub>	M <sub>5</sub>

#### 2.4.2 Charge Compensation

The need to analyze both insulating and conducting materials is common in XPS. A problem arises however, when the photoemission from an insulating material causes electrostatic charging to occur.<sup>92</sup> This charging phenomenon results in peak shifting, typically in the direction of higher binding energy and sometimes results in a complete loss of data. To prevent this from occurring, charge compensation is necessary and two flood gun sources are used; An internal flood gun utilizing low-energy electrons (typically 2 eV electrons) and an external flood gun utilizing Ar<sup>+</sup> ions. In a basic sense, the electrons are used to alleviate the buildup of positive charge on the surface, while the low energy Ar<sup>+</sup> ions help to center the electrons and avoid peak broadening due to overcompensation. The use of low energy electrons is also important, as to not damage the surface being analyzed, but must be of a high enough flux to compensate for the

charging.<sup>93</sup> Throughout this work, charge compensation was used due to the need for analyzing oxide layers and surfactant coatings.

#### 2.4.3 Depth Profiling

While XPS is a surface analysis method, it is possible to use it to provide compositional information as a function of depth. This can be done several ways, of which the most popular are angle-resolved (non-destructive) and noble ion gas sputtering (destructive) depth profiling. Angle resolved profiling manipulates the Beer-Lambert equation either to increase or decrease the integral depth of analysis in a non-destructive manner.<sup>93</sup> To do this in a basic sense, XPS analysis is done at various angles and the photoelectron penetration depth changes as a function of the angle. This technique is useful for analyzing sensitive surfaces such as polymer interfaces. Nobel gas ion sputtering in contrast is a destructive technique, which removes surface material mechanically and examines “freshly” exposed surfaces. This can give a depth profile as a function of the sputtering rates used. Noble ion gas sputtering was used throughout this research and will be discussed briefly.

Although the non-destructive angle resolved method described above is useful for examining the top 1-10 nm of the surface, the analysis of depths greater than that requires the removal of sufficient layers of material. In the most basic sense, ions are used to sputter surface atoms, which in turn expose the underlying atomic layers. An ion gun is used, typically Ar<sup>+</sup> ions, to destroy the surface being analyzed. The energy of the Ar<sup>+</sup> ions is dependent on the surface of the material; polymers or “softer materials” do not require high-energy ions to destroy the surface, while elemental transition metals require more

energy. The ion energy used throughout this research varied depending on the samples analyzed and will be discussed in their respective chapters.

#### 2.4.4 Peak Fitting

Careful peak fitting is important in any XPS analysis and when done correctly allows detailed information to be extracted from the XPS spectra. It is an integral part of all XPS characterization and therefore requires a brief explanation. Blind peak fitting of XPS spectra will yield unreliable data, thus it is important to peak fit with knowledge of the chemical composition. Figure 2.7 depicts how the knowledge of the chemical composition aids in the identification of the C 1s spectra for a basic polymer, polyethylene terephthalate (PET).

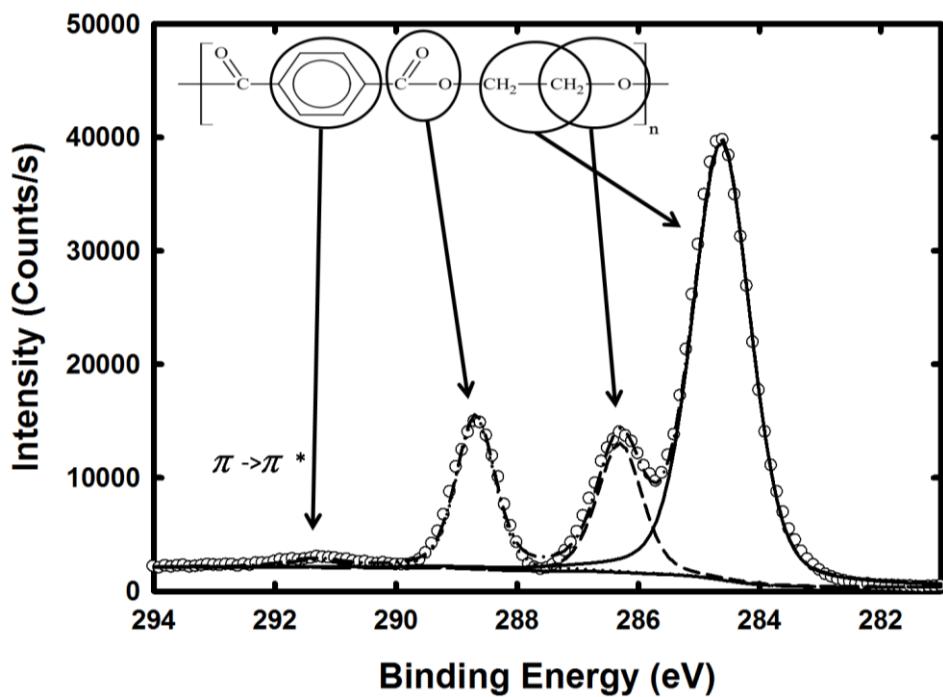


**Figure 2.7.** Common polyethylene terephthalate (PET) polymer C 1s spectra with peak fitting.

Choosing the correct background functions are important in peak fitting and will alter the nature of the peak asymmetry in the line shape of a spectrum. For example, the Mn $2p_{3/2}$  data in Figure 2.8 illustrates the variations possible for the same spectrum after background subtraction where different background strategies were employed. The Mn $2p_{3/2}$  singlet peak reveals that changing the background strategy not only alters the area underneath the peak but also the peak asymmetry slightly. It has been found that the SMART method (which is a modification of the Shirley method) works the best for most situations and was used throughout this research. Detailed explanations of each of these background methods can be found in basic XPS handbooks and will not be discussed further here.

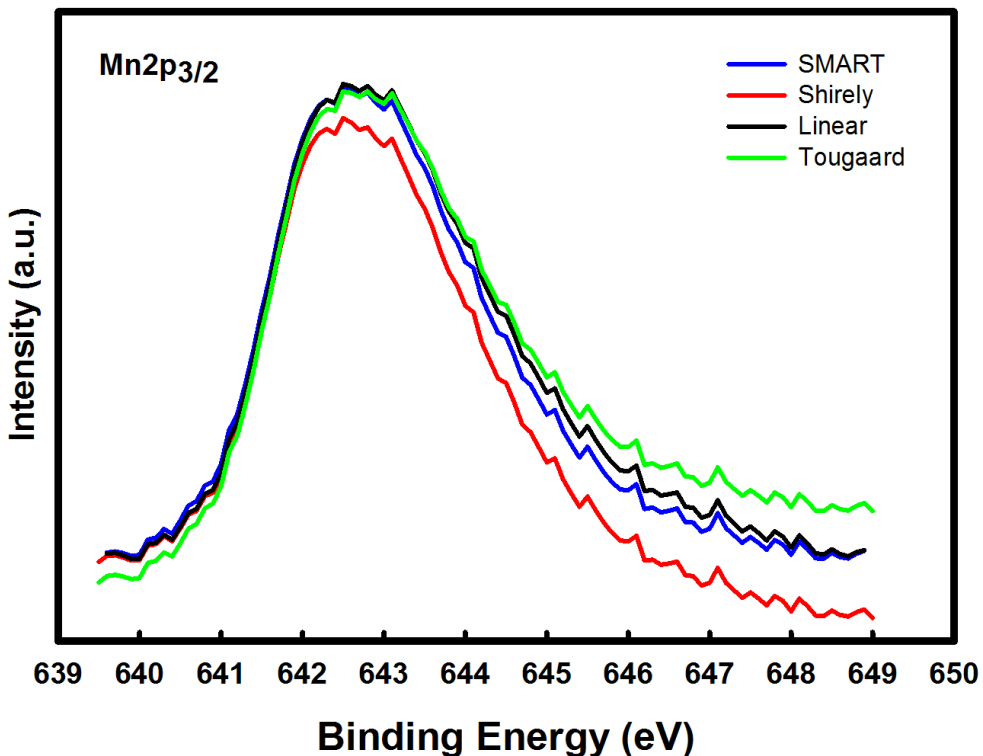


**Figure 2.8.** Mn  $2p_{3/2}$  spectrum of the same sample displayed using background subtracted data, where four different background types are used to model the background.

## 2.5 Vibrating Sample Magnetometry (VSM)

Room temperature vibrating sample magnetometry (VSM) was used in this work to determine the magnetic properties of materials. A Lakeshore model 7300 vibrating sample magnetometer was used for all room temperature analysis. The measuring field was oriented either parallel or perpendicular to the plane of the sample depending on the sample shape (for example pellets were oriented parallel, while powders were oriented perpendicular).

To describe VSM in the most basic sense, a sample is placed in a uniform constant magnetic field. If the sample is magnetic, this constant magnetic field will magnetize the sample by aligning the magnetic domains or magnetic spins with the field. If the sample vibrates in a sinusoidal motion, an electrical signal can be induced between two coils (pick-up coils). This signal has the same frequency of vibration and the amplitude is proportional to the magnetic moment of the material.

## 2.6 X-ray Absorption Spectroscopy (XAS)

X-ray absorption spectroscopy (XAS) was used during the course of this work to determine the local atomic structure and environment of atoms present in the nanomaterials. XAS measurements were carried out at two facilities; The National Synchrotron Light Source (NSLS) on beamlines X-11B and X-23B and the Advance Photon Source (APS) on the 10-BM beamline. All samples were prepared by spreading thin layers of finely ground powders on multiple layers of Kapton tape. Different energy modes and analysis techniques were used depending on the desired analysis and will be discussed individually in each of the chapters where necessary.

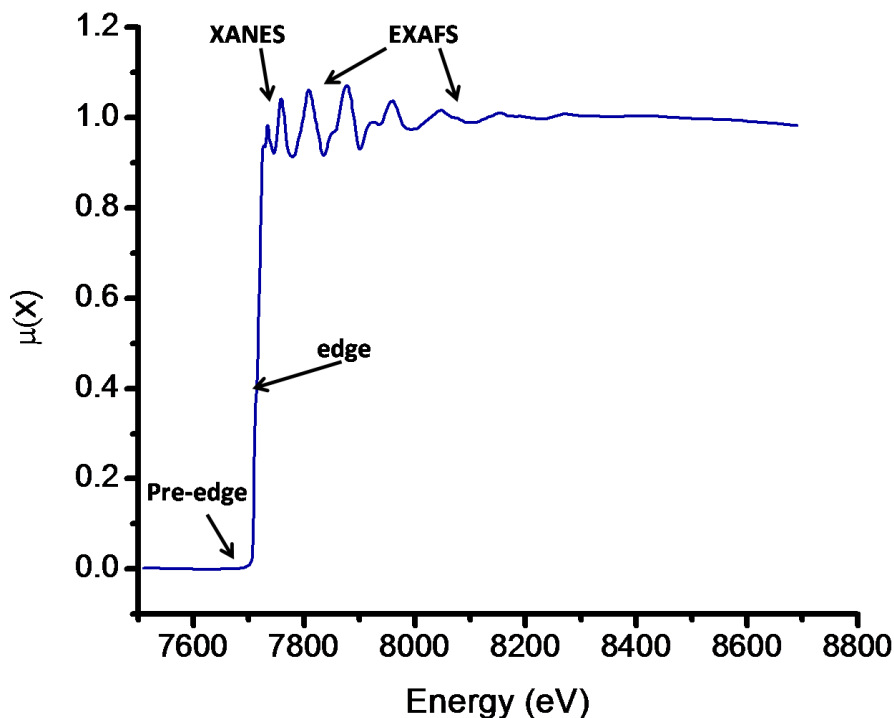


**Figure 2.9.** Typical Spectrum obtained from XAS.

XAFS is a powerful structural probe that provides information on the short-range coordination environment of the atom under study.<sup>94</sup> Figure 2.9 shows a typical elemental copper spectrum from XAS. In this figure, four regions are labeled and will be discussed briefly. First, the pre-edge region is the region prior to the characteristic x-ray absorption for the absorbing atom, in this case copper. The second part, the edge, refers to the absorption edge of the absorbing atom. More specifically, the absorption edge is when the photon energy approaches the necessary energy to lift a core electron from an element present in the sample above the Fermi level. The third part is XANES, or X-ray Absorption Near Edge Structure. This region is typically caused by intra-atomic transitions and is above the edge energy. XANES data can be useful when determining

oxidation states of materials. For example, by utilizing a linear combination fit of a sample that contains elemental Fe and  $\text{Fe}^{2+}$ - $\text{Fe}^{3+}$  $\text{O}_4$  one can get the percentage of each, as shown in figure 2.10.

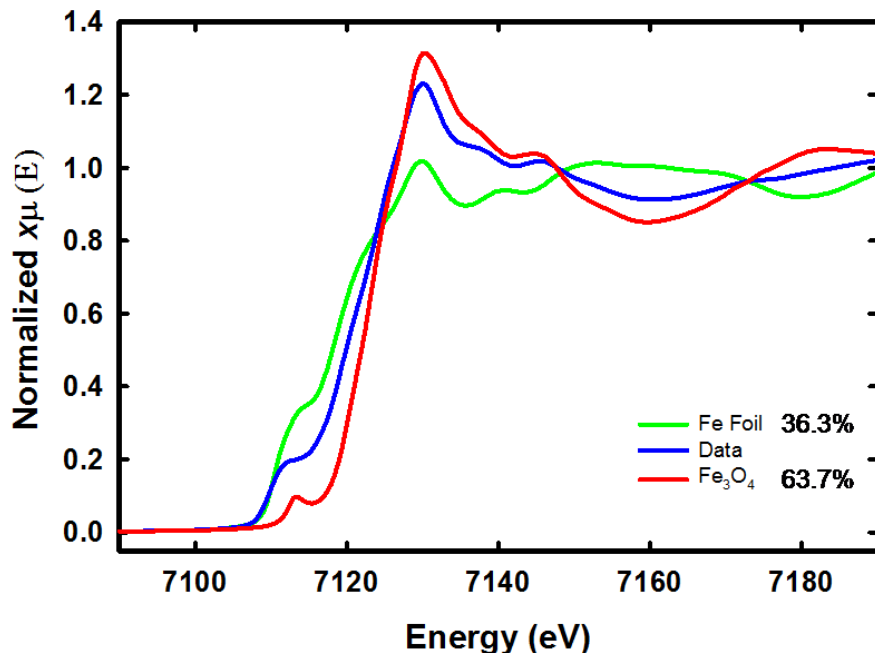


**Figure 2.10.** Linear combination fit of the XANES data of mixed Fe/FeOx nanoparticles.

So far, each of the previous regions were due to intra-atomic transitions. The fourth region is EXAFS, or Extended X-ray Absorption Fine Structure. EXAFS is well away from the absorption edge and results in the analysis of the ejected electron from the absorbing atom and its subsequent scattering from neighboring atoms. Because of this, EXAFS is a strong characterization technique for determining the composition of a material by analyzing the absorbing atoms effect on its nearest neighbors.

### 2.6.1 Experimental

It is possible to collect EXAFS on a lab x-ray source; however, it would take several days and only major features would be determined. Information such as the bond lengths of the nearest neighbors would not be feasible. As a result, much higher intensity x-rays are needed to get quality data. Synchrotron radiation is an excellent source of these high intensity x-rays. Figure 2.11 shows a typical synchrotron setup for collecting XAS.

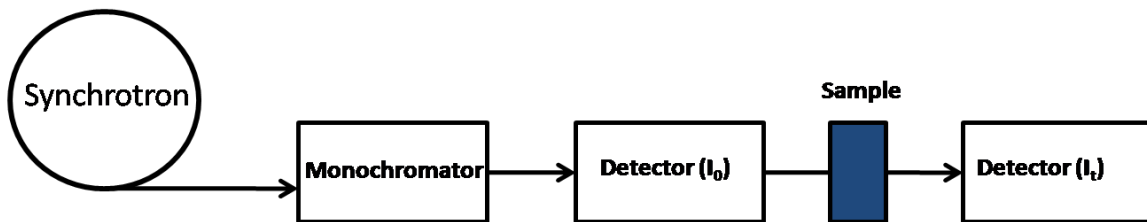


**Figure 2.11.** Schematic of a typical XAS setup at a synchrotron light source.

In the figure, the synchrotron produces a high intensity white x-ray beam which passes through a monochromator. The monochromator works similar to that of XRD, where the x-ray beam experiences an energy-dependent angular dispersion from a crystal. A second crystal is then used to position the x-rays of a desired energy and are diffracted toward the sample. When the Bragg conditions are met, it states that each angle will contain only photons of the desired frequency and of higher harmonics. If the monochromator was not used, and all of the harmonics were allowed to pass, the XAS measurements would be contaminated by photons of undesirable energy.

### 2.7 Thermal Analysis

Thermo-gravimetric (TG) analysis is widely used in chemical laboratories. For all TG analysis in this work a Texas Instrument Q5000 TGA was used. Thermo-gravimetry is the method in which the weight of the sample is continuously recorded during heating

or cooling. The thermo-gravimetric curve obtained expresses the dependence of a weight change as a function of temperature. This information is important in nanomaterials research for several reasons. First, thermo-gravimetry can be used to determine the amount of organic impurities that are adsorbed onto a nanoparticle surface formed during the synthesis procedure. This percentage of organics associated with the total mass of the nanoparticle is important information for magnetization mass correction as it is dependent on the mass of the magnetic material and not the total mass of the system.

Again, thinking about a nanomaterials laboratory, sample size is typically an issue as many synthesis techniques yield low product volumes. TG analysis offers a conservative way to anneal samples in which sample size is an issue, as it can offer different gasses to be present during the annealing process. This also allows researchers to monitor the effects of annealing under different atmospheres. Several nanomaterials and analytical books exist which detail TG analysis in greater detail, but I personally suggest readers to look at the 1972 book by Blazek.<sup>95</sup>

## 2.8 Ultraviolet-Visible Spectroscopy (UV-vis)

Uv-vis was used in this work to analyze the surface of nanomaterials. A Hewlett Packard 8453 photodiode spectrometer was used throughout this work. Nanomaterials often present color changes when dispersed in a solvent, which is correlated to the size or the thickness of a shell in a core-shell nanoparticle. For example, silver nanoparticles with different morphologies and sizes have various color transitions related to the surface curvature and translate to a shift in the plasmon resonance (Figure 2.12). Most of these

transitions occur in the visible portion of the spectrum and can give information about nanoparticle size and morphology.

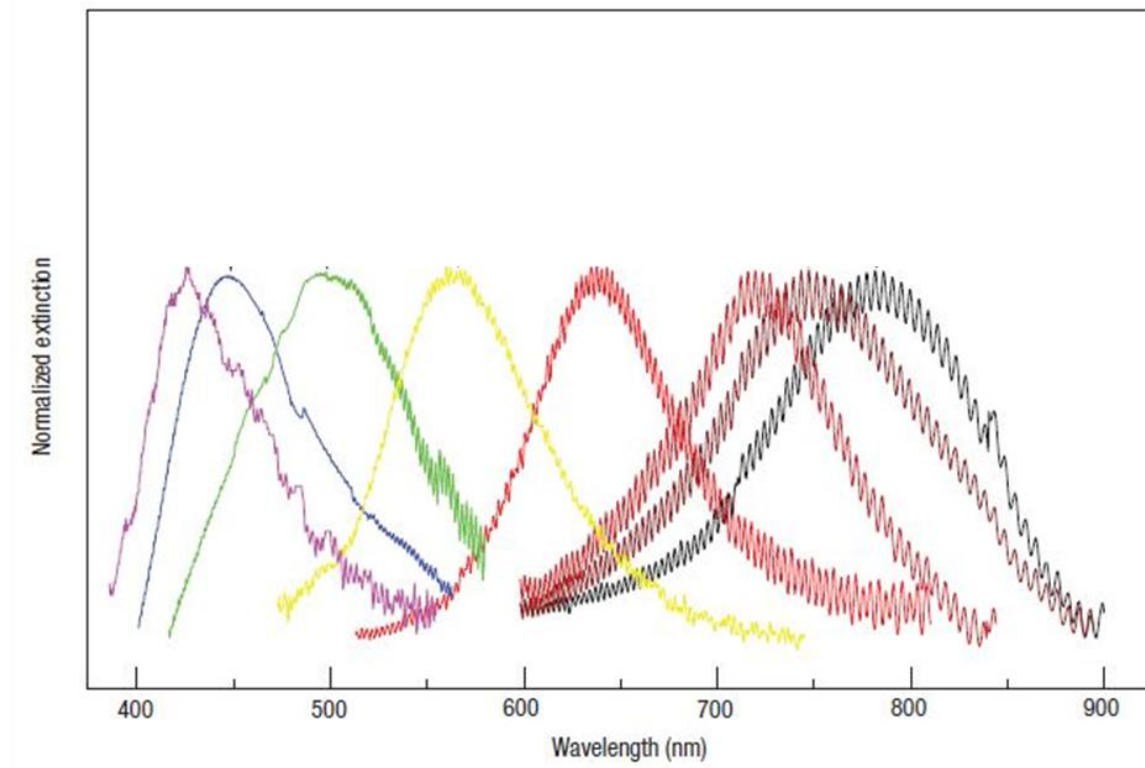


**Figure 2.12.** Effect of size and shape on Plasmon resonance spectrum for silver nanowires and nanodisks(image adapted and altered from reference).<sup>96</sup>

## **Section 1: Aqueous Reduction**

### **Chapter 3: Non-classical Crystallization of Fe Nanoparticles**

### 3.1 Introduction

Single-crystal monodisperse ferromagnetic nanoparticles are an interesting area of research for their use in electronic and biomedical devices. Several papers have highlighted classical methods, such as the self-assembly of nanostructures, for producing crystalline monodisperse ferromagnetic materials.<sup>28,42,71,75,97-101</sup> Amorphous metal nanostructures offer an alternative approach to creating crystalline monodisperse nanoparticles by not relying on the nucleation and growth process, but by inducing crystallization into pre-synthesized particles by thermal annealing.<sup>102</sup> This chapter aims to show a novel and practical route for inducing crystallization into amorphous metals by radio frequency (RF) techniques. RF methods allow for tunable and more controlled heating to orient atoms from an amorphous state to a destabilized crystalline state within a nanostructure.<sup>103-104</sup> The Fe Clusters were synthesized by aqueous reduction using sodium borohydride and sodium citrate.<sup>105</sup>

### 3.2 Experimental Section

The synthesis of Fe nanoparticles was carried out under ambient conditions. A borohydride to metal ratio and a citrate to metal ratio were kept at 2:1 and 10:1, respectively. In a typical experiment, 4.60 mM iron(II) sulfate heptahydrate ( $\text{FeSO}_4 \cdot 7\text{H}_2\text{O}$ ) and 0.460 mM trisodium citrate dihydrate were mixed vigorously for 10 minutes using a magnetic stir-bar in 2 L of DI-H<sub>2</sub>O to ensure total dissolution. Sodium borohydride ( $\text{NaBH}_4$ ) (8.80 mM) was then added to the mixture and allowed to react for 10 minutes. The resulting black precipitate was washed several times with ethanol and

magnetically extracted using a rare earth (1T) permanent magnet. The particles were then placed in a vacuum oven to dry overnight prior to RF exposure.

### 3.2.1 RF Exposure

Radio Frequency exposure was conducted using an Ameritherm HOTSHOT 2kW RF generator. Approximately 0.1 grams of the as-prepared powder was placed in a glass test tube. Then 5 mL of the solvent was added to the test tube and mixed to disperse the particles. Initial and final temperatures of the solution were recorded. After exposure, the particles were collected by magnetic separation, and washed with ethanol three times. The sample was then dried in a vacuum oven prior to characterization.

### 3.3 Results and Discussion

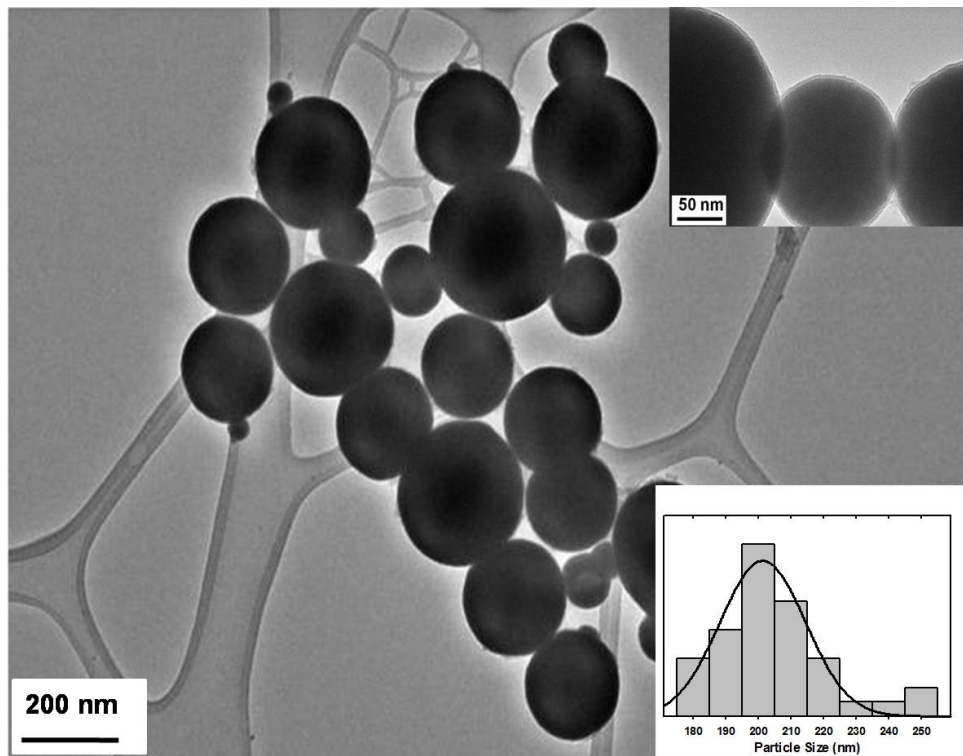


**Figure 3.1.** TEM image of the as-prepared amorphous nanoparticles. The particle size is about 200 nm. The bottom inset shows the histogram of the particles size distribution.

The dried powders were characterized by several techniques to determine the phase, morphology, and temperature dependent magnetic properties. A typical high-resolution transmission electron microscopy (HRTEM) image of the as-prepared amorphous nanoparticles is shown in figure 3.1. From the size distribution histogram (inset), an average particle size of  $204 \pm 1.9$  nm was estimated with a relatively small particle size distribution. About 75 particles were considered to obtain the size distribution histogram. In addition, the image shows a lighter shell around the particles, which is hypothesized to be a thin  $\text{Fe}^{2+}$  shell as determined by x-ray photoelectron spectroscopy.

High-resolution photoelectron spectra were recorded using an ESCALAB 250 spectrometer. An  $\text{Ar}^+$  ion flood gun was used for charge compensation and an ion etch gun (3 kV, 3 mA) was used for depth profiling. Figure 3.2 shows the graph of the depth profile for the Fe2p region scan. The analysis of the depth profile suggests that at first there is a higher concentration of  $\text{Fe}^{2+}$  ( $B_e \sim 710$  eV) relative to  $\text{Fe}^0$  ( $B_e \sim 707$  eV). After several etch levels, you can see that the  $\text{Fe}^{2+}$  intensity decreases as the  $\text{Fe}^0$  peak intensity increases. This analysis confirms that the surface is rich in  $\text{Fe}^{2+}$  ions that passivate the surface of the nanoparticles and prevents the metallic iron core from complete oxidation. The C1s spectra reveal three peaks that correspond to a surface of adsorbed citrate (Figure 3.3). The peaks are consistent with C-C, C-O, and C=O bonds. The depth profile analysis also indicates that at the surface of the nanoparticles, the carbon peak intensities are much higher than after several etch levels. From the C 1s and the Fe 2p depth profile analysis it is hypothesized that the surface of the nanoparticles are composed of an amorphous Fe-citrate shell.

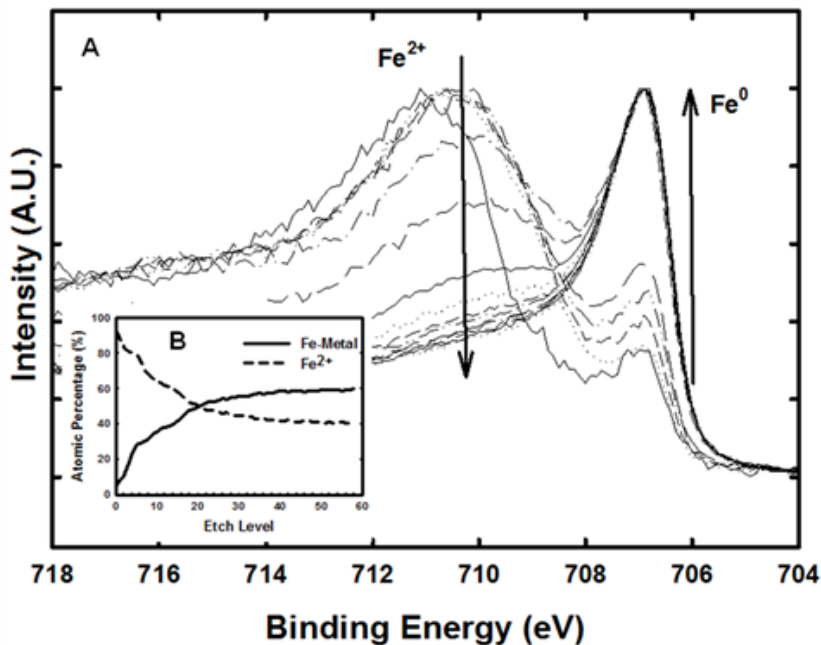


**Figure 3.2.** (A) Depth profile of the Fe2p XPS region spectra. (B) Atomic percentage versus etch level which shows a decrease in  $\text{Fe}^{2+}$  and an increase in elemental Fe as the etch level increases. This suggests that a layer of  $\text{Fe}^{2+}$  is present at the surface and not in the bulk.

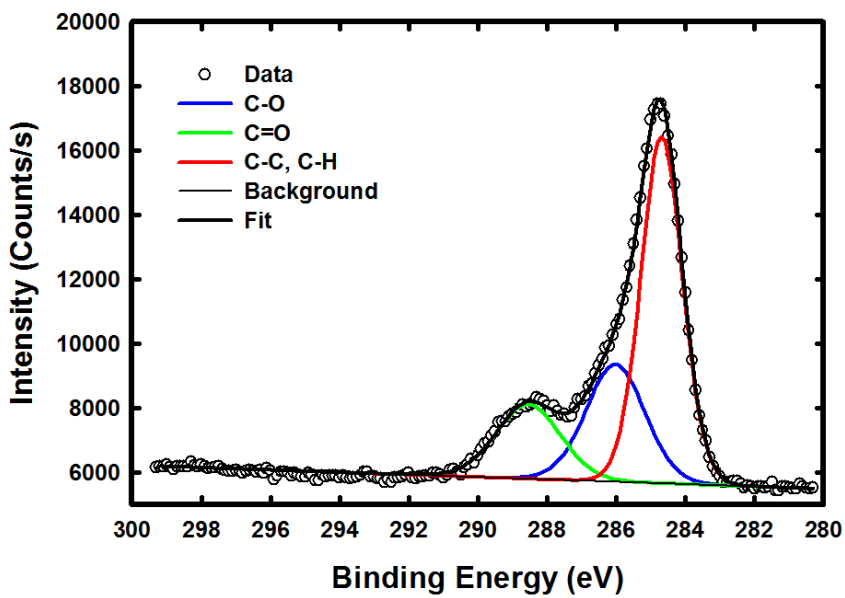


**Figure 3.3.** Representative C1s region scan of the as-prepared nanoparticles. The region scan shows 3 peaks which correspond to C-O (blue), C=O (green), and C-C (red). The analysis is representative of a citrate ion.

Figure 3.4 represents a series of powder x-ray diffraction patterns obtained on the dried powders at different RF exposure times. It should be noted that several solvents were used to determine their effects as a RF solvents for the annealing of Fe nanoparticles. This study, however, only discusses the results using ethanol as a solvent. In figure 3.4, an increase in crystallinity is seen from the as-prepared sample to an RF exposure time of 45 seconds. The Scherrer equation was used to calculate the mean crystallite size using the full width at half maximum (FWHM) of the most intense diffraction peak. Figure 3.5 represents how the calculated mean crystallite size changes as a function of the RF exposure time. For example, the crystallite size increases from 5 to 30 nm for particles with 0 to 45 seconds of RF exposure. It is important to note that this method for determining the mean crystallite size is difficult, especially when dealing with amorphous nanoparticles. The FWHM broadening increases in amorphous material due to a lack of significant long range ordering. Due to a lack of appropriate high-resolution imaging and synchrotron radiation techniques, this was the only way to determine the amount of crystallinity in the sample. The TEM and dynamic light scattering (DLS) analysis, as we had hypothesized, did not show any change in the nanoparticle morphology. This suggests that the RF exposure of the Fe nanoparticles in ethanol did not create aggregation, but did increase the crystallinity in the individual nanoparticles.

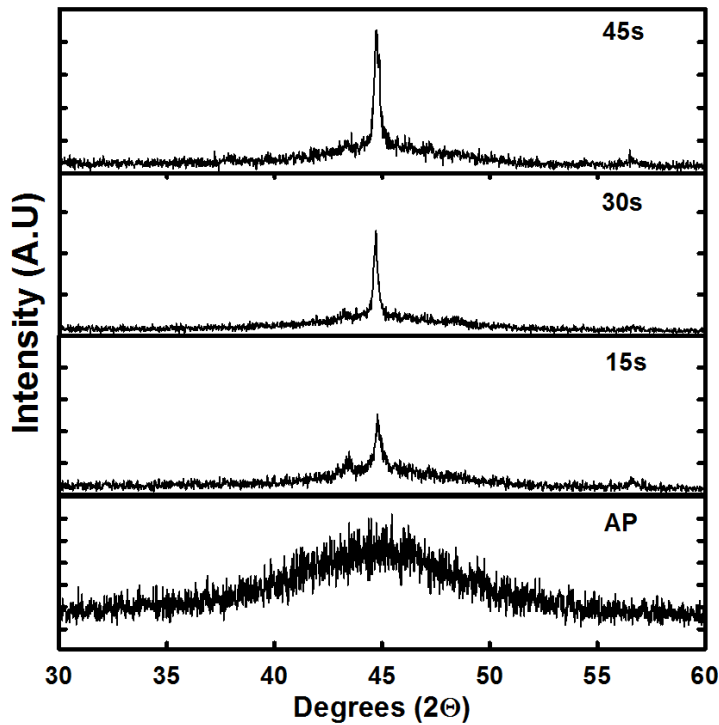


**Figure 3.4.** X-ray diffraction patterns of the resulting particles. As the RF exposure increase from 0s to 45s an increase in the crystallinity is seen.

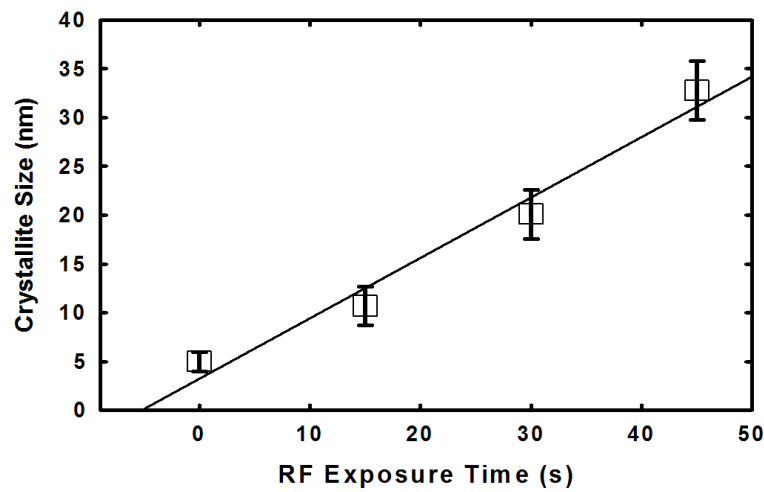


**Figure 3.5.** Graph of crystallite size (nm) versus RF exposure time (s) for Fe nanoparticles.

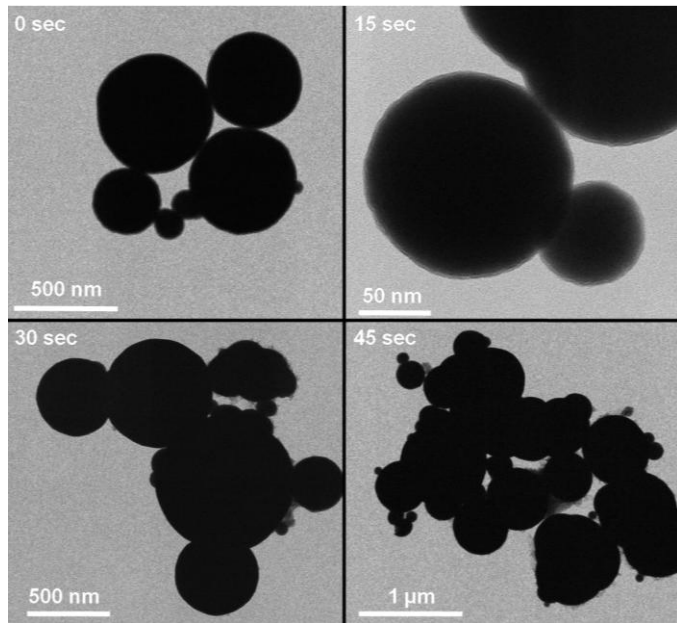


**Figure 3.6.** Transmission electron microscopy images of the nanoparticles at various RF annealing times.

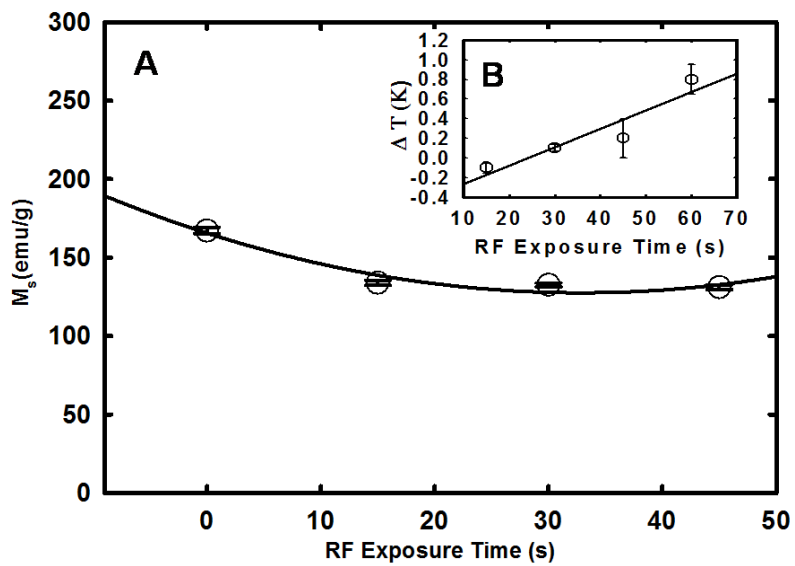


**Figure 3.7.** Magnetization saturation values as a function of RF exposure times. The inset shows how the temperature of the Fe/ethanol solution is affected by the RF exposure time. The solid line is meant as merely a guide for the eye.

To further characterize the nanoparticles and the effect of RF annealing, room temperature vibrating sample magnetometry (VSM) was conducted. Figure 3.7 represents saturation magnetization versus RF exposure time. There is a slight decrease in saturation magnetization as the RF exposure time is increased. The change in temperature of the solvent versus RF exposure time was also investigated (Figure 3.7, inset). A linear correlation is seen which can be explained by the particles heating in the RF field causing the solution to increase in temperature. The error bars represent the uncertainty in the temperature measurements. Figure 3.8 represents the raw hysteresis loop curves. The hysteresis loop shapes are similar and differ merely in their magnetization saturation, while, the coercivities remain relatively constant throughout the heat treatments.

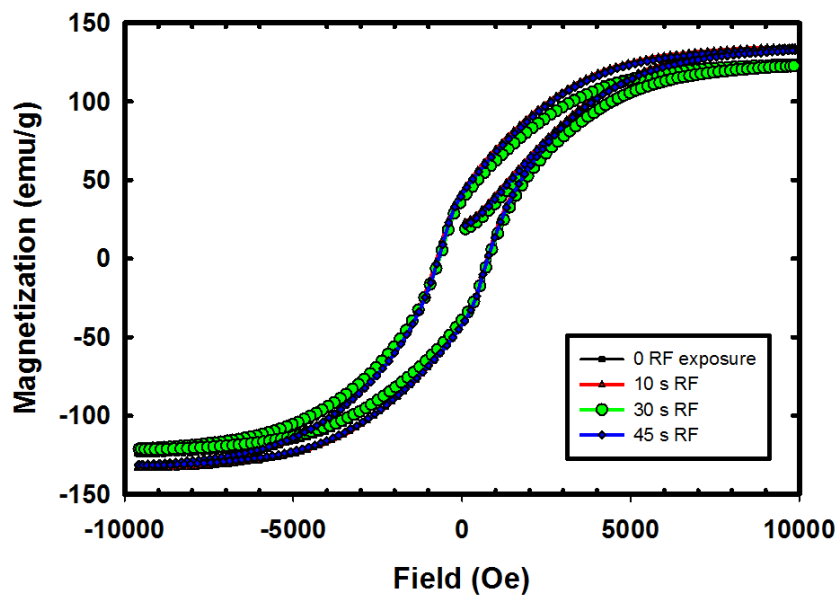


**Figure 3.8.** Room temperature hysteresis loops with various RF exposure times.

### 3.4 Conclusion

This chapter discussed an aqueous synthesis of Fe(II) sulfate using sodium borohydride and sodium citrate. These exact synthesis parameters produced spherical amorphous Fe nanoparticles that served as the starting material for the study of non-classical crystallization. These results show promise in the area of RF techniques for the production of well-defined single crystal nanoparticles for electronic and biomedical devices. Ethanol, as a solvent, helped to dissipate heat to and from the particles for crystallization, which prevented agglomeration and oxidation. In this non-classical method, the RF technique provided enough energy to the Fe atoms to cause them to reorient to a more ordered crystalline state.

## **Chapter 4: Design of $\text{Fe}_x\text{Co}_{100-x}$ Nanoparticles**

#### 4.1 Introduction

The design, synthesis, characterization, and implementation of novel ferromagnetic nanoparticles and their alloys have been of significant interest over the past decade. FeCo based alloys have specifically gained interest due to elevated magnetization along with a high Curie temperature (~900°C), good permeability, and good mechanical strength.<sup>106-107</sup> These ferromagnetic alloys have been prepared several ways, including thermal decomposition, sonochemical reduction, arc-discharge, laser-pyrolysis, polyol process, and aqueous reduction by borohydride derivatives.<sup>97,105,108-110</sup> These synthesis techniques have produced several shapes including spheres, cubes, dice, and wires. Aqueous reduction by borohydride has been used for producing monometallic nanoparticles of CoB and FeB.<sup>77-78,80-81,83,111</sup> Recently, Ekeirt et al. have shown that by using a capping agent, such as sodium citrate, they can eliminate the formation of FeB/Fe<sub>2</sub>B nanoparticles to form elemental  $\alpha$ -Fe.<sup>84</sup>

This chapter discusses a new method for producing  $\text{Fe}_{x}\text{Co}_{100-x}$  nanoparticles by using a capping agent such as sodium citrate. Various metal ratios were synthesized and heat-treated to study the resulting crystallization effects. Several characterization techniques were used to elucidate the structural and magnetic changes as a function of heat treatments.

#### 4.2 Experimental

The synthesis of  $\text{Fe}_{x}\text{Co}_{100-x}$  nanoparticles was carried out under ambient conditions. Several ratios of cobalt and iron were analyzed. Similar to the previous chapter, a borohydride to metal ratio and a citrate to metal ratio were kept at 2:1 and 10:1,

respectively throughout each trial. In a typical experiment X mM  $\text{FeSO}_4 \cdot 7\text{H}_2\text{O}$ , Y mM cobalt(II) sulfate tetrahydrate ( $\text{CoSO}_4 \cdot 4\text{H}_2\text{O}$ ) (such that,  $X+Y= 4.60$  mM), and 0.460 mM trisodium citrate dihydrate were mixed vigorously using a magnetic stir-bar in 2 L of DI- $\text{H}_2\text{O}$  to ensure total dissolution.  $\text{NaBH}_4$  (8.80 mM) was added to the mixture and allowed to react for 10 minutes. The particles were magnetically separated and washed several times with ethanol. After washing, the particles were placed in a vacuum oven to dry overnight prior to analysis. Annealing was performed on the dried nanoparticles using a Q200 TA Instruments differential scanning calorimeter (DSC) under forming gas.

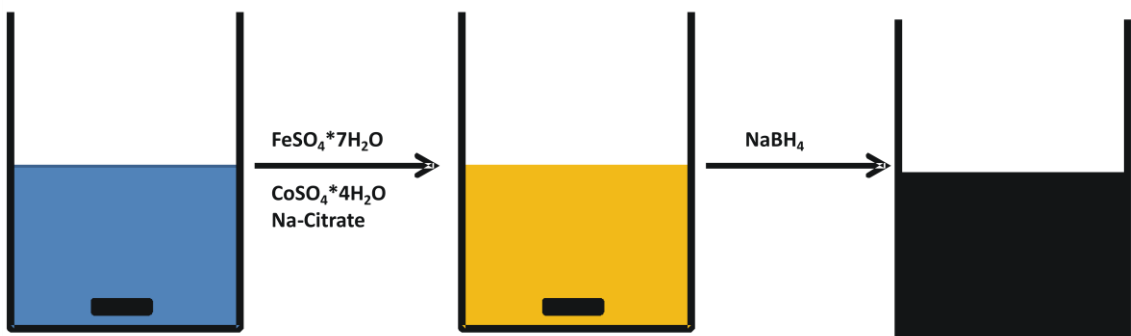


**Figure 4.1.** Graphical representation of the color changes seen during the synthesis of FeCo nanoparticles synthesized by aqueous reduction.

The dried alloyed nanoparticles were characterized by x-ray photoelectron spectroscopy, x-ray diffraction, transmission electron microscopy, and vibrating sample magnetometry for the determination of phases, morphology, and temperature dependent magnetic properties. Elemental compositions for all alloys were confirmed by using a Varian Vista-MPX CCD inductively coupled plasma - optical emission spectrometer (ICP-OES). Annealing temperatures of 450°C and 600°C were chosen from differential

scanning calorimetry (DSC) to represent the before and after crystallization events of the samples. Prior to annealing, the powders were pressed into 3 mm sized pellets and placed in a DSC aluminum pan; the powders were pressed to ensure uniform heating. The samples were then annealed at a ramp rate of 5°C/min and held at the final temperature for 10 minutes. Room temperature magnetometry was performed on a Lakeshore Cryotronics Inc. Model 7300 VSM. Field cooled and zero field cooled temperature dependence of magnetization measurements were performed by using a Quantum design MPMS XL-5 SQUID magnetometer. The temperature range was between 10 to 400 K with an applied dc magnetic field of 100 Oe.

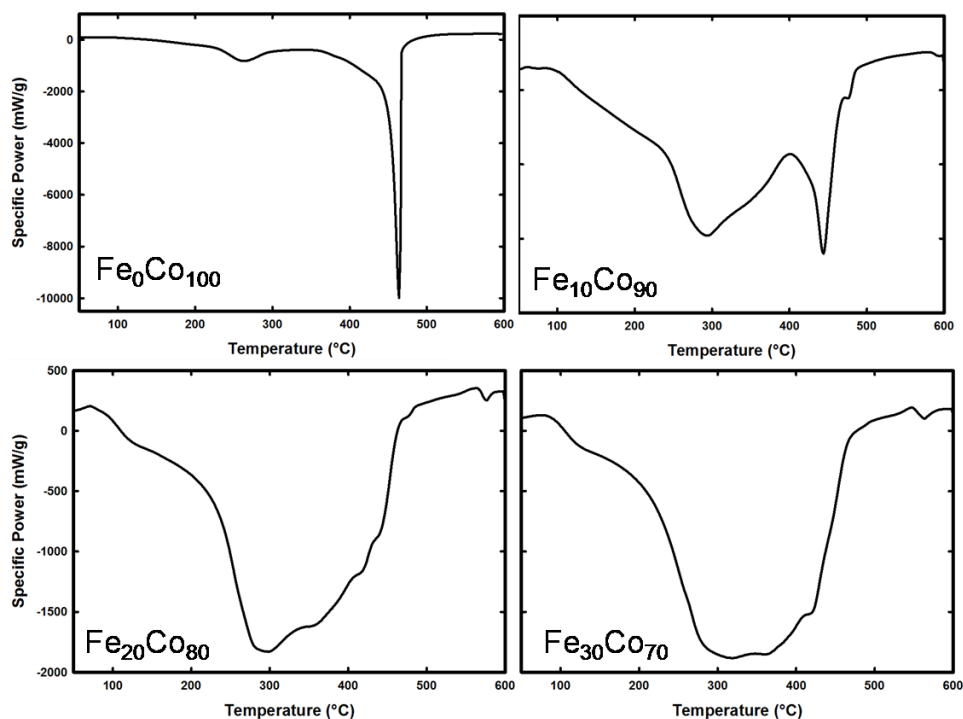


**Figure 4.2.** Differential Scanning Calorimetry patterns of 4 different ratios of nanoparticles.

### 4.3. Results and Discussion

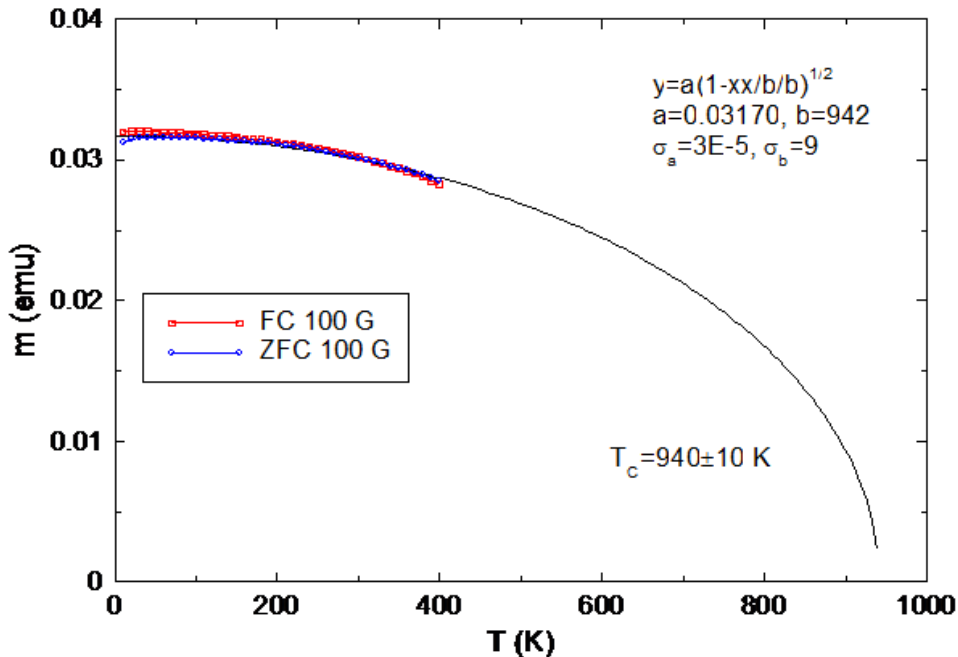


**Figure 4.3.** SQUID data of the as-prepared 50 at. % Co content nanoparticles.

SQUID measurements were conducted to investigate the nature of the magnetic ordering of the alloyed nanoparticles. Figure 4.3 shows a FC/ZFC plot of moment (emu) versus temperature (K) of the as-prepared  $\text{Fe}_{50}\text{Co}_{50}$  sample. The graph shows that the alloyed nanoparticles have ferromagnetic ordering with a curie temperature of 940K.

Table 4.1 lists the magnetization saturation and coercivity results with different heat treatments for all samples. As shown in the table, the Magnetization saturation ( $M_s$ ) decreases with increasing Co content for the as-prepared alloys; this is also depicted in Figure 4.4. Several papers in the literature show that the alloyed content with the largest  $M_s$  value (~230 emu/g) is the  $\text{Fe}_{60}\text{Co}_{40}$ .<sup>97,106,108-109</sup> The difference in the results presented here is thought to be due to the particle size and morphology of the nanoparticles. Due to

a lack of long range order or crystallinity in the as-prepared samples an overall decrease in the saturation magnetization is expected compared to crystalline FeCo samples presented in the other papers.<sup>105</sup> From table 4.1, no linear trend in coercivity can be seen. FeCo alloys tend to be ferromagnetic and have a low coercivity. However, it seems that our Fe<sub>50</sub>Co<sub>50</sub> and Fe<sub>60</sub>Co<sub>40</sub> samples had the largest coercivity while the pure metals had the lowest. It is hypothesized that some of the coercivity seen from the nanoparticles could be a result of oxides forming on the surface due to un-reacted Co and Fe ions reacting with the citrate ions.

Hysteresis curves were measured for heat-treated samples as well. For example, Figure 4.5 shows how the temperature affected the hysteresis loops for Fe<sub>50</sub>Co<sub>50</sub> particles. An increase in both magnetization saturation and coercivity is seen for the 450°C sample as compared to the as-prepared samples. The 600°C sample however shows an increase in magnetization saturation relative to the as-prepared, but it is lower than the 450°C sample. One notable difference in the hysteresis loops is that the remanent magnetization is the highest for the 450°C sample. What the data is suggesting is that the formation of an intermediate phase is occurring during the annealing of the sample below 450°C. Once the temperature reaches 600°C the intermediate phase is eliminated, and the magnetic character reverses back to the as-prepared sample. To investigate the intermediate phase, XRD measurements were conducted and will be discussed below.

**Table 4.1.** Magnetization saturation ( $M_s$ ) and coercivity ( $H_c$ ) values of the various annealed alloy nanoparticles and the composition differences.

Sample Co/(Co+Fe) (at. %)	AP		450°C		600°C	
	Ms (emu/g)	Hc (kOe)	Ms (emu/g)	Hc (kOe)	Ms (emu/g)	Hc (kOe)
0	151.88	0.55	152.508	0.611	N/A	N/A
10	121.99	0.65	112.501	0.993	69.78	0.73
20	101.59	0.67	59.62	0.837	34.56	0.84
30	93.85	0.7	67.51	0.874	53.66	0.82
40	102.78	0.81	114.28	1.323	106.44	0.77
50	82.18	0.83	112.98	1.496	65.59	0.71
60	82.59	0.66	98.86	1.338	103.14	0.71
70	67.82	0.62	83.13	1.286	108.18	0.77
80	57.52	0.55	113.86	1.102	122.26	0.72
90	50.47	0.51	116.47	0.914	89.71	0.84
100	46.21	0.49	97.46	0.783	92.54	0.82

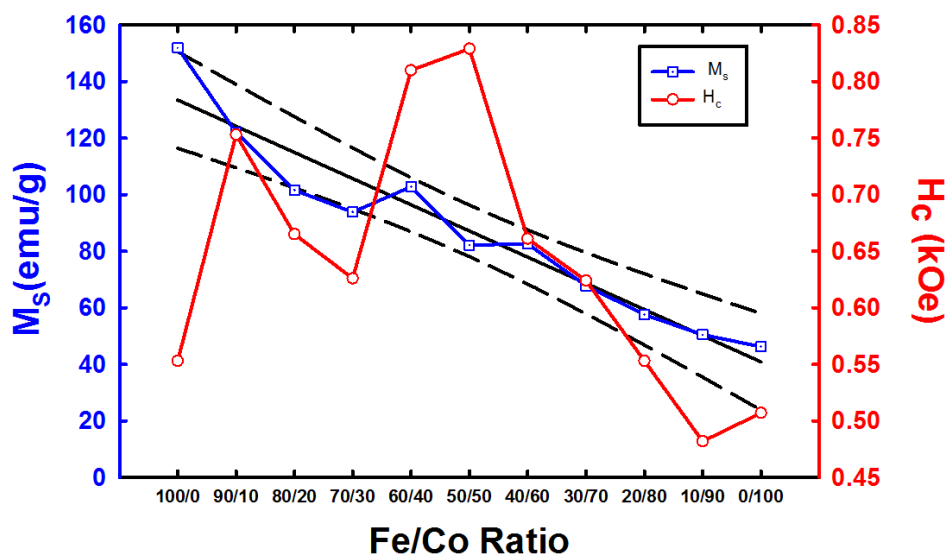


**Figure 4.4.** Plot of Magnetization and Coercivity versus Fe/Co ratio.

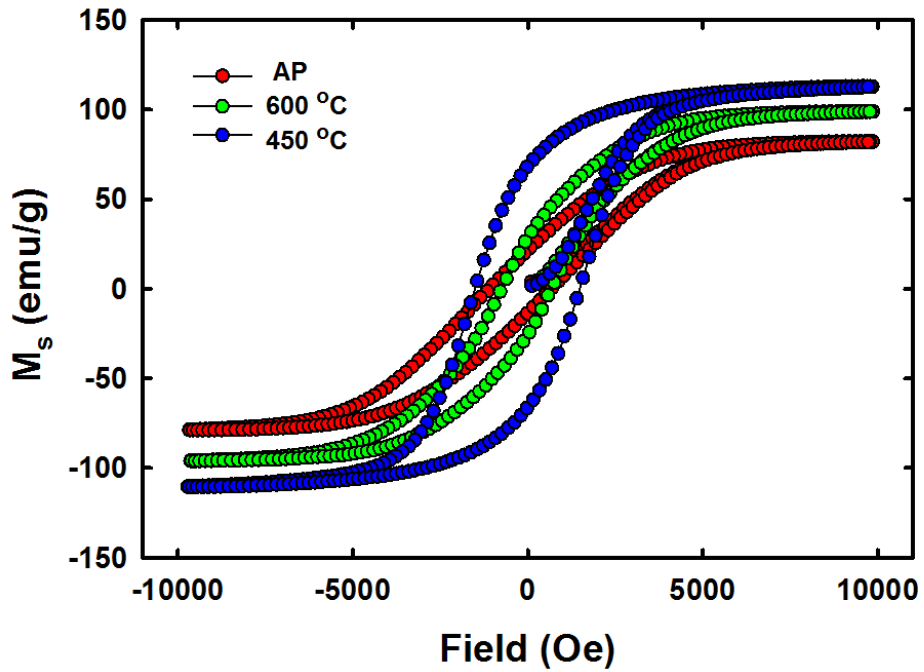


**Figure 4.5.** Magnetization hysteresis loops of  $\text{Fe}_{50}\text{Co}_{50}$  content nanoparticles at various annealing temperatures.

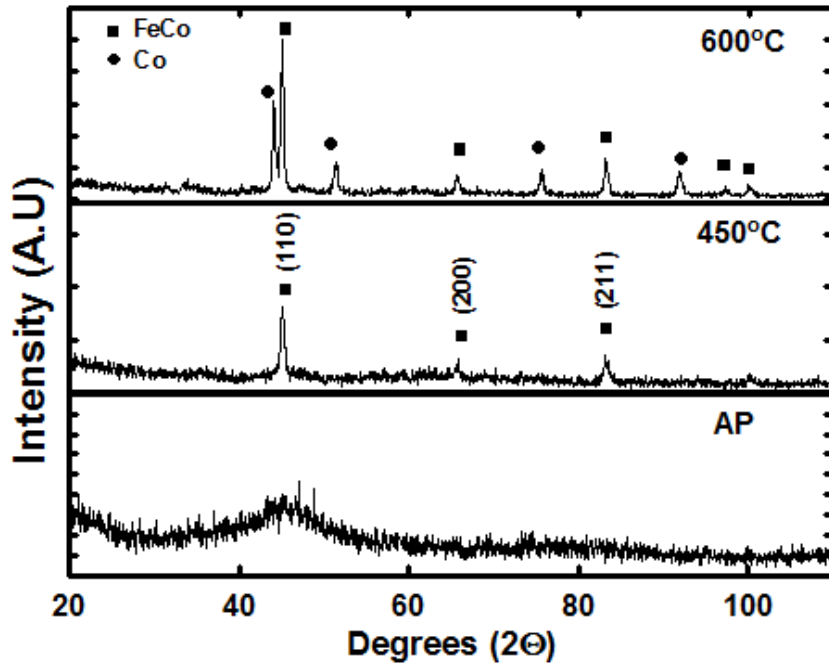


**Figure 4.6.** Powder x-ray diffraction patterns of  $\text{Fe}_{30}\text{Co}_{70}$  content nanoparticles at various annealing temperatures.

X-ray powder diffraction (XRD) was taken on a PANalytical X'pert pro diffractometer at a scanning step of  $0.500^\circ$ , in a  $2\theta$  range from  $20^\circ$  to  $110^\circ$  with monochromated Cu-K $\alpha$  radiation ( $\lambda=0.51418$  nm). The diffraction patterns were analyzed to determine the phases present in each of the nanoparticles. All dried powders were analyzed as-synthesized and after each annealing cycle. Figure 4.6 shows the diffraction patterns for the Fe<sub>30</sub>Co<sub>70</sub> nanoparticles at various annealing temperatures. The Bragg diffraction peaks are labeled and referenced from the JCPDS reference powder diffraction files of Fe<sub>30</sub>Co<sub>70</sub> (50-0795) and Co (25-0806). The other alloys match similarly to the JCPDS reference powder diffraction files, with their respective alloy compositions. The as-prepared XRD patterns show that the nanoparticles are highly amorphous and show the presence of two very broad peaks centered around  $50^\circ$  and  $80^\circ$   $2\theta$ . After the  $450^\circ\text{C}$  anneal, some of the features in the XRD become resolved. For example in the Fe<sub>30</sub>Co<sub>70</sub> sample, all the peaks can be indexed to the same-alloyed composition using Highscore Plus. Three peaks at  $44.45^\circ$ ,  $68.58^\circ$ , and  $82.44^\circ$  correspond to the (110), (200), and (211) miller indices, respectively. Once the sample is heated to  $600^\circ\text{C}$  there seems to be a slight phase separation resulting in extra peaks in the XRD pattern that are associated with fcc cobalt. These results were seen in most of the alloyed compositions; however, in some cases, the result was hcp cobalt. It is therefore hypothesized that the initial synthesis of the nanoparticles was not that of FeCo alloys, but that of nanoparticles of Fe and Co rich regions. Once the particles are annealed the formation of the alloys occurred.

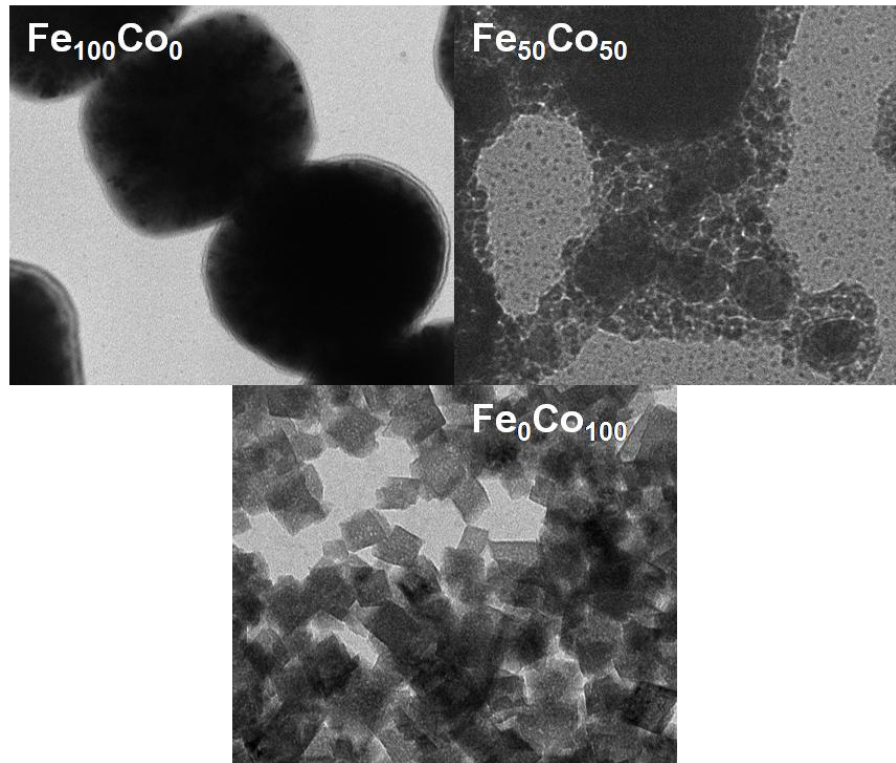


**Figure 4.7.** Transmission electron micrographs of various as-prepared nanoparticles.

To further investigate the nature of the particle size and morphology, the powders were characterized using a JEOL JEM-1230 transmission electron microscope at 150 kV with a Gatan Ultra Scan 4000 SP 4Kx4K CCD camera. Samples for transmission electron microscopy (TEM) were prepared by dispersing a drop ( $7\mu\text{L}$ ) of liquid suspension onto a carbon film supported by copper mesh (400 grid mesh) followed by evaporation of the liquid medium. Figure 4.7 (a-c) depicts transmission electron microscopy images. The TEMs show a morphological transition from spherical to cubic as the cobalt is increased. The  $\text{Fe}_{50}\text{Co}_{50}$  nanoparticles show core/shell character with a large size distribution. The nanoparticles show slight aggregation, which can be due to the TEM sample preparation

techniques, or it could also be due to citrate ions adsorbed onto the surface of the particles causing aggregation.

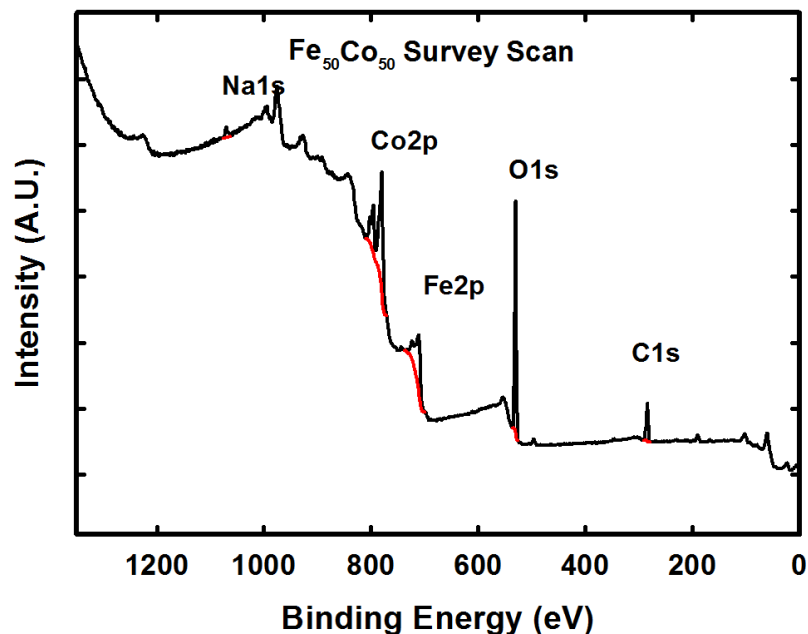


**Figure 4.8.** Representative XPS survey scan of FeCo nanoparticles.

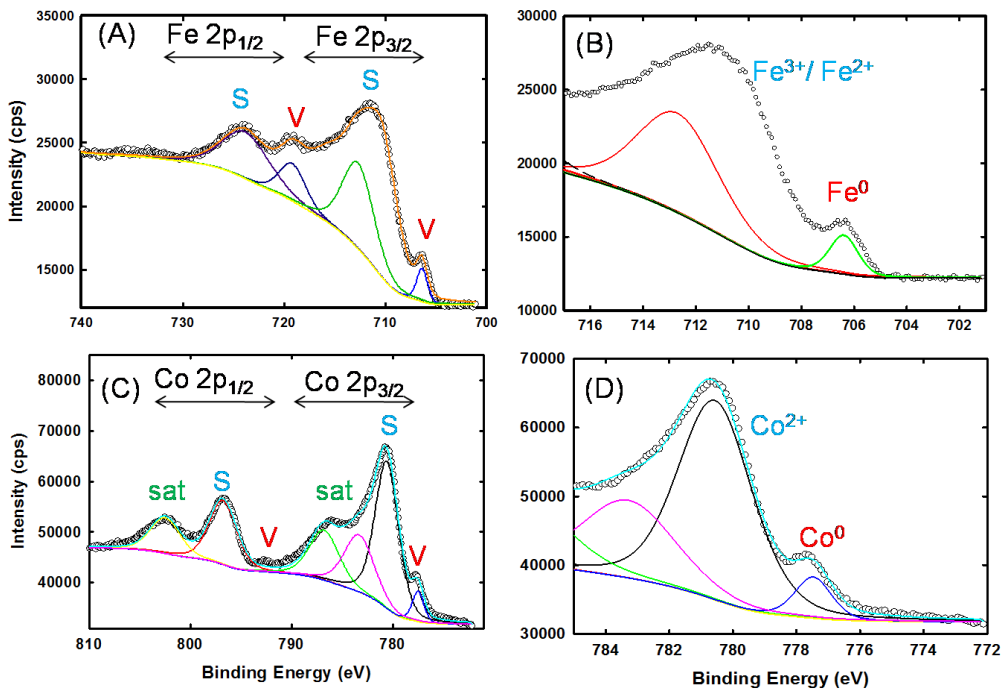


**Figure 4.9.** Representative Co and Fe region scans.

High-resolution photoelectron spectroscopy was conducted using an ESCALAB 250 spectrometer. The  $180^\circ$  hemispherical analyzer and monochromated Al-K $\alpha$  X-ray excitation (Al anode, 12 Kv, 20 mA,  $h\nu = 1486.6$  eV) were applied. The instrument was operated with a magnetic lens in the large area XL-mode with a pass energy of 20 eV. Binding energies are given relative to the binding energy of the C1s peak ( $E_b = 384.6$  eV). An Ar $^+$  ion flood gun was used for charge compensation. XPS survey scans were used to determine elemental surface chemistry. The scans revealed Na, Co, Fe, O, and C on the surface for all samples. Figure 4.8 is a representative survey scan of the as-prepared nanoparticles and no deviations in the spectra were seen with the various ratios. Figure 4.9 shows the Co2p and Fe2p region scans of the Fe<sub>50</sub>Co<sub>50</sub> nanoparticles. In the Fe2p region scan (Figure 4.9 A and B) four peaks are seen. The first doublet, labeled “V”

has a binding energy of 706.4 eV for the core Fe2p<sub>3/2</sub> level and a spin-orbit splitting of 12.8 eV. These values are consistent with the reported literature values for zero-valent iron (ZVI).<sup>112</sup> The second doublet, labeled “S” has a binding energy of 711.6 eV with a similar spin-orbit splitting of 12.7 eV. These peaks are consistent with oxidized iron containing a mixed (Fe(III)/Fe(II)) phase.<sup>112</sup>

For the Co2p region scan (Figure 4.9 C and D) there are six peaks. The doublet labeled “V” has a binding energy of 777.39eV for the Co2p<sub>3/2</sub> level and a spin-orbit splitting of 15.3 eV. These values are in agreement with reference data for metallic Co.<sup>113</sup> The second doublet, labeled “S”, was observed at ~781 eV (Co2p<sub>3/2</sub>) with a spin-orbit coupling of ~16.1 eV. These values are typical for cobalt in the oxidation state Co<sup>2+</sup>.<sup>114</sup> The third and final doublet, labeled “Sat” can be identified as a shakeup satellite feature.

From the analysis of the XPS data the surface of the nanoparticles are rich in oxidized Co and Fe. Our hypothesis is that the citrate molecules bind to the Co and Fe surface atoms equally. If there was preferential binding towards one of the atoms the relative amount of oxidized Co and Fe and zero-valent atoms would be differ.

#### 4.4 Conclusion

This chapter detailed a new synthesis for the formation of Fe<sub>x</sub>Co<sub>100-x</sub> nanoparticles by using an aqueous reduction. The nanoparticles were synthesized by an aqueous reduction of Fe<sup>2+</sup> and Co<sup>2+</sup> with sodium borohydride and sodium citrate. The as-prepared nanoparticles produced unexpected trends in the magnetic behavior. The saturation magnetization decreased with increasing Co content from a maximum of 152 to minimum of 48 emu/g. Although the as-prepared samples exhibit poor magnetic

properties due to the lack of crystallinity, the magnetic properties can be improved by annealing at 450°C under forming gas. These nanoparticle show promise for researchers by introducing the ability to manipulate the magnetic properties by synthetic and thermal annealing mechanisms.

## **Chapter 5: Design of Fe and Ag core/shell Nanoparticles**

### 5.1 Introduction

Bimetallic nanoparticles have shown diverse electronic, magnetic, and optical properties with respect to their monometallic counterparts. The fabrication of bimetallic nanoparticles has thus attracted both fundamental and practical interest because of their potential applications in areas such as biosensing, separation, catalysis, cancer therapy, and drug delivery.<sup>57,63,115-116</sup> Specifically, dual-mode bimetallic nanoparticles with a core/shell morphology offer greater flexibility with both magnetic and optical properties.<sup>117</sup> Cho et al. have recently shown that spherical 15 nanometer iron oxide nanoparticles with a silver shell offer magnetic SERS for the identification of bronchioalveolar stem cells in normal and lung cancer mice.<sup>20,118</sup>

Several synthetic methods have been reported to prepare bimetallic nanoparticles, including chemical reduction, microemulsion techniques, sonochemical reactions, gamma-ray irradiation, and laser ablation.<sup>15,85,115,119-124</sup> While these techniques have shown viability in synthesizing core/shell nanoparticles; the precise control of specific optical properties is essential for many application purposes. For example, Kim et al. has recently shown SERS based detection using Ag-deposited on Fe<sub>2</sub>O<sub>3</sub> particles.<sup>15</sup> We report for the first time on a one-pot aqueous synthesis of Fe/Ag and Ag/Fe core/shell nanoparticles using sodium borohydride and sodium citrate. Among the various core/shell nanoparticles, Fe/Au nanoparticles have been the subject of intense research.<sup>53,125-132</sup> However, recently there has been increasing interest in the design of Fe/Ag core/shell nanoparticles.<sup>14,20,52,133-134</sup> To the best of our knowledge, this is the first paper reporting the formation of Fe/Ag core/shell nanoparticles in a one-pot method.

Conventionally, pre-synthesized Ag nanoparticles are deposited onto pre-synthesized iron oxide nanoparticles by using functional groups such as amines and thiols. While this particular report focuses on the synthesis of Fe/Ag core/shell nanoparticles, this technique extends to other systems as well.

## 5.2 Experimental Section

Iron(II) sulfate heptahydrate ( $\text{FeSO}_4 \cdot 7\text{H}_2\text{O}$ ), silver nitrate ( $\text{AgNO}_3$ ), and sodium borohydride ( $\text{NaBH}_4$ ) were purchased from ACROS Organics. Trisodium citrate dihydrate was purchased from Mallinckrodt chemicals. Ethanol was purchased from Sigma Aldrich. All chemicals were used as received and without further purification.

Stock 0.5M  $\text{AgNO}_3$  aqueous solutions were made and kept under dark conditions in an amber bottle to maintain uniformity between experiments.  $\text{AgNO}_3$  stock solutions were discarded after 1 week to ensure minimal photodegradation.

### 5.2.1 Preparation of Fe nanoparticles.

Fe nanoparticles were synthesized as previously reported.<sup>135-136</sup> Briefly, to produce consistent spherical Fe nanoparticles, a borohydride to Fe ratio and an Fe to citrate ratio were kept at 2:1 and 10:1, respectively. First, a 2.0 L solution containing 4.6 mM  $\text{FeSO}_4 \cdot 7\text{H}_2\text{O}$  and 0.46 mM trisodium citrate dihydrate was mixed using magnetic stirring.  $\text{NaBH}_4$  (8.8 mM) was added to the mixture and allowed to react for 10 minutes. The solution was quenched with ethanol several times and magnetically separated using a rare earth magnet. After washing was complete, the remaining ethanol was decanted and the particles were placed in a vacuum oven at room temperature to dry.

### **5.2.2 Preparation of Fe/Ag and Ag/Fe core/shell nanoparticles.**

By varying the time of addition of  $\text{AgNO}_3$  we were able to manipulate which metal resided in the core and the shell.

The synthesis of Ag coated Fe nanoparticles was carried out under ambient conditions. Several ratios of Ag to Fe were analyzed and times between the addition of  $\text{NaBH}_4$  and  $\text{AgNO}_3$  varied. The Ag precursor addition time is an important parameter for creating the desired core/shell structures and will be discussed in detail below. In the reaction, sodium citrate and iron sulfate are added to 2.0 L of DI- $\text{H}_2\text{O}$  followed by the addition of  $\text{NaBH}_4$ . The solution turns from clear to a grey/black color after the addition of  $\text{NaBH}_4$ .

### **5.3 Characterization**

The dried powders were characterized by X-ray diffraction (XRD), transmission electron microscopy (TEM), X-ray absorption spectroscopy (XAS), and vibrating sample magnetometry (VSM) for the determination of phase, morphology, and magnetic properties. XRD measurements were performed using a Panalytical X'pert pro diffractometer at a scanning step of  $0.05^\circ$ , in a  $2\theta$  range from  $20^\circ$  to  $120^\circ$ , with a graphite monochromated  $\text{Cu-K}_\alpha$  radiation source. Samples were ground and pressed onto a no background, low volume holder. Room temperature magnetometry was performed on a Lakeshore Cryotronics Inc. Model 7300 VSM. The powders were characterized using a JEOL JEM2100 Transmission Electron Microscope and imaged in bright field at an accelerating voltage of 200 keV. Samples were mounted on a 300 mesh lacey carbon TEM grid. The particles were first ultrasonicated in solution for about 9 minutes. During

this time, lacey carbon grids were immersed in chloroform for 30 seconds to dissolve their formvar-backing layer. After sonication, a small pipette was used to transfer a drop of each nanoparticle solution onto a grid. The grids were then placed on a hot plate at 50 °C and allowed to dry for an hour. After drying, each sample was mounted in the instrument. UV-vis absorption analysis was carried out using a Hewlett-Packard 8453 photodiode spectrophotometer. Solutions were prepared in an aqueous environment using a quartz cuvette with a 1 cm path length. X-ray photoelectron spectroscopy (XPS) was performed on a Thermo Scientific ESCALAB 250 microprobe with a focused monochromatic Al K $\alpha$  X-ray (1486.6 eV) source and a 180° hemispherical analyzer with a 6-element multichannel detector. Charge compensation was employed during data collection by using an internal flood gun (2 kV electrons) and a low energy Ar $^+$  external flood gun. Binding energies of the photoelectron are corrected to the aliphatic hydrocarbon C 1s peak at 284.6 eV. A Large area XL magnetic lens with a 500  $\mu\text{m}$  spot size in constant analyzer energy (CAE) mode was utilized with a pass energy of 20 eV. 30 scans per region were taken with a step size of 0.100 eV. The powdered samples were pressed onto a strip of indium foil and mounted on a sample holder using double-sided carbon tape. Fe K edge (7112 eV) XAFS measurements (encompassing both XANES and EXAFS) were performed at beamline 10-BM of Advanced Photon Source (APS). Samples were measured in transmission mode. The energy of the incident X-rays was scanned using a Si(111) reflection plane of a cryogenically-cooled double-crystal monochromator. Detailed XAFS analysis can be found in the supporting information.

## 5.4 Results

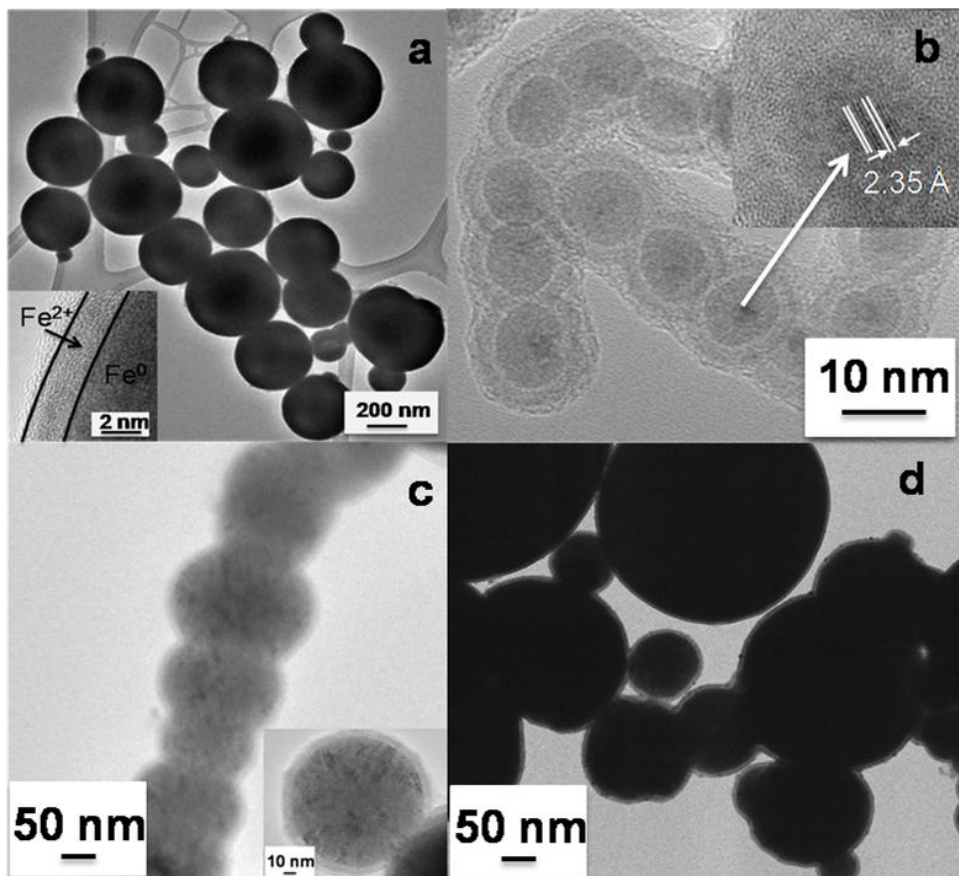


**Figure 5.1.** High resolution TEM image of (a) as-synthesized Fe nanoparticles,(b) Fe/Ag nanoparticles showing a clear distinction between the core (Ag) and shell (FeB/Fe<sub>2</sub>B) (c) Ag/Fe nanoparticles, and (d) Fe nanoparticles with islanding of Ag.

Figure 5.1(A-D) depicts high-resolution transmission electron microscopy images. TEM observations show that if the reaction is left to react for 15 minutes the resulting particles are approximately 5 nm Fe nanoparticles encased in roughly a 200 nm bundle (Figure 5.1a), as reported by others.<sup>84</sup> However, an injection of silver nitrate one minute past the addition of NaBH<sub>4</sub> results in the formation of a Ag core Fe shell (Figure 5.1b). The result is monodisperse Ag/Fe core/shell nanoparticle with a total diameter of 12 nanometers consisting of a 4 nm silver core and an 8 nm shell of amorphous iron. A d-

spacing of 2.350 Å was measured from the HR-TEM image, which is consistent with the d-spacing for the (111) reflection of face-centered cubic (fcc) Ag. Injection of silver nitrate five minutes past the addition of NaBH<sub>4</sub> creates Fe/Ag core/shell nanoparticles (Figure 5.1c). Lastly, if the addition of silver nitrate is prolonged to 15 minutes, the formation of 200 nm Fe clusters with island shells of Ag is seen (Figure 5.1d).

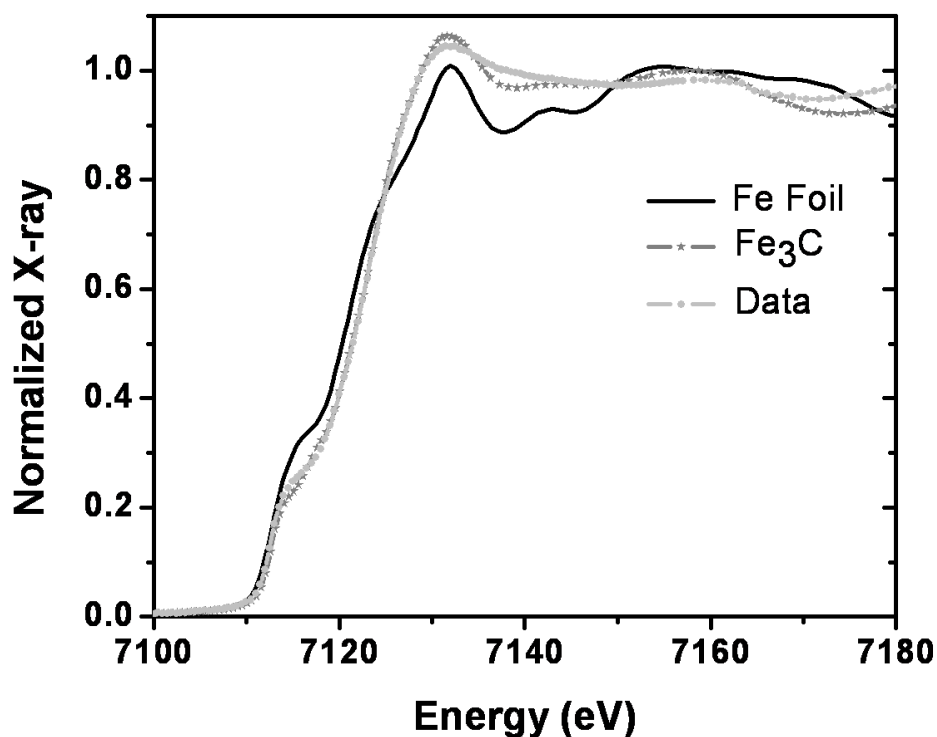


**Figure 5.2.** XANES spectra of the sample plotted with spectra collected from Fe metal foil and Fe<sub>3</sub>C standards.

XAFS is a powerful structural probe that provides information on the short-range coordination environment of the atom under study.<sup>94</sup> Figure 5.2 shows the XANES data of the as-synthesized Ag/Fe core/shell nanoparticles plotted with spectra collected from Fe<sub>3</sub>C and from Fe metal foil. The pre-edge and edge features of the iron nanoparticles are

clearly different from bcc Fe and match well with the Fe<sub>3</sub>C standard. Post-edge features are susceptible to longer-range structure and appear different from both the Fe<sub>3</sub>C standard and Fe foil. Given the 8 nm thickness of the Fe shell of the core/shell nanoparticles as shown by TEM, the post-edge features could not be unambiguously assigned from XANES. EXAFS analysis rules out a body-centered cubic (bcc) Fe coordination environment. However, inclusion of carbon or boron atoms in addition to Fe atoms in the first shell resulted in statistically significant improvement in the fitting results of the sample. Hence, the two most reasonable models (i.e., carbide and boride) will be discussed further.

Comparisons of the FT EXAFS data (Figure 5.3a) of the Fe nanoparticles to that of bcc Fe metal show that the first FT peak is of much smaller amplitude and shifted to shorter distances, similar to what is observed by Qadri et al. with Fe-boride nanoparticles.<sup>137</sup> Since FeSO<sub>4</sub> was reduced with borohydride as the starting material, formation of Fe-boride is consistent with the chemical composition of the system. Fe-boride standard spectrum was not available for comparison. The Ag/Fe spectrum also showed similarity to the Fe-carbide standard. However, Fe-carbide can be excluded based on the chemical composition of the material. Below we discuss a fitting model based on the observed spectral similarity between the unknown sample and Fe-boride.

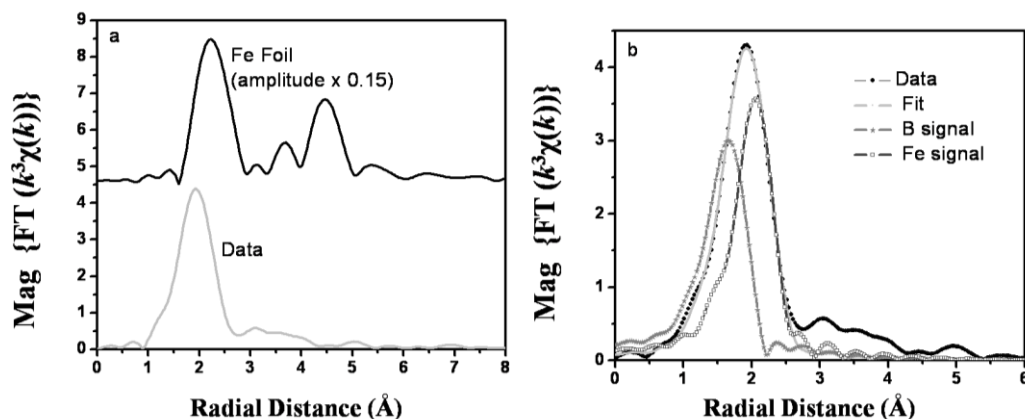


**Figure 5.3.** a) Comparison of Fourier Transform EXAFS spectra of Fe foil and Ag/Fe; b) Fourier Transform magnitude of the data and the fit plotted with the contributions of Fe and B signals.

A single Fe shell does not reproduce well with the main FT peak in a fitting procedure. The inclusion of B atoms in addition to Fe atoms in the first shell resulted in statistically significant improvement in the fitting results of the sample. Fitting parameters for Fe-boride are given in Table 1. Magnitudes of the Fourier transform data and fit with the contribution of Fe and B signals are shown in Figure 5.3b. Fitting with Fe and B signals result in an average coordination numbers of  $\sim 3.5$  Fe atoms and  $\sim 2.8$  B atoms around Fe at an average distance of 2.63 and 2.18  $\text{\AA}$ , respectively. These distances match well with both the previously reported crystallography as well as EXAFS analysis of Fe-boride compounds.<sup>137-138</sup> However, the coordination numbers reported in our study are smaller than the typical Fe and B coordination numbers in FeB/Fe<sub>2</sub>B nanoparticles. This can possibly arise from a thin coating of FeB/Fe<sub>2</sub>B over a Ag core, consistent with the TEM results. The lack of second and higher shell structure in the Fourier transform of the sample (Figure 5.3a) is also consistent with a thin disordered Fe-boride coating over a

Ag core. Since the Fe-Fe distance reported in this study ( $2.63\text{ \AA}$ ) falls in the distance range seen for both FeB ( $2.62 - 2.95\text{ \AA}$ ) and  $\text{Fe}_2\text{B}$  ( $2.40 - 2.72\text{ \AA}$ ), the EXAFS analysis cannot unequivocally distinguish between the formation of FeB from  $\text{Fe}_2\text{B}$  coating over the Ag core.<sup>138</sup>

**Table 5.1. Fitting with Fe and B paths.**

Path	N	R (Å)	$\sigma^2$ ( $10^{-3}\text{ \AA}^{-2}$ )	$\chi^2_v$	R factor	E <sub>0</sub> (eV)
<b>Fe-B</b>	<b><math>2.82 \pm 0.14</math></b>	<b><math>2.18 \pm 0.01</math></b>	<b>15.5*</b>	<b>67</b>	<b>0.0014</b>	<b><math>-5.9 \pm 1.8</math></b>
<b>Fe-Fe</b>	<b><math>3.52 \pm 0.21</math></b>	<b><math>2.63 \pm 0.01</math></b>	<b>11.8*</b>			

\*Fixed to Best Fit Value

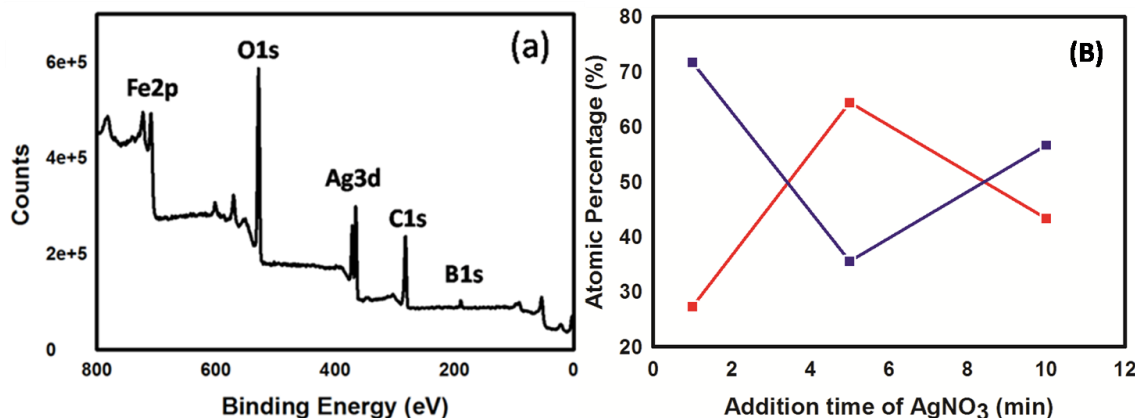


**Figure 5.4.** (a) High-resolution XPS survey scan of a representative Fe/Ag core/shell nanoparticle (b) Atomic percentage of Fe2p and Ag3d as a function of  $\text{AgNO}_3$  addition time determined by survey scans and standard sensitivity factors.

Figure 5.4a presents the high-resolution XPS survey scan of freshly prepared Fe/Ag core/shell nanoparticles. The photoelectron peaks reveal that the nanoparticle surface consists of mainly Ag, O, C and Fe, as well as trace amounts of B, C1s and O1s

region scans suggest that the nanoparticle surface contains some adsorbed citrate, which is consistent with literature.<sup>84</sup> Two peaks at ~192 eV and ~188 eV in the B1s region spectra could be due to an oxidized boron (borate) adsorbed on the surface or B from FeB/Fe<sub>2</sub>B, respectively. Both of which are common with borohydride reduction.<sup>139</sup> Shakeup and satellite peaks can be seen at 712 eV and 716 eV.<sup>140-141</sup> Literature suggests that the smaller peak at 706.82 eV which typically corresponds to elemental Fe could also be associated with FeB/Fe<sub>2</sub>B.<sup>142-147</sup> Table 1 lists the binding energies of the Fe and B core levels observed at various AgNO<sub>3</sub> introduction times and is compared to the literature core level values. Binding energy shifts for the corresponding elemental Fe and boride core levels are very small (within 0.3 eV) and the B1s level binding energies are very similar, making the identification of elemental Fe and FeB/Fe<sub>2</sub>B very difficult, especially since the literature values for elemental Fe shift from 706.9 to 707.4 eV. Photoelectron peaks at ~710 and ~721 eV correspond to the binding energies of Fe 2p<sub>3/2</sub> and 2p<sub>1/2</sub> for Fe<sup>2+</sup>, respectively. Figure 5.5 shows that the amount of Fe<sup>2+</sup> decreases depending on the introduction time of AgNO<sub>3</sub>. The particles that were formed after 1 minute AgNO<sub>3</sub> introduction formed Ag/Fe core/shell nanoparticles, which would allow the surface of Fe to become easily oxidized and result in a larger intensity of Fe<sup>2+</sup>. However, the particles that were formed after five-minute AgNO<sub>3</sub> introduction formed Fe/Ag core/shell nanoparticles, where the Ag prevented the surface of Fe from being oxidized.

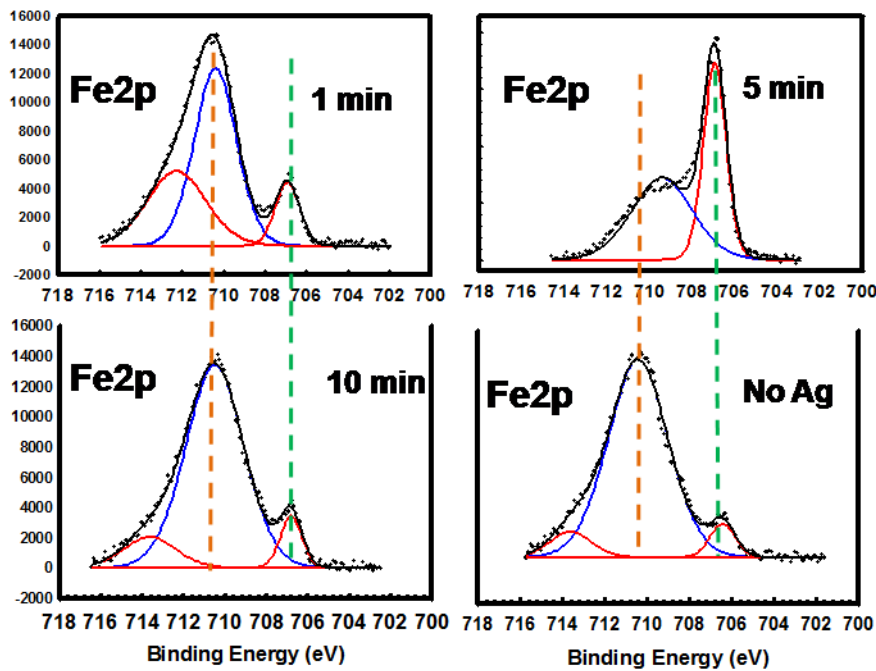


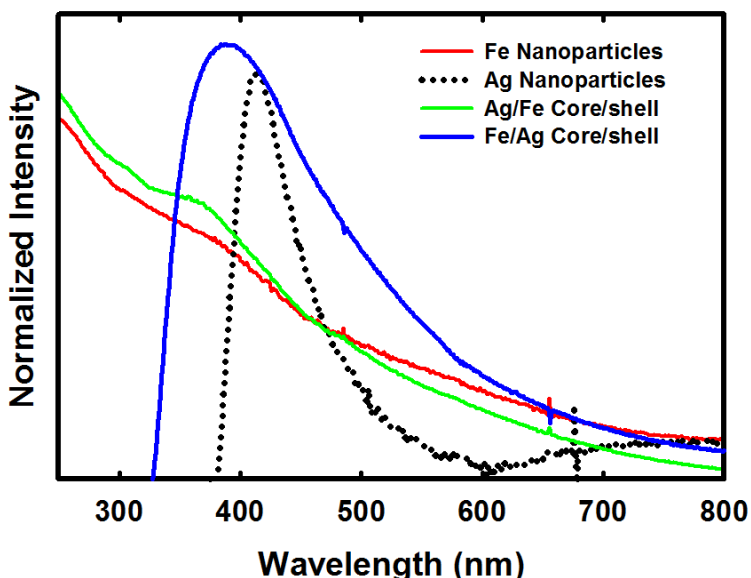
**Figure 5.5.** Fe2p region scans at with different  $\text{AgNO}_3$  addition times which produced various core/shell nanoparticles with various Fe environments.

**Table 5.2.** XPS binding energies of FeB,  $\text{Fe}_2\text{B}$ , and elemental Fe core levels.

Literature			Observed				
Fe2p			Fe2p				
	1/2	3/2	B1s		1/2	3/2	B1s
Fe	720	706.9-707.4	-	1 min	719.5	706.9	187.77
FeB	720.3	707.2	188.1	5 min	719.98	707	187.84
$\text{Fe}_2\text{B}$	720.2	707.1	188.1	10 min	719.77	706.98	187.92

In addition, an increase in the intensity of the  $\sim 707$  eV peak is seen at various  $\text{AgNO}_3$  introduction times. This increase is due to the different core/shell formations. Figure 4b is a representative atomic percentage of the core level  $\text{Ag}3\text{d}$  and the  $\text{Fe}2\text{p}$  associated with either elemental Fe or  $\text{FeB}/\text{Fe}_2\text{B}$  as a function of different introduction

times of  $\text{AgNO}_3$ . The atomic percentage was derived from integrated peak areas using standard sensitivity factors. What this suggests is that the surface composition of Fe2p is changing due to the formation of Ag nanoparticles on the surface, which indicates the formation of Fe/Ag core/shell nanoparticles.



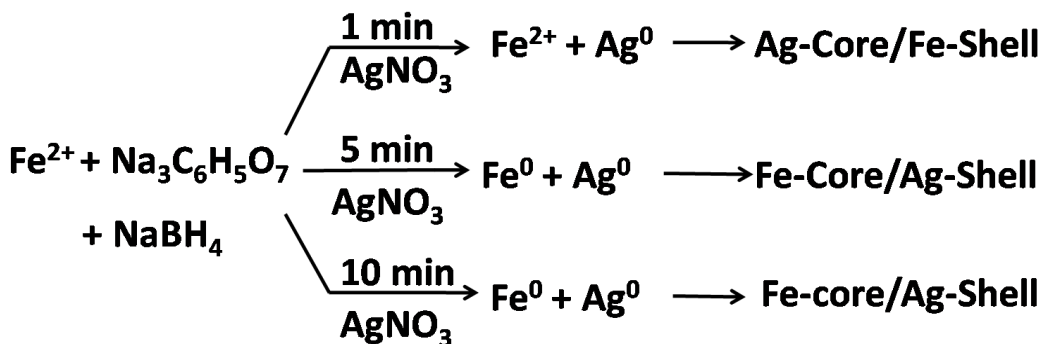
**Figure 5.6.** UV-vis absorption spectra of the Fe/Ag (solid blue line), Ag/Fe (solid green line), pure Ag (dotted black line), and pure Fe (solid red line) nanoparticles.

Figure 5.6 shows UV-vis absorption data of synthesized Fe/Ag, Ag/Fe, Fe, and Ag nanoparticles showing various Plasmon absorption properties. The absorption band of pure Ag nanoparticles is at 410 nm, and is consistent with the literature values.<sup>21,51,148-149</sup> A plasmon shift in the absorption band to 380 nm is seen along with a broadening of the band for Fe/Ag core/shell nanoparticles and is due to the small surface layer of Ag.<sup>150</sup> Comparing the pure Fe nanoparticles with the Ag/Fe nanoparticles shows similar absorption properties consistent with a Ag core. The absorption properties of Fe are similar to literature data and consist of two small bands at 200 nm and 360 nm.<sup>151</sup> The

band at 200 nm corresponds to the citrate ion while the band at 360 nm corresponds to the small Fe nanoparticles.<sup>152</sup>

### 5.5 Discussion

The above results suggest that the formation of various core/shell nanoparticles is directly determined by the various introduction times of  $\text{AgNO}_3$  after the  $\text{NaBH}_4$  addition. Figure 5.7 depicts how the introduction of  $\text{AgNO}_3$  at different times after the addition of  $\text{NaBH}_4$  creates different scenarios.



**Figure 5.7.** The proposed reaction scheme for the reduction of sodium citrate,  $\text{FeCl}_2 \cdot 7\text{H}_2\text{O}$  and  $\text{NaBH}_4$ . Addition of  $\text{AgNO}_3$  at various times after the addition of  $\text{NaBH}_4$  produced various core/shell morphologies.

This can be explained kinetically by the fact that the reduction of Fe is a two-electron process, thereby requiring a slightly longer reaction time to complete as compared to the one electron reduction that is occurring with the Ag.<sup>153-154</sup> In this sense, for the one-minute introduction time after the addition of  $\text{NaBH}_4$ , the Ag is formed by classical homogeneous nucleation and growth resulting in 4-5 nm spherical nanoparticles. These Ag nanoparticles serve as nucleation sites for the Fe nanoparticles to grow, which simulates a heterogeneous nucleation and growth process.<sup>51,149,152,155-157</sup> For the five-

minute reaction, the Fe nanoparticles have already formed and therefore act as nucleation sites for the Ag nanoparticles to form and grow, creating an Fe/Ag core/shell nanoparticles. Lastly, the 10 minute introduction of  $\text{AgNO}_3$  produces  $\sim 150$  nm Fe clusters, as previously reported.<sup>84,158</sup> These Fe clusters again act as nucleation sites for the Ag to form. This scenario creates islands of Ag nanoparticles on the larger Fe clusters. While we were unable to definitively determine if the Fe nanoparticles formed were that of elemental Fe, FeB, or  $\text{Fe}_2\text{B}$ , the room temperature VSM data (Figure 5.8) shows that the particles do in fact have a high magnetization saturation ( $M_s$ ) with respect to the previous reported  $\text{FeOx}/\text{Ag}$  nanoparticles. The higher  $M_s$  value of these nanoparticles allows them to be incorporated into real-world distribution/recollection applications such as the detection of chemical, biological, radiological, nuclear, and explosive (CBRNE) threats.<sup>159</sup>

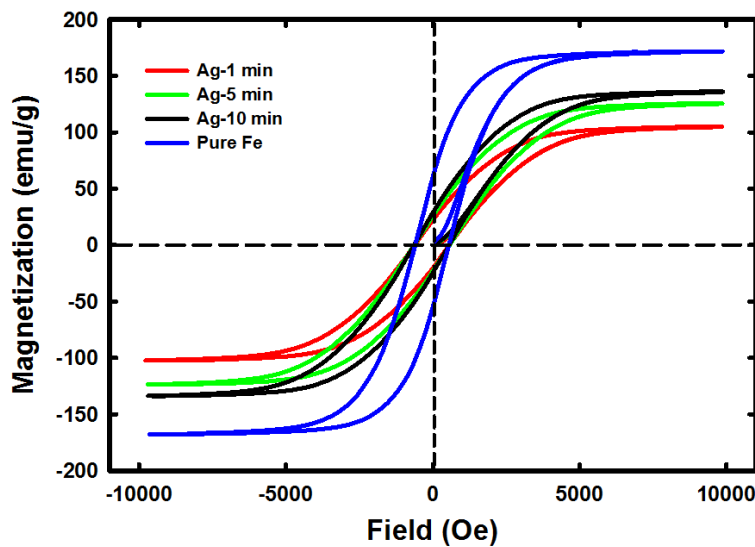


**Figure 5.8.** Room temperature VSM data showing how the magnetization is affected by the addition time of  $\text{AgNO}_3$  compared to as-synthesized iron nanoparticles.

Figure 5.9 presents a representative set of X-ray diffraction data for as-synthesized nanoparticles of bcc Fe, fcc Ag, and Ag/Fe. The XRD patterns of Ag/Fe and Fe show that the nanoparticles are slightly amorphous, lacking long-range order, due to the broadness of the diffraction peaks while the Ag is crystalline. The obtained raw data is depicted with miller indices from JCPDS reference powder diffraction files  $\alpha$ -Fe (01-089-7194) and Ag (03-065-2871). It is clear from the data that the iron present has no oxide impurities. However, the diffraction lines of amorphous FeB/Fe<sub>2</sub>B are similarly positioned to that of bcc Fe and cannot be completely ruled out.<sup>138</sup>

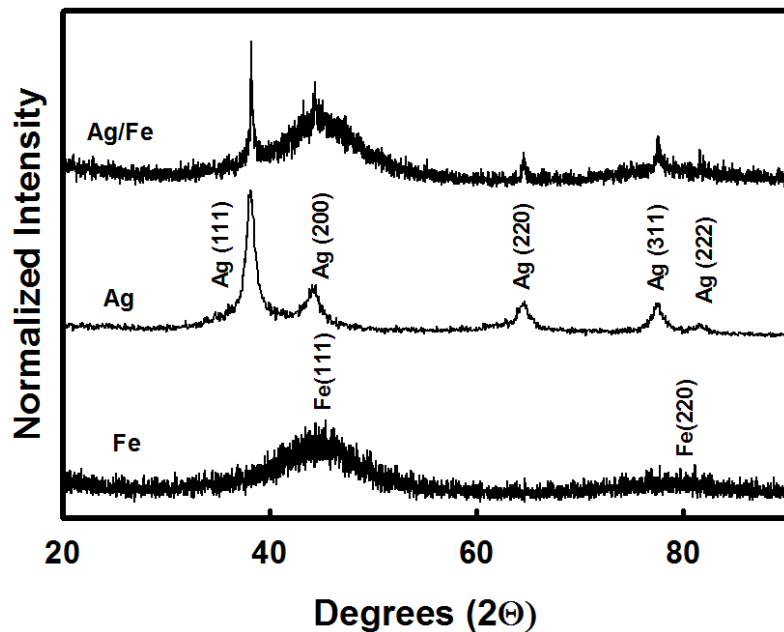


**Figure 5.9.** Representative XRD patterns of synthesized Fe, Ag, and Ag/Fe core/shell nanoparticles with their associated miller indices from JCPDS reference.

### 5.6 Surface Enhanced Raman Scattering

To further examine the presence of a Ag shell, surface enhanced Raman scattering (SERS) data were collected. This work has led us to design a novel collection and

detection method, which can be used as an alternative for conventional SERS and will be described briefly below.

SERS is an extremely sensitive technique exploited in laboratory investigations to provide single molecule detection. In sensor applications, this sensitivity is not well understood in part due to the low scattering efficiency. This low efficiency diminishes signal-to-noise, reducing sensitivity. We hypothesize that to improve this efficiency, it is necessary to concentrate the analyte with magnetic nanoparticles. While this is impossible with conventional noble metal nanoparticles, it becomes possible with core/shell nanoparticles. To test this hypothesis, we show through experimentation that by utilizing core/shell nanoparticles, where the surface is a noble metal and the core is magnetic, the nanoparticles can be concentrated along magnetic field gradients. It is believed that by pre-concentrating the particles utilizing a magnetic field, it will ultimately enhance the SERS observed from the particles. This enhancement could arise from a combination of two particular scenarios. The first scenario is indicative of the analyte of interest localized by the magnetic field providing an increase in the observed Raman signal. The second scenario is related to the aggregation of silver particles and leads to “hot spots” showing an increased SERS response (Figure 5.10). Several authors including Kniepp et al.,<sup>16-17,160</sup> Brus et al.,<sup>19</sup> and Nie and Emory<sup>161-162</sup> have shown that the aggregation of individual particles can lead to intense SERS enhancement through the formation of “hot spots” (an intense plasmon resonance that exists between two particles in close proximity). Individually, Xa et al.<sup>25</sup> and Van Duyne et al.<sup>163-165</sup> have reported that the enhancement factors via a “hot spot” is sufficient for single molecule detection

of  $10^{13}$  to  $10^{14}$  orders of magnitude enhancement. However, it has not been shown that by introducing a magnetic field to concentrate particles the same effect could arise. We report for the first time on a technique that aims to exploit this.

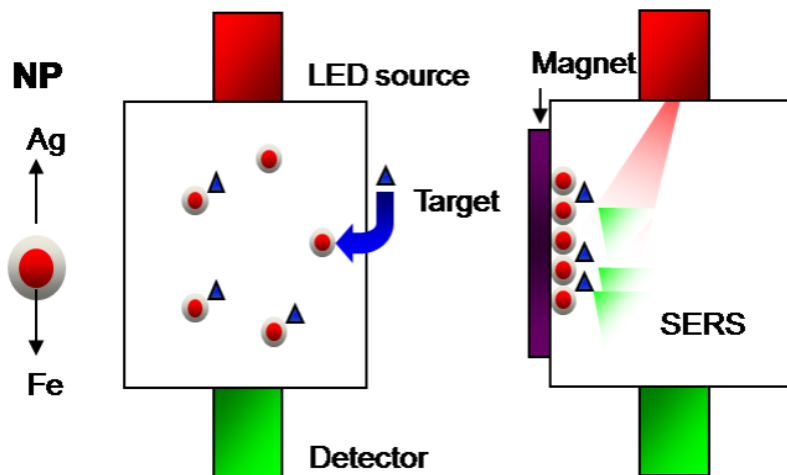


**Figure 5.10.** Utilizing magnetic core shell particles to pre-concentrate the target analyte for improved sensitivity.

In order to determine the effect of the novel magnetic pre-concentration method we are proposing on the SERS response, first we collected Raman spectra of pyridine, a compound commonly used in SERS studies (Figure 5.11). The data was collected using a Raman Systems R-3000 spectrometer equipped with a 785 nm laser. The pyridine solution also contained 5 ml of ethanol, which served as our internal intensity standard. In a typical experiment, magnetic SERS particles were then added to the standard pyridine solution and left to set for up to 20 minutes. Due to the high concentration of particles added, we were unable to collect SERS spectra of the dispersed particles. This missing data point complicates the analysis since we are unable to compare the effect of the pre-concentration phenomena directly to the conventional SERS observed for dispersed

particles. To demonstrate that we can pre-concentrate absorbed analytes with a magnetic field; it was experimentally determined that the best enhancement was achieved when a high concentration of particles were used. The SERS mechanism for dispersed particles appears to be remarkably different when the particles are aggregated by the magnetic field. Our goal is not merely to collect SERS of dispersed particles that happen to possess a magnetic core, but to induce a magnetic field to concentrate the particles and see that the SERS response is still viable.

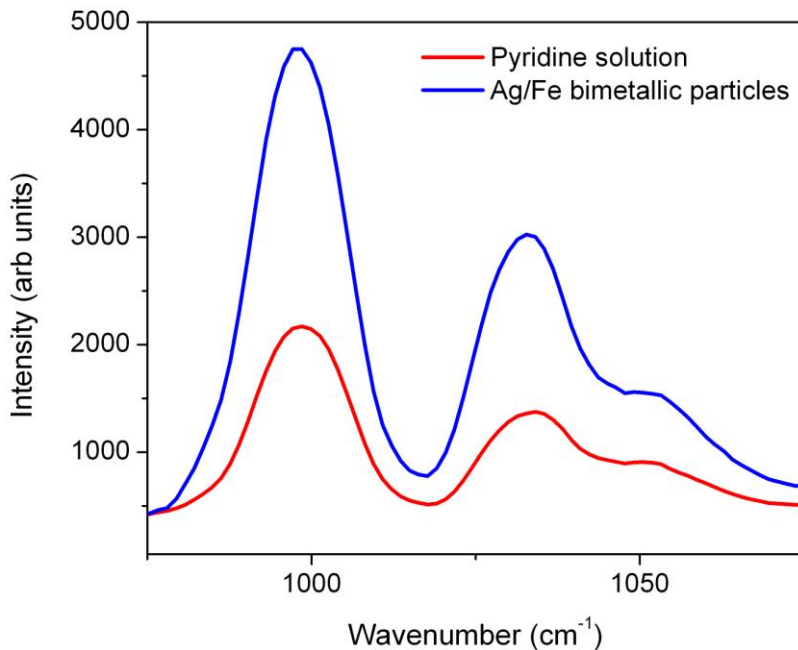


**Figure 5.11.** The SERS is dominated by two intense bands at about  $1,008$  and  $1,036\text{ cm}^{-1}$ , corresponding to the ring breathing and to the triangular-deformation modes, respectively. The enhancement is seen only with the Fe core Ag shell nanoparticles.

In the presence of an external magnetic field, all of the particles were collected to one side of a cuvette and the SERS spectra was collected and is indicated in Figure 5.10.

It is significant to note that the Raman spectra did, in fact, increase after the magnetic field was applied. This is indicative of two scenarios. First, pyridine is chemisorbed onto the modified magnetic particles and after the magnetic field is applied, the increased signal is proportional to the higher concentration of localized pyridine. Secondly, the increased SERS signal stems from “hot spots” generated by the aggregation of the modified magnetic particles. However, since we are using a 785 nm laser which is somewhat removed from the plasmon resonance of the silver surface, typically around 480 nm, it is reasonable to assume that the first scenario likely holds true. Future experiments will incorporate the use of Nd:YAG, 532 nm, which operates closer to the plasmon resonance of silver in order to determine if “hot spots” are indeed forming. While further work is needed to systematically identify the exact scenarios affecting the pre-concentration enhancement, we have proven that SERS is possible by the novel technique we proposed. The next chapter discusses how the enhancement can be increased by several factors by designing a SiO<sub>2</sub> layer between the magnetic and the noble metal nanoparticles.

### 5.7 Conclusion

This chapter discussed a novel one-pot aqueous synthesis of Fe/Ag and Ag/Fe core/shell nanoparticles synthesized using sodium borohydride. Based on TEM, XAS, and XPS characterization, we demonstrated that varying the addition times of silver nitrate we could form various core/shell morphologies consisting of Fe and Ag. This work demonstrates a novel route to chemically manipulating the formation of core/shell nanoparticles and can be tailored to various other core/shell nanoparticle systems with

relative ease. We have also demonstrated a novel technique using Raman spectroscopy and that the Fe/Ag core/shell nanoparticles are SERS-active and show practical applications for SERS based detection.

## **Chapter 6: Design of Fe/SiO<sub>2</sub>/Au Nanoparticles**

## 6.1 Introduction

In this chapter, we investigate a novel two-step synthesis of Fe/SiO<sub>2</sub>/Au core/shell nanoparticles by aqueous reduction using sodium borohydride. This chapter builds on the previously reported data from chapter 5 and shows that by using SiO<sub>2</sub> as a barrier between Fe and Au an increase in the SERS can be observed.

## 6.2 Synthesis of Fe/SiO<sub>2</sub> NPs

A total of 1.50 g of Fe NPs were added to 20 mL of DI-H<sub>2</sub>O and 200 mL ethanol under magnetic stirring in an Erlenmeyer flask. Then 1 mL of TEOS was slowly added for 30 minutes using an addition funnel and then allowed to react for 6 hours.

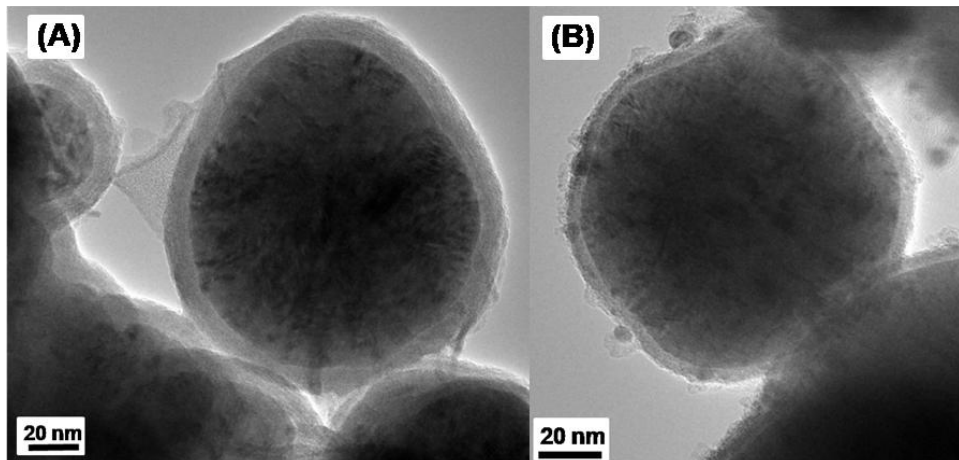
## 6.3 Synthesis of Fe/SiO<sub>2</sub>/Au NPs

To the Fe/SiO<sub>2</sub> NP solution 1 mL of 0.490 M HAuCl<sub>4</sub> was added. Then 0.204 g of sodium borohydride was added to the solution and the reaction was allowed to react for 10 minutes. The solution was quenched with ethanol several times and magnetically separated. After washing, the particles were placed in a vacuum oven at room temperature to dry prior to analysis.

## 6.4 Heat Treatment

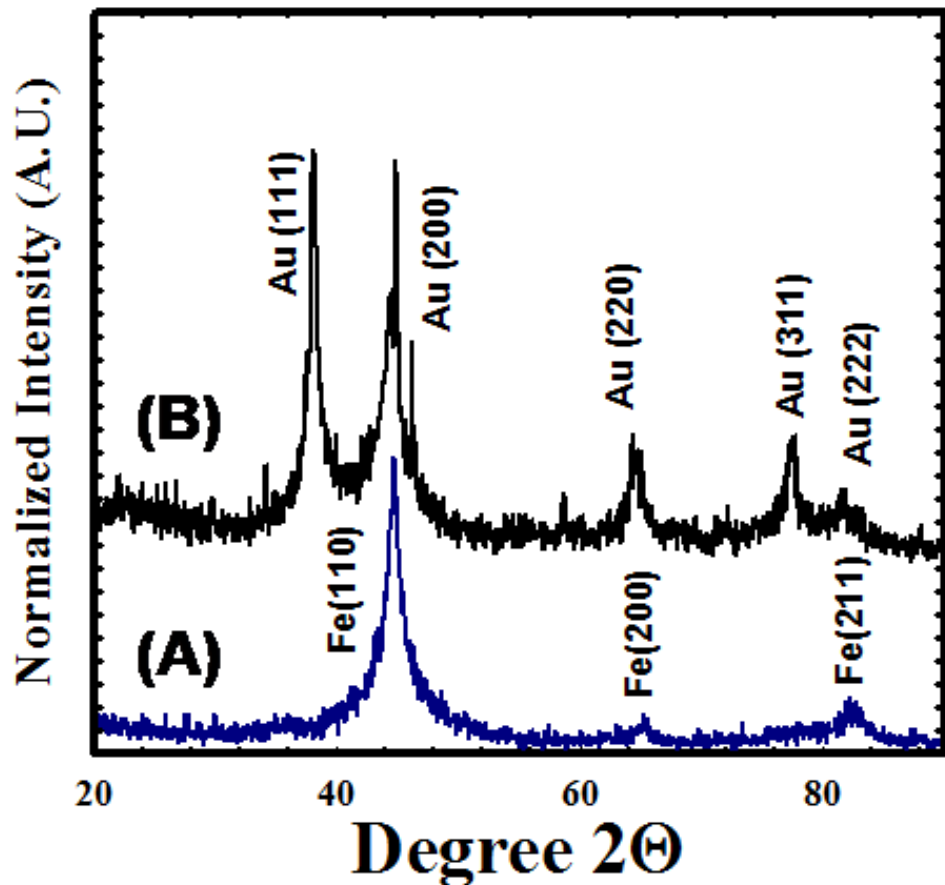
The dried Fe/SiO<sub>2</sub>/Au nanoparticles were heated in an oven under N<sub>2</sub> atmosphere to 400 °C for 30 minutes with a 10 °C/min ramp rate.

## 6.5 Results and Discussion



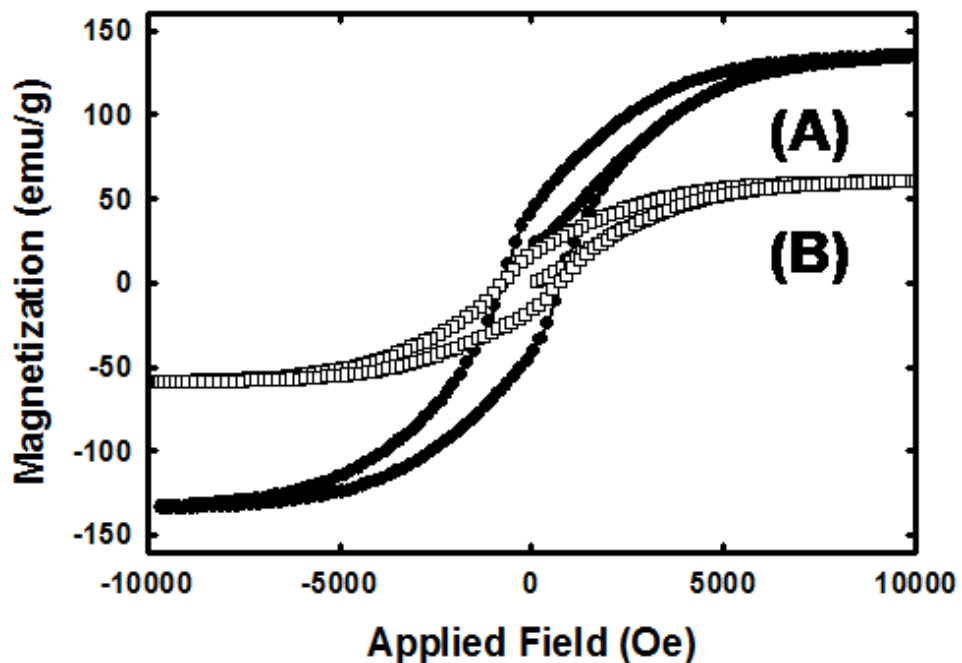
**Figure 6.1.** TEM images of (A) Fe/SiO<sub>2</sub> nanoparticles and (B) Fe/SiO<sub>2</sub>/Au nanoparticles.

Figure 6.1 shows typical TEM images of the as-prepared 80 nm Core/shell Fe/SiO<sub>2</sub> NPs with an iron core of 75 nm and a SiO<sub>2</sub> shell of 5 nm and the Fe/SiO<sub>2</sub>/Au NPs with Au islands of 4-5 nm.



**Figure 6.2.** XRD patterns of (A) as-synthesized Fe/SiO<sub>2</sub> nanoparticles and (B) as-synthesized Fe/SiO<sub>2</sub>/Au nanoparticles.

The XRD patterns of the as-prepared core/shell nanoparticles are presented in figure 6.2. All of the diffraction peaks of Au can be indexed to fcc crystal structure while the Fe can be indexed to bcc structure. In the figure, the data is presented with the miller indices from the JCPDS reference powder diffraction files  $\alpha$ -Fe (01-089-7194) and Au (01-04-0784). From the diffraction data, it can be seen that there are no Fe oxide impurities.



**Figure 6.3.** Room temperature Hysteresis loops for (A) as-synthesized Fe nanoparticles and (B) as-synthesized Fe/SiO<sub>2</sub>/Au nanoparticles.

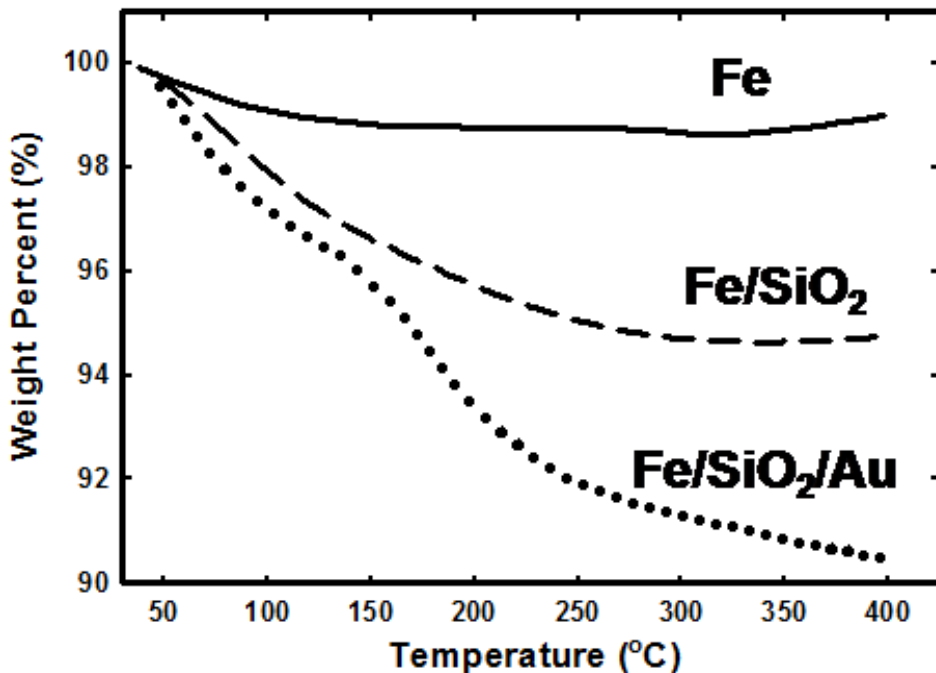


**Figure 6.4.** TGA analysis of Fe, FeSiO<sub>2</sub>, and Fe/SiO<sub>2</sub>/Au nanoparticles.

Room temperature hysteresis loops are shown in figure 6.3. The as-synthesized saturation magnetizations of Fe and Fe/SiO<sub>2</sub>/Au nanoparticles were found to be 148 emu/g and 58 emu/g, respectively. From the TGA data (Figure 6.4) it can be seen that roughly 10 percent of unreacted citrate is adsorbed onto the Fe/SiO<sub>2</sub>/Au nanoparticles and using a mass correction the corrected magnetization was calculated to be roughly 69 emu/g. Using the TGA the Fe/SiO<sub>2</sub>/Au samples were heat treated to 400 °C using N<sub>2</sub> gas. As mentioned above, about 10 percent weight loss was seen when the samples were heated. It is hypothesized that this reduction is due to the loss of organics that were adsorbed onto the surface of the particles along adsorbed H<sub>2</sub>O.

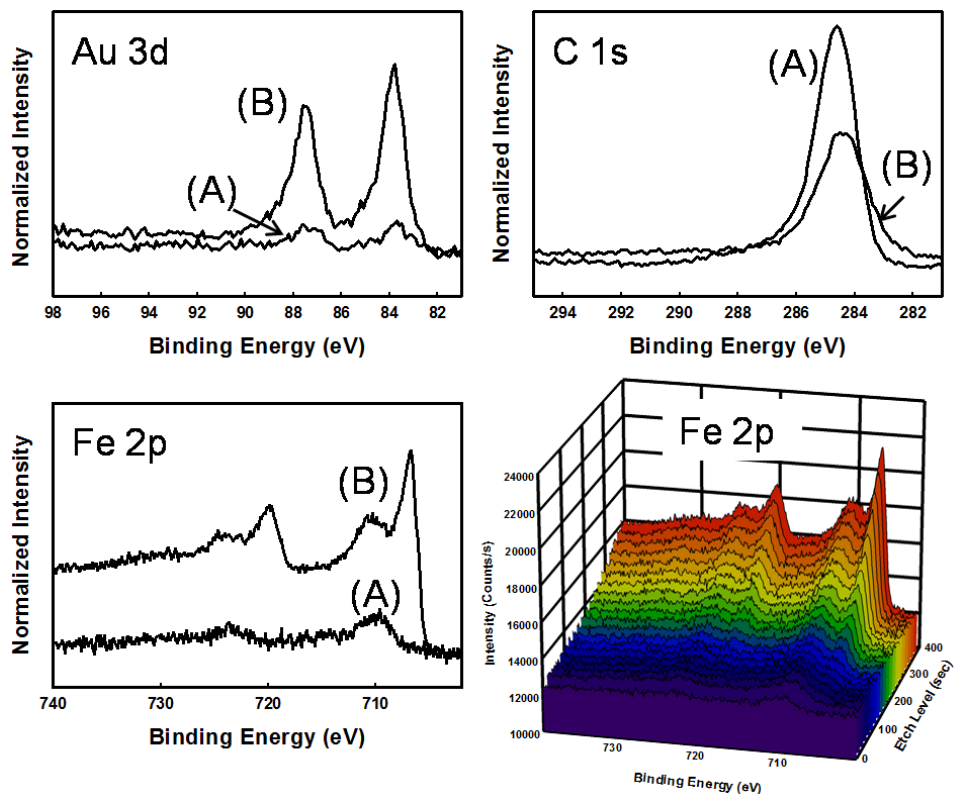


**Figure 6.5.** XPS spectra before (A) and after (B) annealing of Fe/SiO<sub>2</sub>/Au nanoparticles.

To confirm this, XPS analysis was conducted on the pre- and post-annealed samples. Figure 6.5 depicts the results of the XPS analysis. From the C 1s spectrum a decrease in the intensity of the C-C peak is seen after the samples are annealed under N<sub>2</sub> gas. This decrease is coupled with an increase in the intensity of the Au 3d peak, which supports the hypothesis that organics were on the surface obstructing the Au surface. In addition, an increase in the Fe 2p peak is seen. A high-resolution depth profile analysis shows that as the sample is etched, the intensity of the Fe 2p increases. More importantly, an increase in the metallic Fe (BE=709 eV) peak correlates with the XRD analysis.

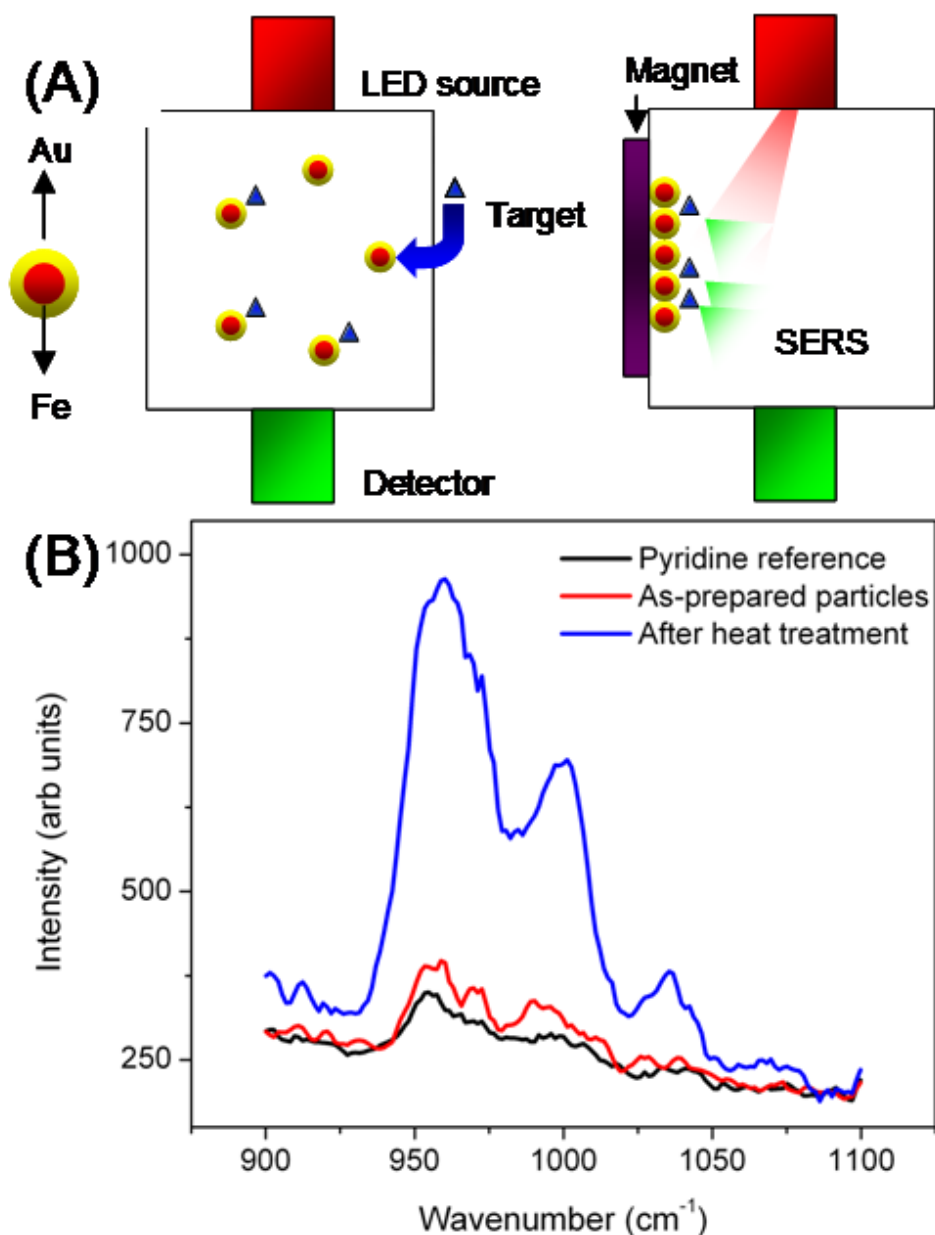


**Figure 6.6.** (A) Utilizing magnetic core/shell particles to pre-concentrate the target analyte for improved sensitivity. (B) SERS of the pyridine reference and Fe/SiO<sub>2</sub>/Au core/shell nanoparticles before and after heat treatment. The SERS is dominated by two intense bands at about 1,008 and 1,036 cm<sup>-1</sup>, corresponding to the ring breathing and to the triangular-deformation modes, respectively.

The aggregation of nanoparticles occurs naturally in solution due in part to the reduced surface energy after aggregation. Aggregation can also be enhanced by utilizing magnetic fields and magnetic nanoparticles. While it is difficult to collect SERS on magnetic nanoparticles consisting solely of Fe, Co or Ni, it becomes possible with core-shell nanoparticles. To test this hypothesis, we show through experimentation that by utilizing the Fe/SiO<sub>2</sub>/Au core/shell nanoparticles the nanoparticles can be concentrated along magnetic field gradients. This offers the distinct advantage of piloted movement of the target analyte. The observed SERS enhancement could arise from a combination of two particular scenarios (Figure 6.6 A). The first scenario is indicative of the analyte of interest localized by the magnetic field providing an increase in the observed Raman signal. The other scenario is related to the aggregation of gold particles. The aggregation of gold particles leads to “hot spots” which show increased SERS response.

In order to determine the affect of magnetic pre-concentration on the SERS response, we collected Raman spectra of pyridine, a compound commonly used in SERS studies, using a Raman Systems R-3000 spectrometer equipped with a 785 nm laser. The pyridine solution also contained 5 ml of ethanol which served as our internal intensity standard. In a typical experiment, magnetic SERS particles were then added to the standard pyridine solution and left to set for up to 20 minutes. In the presence of an external magnetic field of all the particles were collected to one side of a cuvette and the SERS spectra was collected and is indicated in Figure 6.6. It is significant to note that the Raman spectra of the heat treated particles did in fact increase after the magnetic field was applied. Previously we alluded to two possible scenarios for enhancement. First,

pyridine is chemisorbed onto the modified magnetic particles and after the magnetic field is applied the increased signal is proportional to the higher concentration of localized pyridine. Secondly, the increased SERS signal stems from “hot spots” generated by the aggregation of the modified magnetic particles. Since we are using a 785 nm laser which is somewhat removed from the plasmon resonance of the gold surface, typically around 520 nm, it is reasonable to assume the first scenario likely holds true. Future experiments will incorporate the use of Nd:YAG, 532 nm, which operates closer to the plasmon resonance of gold in order to determine if “hot spots” are indeed forming.

## 6.6 Conclusion

This chapter discusses a novel two-step synthesis of Fe/SiO<sub>2</sub>/Au core/shell nanoparticles by aqueous reduction using sodium borohydride. Based on TEM, XRD, XPS, and TGA characterization, this chapter demonstrated that the as-prepared particles are not SERS active and require heat treatment to remove citrate from the surface. The methods presented in this chapter offer greater SERS-active response than the previously reported Fe/Ag nanoparticles and shows more promise for SERS based detection.

## **Section 2: Polyol Method**

## **Chapter 7: Design of Cu and Ni nanoparticles**

## 7.1 Introduction

There has been extensive research into the synthesis of preparing metal particles by the polyol process over the past decade, and it continues to generate numerous publications.<sup>62,166-211</sup> Figure 7.1 shows that the number of publications involving the polyol process for the reduction of metal salts continues to increase each year. The graph was generated by searching Scifinder scholarly and Web of Science databases. Search phrases such as, “polyol process”, “polyol method”, and “metal reduction by polyol” were used to generate these numbers. The polyol process has been used to prepare elemental Co, Ni, Cu, Ag, Au, Pt, Pd, Cd, Fe, and also bimetallic alloys of CoNi, AgPd, AuPt, and FePt.<sup>178,212-216</sup> Several papers also highlight the formation of metal oxides such as Fe<sub>3</sub>O<sub>4</sub>, CoFe<sub>2</sub>O<sub>4</sub>, CuFe<sub>2</sub>O<sub>4</sub>, and ZnFe<sub>2</sub>O<sub>4</sub>.<sup>166,217-218</sup> More recently, the polyol process has been used to prepare aqueous ferrofluids as MRI contrast agents, bimetallic core/shell nanoparticles for catalysis, TiO<sub>2</sub> nanocomposites for monolithic dye-sensitized solar cells, Cobalt Carbide nanoparticles for permanent magnet research, and Ag and Ag/Au nanoparticles for Surface Enhanced Raman Scattering.<sup>14-15,18,219-224</sup>

Although the physical properties such as size, shape, and crystal structure of the particles have been controlled by manipulating the synthetic conditions that influence the nucleation and growth steps, there are limited attempts to fully understand the reaction mechanism. Consequently, nanoparticles are synthesized only through trial and error by running large numbers of experiments and randomly varying the parameters. Larcher et al. were the first to use theoretical calculations to prepare a thermodynamic approach to a mechanism for the polyol process.<sup>225</sup> However, in their calculations they assumed that the

reduction of the precursor into metal comes with a total oxidation of ethylene glycol into CO<sub>2</sub> and H<sub>2</sub>O. In this situation, the polyol has the maximum reducing power. Experimental research on Cu and Ni shows that these conditions are not always needed for the reduction.

In this chapter, we report on a combination of theoretical and experimental data from the formation of elemental Cu and Ni nanoparticles produced using various polyols to more accurately determine a mechanism for the polyol process. From this approach, we believe that the mechanism can be extended to other metal systems as well. Following this, a detailed explanation of the work conducted in this dissertation will be presented as separate chapters for the formation of core/shell nanoparticles, ferrofluids, and Cobalt Carbide nanoparticles.

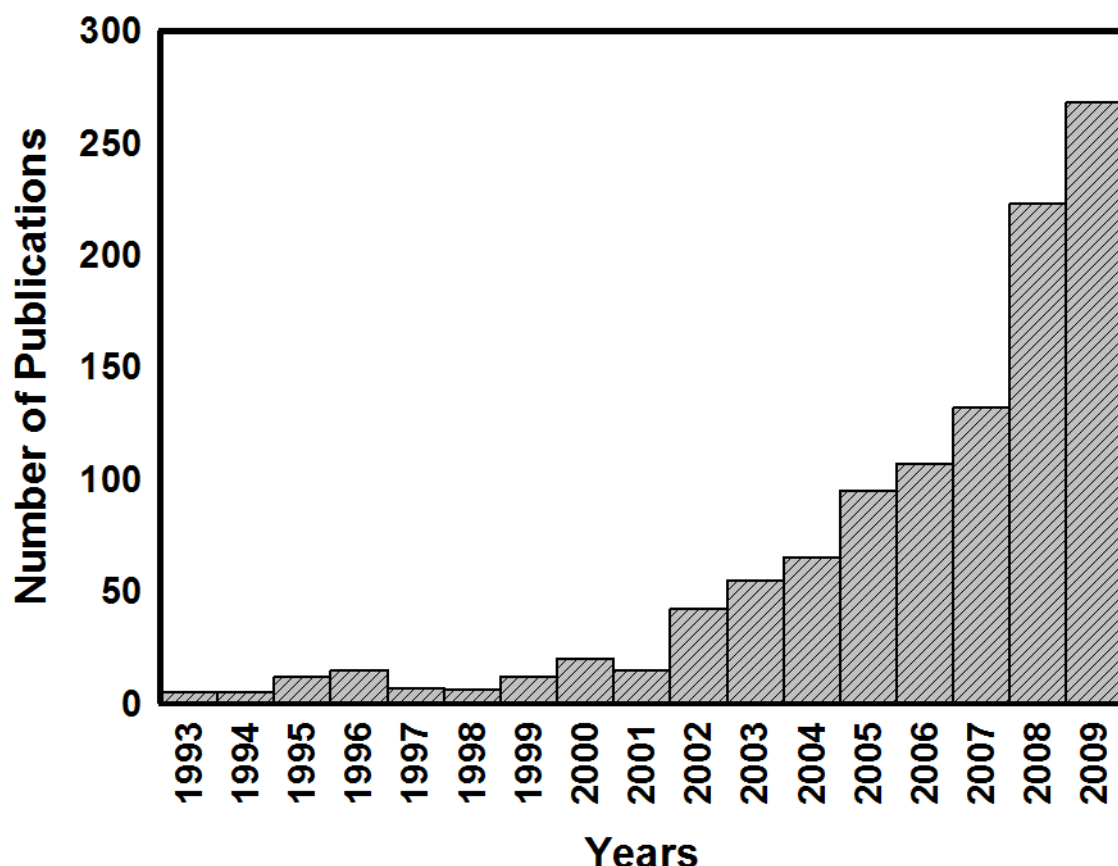


**Figure 7.1.** Graph depicting the number of publications involving the polyol process as a medium for the reduction of metals, oxides, and mixed metal oxide nanoparticles. The polyol process became highly published after 2001. The results are from a combined search for “polyol process”, “polyol method”, and “metal reduction by Polyol” in the Web of Science and Scifinder databases.

## 7.2 History of the Polyol Process

The reaction was first proposed by Fievet and Blin et. al. in a 1984 French patent, followed by a dissertation, and then later a publication (1989) in solid state ionics.<sup>171-172,183,226</sup> The papers describe a new process for the preparation of finely divided micron and submicron powders of easily reducible metals. They state that the uniqueness of this process is because the reduction reaction proceeds through the solution rather than in the solid state. What this offers is the control of the reduction mechanism through the

separation of the nucleation and growth steps, as previously described in chapter 1. Following this, they propose that the reaction proceeds through discrete steps. 1) dissolution of the precursor, 2) reduction of dissolved metallic species by the polyol, and 3) homogeneous nucleation and growth of the metal particles in solution. This general scheme led to the first mechanism of the polyol (figure 7.2).

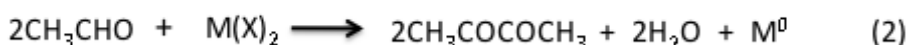
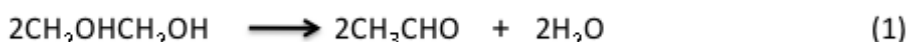


**Figure 7.2.** Proposed mechanism by Fievet. et.al. Ethylene glycol dehydrates to acetaldehyde followed by the formation of diacetyl. X represents anions such as: Cl or  $\text{SO}_4^{171}$

Fievet et. al. briefly explain that the oxidation of ethylene glycol forms diacetyl as a main oxidation product. They explain this process as a duplicative oxidation of acetaldehyde produced by the dehydration of ethylene glycol.<sup>171</sup> However, due to a lack of investigation, it was still unclear what byproducts were actually formed during the addition of metal precursors. Because of this, most of the work up to 2000 was restricted to the synthesis of some first row transition metals and precious metals such as: Co, Cu, Ag, Ni, and Cd.<sup>227-229</sup> In the reduction of some metals, the formation of different solid phase intermediates in the polyol make the reaction mechanism more complex. Less reducible Fe, Cd, Ir, Bi, Pb, Rh, and Ru were only reported a few times. It was not until 2000 that the first thermodynamic investigation was published to explain the preparation of metallic powders.<sup>225</sup> Patrice et al. explained that the degradation of ethylene glycol and the reduction of metal species must take place in two discrete steps (figure 7.3).

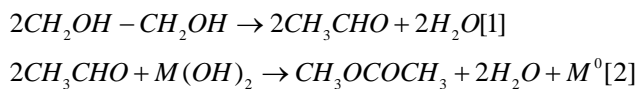


**Figure 7.3.** Mechanism showing duplicative oxidation of ethylene glycol proposed by Patrice et al. .

The first step involves the dehydration of ethylene glycol, forming acetaldehyde. The second step is the duplicative oxidation of the acetaldehyde, forming the diacetyl seen by Fievet et al. They hypothesized that the transformation of the diacetyl takes place concomitantly with the formation of metallic powder. They continued to explore the thermodynamic approach by assuming that the reduction of metallic powders occurred only during total oxidation of ethylene glycol into  $\text{CO}_2$  and  $\text{H}_2\text{O}$  and this led them to a proposed mechanism (figure 7.4).



**Figure 7.4.** Proposed mechanism for the formation of Metal nanoparticles from metal oxide precursors. The reaction assumes that a complete oxidation of ethylene glycol produces gaseous carbon dioxide and water.

Following the work of Larcher and Patrice in 2000, there have been many ambiguities and inconsistencies in recent literature that leaves open a need for a more comprehensive study of the reduction power of the polyol process; specifically in the choice of metal precursors. From the research that we have conducted and the knowledge of previous work, we were also able to extend the polyol process to core/shell systems. Understanding how Cu and Ni form core/shells over alloys should help the investigation of the polyols role in the reduction of metal salts.

### 7.3 Experimental

#### 7.3.1 Sample Preparation

All hydrated metal salts (acetates, hydroxides, and chlorides), polyols (ethylene glycol (EG), propylene glycol (PG), diethylene glycol (DEG), tetraethylene glycol (TEG), and butylenes glycol (BG)), NaOH, and methanol were used without any further purification.

The general procedure involves the addition of 0.1 M metal salt in 50 mL of polyol, followed by the addition of 0.3 M NaOH. Two reaction conditions, reflux or distillation, were used and the reaction was allowed to proceed for up to 2 hours. The final products were centrifuged and washed several times with methanol. The particles were then dried in a vacuum oven at room temperature prior to analysis.

#### 7.3.2 Characterization

Thermal analysis (TGA) was performed on a TA instruments Q5000 under N<sub>2</sub> gas flow from 30-600 °C. Powder x-ray diffraction (XRD) patterns were recorded on a Panalytical X'pert pro diffractometer ( $K\alpha = 1.541 \text{ \AA}$ ). Transmission electron microscopy (TEM) was done on a JEOL JEM-1230 TEM at 150 KV fitted with a Gatan Ultra Scan 4000 CCD camera. Room temperature magnetic data was collected using a vibrating sample magnetometer (VSM) by Lakeshore Cryotronics Inc. model 7300 VSM. X-ray photoelectron spectroscopy (XPS) was performed on a Thermo Scientific ESCALAB 250 spectrometer.

### 7.3.3 Theoretical Investigation

First principles theoretical studies within the generalized gradient density functional formalism were carried out to aid in the investigation of the polyol process reaction mechanism,<sup>230</sup> and to explain the experimental results. All calculations were performed using the deMon2k software.<sup>231</sup> A variational fitting of the Coulomb potential was employed in order to avoid the calculation of four-center electron repulsion integrals.<sup>232</sup> The auxiliary density functional theory method was used in which the exchange-correlation potential is calculated via a numerical integration from the auxiliary function density<sup>233</sup> using the GEN-A2 function set.<sup>234</sup> All electrons of the Cu, Ni, C, O and H atoms were treated explicitly using the double- $\zeta$  valence plus polarization basis sets.<sup>235</sup> A quasi-Newton method in delocalized internal coordinates was used for the geometry optimizsation.<sup>236</sup> Several initial configurations were considered and the geometries were fully optimized without any symmetry constrain to determine the ground state. The resulting ground states were further ascertained upon frequency analysis.

## 7.4 Results and Discussion

### 7.4.1 X-ray and Morphological Characterization

The reduction of Cu salt precursors (Cu hydroxide, Cu chloride, and Cu acetate) dissolved in various polyols (EG, PG, DEG, and TEG) under both refluxing and distillation conditions were investigated. In each case, the color of the solution changed gradually from an initial green color to blue, then to brown, and finally to a brownish-red color, which was also seen by others.<sup>212,237-239</sup> We have recently shown that the trapped blue intermediate in EG is that of a Cu-glycolate complex which forms after dissolution

of the Cu salt precursor in the polyol.<sup>212,240</sup> This will be explained in more detail later in this chapter.

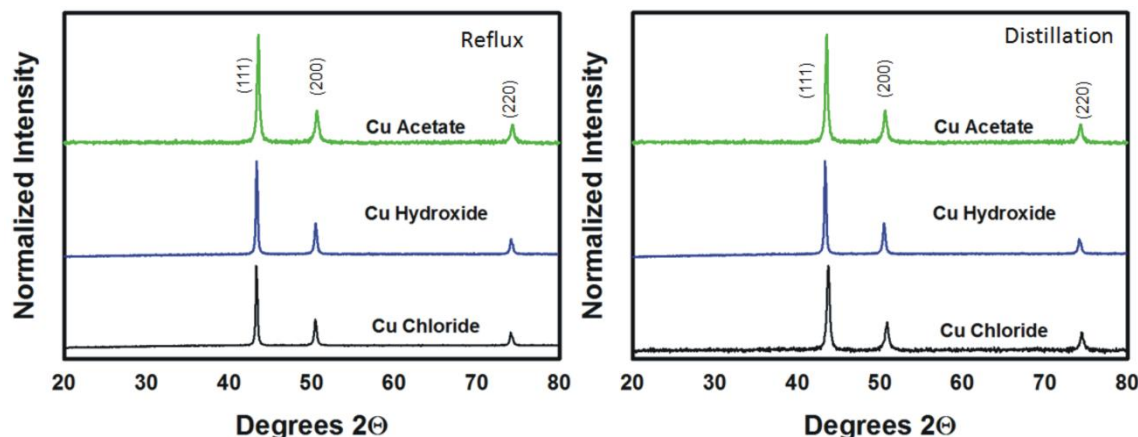


**Figure 7.5.** X-ray diffraction patterns of Cu salt precursors in ethylene glycol under refluxing and distillation conditions. In each case, the result is elemental Cu.

Regardless of the solvent and metal precursor used, the x-ray diffraction patterns show the formation of elemental Cu (Figure 7.5). The nanoparticles crystallized into a face centered cubic (fcc) structure with diffraction peaks at  $43.567^\circ$ ,  $50.438^\circ$ , and  $74.312^\circ$  which correspond to the (111), (200), and (220) planes, respectively. The high purity of elemental Cu was verified by the absence of oxide, hydroxide, and precursor reflections observed within the detection limit of the XRD measurements. The refinement of the XRD patterns was done by the Rietveld method in order to calculate the unit cell parameters.

Peak fitting was carried out by the Fullprof software using the fcc Cu (ICDD,  $\text{fm} \bar{3} \text{m}$ , card # 85-1326) as a reference structure. The lattice parameter ( $\text{Cu}_{\text{bulk}} = 3.6150 \text{ \AA}$ ) of the formed elemental Cu varies slightly between the solvents and the Cu precursors from  $3.6143 \text{ \AA}$  ( $\text{CuOH, PG, reflux}$ ) to  $3.6181 \text{ \AA}$  ( $\text{CuOH, TEG, reflux}$ ). By analyzing the average peak widths of the (111), (200), and (220) reflections, the lattice strain, and mean

crystallite size were calculated (Table 7.1). The mean crystallite size, using the Scherrer equation, varied slightly between the different solvents and the various metal precursors. This can be attributed to the change in particle shape as well as the possibility of multiple crystalline regions within each nanoparticle. A slight increase in the lattice strain is also seen which is explained by a shift in both the lattice parameter and a change in particle shape. Figure 7.6 shows TEM images with a histogram showing the average particle size for various glycols. It was seen by TEM that changing the solvent from a short chain (EG) to a long chain (TEG) shifted the particle shape from spheres to rods (Fig.7.7). There was little deviation seen between the mean crystallite size from XRD and the particle size observed from TEM which indicates that the majority of the particles seen on TEM are not polycrystalline.

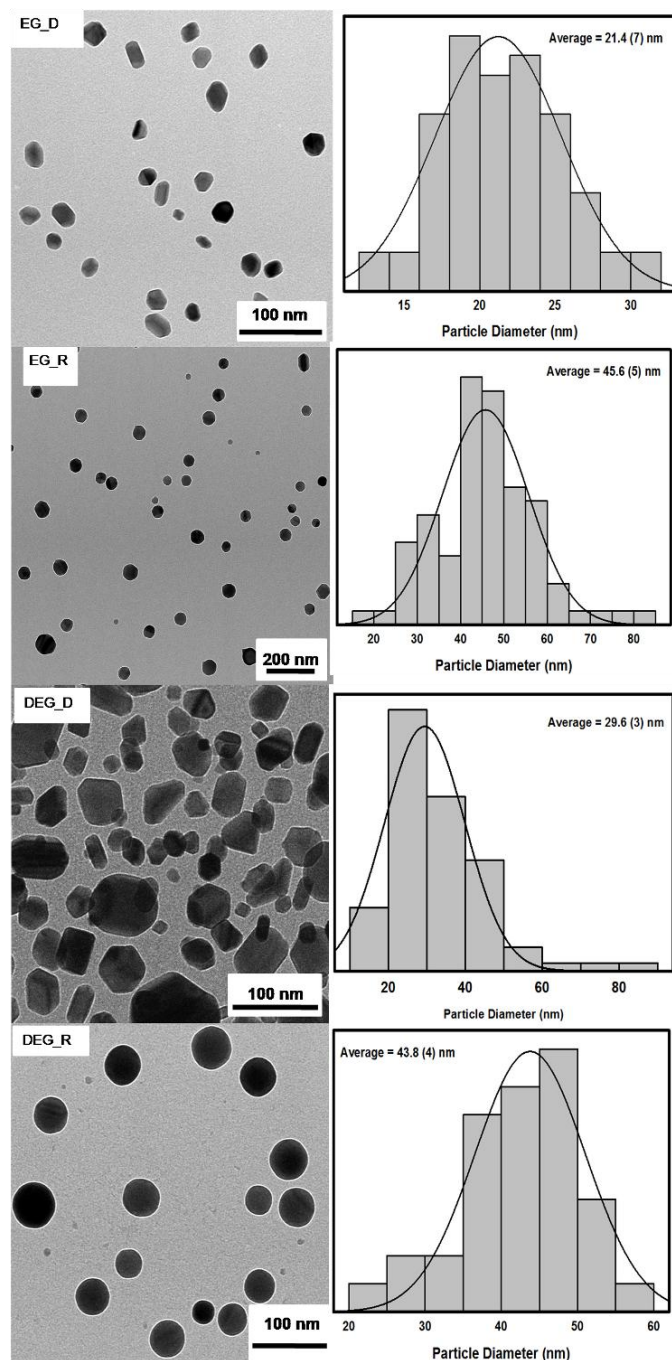


**Figure 7.6.** TEM images of elemental Cu nanoparticles synthesized using Cu Chloride with EG and DEG under either refluxing(-R) or distillation(-D) conditions.

**Table 7.1.** Results from the analysis of the Cu XRD patterns showing the mean crystallite size, lattice strain, and lattice parameters.

Solvent	Precursor	System	Lattice Parameter (Å)	D <sub>x</sub> (nm)	Lattice Strain (%)
EG	Cu Chloride	reflux	3.6153 (6)	36	0.0747 (6)
		distillation	3.6156 (2)	35	0.0813 (9)
	Cu Acetate	reflux	3.6154 (6)	42	0.0648 (9)
		distillation	3.6151 (5)	42	0.0667 (1)
	Cu	reflux	3.6161 (7)	38	0.0720 (3)
PG	Hydroxide	distillation	3.6153(1)	32	0.0886 (9)
	Cu Chloride	reflux	3.6152 (9)	45	0.0345 (3)
		distillation	3.6148 (2)	40	0.0734 (4)
	Cu Acetate	reflux	3.6154 (6)	34	0.0648 (9)
		distillation	3.6151 (5)	32	0.0447 (4)
DEG	Cu	reflux	3.6161 (7)	33	0.0642 (3)
	Hydroxide	distillation	3.6153(1)	28	0.0142 (7)
	Cu Chloride	reflux	3.6153 (8)	55	0.0347 (6)
		distillation	3.6150 (2)	80	0.0443 (3)
	Cu Acetate	reflux	3.6170 (3)	38	0.0884 (6)
		distillation	3.6159 (7)	36	0.0799 (1)
TEG	Cu	reflux	3.6143 (4)	39	0.0720 (3)
	Hydroxide	distillation	3.6167(3)	32	0.0886 (9)
	Cu Chloride	reflux	3.6161 (3)	47	0.0889 (2)
		distillation	3.6179 (9)	67	0.0885 (3)
	Cu Acetate	reflux	3.6160 (5)	69	0.0928 (3)
		distillation	3.6169 (3)	29	0.0633 (8)
Cu	reflux	3.6152 (1)	25	0.0107 (9)	
	Hydroxide	distillation	3.6181(9)	36	0.0755 (0)

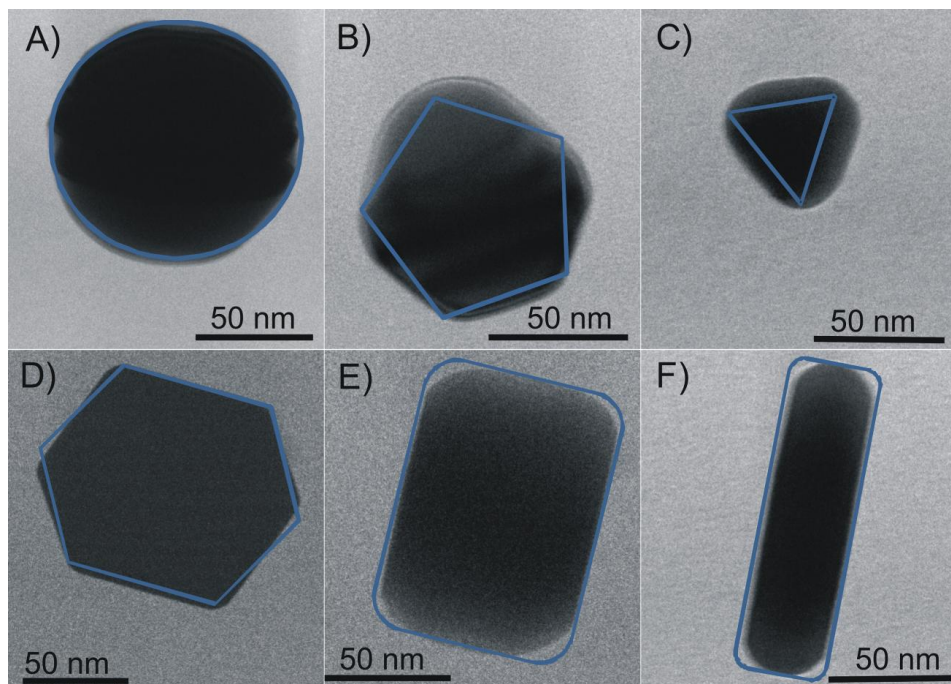


**Figure 7.7.** The synthesis of the polyol reaction can yield various elemental Cu morphologies by simply varying the reaction medium. In the case of these 6 nanoparticles, the solvents varied from A) EG under reflux, B) EG under distillation, C) PG under reflux, D) DEG under reflux, E) DEG under distillation, and F) TEG under distillation to TEG. It is thought that the morphology is dependent on the chain length of the polyol.

Our work on Cu nanoparticles led us to the reduction of Ni nanoparticles by the polyol process. As with the investigation of Cu nanoparticles, the reduction of Ni salt precursors (Ni hydroxide, Ni chloride, and Ni acetate) dissolved in various polyols (EG, PG, DEG, and BG) under both refluxing and distillation conditions was investigated. For all of the Ni precursors under distillation and refluxing conditions, the product was elemental Ni, with the exception of  $\text{NiCl}_2$  in EG, which will be discussed below. Figure 7.8(1) shows representative Ni nanoparticles reduced under distillation conditions with various solvents. The nanoparticles crystallized into the stable fcc Ni (ICDD,  $\text{fm}\bar{3}\text{m}$ , card

#04-0850) form with reflections at  $44.25^\circ$ ,  $51.65^\circ$ , and  $76.125^\circ$  which corresponds to the (111), (200), and (220) diffraction planes, respectively. There was a slight shift in the lattice parameter ( $\text{Ni}_{\text{bulk}} = 3.5238 \text{ \AA}$ ) with all of the nanoparticles analyzed and the mean crystallite size was significantly smaller than that observed from the TEM images (Figure 7.9), suggesting that the particles are polycrystalline. It is also interesting to note that the formation of mixed phase fcc and hexagonal closed packed (hcp) Ni occurs with the 3M NaOH and when the NaOH concentration was decreased to 1M, no hcp Ni formed. Ying et al. speculated that there is a direct correlation between the increase in the NaOH concentration and the increased formation of hcp Ni with respect to fcc Ni.<sup>241</sup> Hinotsu et al. suggest that the presence of hydroxyl ions in the polyol influences the overall reaction kinetics.<sup>242</sup> The introduction of  $\text{OH}^-$  ions altered the overall morphology and size of their Ni nanoparticles from micron to plate-like structures to spherical nanoparticles. In order to form the unstable hcp Ni phase the reaction kinetics must be increased enough so that the stable fcc Ni does not have time to form. Figure 7.10 shows room temperature VSM hysteresis curves for 1 M and 3 M NaOH concentrations in various polyols. A decrease from 58 emu/g to 20 emu/g in the magnetization saturation is due to the incorporation of non-magnetic hcp Ni. While the polyol process has only provided one report of the preparation of pure phase hcp Ni,<sup>243</sup> other methods such as the sol-gel method have also been able to produce hcp Ni.<sup>244</sup>

As mentioned above,  $\text{NiCl}_2$  in EG reaction was the exception by not showing pure reduction and formation of solely metal nanoparticles. Figure 7.8(2) shows that even after 36 hours of refluxing  $\text{NiCl}_2$  could not be fully reduced to elemental Ni. The predominate

phase is a Ni-layered hydroxyl salt (LHS), which has been shown to form only when metal acetates are used with polyols.<sup>245-246</sup> What this shows, is that for the first time a Ni-LHS can be formed without the presence of an acetate precursor ion. In this case, a Ni-glycolate structure is forming where the deprotonated EG has bidentate character, as seen in previous x-ray diffraction studies.<sup>247</sup>

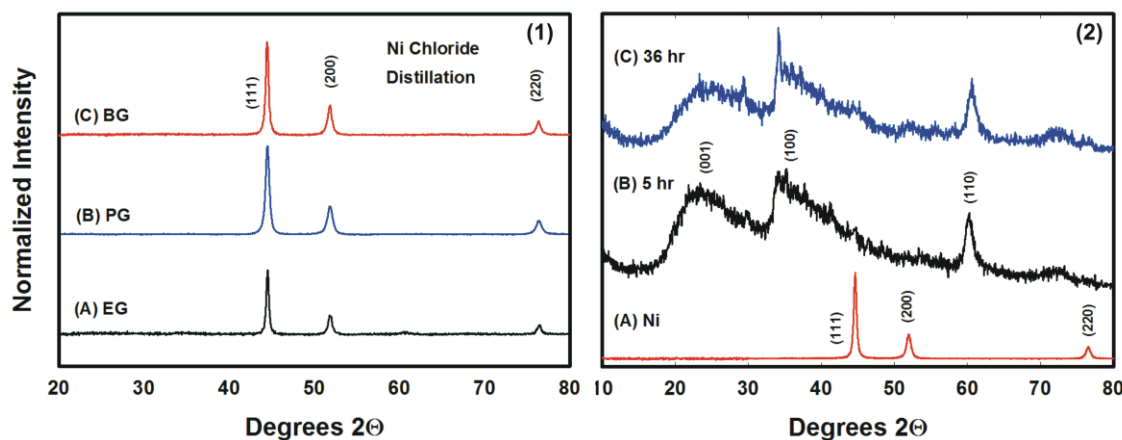


**Figure 7.8.** (1) XRD patterns of Ni nanoparticles reduced with various polyols under distillation. (2) The results of Ni chloride under refluxing conditions. A Ni-LHS forms instead of elemental Ni.

**Table 7.2.** Results from the analysis of the Ni XRD patterns showing the mean crystallite size, lattice strain, and lattice parameters.

Precursor	Solvent/NaOH	Crystal structure	a,b (Å)	c (Å)	D <sub>x</sub> (Å)	e (%)
Ni Chloride	DEG/3M NaOH	fcc	3.534 (1)		118	0.00196 (7)
		hcp	2.640 (3)	4.328 (3)	121	0.00567 (3)
		fcc	3.525 (8)		190	0.00147 (3)
Ni Chloride	EG/3M NaOH	hcp	2.650 (4)	4.335 (8)	326	0.00606 (5)
		fcc	3.525 (9)		183	0.00153 (5)
Ni Chloride	PG/1M NaOH	fcc	3.525 (4)		144	0.00248 (8)
Ni Chloride	PG/3M NaOH	fcc	3.528 (3)		126	0.00247 (7)
Ni Chloride	BG/3M NaOH	fcc	3.523 (1)		173	0.00267 (9)
Ni Acetate	EG/3M NaOH	fcc	3.526 (3)		241	0.00115 (4)
		fcc	3.534 (7)		95	0.00419 (5)
Ni Acetate	DEG/3M NaOH	hcp	2.641 (1)	4.336 (2)	157	0.00419 (4)
Ni Hydroxide	EG/3M NaOH	fcc	3.522 (8)		184	0.00247 (9)
Ni Hydroxide	DEG/3M NaOH	fcc	3.527 (3)		169	0.00236 (7)
		hcp	2.638 (9)	4.329 (1)	181	0.00234 (3)

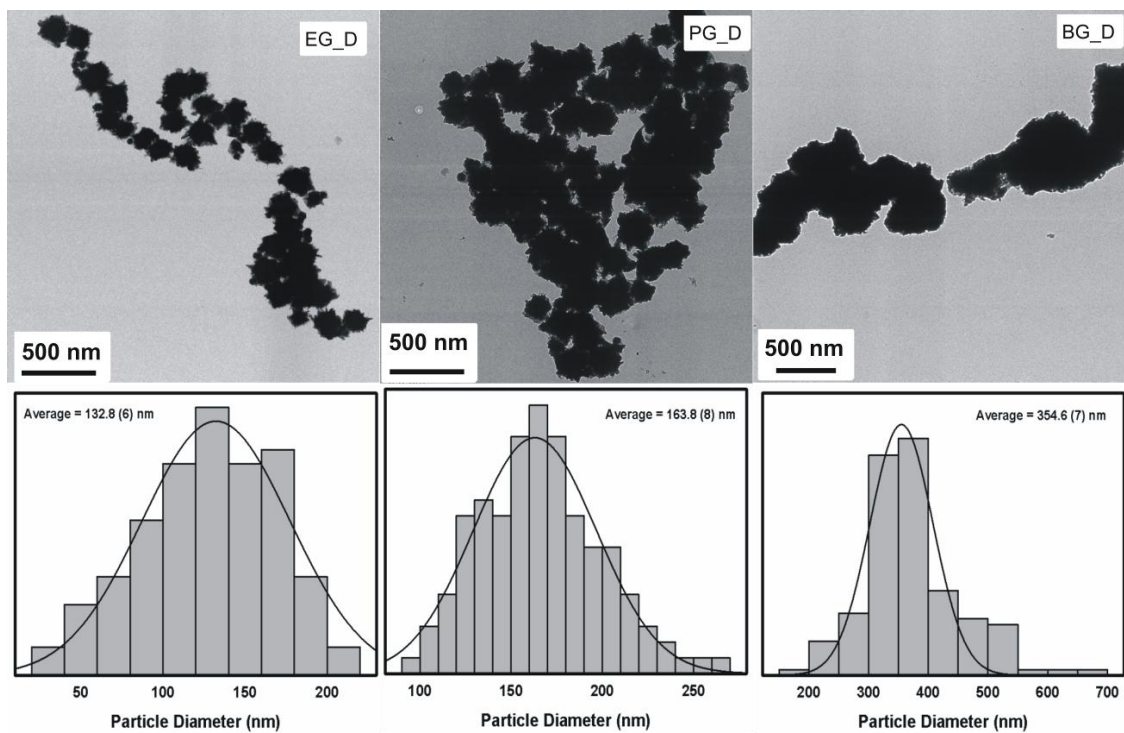


**Figure 7.9.** TEM images of Ni nanoparticles reduced under various glycol environments.

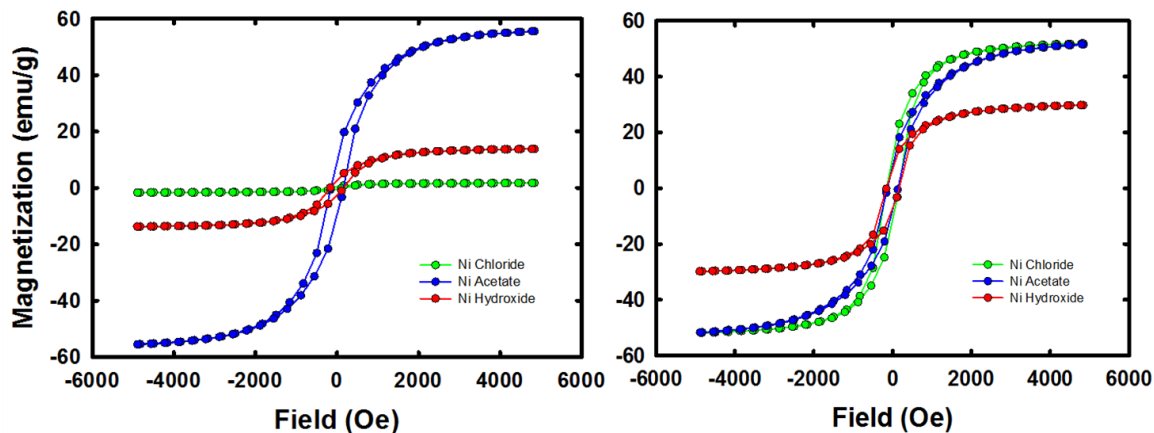


**Figure 7.10.** XRD graphs of (left) Ni salts reduced under refluxing conditions and (right) Ni salts reduced under distillation conditions using EG.

### 7.4.2 XPS Results

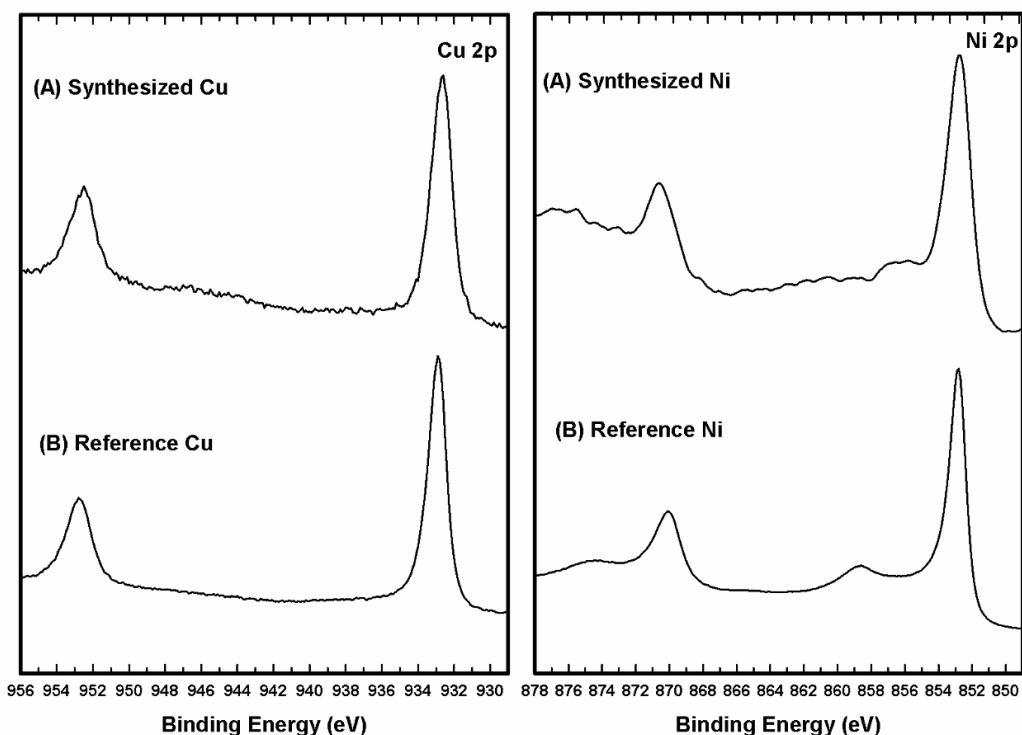


**Figure 7.11.**(A) Cu 2p and Ni 2p region scans and (b) reference Cu 2p and Ni 2p.

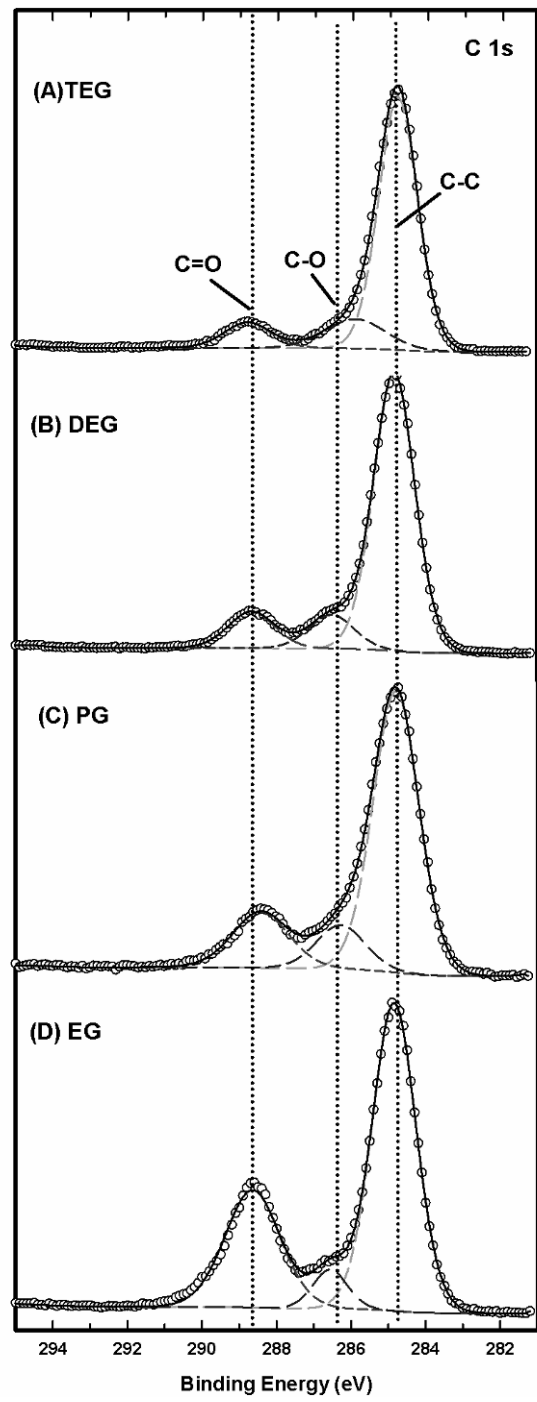


**Figure 7.12.** XPS data of the C 1s region scans using different glycols.

The C 1s, Cu 2p, and Ni 2p region scan spectra of Cu and Ni nanoparticles reduced under various solvents were analyzed. Figure 7.11 shows a representative Cu 2p and Ni 2p region scan. The spectra of the Cu 2p reveals a  $2p_{3/2}$  peak and a  $2p_{1/2}$  peak at ~932 eV and ~952 eV, respectively. The spectra of the Ni 2p reveals a  $2p_{3/2}$  peak and a  $2p_{1/2}$  peak at ~853 eV and 870 eV, respectively. Also, peaks at ~ 857 eV and ~874 eV are satellite peaks. For comparison, a reference Cu 2p and Ni 2p scan are shown (Figure 7.11). Representative C 1s region scans are shown in Figure 7.12. From the analysis of the spectra, three peaks can be fit. First, a slight asymmetric peak at 284.7 eV can be attributed to C-C bonding with a broad peak at a slightly higher binding energy ~286.5 eV with relatively lower intensity (5-10% of main peak) due to C-O bonding. A third peak at ~288.7 eV can be attributed to carbon atoms bound to one oxygen with a double bond (C=O). It is interesting to note that the intensity of the C=O decreases with an increase in the polyol chain length. It is hypothesized that the product formed during the reaction is a diacetyl (O=C-C=O) compound. Thus it makes sense that spectra of longer chain polyols would show the relative abundance of C=O to be smaller with respect to C-C and C-O bonds.

#### 7.4.3 Crystal Growth

Several early papers on the polyol process have described the polyols as being a solvent, a mild reducing agent, and a protective or capping agent.<sup>183-184,248</sup> Ung et al. reported in 2007 on the formation and anisotropic growth of NiCo nanoalloys as being driven by the pH of the system. By raising the [NaOH] in PG to 0.25 M they were able to form isotropic spherical nanoparticles. However, when the [NaOH] decreased below 0.25

M (between 0.1 and 0.2 M) they were able to form anisotropic growth consisting of nanoplatlets, nanodumbells, and nanowires. The use of capping agents has also been reported to play a critical role in controlling the formation of nanocrystals. For example, Sun et al. reported that by using poly(vinyl pyrrolidone) (PVP) in EG solutions with  $\text{AgNO}_3$  they were able to grow uniform 50  $\mu\text{m}$  Ag nanowires.<sup>249</sup>

We studied the effect of the polyol process on the growth of Cu nanoparticles and maintained a constant  $[\text{NaOH}]$  of 3 M without the use of other components as capping agents. We have found that by changing the polyol from EG to TEG, and keeping all other parameters constant, we are able to form spheres, pentagons, triangles, hexagons, and rods. In this sense, the main effects of the polyol its use as a capping agent and its influence on the nucleation and growth rates of the Cu crystals. It is clear that the reduction rate of Cu-TEG was lower than that of Cu-EG, which increases the time for Cu atoms to reach super saturation and thus produces a faster nucleation rate and in turn a slower growth rate. Another explanation is that the various chain lengths of the polyol influence the growth of nanoparticles by altering the ligand exchange rate. For example, the longer the chain length of the polyol, the slower the ligand exchange rate. This occurs due to an increase in the sterics associated with the larger molecules and allows for a slower growth rate of the metal. The result is that the larger molecules, like TEG, prevent the Cu atoms from reaching the surface and subsequently results in the anisotropic growth seen in the TEM image (Figure 7.7). Therefore, it is believed that the nucleation rate of Cu crystallites decreases with increasing the chain length of the polyol.

## 7.5 Crystallization of Copper-glycolate

There has been considerable interest in the coordination chemistry of metal ions in a polyol medium owing to its importance in understanding reaction kinetics and solvent and ion exchange for the formation of a mechanism of reduction. Up to now, several papers have illustrated the mechanism of the polyol process by studying kinetic data obtained by UV-vis and IR spectroscopy.<sup>183,250-252</sup> From this data, assumptions of the formation of metal glycolates as an intermediate were formulated. This method does not give the best idea about the direct intermediates during the formation of metals in the polyol process, as the polyol itself is a mild reducing agent. There have not, however, been a large number of investigations on the crystal packing in the intermediate form. This section presents a simple copper reaction where we trap the polyol intermediate and determine its structure crystallographically. The results of the trapped intermediate are consistent with a di-chelate formation stabilized by sodium ions. A survey of the literature reveals only four examples of complexes containing the bis-ethylene glycolate Cu(II)<sup>2-</sup> anion that have been crystallographically characterized.<sup>253-255</sup> These complexes contain Li, Ba, or Sr as counterions. To the best of our knowledge this is the first crystal structure determined for an ethylene glycolate copper(II) anion stabilized by ethylene glycol coordinated sodium counterions. Here we report the structure of  $[\text{Na}_2(\text{C}_2\text{H}_6\text{O}_2)_6][\text{Cu}(\text{C}_2\text{H}_4\text{O}_2)_2]$ . From the understanding of this crystal structure, we will be able to use computational modeling to give insight into a possible mechanism for the polyol process.

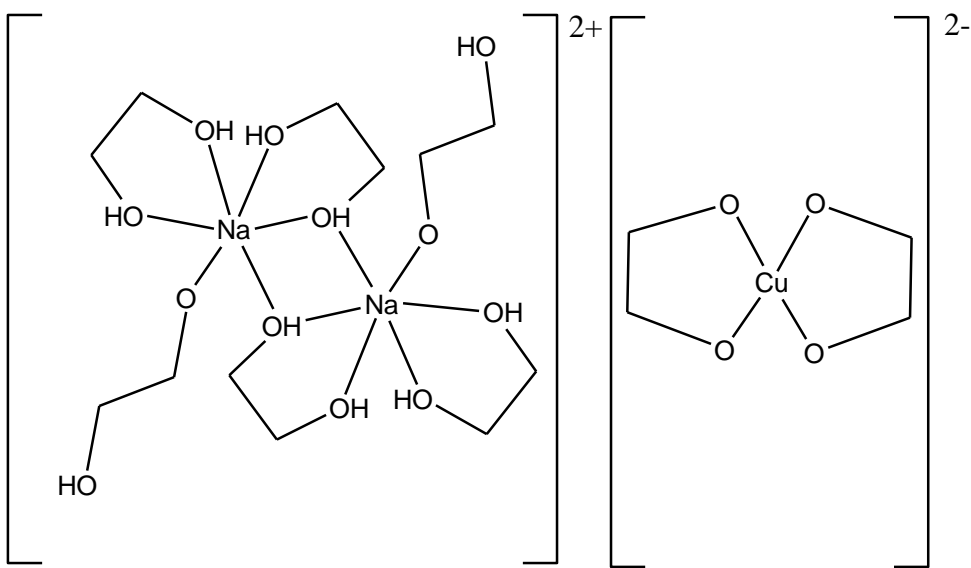


**Figure 7.13.** Representation of the crystallized counterions forming the copper-glycolate superstructure.

Crystals suitable for x-ray analysis were obtained from the solution by cooling to 248 K for 3 days in a sealed flask under N<sub>2</sub>. The EG was decanted off and the crystals were washed with diethyl ether (2x50ml) and hexanes (2x50ml). The un-optimized yield was 2.4g, or 68% based on Cu.

The crystals are deliquescent and readily form droplets within an hour of sitting in the atmosphere. The crystals are insoluble in common organic solvents, but dissolve readily with decomposition in alcohols and water. The reaction is quenched after changing to dark blue as above.

The molecular structure of complex (I) is illustrated in Figure 7.14. Selected bond lengths and angles are listed in Table 7.1. The anionic moiety consists of a bis-ethylene glycolate Cu<sup>II</sup> dianion with the Cu atom on an inversion center, while the cation

comprises two inversion-related Na ions complexed by chelating, bridging and monodendate ethylene glycol units.

**Table 7.3.** Selected bond lengths(Å) for the copper glycolate structure.

Na1-O6	2.3816 (16)	Na1-O5	2.4052 (16)
Na1-07	2.3858 (16)	Na1-O4	2.4453 (15)
Na1-03	2.3945 (16)	Na1-03 <sup>i</sup>	2.4545 (15)

Symmetry code: (i) -x, -y, -z.

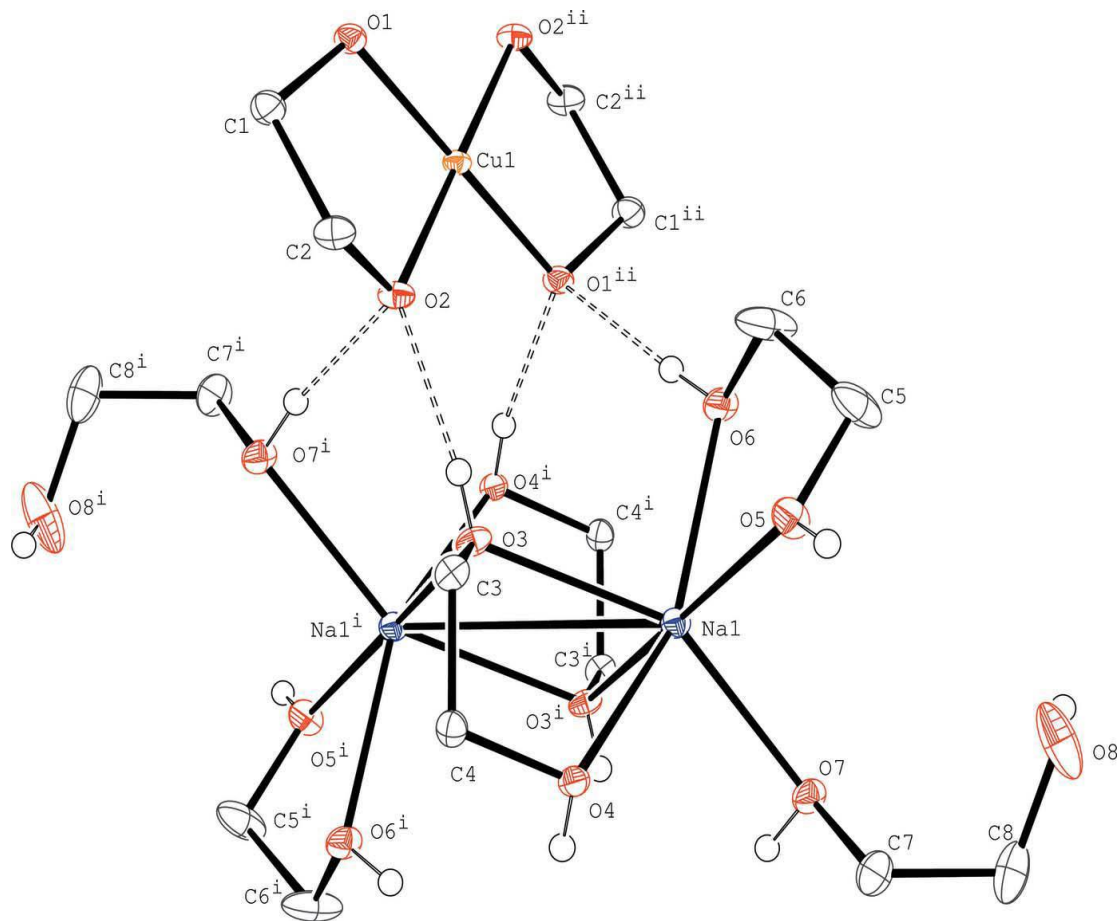


**Figure 7.14.** The molecular structure of (I), showing the atom-numbering scheme. Displacement ellipsoids are drawn at the 40% probability level. The disordered atom 08b and methylene H atoms have been omitted for clarity. [symmetry codes: (i) -x; -y; -z (ii) -x; -y; 1-z]

The anion is square planar with the ethylene glycolate ligands being fully deprotonated and chelating about the Cu<sup>2+</sup> ion. Cu1-O1 [1.9317(13) Å] and Cu1-O2 [1.9252(13) Å] distances fall between the previously reported Cu-O distances for Cu[C<sub>2</sub>H<sub>4</sub>O<sub>2</sub>]<sup>2-</sup>.<sup>253-255</sup> A comparison of the Cu-O distances and angles from the previously reported structures of both ethylene glycolate and EG copper complexes are given in Table 7.4. The Cu-O distances are consistently longer in the EG complexes

versus the glycolate complexes. More significantly, the bite angle of the glycolate ligand is much larger than the protonated form by an average of 8 degrees.

**Table 7.4.** Comparison of known ethylene glycolate and ethylene glycol complexes.

Complex	CSD Ref. code	Average Cu-O (Å)	Bite Angle of C <sub>2</sub> H <sub>4</sub> O <sub>2</sub> (%)
Na <sub>2</sub> Cu(C <sub>2</sub> H <sub>6</sub> O <sub>2</sub> ) <sub>6</sub> (C <sub>2</sub> H <sub>4</sub> O <sub>2</sub> ) <sub>2</sub>	This Work	1.929 (3)	87.11 (5)
BaCu(C <sub>2</sub> H <sub>6</sub> O <sub>2</sub> ) <sub>3</sub> (C <sub>2</sub> H <sub>4</sub> O <sub>2</sub> ) <sub>2</sub>	PAHFEJ <sup>a</sup>	1.921 (4)	88.6 (3)
BaCu(C <sub>2</sub> H <sub>6</sub> O <sub>2</sub> ) <sub>6</sub> (C <sub>2</sub> H <sub>4</sub> O <sub>2</sub> ) <sub>2</sub>	PAHFAF <sup>b</sup>	1.923 (5)	86.65 (15)
Li <sub>2</sub> Cu(C <sub>2</sub> H <sub>4</sub> O <sub>2</sub> ) <sub>2</sub>	VOWKAT <sup>b</sup>	1.931 (13)	87.22 (6)
CuCl <sub>2</sub> (C <sub>2</sub> H <sub>6</sub> O <sub>2</sub> ) <sub>2</sub>	CETDCU10 <sup>c</sup>	1.978 (19)	79.1 (1)
CuCl <sub>2</sub> (C <sub>2</sub> H <sub>6</sub> O <sub>2</sub> ) <sub>2</sub> H <sub>2</sub> O	GLYCUH <sup>c</sup>	1.986 (18)	79.9 (1)
CuCl <sub>2</sub> (C <sub>2</sub> H <sub>6</sub> O <sub>2</sub> ) <sub>3</sub> (SO <sub>4</sub> )	ETDOCU <sup>d</sup>	2.10 (10)	79.2 (10)

<sup>a</sup>, Pico *et al.*(1997); <sup>b</sup>, Habermann *et al.* (1992); <sup>c</sup>, Antti (1976); <sup>d</sup>, Antti *et al.* (1972).

In the [Na(C<sub>2</sub>H<sub>6</sub>O<sub>2</sub>)<sub>3</sub>]<sup>2+</sup> cation, the unique Na ion is bound by two chelating EGs, one bridging oxygen from an EG that is chelating to the other inversion-related Na atom, and one monodentate EG. The unique Na ion has a distorted octahedral coordination environment with Na-O distances in the range 2.3816(16) to 2.4545(15) Å, the shortest distances came from the non-bridging chelating oxygens Na1-O7, and the longest distances arose from the bridging interaction of a chelating EG Na1-O3 (-x, -y, -z). A search of the Cambridge Structural Database (CSD, version 5.30 plus three updates)<sup>256-257</sup> reveals only one previously reported structure with ethylene glycol bound to sodium ions (CSD ref. code: OBOBAI).<sup>258</sup> In this structure, the sodium ions are directly attached to

the anionic portion of the structure through bridging ethylene glycols and therefore not part of an independent sodium-ethylene glycol cluster as reported here.

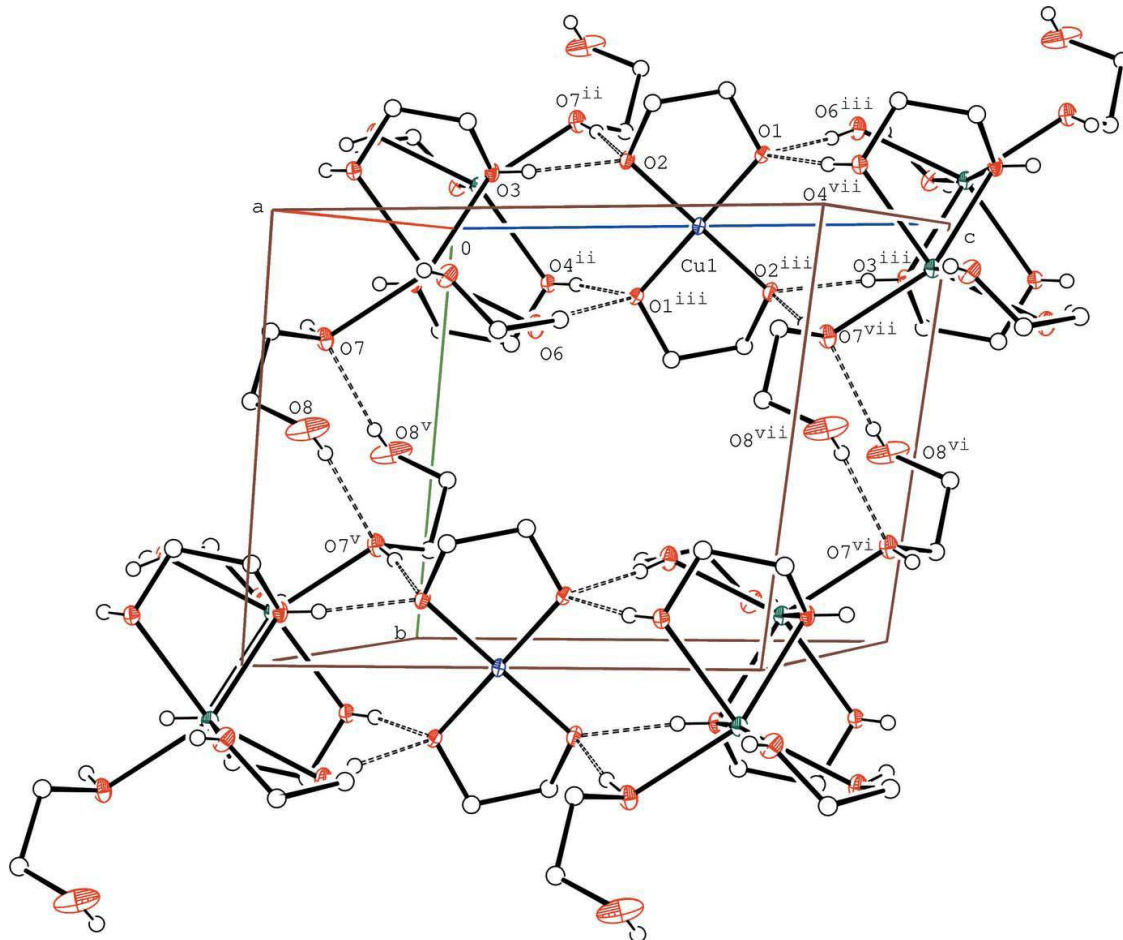


**Figure 7.15.** A packing diagram of (I) viewed approximately down the  $a$  axis showing the hydrogen-bonding interactions between the anionic and cationic units. H atoms not involved in hydrogen bonding and the disordered atom O8B have been omitted for clarity. [Symmetry codes: (ii)  $-x, -y, -z$ ; (iii)  $-x, -y, 1-z$ ; (v)  $1-x, 1-y, -z$ ; (vi)  $1-x, 1-y, 1-z$ ; (vii)  $x, y, 1+z$ .]

The cations are linked by O-H- - -O hydrogen bonds through interactions involving O5-H5---O4<sup>iv</sup> and O8-H8---O7<sup>v</sup> (see Table 7.5) to form sheets parallel to the (OO1) plane. The deprotonated oxygen atoms, O1 and O2, of the anion are each

hydrogen bonded to two different ethylene glycol oxygen atoms of the cation as shown in figure 2 with details in table 3. The association of the two cations and anions via classical O-H---O hydrogen bonding (Table 7.5) results in a three-dimensional network with alternating layers of cations and anions down the c-axis (Figure 7.14).

**Table 7.5.** Hydrogen bond geometry ( $\text{\AA}$ ,  $^\circ$ )

D-H---A	D-H	H---A	D---A	D-H---A
06-H6---O1 <sup>ii</sup>	0.75 (3)	1.93 (3)	2.683 (2)	175 (3)
O4-H4---O1 <sup>iii</sup>	0.74 (3)	1.89 (3)	2.6152 (19)	168 (3)
O5-H5---O4 <sup>iv</sup>	0.75 (3)	2.05 (3)	2.779 (2)	164 (3)
O7-H7---O2 <sup>i</sup>	0.81 (3)	1.81 (3)	2.612 (2)	171 (3)
O3-H3---O2	0.72 (3)	1.94 (3)	2.6566 (19)	172 (3)
O8-H8---O7 <sup>v</sup>	0.69 (3)	2.14 (3)	2.815 (3)	167 (4)

Symmetry codes: (i) -x, -y, -z; (ii) -x, -y, -z+1; (iii) x, y, z-1; (iv) -x, -y, -z; (v) -x+1, -y+1, -z.

Analysis of the IR spectroscopy reveals weak C-O stretches at 1245 and 1218  $\text{cm}^{-1}$  and weak M-O stretches at 541 and 606  $\text{cm}^{-1}$ . These values are consistent with results obtained for a similar Cu-Sr structure,  $[\text{Sr}(\text{C}_2\text{H}_6\text{O}_2)_5][\text{Cu}(\text{C}_2\text{H}_4\text{O}_2)_2]$ .<sup>253</sup>

### 7.5.1 Refinement Details

The pendant oxygen from the non-chelating ethylene glycol bound to sodium was disordered over two positions, O8A and O8B, whose occupancy factors were refined and then fixed at 0.9143 and 0.0857 respectively. The C8-O8A and C8-O8B distances were restrained to be equivalent. All methylene H-atom positions were calculated using the appropriate riding model, with  $U_{\text{iso}}(\text{H})$  values 1.2 times  $U_{\text{eq}}$  of the parent atoms, and with

C-H distances of 0.99 Å. The hydroxy H atoms were located in a difference Fourier map and refined freely.

### 7.6 Mechanism Study

Despite the high number of publications describing the synthesis of metals and metal oxides by the polyol method, a convincing mechanism still lacks. There have been several empirical studies and to the best of our knowledge only one theoretical study. Larcher et al. describe the mechanism thermodynamically.<sup>225</sup> In their report, however, they assume that the reduction to metal occurs concomitantly with the total oxidation of EG (200°C). Several experimental results indicate that reduction of metal salts can occur much lower than at the boiling point of EG. Therefore, a more experimentally driven description of the mechanism is needed to describe the reduction of metal precursors in the polyol method.

A report by Bonet et al. highlighted an electrochemical investigation based on the study of the redox potential of EG.<sup>214</sup> In this study the authors state that the shift between the oxidation potential of EG and the reduction potential of a metal species is due to energy barriers. They state that for the polyol process to successfully reduce metal species, an energy barrier must be overcome by heating the EG. They also state that the spontaneous reduction of a metal species by a polyol will occur only if the thermodynamic  $M^{n+}/M$  reduction potential in the polyol is more positive than the oxidation potential of the reducing agent. The redox potentials for  $Ni^{2+}$  and  $Cu^{2+}$  ions are remarkably different from each other ( $Ni^{2+} + 2e^- \rightleftharpoons Ni, -0.257V$ ,  $Cu^{2+} + 2e^- \rightleftharpoons Cu, 0.342V$ ). Therefore, we can see that the  $Cu^{2+}/Cu$  could occur at lower temperatures than that of

$\text{Ni}^{2+}/\text{Ni}$ . This serves as a starting point for the differences in the ability to reduce metal species in the polyol process. In the next chapter, we explain the differences seen in the formation of Cu/Ni core/shell nanoparticles and speculate that the stability of the hydrated forms ( $\text{CuCl}_2(\text{H}_2\text{O})_2$  vs  $\text{NiCl}_2(\text{H}_2\text{O})_2$ ) differ. Our experimental evidence from the crystallization of the intermediate Cu-glycolate, as explained previously, is the base for the investigation of a possible mechanism for the reduction of  $\text{CuCl}_2$  in the polyol. To begin the theoretical investigation, we first took the starting precursors ( $\text{NiCl}_2$  and  $\text{CuCl}_2$ ) and then attempted to bind EG molecules to the metal species. We monitored the incremental binding energies associated with the formed complexes to determine the stability of adding a subsequent EG molecule (Figure 7.16). We show that the Cu prefers two EG molecules, which is consistent with the experimental results from the trapped Cu-glycolate intermediate. The  $d^9$  configuration makes Cu (II) subject to Jahn-Teller distortion and this is shown in Figure 7.16. When we attempt to make the complex six coordinate (three EG molecules) and adopt an octahedral geometry, the complex becomes highly unstable (-1.9 kcal/mol). However, in the case of the  $d^8$  Ni(II) species, the more favorable configuration is the octahedral complex where there are three EG molecules surrounding the Ni center. From this, we can also see that the EG molecules bind much stronger to Ni than to Cu. This suggests that when the reaction proceeds, Cu nanoparticles form faster due to the  $\text{Cu}(\text{EG})_2$  complex being less stable than the  $\text{Ni}(\text{EG})_3$  complex at lower temperatures.

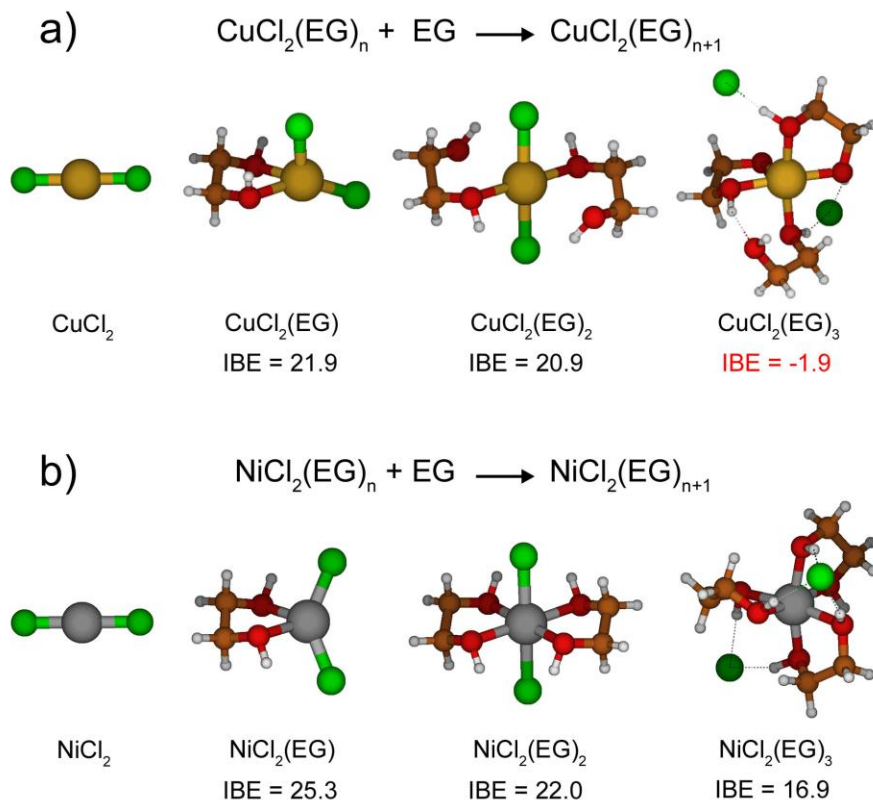


**Figure 7.16.** Optimized geometries for the successive binding of EG to  $\text{CuCl}_2$ , a), and  $\text{NiCl}_2$ , b). The incremental binding energies (IBE) in units of kcal/mol are also given.

We were then able to calculate the change in energy ( $\Delta E$ ) for each step of our proposed reaction processes. Figures 7.17 and 7.18 show the graphical representation of the proposed reaction processes plotted with the  $\Delta E$  (kcal/mol) for Cu and Ni, respectively. The two metals proceed through the previously reported intermediate phase with the EG molecules bound to the metal centers and reduction proceeds to occur through the C-O-M bond formation. The Cu formation is an exothermic process while the Ni formation is endothermic.

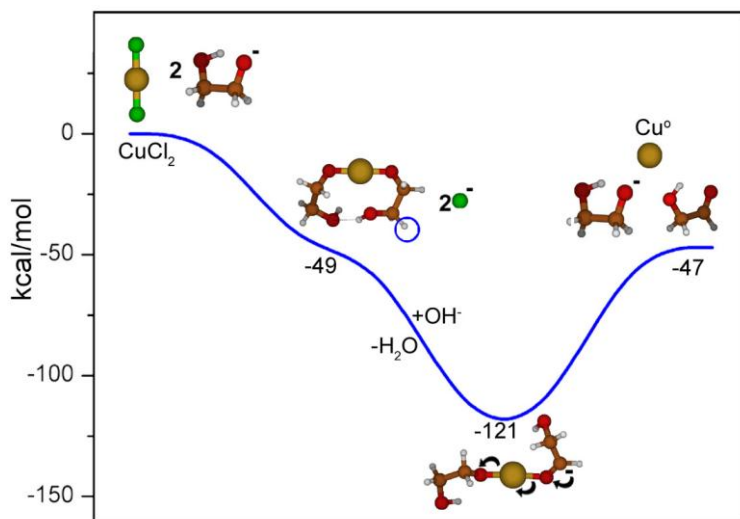


**Figure 7.17.** Plot of the calculated change in energy ( $\Delta E$ ) for each step of the proposed reaction mechanism of the  $\text{Cu}^{2+}$  reduction pathway by the polyol process using ethylene glycol (EG) in a basic medium.

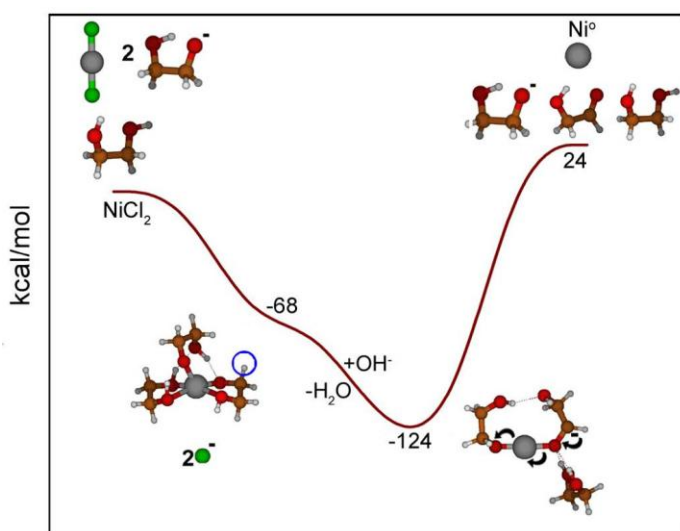


**Figure 7.18.** Plot of the calculated change in energy ( $\Delta E$ ) for each step of the proposed reaction mechanism of the  $\text{Ni}^{2+}$  reduction pathway by the polyol process using ethylene glycol (EG) in a basic medium.

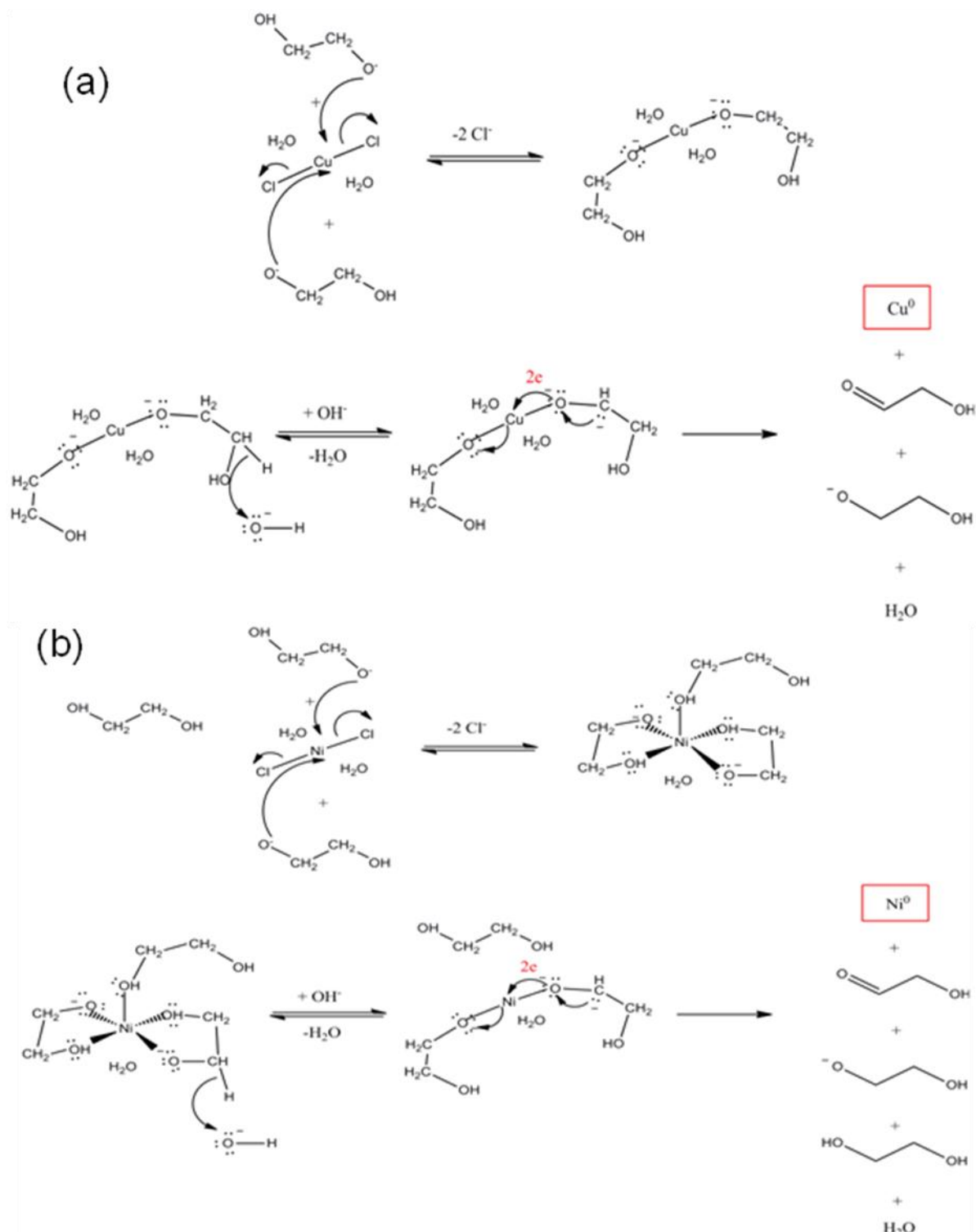


**Figure 7.19** Proposed Mechanism for (a) the reduction of  $\text{CuCl}_2$  to Cu-metal and (b) the reduction of  $\text{NiCl}_2$  to Ni-metal.

Figure 7.19 is our proposed mechanism for the formation of Cu and Ni metal nanoparticles. In this mechanism, there are four steps required for the reduction to metal. First, the ligand exchange forming the M-glycolate ( $M=Cu,Ni$ ) species occurs once the metal salt precursor is dissolved in the glycol. UV-vis and IR data from several reports suggest that the formation of M-glycolate occurs. In addition, our recent efforts to trap the Cu-glycolate intermediate and determine the structure crystallographically was successful. This enabled us to confidently use this intermediate in our mechanism. The reaction proceeds when  $OH^-$  and a H atom, from the alpha-Carbon, form water and leaves a carbanion. This hypothesized carbanion is the source for the two electrons that are required for the reduction of the metal species and occurs through the oxygen atom. The products of this reaction are zero-valent metal, 2-hydroxyacetaldehyde, and 2-hydroxyethanol, all of which have been experimentally determined before.

## 7.7 Conclusion

This chapter carried out both experimental measurements and computational modeling to gain insight into the mechanism of the polyol method. The experimental work on the formation of copper and nickel metal using a variety of polyols allowed for an elucidation that in ethylene glycol, nickel chloride will only form a nickel hydroxy-salt under refluxing conditions. This is most likely due to the enhanced stability of the  $Ni(EG)_3$  hydrated intermediate complex. When the reaction is switched to distillation, where water is evaporated out of the system, the formation of elemental nickel is possible. In contrast, the  $Cu(EG)_2$  hydrated intermediate complex was less stable, and the formation of elemental copper could be achieved under both refluxing and distillation

conditions. The intermediate metal-glycolate has been proposed several times by others, but our work provides the first crystal structure of the trapped Cu-glycolate intermediate. This allowed us to more reliably use computational modeling to determine the metal-glycolate stability for both Cu and Ni complexes. The next chapter shows how we can use this information to create a novel one-pot synthesis of Cu/Ni core/shell nanoparticles by first refluxing the solution to produce Cu nanoparticles. The Cu nanoparticles were seeds for the heterogeneous nucleation and growth of Ni shells once the system was set to distill off the water.

## **Chapter 8: Design of Cu/Ni core/Shell Nanoparticles**

### 8.1 Introduction

The physical and chemical properties of bimetallic core/shell nanoparticles (CSNPs) can differ in significant ways from the corresponding bulk materials, and chemically homogeneous nanoparticles of the same overall composition.<sup>259-261</sup> These observations have lead to great interest in the development of new synthesis strategies to prepare CSNPs, particularly if they are straightforward to implement and can be applied to potentially useful materials. Motivated by these considerations we have developed a simple chemical procedure for the preparation of Cu core/Ni shell (Cu/Ni) and Ni core/Cu shell (Ni/Cu) CSNPs based on the well known polyol method.<sup>262</sup> Because of their potentially useful catalytic and magnetic properties we have focused exclusively on the Cu-Ni system,<sup>263-265</sup> although we believe the general approach described below may be applicable to other important materials systems as well.

Various implementations of the polyol method have previously been used to prepare elemental Cu nanoparticles, Ni nanoparticles, and Cu-Ni nanoalloys.<sup>181,239,266-270</sup> To the best of our knowledge, however, there has only been one previous report in which the polyol method was used to prepare CSNPs consisting of *elemental* Cu and Ni.<sup>266</sup> In that case, Cu/Ni CSNPs were obtained after heating hydrated Cu and Ni nitrates dissolved in ethylene glycol (EG) for 4 hours at 196 °C. The formation of a core/shell structure was attributed to the different thermal stabilities of Cu and Ni glycolates formed during the reaction. In particular, the transformation of Cu glycolate to elemental Cu was observed to precede the transformation of Ni glycolate to elemental Ni. The Cu

nanoparticles then served as a heterogeneous nucleation site for the deposition of Ni, leading to the formation of a core/shell structure.

In this chapter, a series of experiments were carried out in which hydrated Cu chloride ( $\text{CuCl}_2 \cdot 2\text{H}_2\text{O}$ ), hydrated Ni chloride ( $\text{NiCl}_2 \cdot 6\text{H}_2\text{O}$ ), and sodium hydroxide (NaOH) were dissolved in EG and rapidly heated to the boiling point of the solution. By exploiting the strong dependence of the boiling temperature of these solutions on the relative quantities of dissolved salt, the associated water of hydration, NaOH, and solvent, two stabilized reaction temperatures could be obtained without the need for active temperature control by simply switching between reflux and distillation conditions. In particular, a solution containing 0.5 g Cu chloride, 0.5 g Ni chloride, and 3 g of NaOH dissolved in 25 ml of EG was found to boil at a temperature of about 165 °C, well below the temperature of 196 °C at which the EG itself boiled (pure EG boils at about 197 °C). After removing the water of hydration from the solution, the boiling point was observed to increase to about 175 °C. This 10-degree difference was sufficient to separate the formation of elemental Cu under reflux conditions from the formation of elemental Ni under distillation conditions. At the reflux temperature of 165 °C, the Cu reaction was complete in less than 30 minutes insuring that elemental Ni (rather than a Cu-Ni alloy) was formed during the higher temperature distillation step of the reaction. As noted earlier, Cu/Ni CSNPs formed because the Cu nanoparticles served as preferential nucleation sites for the deposition of Ni. Although the temperature was the reaction parameter used to separate the formation of elemental Cu and Ni in these experiments, it

is worth noting that the presence or absence of water may also play an important role in the actual reaction mechanism.

The asymmetry of the reaction conditions that allowed the formation of Cu/Ni CSNPs does not allow the formation of Ni/Cu CSNPs from a mixed metal-salt solution. Nevertheless, a modification of the procedure described above allowed Ni/Cu nanoparticles to be prepared in a two-step process. In the first step, a Ni chloride solution was distilled until Ni nanoparticles were formed. After completion of the reaction, which could also be terminated prior to completion by quenching the solution in an ice bath, a Cu chloride solution was added and heated at reflux leading to the formation of Cu shells on the Ni nanoparticles.

## 8.2 Synthesis

### 8.2.1 Materials.

Copper (II) chloride dihydrate ( $\text{CuCl}_2 \cdot 2\text{H}_2\text{O}$ ), nickel (II) chloride hexahydrate ( $\text{NiCl}_2 \cdot 6\text{H}_2\text{O}$ ), and sodium hydroxide (NaOH) were all purchased from Fisher. Ethylene glycol (EG) was purchased from Acros Organics. All chemicals were used as received.

### 8.2.2 Synthesis of Cu-Ni CSNPs.

Approximately 0.5 g  $\text{CuCl}_2 \cdot 2\text{H}_2\text{O}$ , 0.5 g  $\text{NiCl}_2 \cdot 6\text{H}_2\text{O}$ , and 3 M NaOH were dissolved in 25 mL of EG. The solution was refluxed for 30 to 60 minutes. Following reflux, a distillation apparatus was attached to the boiling solution for an additional 30 to 60 minutes. After cooling to room temperature, the precipitate was isolated by magnetic extraction, washed several times with methanol, and vacuum dried.

### 8.2.3 Synthesis of Ni-Cu CSNPs.

Approximately 0.5 g  $\text{NiCl}_2 \cdot 6\text{H}_2\text{O}$  and 3 M NaOH were dissolved in 25 mL of EG. The solution was distilled for 30 to 60 minutes to fully reduce the Ni. In a separate flask, 0.5 g  $\text{CuCl}_2 \cdot 2\text{H}_2\text{O}$  was dissolved in 25 mL of EG and added to the Ni solution. The solution was then heated to reflux for 30 to 60 minutes. The particles were magnetically separated, washed several times with methanol, and vacuum dried.

### 8.3 Results and discussion

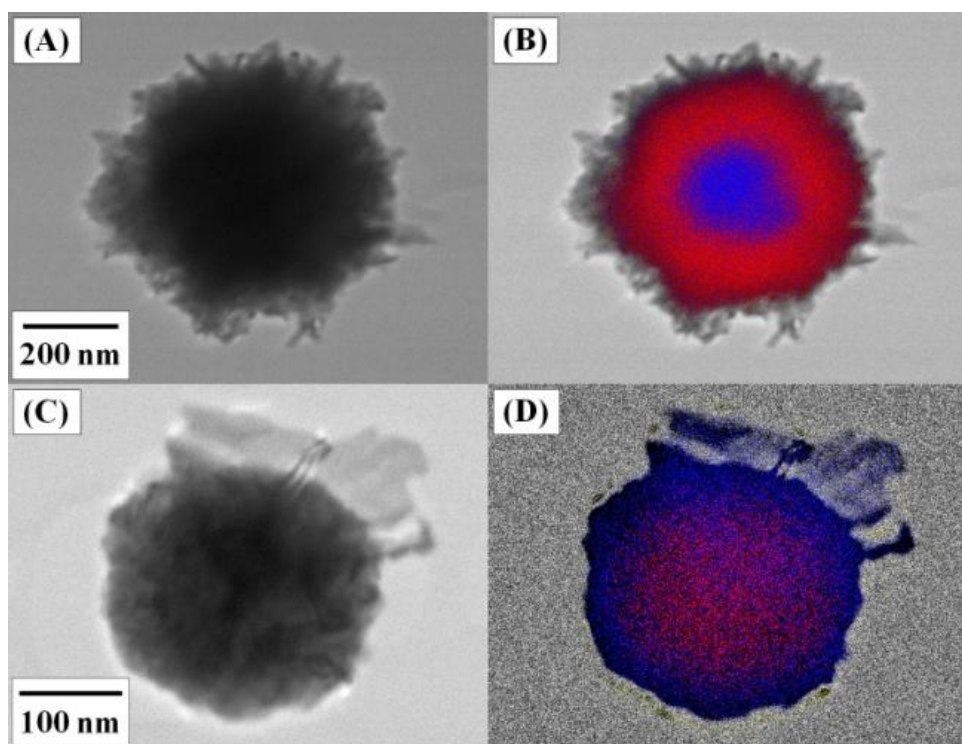


**Figure 8.1.** TEM images and composition maps (red and blue corresponding to Cu and Ni, respectively) of typical of A,B) Cu/Ni and C,D) Ni/Cu CSNPs. The uncolored coating on the composition maps corresponds to residual organic material.

TEM images of typical Cu/Ni and Ni/Cu CSNPs and the corresponding composition maps of elemental Cu and Ni distributions are shown in Figure 8.1. These data clearly show the formation of core/shell type structures.

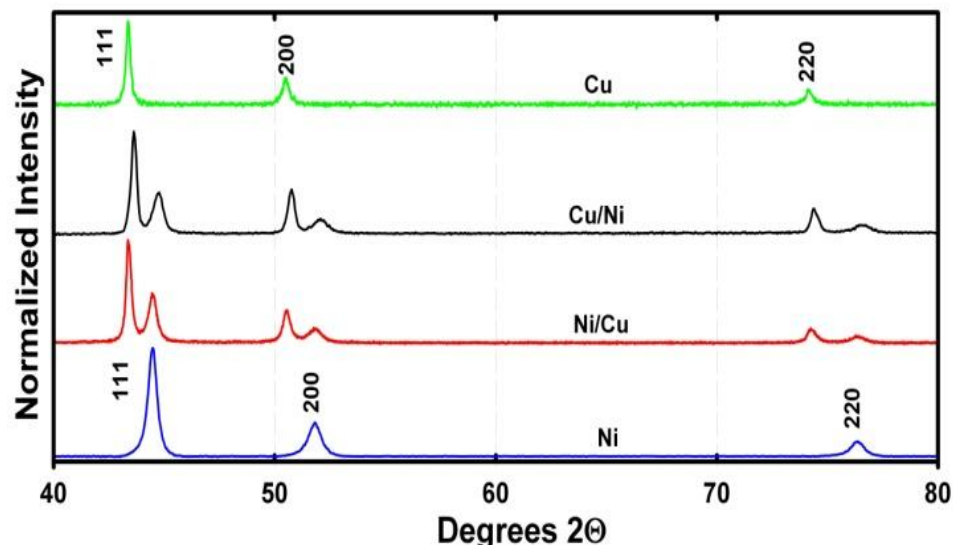


**Figure 8.2.** XRD patterns of elemental Cu, Cu/Ni, Ni/Cu, and elemental Ni. The elemental metals were prepared using the respective metal chlorides (see the Supporting Information).

The XRD patterns of the Cu/Ni and Ni/Cu CSNPs are shown in Figure 8.2. The fitted line positions yielded best fit Cu lattice parameters of 0.3609(13) nm and 0.3609(6) nm for the Cu/Ni and Ni/Cu CSNPs, respectively, with corresponding Ni lattice parameters of 0.3519(4) nm and 0.3529(15) nm, respectively. Within the experimental uncertainties these values are consistent with the bulk Cu (0.36148 nm) and Ni (0.35232 nm) lattice parameters,<sup>271</sup> indicating that in both cases the core and shell material is

comprised of essentially unalloyed elemental Cu and Ni. In the case of the Ni/Cu CSNPs we were also able to obtain XAS data for comparison with the XRD data.

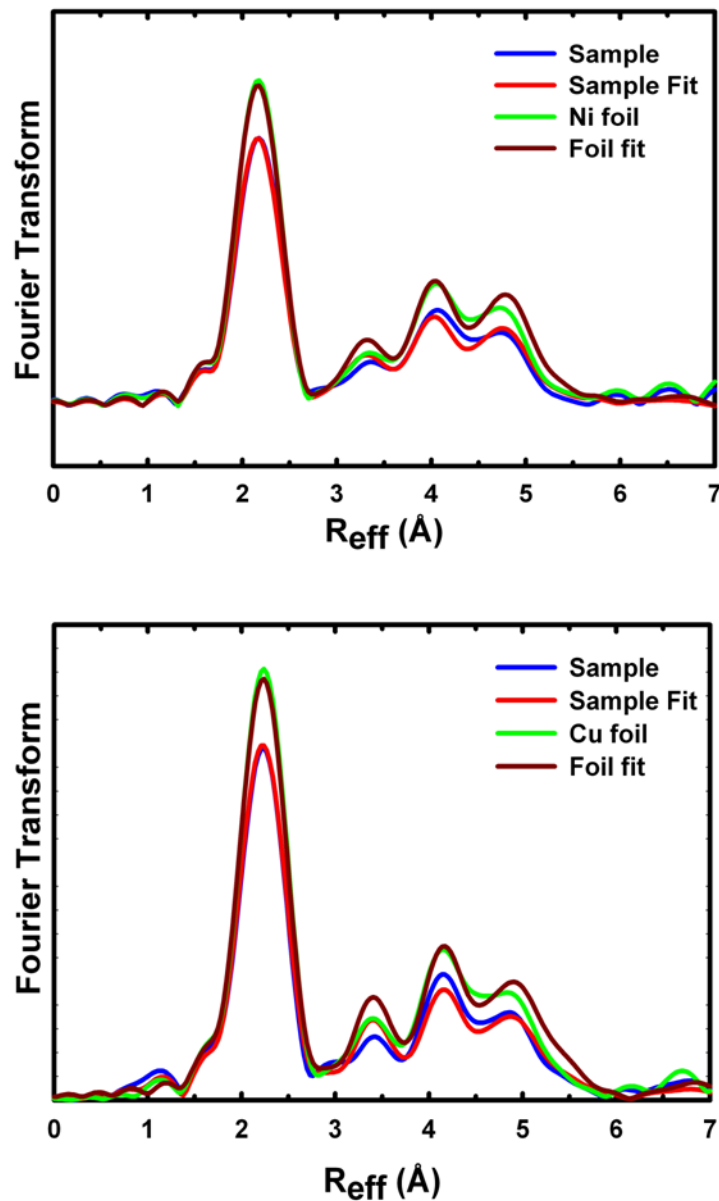


**Figure 8.3.** Fourier transforms of the EXAFS signals from the Ni/Cu CSNPs, the pure metal reference foils, and their respective fits. The foil and foil fit are presented to show the expected differences in the transform.

Analysis of the extended x-ray absorption fine structure (EXAFS) region of these data yielded a Cu lattice parameter of 0.3623(5) nm and a Ni lattice parameter of 0.3534(6) nm (Figure 8.3). In addition, the 2<sup>nd</sup> and 3<sup>rd</sup> cumulants of the Cu-Cu and Ni-Ni interatomic distances, corresponding to the variance and asymmetry of those distances, were also consistent with unalloyed elemental Cu and Ni.

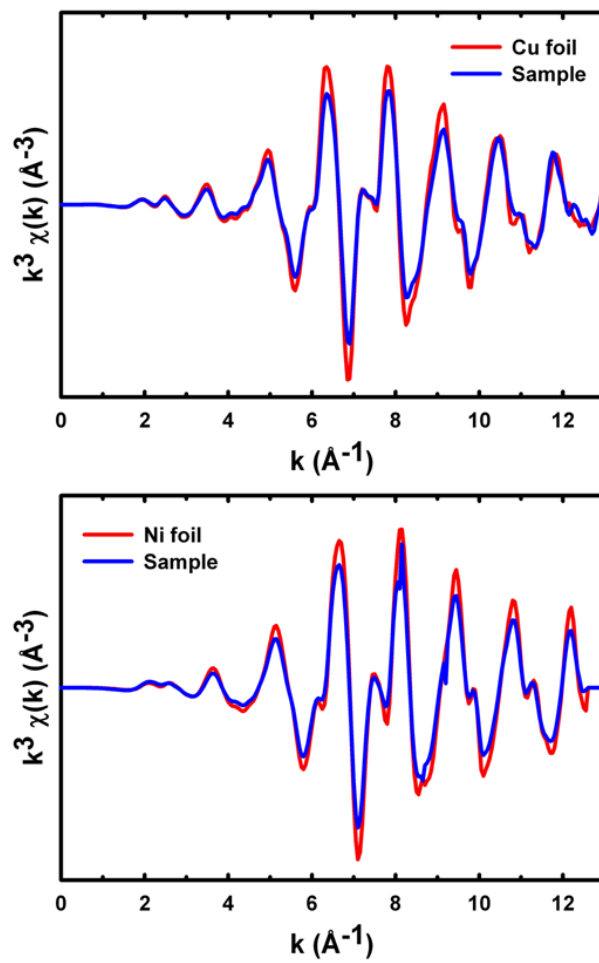


**Figure 8.4.** EXAFS spectra of Ni/Cu CSNPs and the corresponding pure metal reference foils.

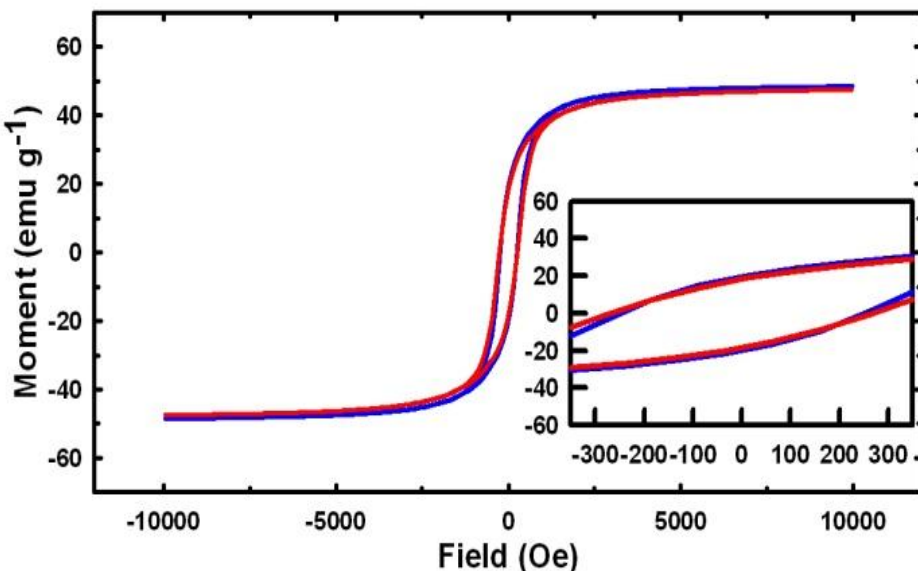


**Figure 8.5.** Room temperature hysteresis loops for the Cu/Ni (blue) and Ni/Cu (red) CSNPs. The magnetization axis has been scaled based on the ICP-OES measured composition to indicate the magnetization per gram of Ni in the sample.

The corrected room temperature hysteresis loops of the Cu/Ni and Ni/Cu CSNPs are shown in Figure 8.5. The saturation magnetization was obtained by extrapolating a fit of the measured high field magnetization versus the inverse of the applied magnetic field to infinite field. This procedure yielded saturation magnetization values of 18.15(3) emu/g and 19.65(3) emu/g of sample (i.e. based on the total sample mass) for the Cu/Ni and Ni/Cu CSNPs. Assuming the presence of only elemental Cu and Ni in these materials and that all the Ni atoms carry the bulk Ni magnetic moment of 54.4 emu/g, the saturation magnetization values result in particle compositions (at.%) of Cu<sub>64</sub>Ni<sub>36</sub> for the Cu/Ni CSNPs and Ni<sub>38</sub>Cu<sub>62</sub> for the Ni/Cu CSNPs.

The compositions of the core/shell nanoparticles were also directly determined by ICP-OES. These measurements yielded the compositions Cu<sub>59</sub>Ni<sub>41</sub> and Ni<sub>45</sub>Cu<sub>55</sub>. The origin of the somewhat larger ICP-OES Ni concentrations relative to the magnetization based values is currently under investigation but may arise from a small (and undetected) amount of alloying at the core/shell interface resulting in a reduced Ni moment for interface Ni atoms. Alternatively, a reduced Ni moment due to finite size effects could also account for this discrepancy.<sup>272-273</sup>

**Table 8.1.** EXAFS fitting parameters for the copper and nickel edges of the Ni/Cu CSNPs and the pure metal reference foils.

	Cu edge: sample	Cu edge: foil	Ni edge: sample	Ni edge: foil
$S_o^2$	1.02(5)		0.92(4)	
$E_o$	8986.7(5) eV		8341.1(5) eV	
Lattice parameter	3.623(5) Å	3.628(4) Å	3.534(6) Å	3.528(4) Å
Debye temperature	321(8) K	316(6) K	401(13) K	394(9) K
Third cumulant	0.00026(5) Å <sup>3</sup>	0.00023(4) Å <sup>3</sup>	0.00016(6) Å <sup>3</sup>	0.00013(3) Å <sup>3</sup>
Crystallite radius	10(2) Å	---	10(2) Å	---
$\mathcal{R}$ -factor	0.008	0.007	0.005	0.006

#### 8.4 Conclusions

In conclusion, this section identified a new and simple procedure for separating the formation of elemental Cu and Ni in a polyol-type reaction. In particular, the formation of Cu/Ni CSNPs from a mixed metal-salt/NaOH/EG solution was facilitated by manipulating the boiling temperature of the solution. A two step procedure in which Ni

nanoparticles were first prepared from a Ni chloride solution followed by the addition of a Cu chloride solution was also used to prepare Ni/Cu CSNPs. These core/shell nanoparticles are potentially useful for their catalytic and magnetic properties, as they are superior to their monometallic counterparts.

## **Chapter 9: Design of Aqueous Based Ferrofluids**

### 9.1 Design of Fe-FeOx Nanoparticles

Stable colloidal suspensions of magnetic nanoparticles have many appealing qualities that have attracted them to areas of industry, biomedical engineering, physics, and chemistry. Many ferrofluids are used commercially as heat transfer fluids for dampeners in loud speakers, in electronic devices as a form of liquid seals for drive shafts in hard disks, and in medicine as contrast agents for MRI imaging due to their  $T_1$  and greater  $T_2$  enhancement.<sup>274-277</sup> There are two main types of stabilizers for dispersing magnetic nanoparticles: surfactant/polymer stabilized nanoparticles and ionically stabilized nanoparticles. These stabilizers allow for the formation of colloidal metal and metal oxide nanoparticles by various types of chemical and physical interactions. For polar solvent ferrofluids, tetramethylammonium hydroxide (TMAOH) is commonly used as an ionic stabilizer: the hydroxyl group forms at the surface of the nanoparticle, providing a negatively charged surface layer. The positively charged tetramethylammonium cation ( $\text{N}(\text{CH}_3)_4^+$ ) forms a diffuse shell in which neighboring particles will encounter electrostatic repulsion.<sup>278-288</sup> For non-polar solvent based ferrofluids, surfactants or polymers that attach to nanoparticles, such as oleic acid, impose steric effects on the neighboring nanoparticles. The hydrocarbon has a polar head that has an affinity for the nanoparticle; the tail of the surfactant prevents the agglomeration of neighboring nanoparticles.<sup>289</sup> In each case, there are stringent rules which must be met in order to achieve effective stabilization. These rules affecting colloidal stability include parameters such as optimum size range of the nanoparticles, viscosity of the carrier liquid, length of the surfactant, temperature, and magnetic field

strength. Various techniques have been shown to produce magnetic nanoparticles such as: wet grinding, co-precipitation, microemulsion, and aqueous reduction of metal salts.<sup>290-296</sup>

After the synthesis of the nanoparticles, additional steps are typically required to coat them with the appropriate stabilizer. In most cases, where the goal is an aqueous ferrofluid, the resulting nanoparticle is strictly an iron oxide. This work shows enhanced magnetic properties by forming aqueous stabilized metal/oxide core/shell nanoparticles.

The oxide shell forms a passivation layer preventing further oxidation.<sup>157</sup>

This chapter first describes an alternative synthetic method for the formation of metal/oxide composite nanoparticles by a modified polyol process. This modified process enabled the liquid polyol to act not only as a solvent, but also as a mild reducing agent and a surfactant for the stabilization of the nanoparticles in aqueous media. The ferrofluid was then investigated *in vitro* by magnetic resonance relaxivity measurements and *in vivo* for its application in MRI. Also, by using the ferrofluid as a precursor media for the formation of a magnetic/luminescent core/shell nanoparticle we were able to produce a spectrally tunable material with the ability to be recollected when implemented in environmental applications.

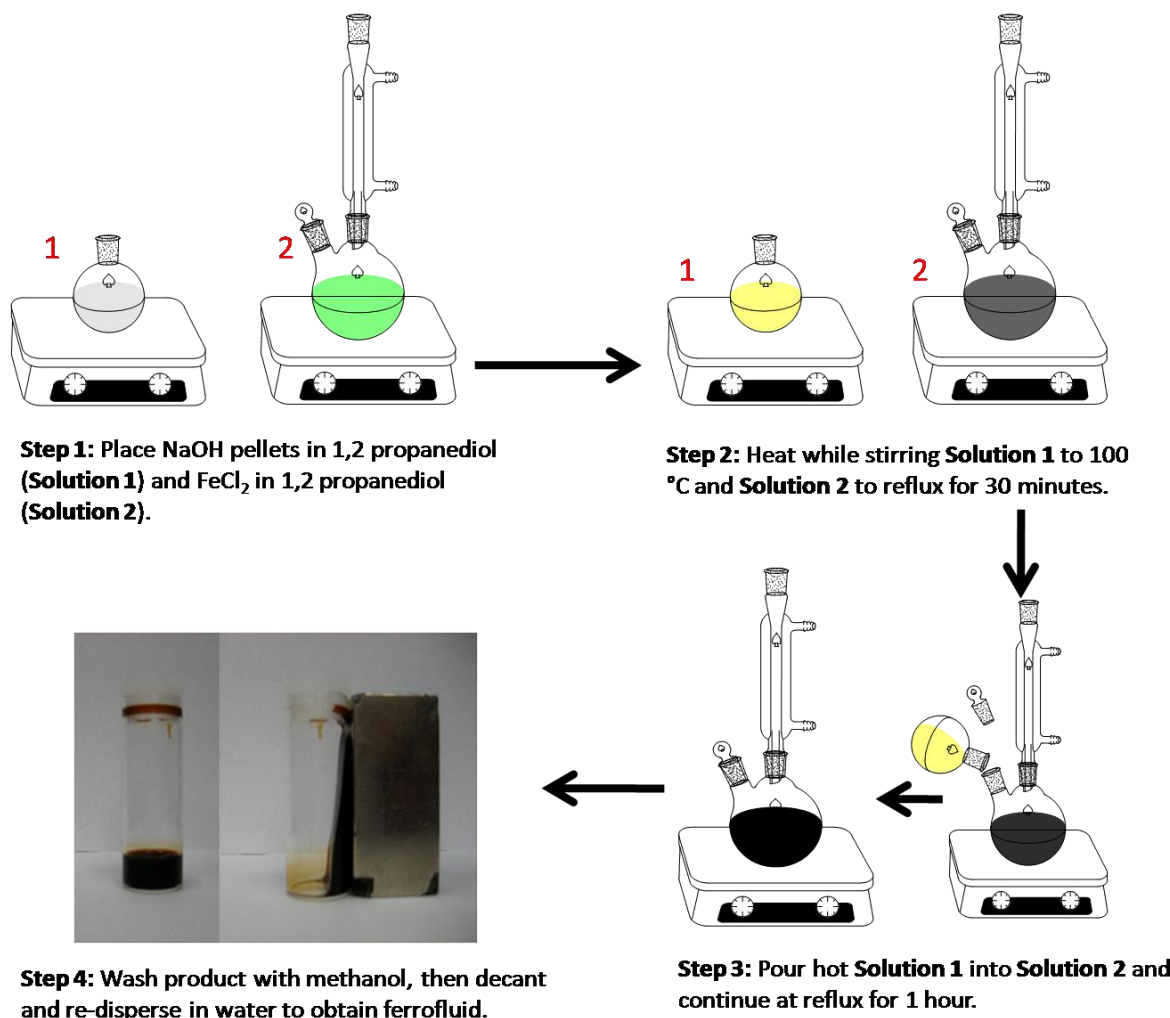


**Figure 9.1.** Synthesis scheme for the design of an aqueous based Fe/FeO<sub>x</sub> ferrofluid.

## 9.2 Synthesis

The synthesis of Fe/FeO<sub>x</sub> nanoparticles was carried out under ambient conditions using a modified polyol method. First, two separate solutions were prepared, solution 1 and solution 2. Solution 1 contained 0.25M iron(II) chloride tetrahydrate and 1,2 propanediol in a 500-mL round bottom flask and was heated to refluxing conditions for 30 minutes. Solution 2 contained 5.2M NaOH and 1,2 propanediol was heated simultaneously at 100°C with magnetic stirring. Hot Solution 2 was subsequently added

to solution 1 and heating was continued to refluxing conditions for one hour. The solution underwent a color change from dark orange, to grey, and then finally to jet black 20 minutes post addition. After 1 hour of refluxing, the solution was allowed to cool to room temperature and then was quenched by the addition of methanol. Throughout the reaction the particles did not seem to stick to the magnetic stirrer during the reaction. The particles were washed with methanol several times and magnetically separated using a rare earth magnet. To prepare an aqueous ferrofluid, the particles were added to a vial with deionized water and sonicated to help the dispersion. A rare earth permanent magnet was used to test the colloid stability. For example, if the ratio of nanoparticles was too large, the particles would aggregate and pull out of solution to the magnet. Once the particles were dispersed in the appropriate amount of water, they were sonicated for 20 minutes. The resulting particles are stable in the aqueous media for over one year without visual degradation.

### 9.3. Results and Discussion

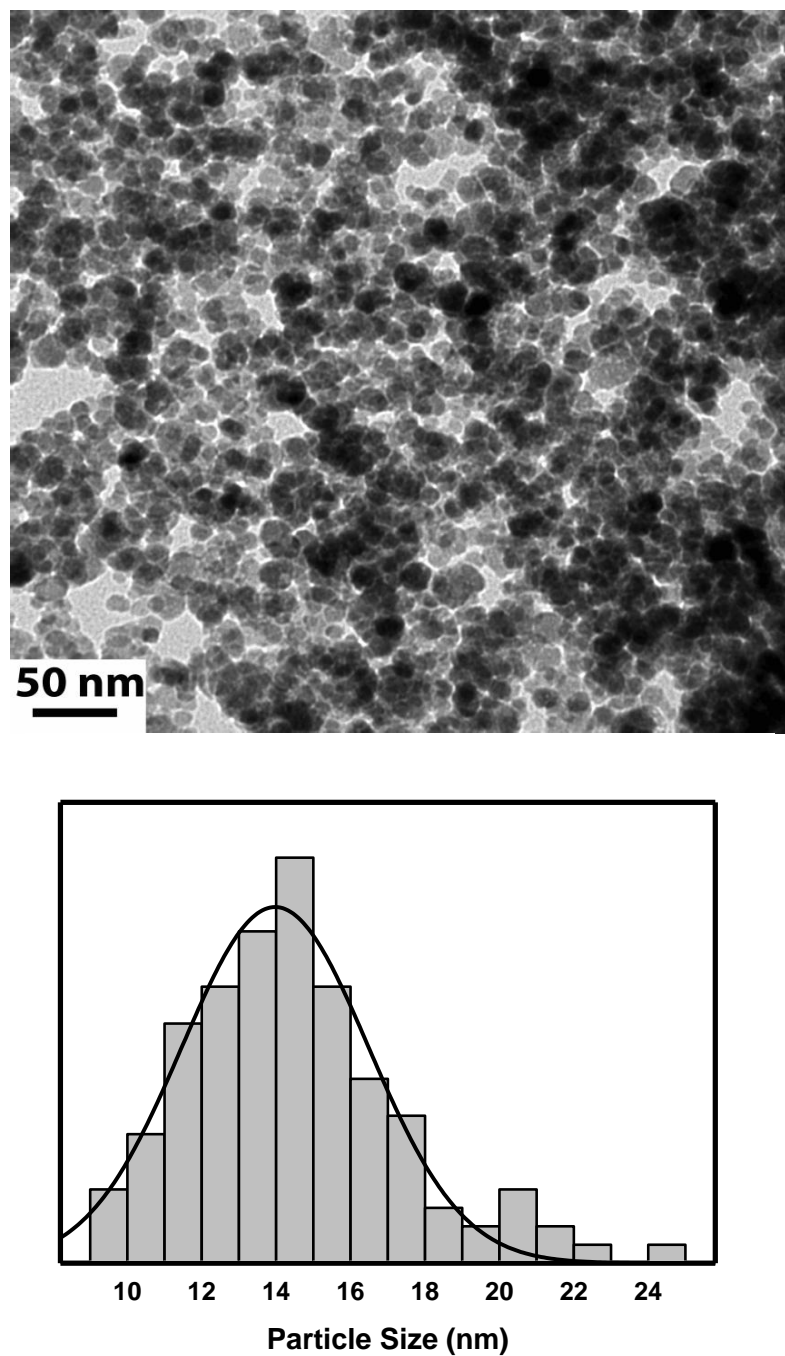


**Figure 9.2.** (A) TEM image of magnetite/α-Fe particles prepared by the polyol process in 1,2 propanediol. The TEM shows that the particle size distribution is relatively monodispersed. (B) A histogram of the particle size from the TEM with an average particle size of 14.5 nm.

The nanoparticle morphology was confirmed by transmission electron microscopy (Figure 9.2), which revealed relative size uniformity with an average diameter of 14.6 ( $\pm 3.12$ ) nanometers. The histogram was developed by taking, at random, 150 of the nanoparticles from the TEM and using an imaging program. From the TEM image, the spherical nanoparticles seem to be slightly aggregated and not monodisperse. However, this could arise from the TEM grid preparation. To prepare the nanoparticles for TEM analysis 7  $\mu\text{L}$  of dried product dispersed in methanol was placed on a copper mesh grid and allowed to dry at room temperature. The TEM analysis was not done on the aqueous ferrofluid itself and we believe that by drying the particles, you induce some aggregation, and that is what is seen above. A better representation of the aqueous colloidal system can be seen in bottom left of Figure 9.1.

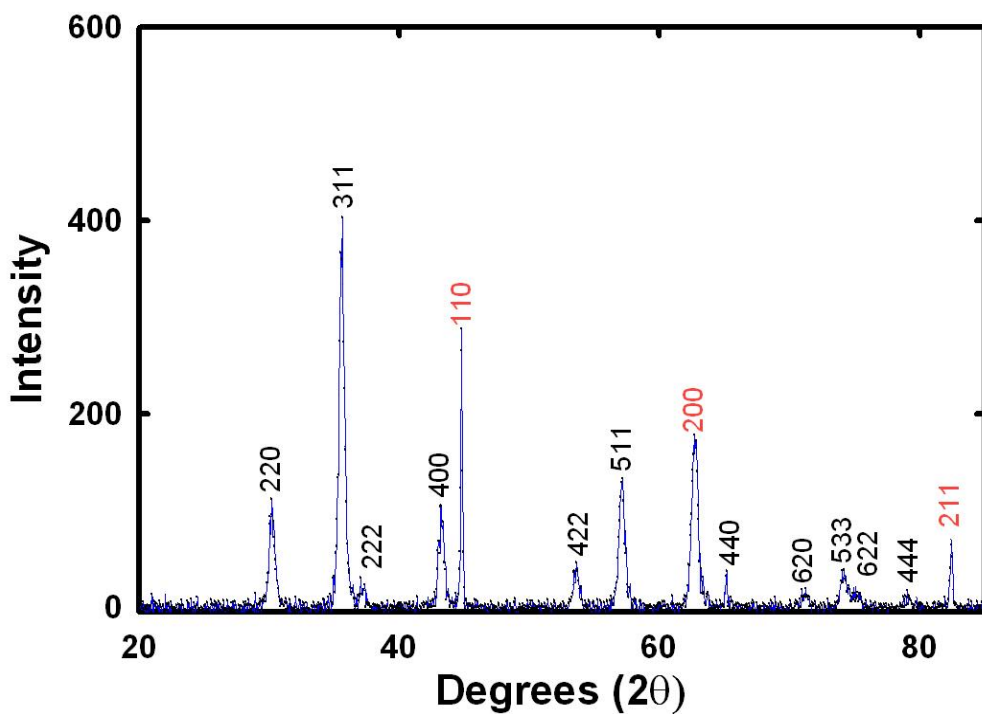


**Figure 9.3.** XRD pattern showing a two-phase system of iron oxide and  $\alpha$ -iron.

X-ray powder diffraction (Figure 9.3) shows a mixed phase system of magnetite ( $\text{Fe}_3\text{O}_4$ ) and iron ( $\alpha\text{-Fe}$ ). Major Diffraction peaks for magnetite at  $30.125^\circ, 35.483^\circ, 37.117^\circ, 43.124^\circ, 53.501^\circ$ , and  $57.033^\circ$  correspond to the (220), (311), (222), (400), (422), and (511) miller indices, respectively. The diffraction peaks for iron at  $44.663^\circ, 65.008^\circ$ , and  $82.314^\circ$  correspond to the (110), (200), and the (211) miller indices, respectively. The peaks were indexed by the ICDD database for magnetite (fd3m, card#03-065-4899) and Fe (Im3m, card#01-075-4899). Rietveld refinement produced a relative percentage of magnetite and iron to be 78% and 22%, respectively. This correlated well with the XAS data.

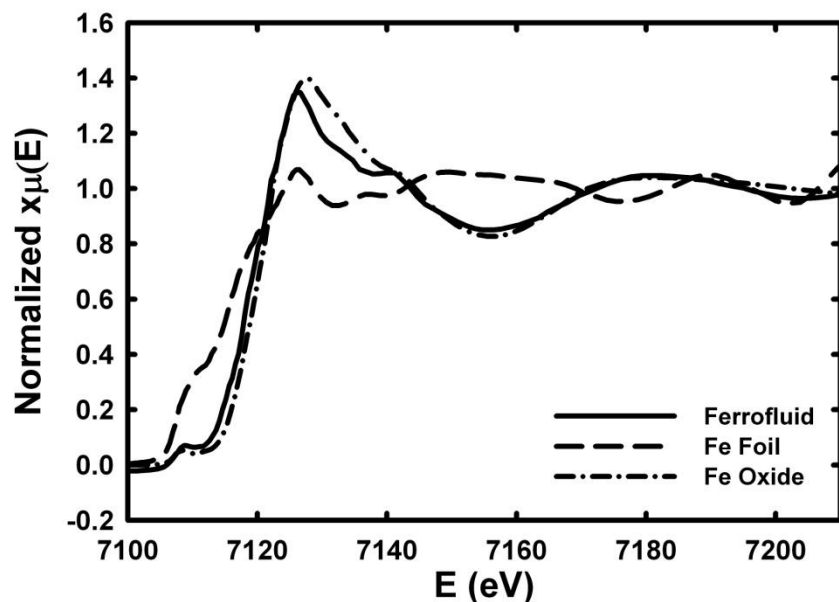


**Figure 9.4.** XANES spectra for the ferrofluid material, iron foil, and iron oxide standards.

A linear combination fit to X-ray absorption near edge structure (XANES) data determined a composition of 20% metal and 80% oxide. Figure 9.4 shows the XANES

spectra for the ferrofluid material, metallic iron foil and an iron oxide standard. From both x-ray characterization analyses, a general assumption that the proposed modified polyol process produces a mixed phase system of Fe oxide and metallic Fe can be made.

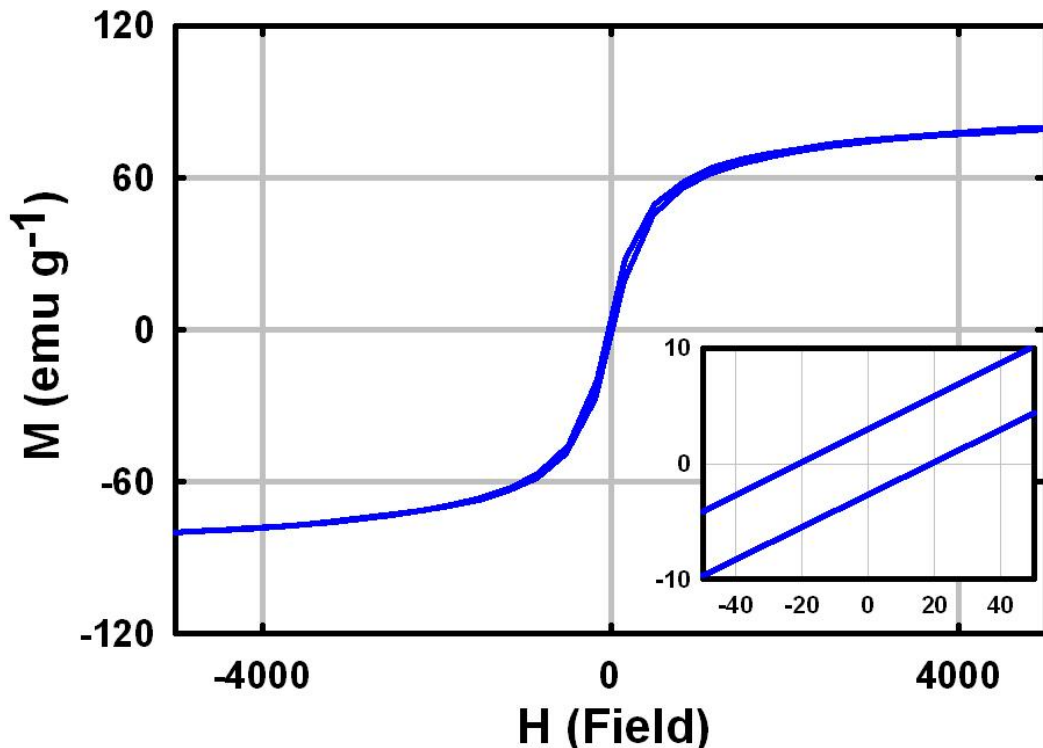


**Figure 9.5.** Room temperature VSM data of the as-prepared ferrofluid material plotted as magnetization (emu/g) versus applied field (Oe).

Room temperature vibrating sample magnetometry revealed a saturation magnetization of 100 emu/g (Figure 9.5). The saturation magnetization ( $M_s$ ) was obtained from a magnetization versus  $1/H$  plot extrapolated to the point where  $1/H$  is equal to zero. The values for bulk Fe and  $\text{Fe}_3\text{O}_4$  are 220 emu/g and 80-120 emu/g, respectively. This

value in magnetization for nanoparticles containing both iron and iron oxide is expected for the percentages of each component in this mixed phase system.

The nanoparticles also have a surfactant-type coating, which will affect the magnetic characteristics of the nanoparticles as well as act as the colloidal stabilizing agent. Thermal analysis of the dried particles reveals a 20% weight drop that correlates with an organic decomposition at 195°C. The progressive heating of sodium hydroxide in the polyol not only reduces the Fe<sup>2+</sup> to produce the nanoparticles, but also forms a solution that plays an important role in the overall reaction dynamics. It is hypothesized that a sodium glycolate-type structure or 1,2 propanediol is adsorbed onto the surface of the particles allowing for *in situ* water stabilization. Further surface characterization will be needed to distinguish between the two possibilities. It is important to note that the saturation magnetization decreased by less than 5% after one year of aqueous exposure. It is thought that this polymer-type structure formed around the nanoparticle gives both the colloidal stability and aids in the resistance to oxidation of the iron metal.

### 9.3.1 MRI Contrast Agent

This ferrofluid was also investigated *in vitro* by magnetic resonance relaxivity measurements and *in vivo* for its application in magnetic resonance imaging. The magnetic resonance imaging (MRI)/spectroscopic experiments were performed on a 2.4 T/40 cm bore MR system (Biospec/Bruker). Spectroscopic T<sub>1</sub> and T<sub>2</sub> <sup>1</sup>H relaxation measurements of the aqueous ferrofluid were conducted using an inversion recovery sequence with eight inversion times (TI) and repetition times (TR) at least five times the expected T<sub>1</sub> value. For the T<sub>2</sub> measurements, a multi-spin-echo CPMG sequence was

employed with several echo times (TE) and TR values at least five times the expected  $T_1$ . The relaxation times were computed from least-squares fitting of the exponentially varying signals using analysis routines available at the MR system. Relaxivities were extracted from graphs of relaxation rates ( $1/T_1$  and  $1/T_2$ ) versus concentration. The  $r_1$  and  $r_2$  relaxivities were found to be  $8.6$  and  $382 \text{ s}^{-1}\text{mM}^{-1}$ . These values should be compared to those reported for the commercial contrast agent Feridex, which are  $12.3$  and  $191 \text{ s}^{-1}\text{mM}^{-1}$ .

<sup>1</sup> 297

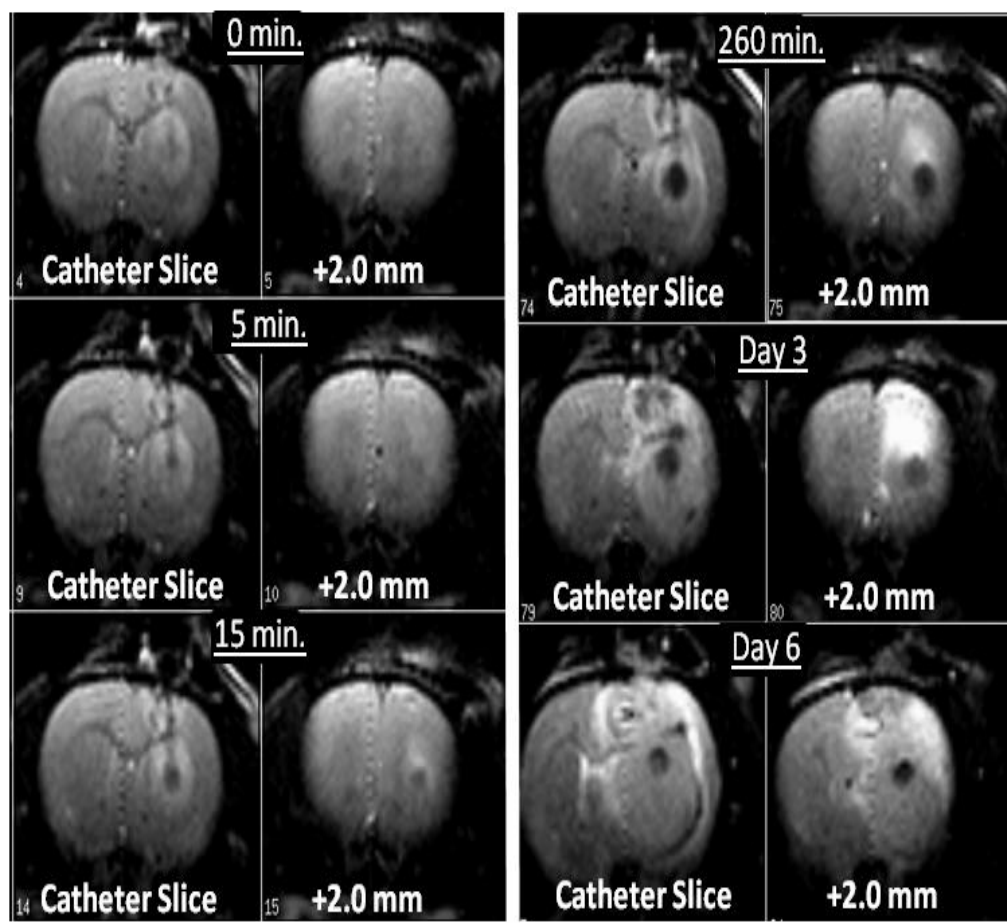


**Figure 9.6.** T<sub>2</sub>W images of a tumor-bearing rat infused with aqueous ferrofluid (0.34 mM iron concentration, 18  $\mu\text{L}$ ) at different time points. The infusate appears dark within the implanted T9 tumor (right side of the tumor). Note that at 6-days post infusion, some of the iron/iron oxide particles have migrated in the tumor periphery (dark ring).

The *in vivo* investigation was performed by intratumoral infusion of the aqueous ferrofluid via convection enhanced delivery (CED)<sup>298-300</sup> into a tumor bearing rat, 13 days post T9 tumor cell implantation. The aqueous ferrofluid was infused at pH 7.5, an iron concentration of 0.34 mM, and a rate of 0.2 µL/min for a total volume of 18 µL infused. The T<sub>2</sub>-weighted images (Figure 9.6) were acquired during the infusion and up to 6 days post-infusion. The dark contrast due to the ferrofluid is clearly seen in the center of the tumor during the infusion and shortly after. Then 6 days post infusion, some of the ferrofluid has pushed to the periphery, thereby more clearly defining the edge of the tumor.

### **9.3.2 Magnetic/RE luminescent Core/Shell Design**

The objective of this section was to use the previously prepared ferrofluid and coat the nanoparticles with a luminescent rare earth (RE) material for the design of a spectrally tunable (in terms of their electromagnetic signal) shell and a magnetic core. The ferrofluid precursor served as a seed for the heterogeneous nucleation and growth of the RE luminescent shell. The emphasis of this section is focused on developing a sensor material that can be suitably distributed and recollected in environmental applications, specifically for the detection of CBRNE threats. However, these nanoparticles can also be used as fluorescent markers for immunoassays/cell labeling as well as MRI contrast agents. Rare earth luminescent nanoparticles are currently being used as alternatives to semiconductors due to their long fluorescent lifetime, high quantum yields, low photobleaching, high chemical stability, and their resistance to degradation over time.<sup>301-</sup><sup>305</sup> In addition to a luminescent shell, the addition of a magnetic core allows the

distributed particles to be easily recollected using a permanent magnet. There have been several magnetic/semiconductor core/shell nanoparticles reported in literature, however, semiconductors suffer from photobleaching.<sup>31,306-308</sup> Currently there have been only a few reports on the preparation of magnetic core and RE luminescent shell nanoparticles.<sup>309-311</sup> This section reports on spectrally tunable magnetic/luminescent core/shell nanoparticles by coating a ferrofluid precursor with various RE dopants in the YVO<sub>4</sub> lattice.

The prepared ferrofluid was placed into a Parr bomb and 8.9 mmol Y(NO<sub>3</sub>)<sub>3</sub>, 0.47 mmol Eu(NO<sub>3</sub>)<sub>3</sub>, and 7.5 mmol of Na<sub>3</sub>VO<sub>4</sub> were dissolved with 30 ml of distilled water. While stirring a white precipitate formed. The bomb was then sealed and placed in a conventional microwave oven for one min. The precipitate was suspended in 40 ml of distilled water, and 9.38 mmol of 1-hydroxyethane-1,1-diphosphonic acid was added. The resulting solution was made basic by adding sodium hydroxide and the solution was left to stir overnight. The brown precipitate was magnetically separated, washed several times with DI water and vacuum dried. The as-prepared core/shell nanoparticles were characterized using TEM, XRD, and XRF. The magnetic properties were characterized using a SQUID magnetometer.

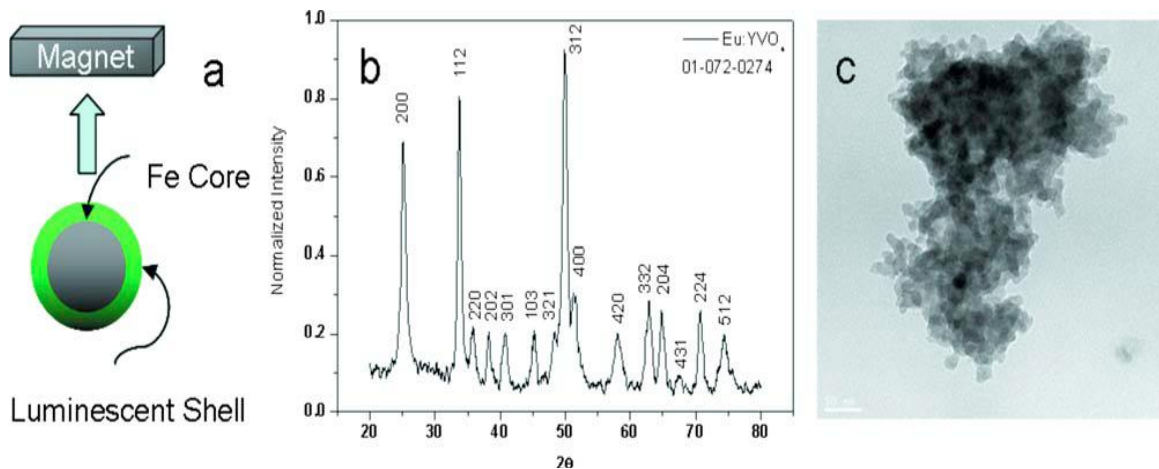


**Figure 9.7.** (a) Proposed structure of magnetic core luminescent shell particles, (b) XRD pattern of the as synthesized particles, and (c) TEM micrograph. The scale bar is 50 nm.

The primary advantage of starting with a ferrofluid is that the magnetic nanoparticles are well isolated from each other and provide a good nucleation source for subsequent shell formation as indicated in Figure 9.7 (a). Yttrium vanadate ( $\text{YVO}_4$ ) was chosen as the luminescent shell surrounding the magnetic core. High luminescent quantum yield phosphors, in a variety of colors, can be prepared by co-doping the  $\text{YVO}_4$  lattice with RE ions.<sup>312</sup> In particular, Eu doped  $\text{YVO}_4$  is an important commercial phosphor possessing a quantum yield of about 70%. It is commercially used in color televisions and high-pressure mercury lamps. The XRD pattern of the resulting 5% Eu doped  $\text{YVO}_4$  shell particles synthesized in the presence of ferrofluid is provided in Figure 9.7 (b). The diffraction pattern indicates that the  $\text{YVO}_4$  adopts a tetragonal zircon structure known for bulk  $\text{YVO}_4$ . The miller indices indicated in the Figure are from the ICDD database (#:01-072-0274). It is significant to note that no indication of Fe or any FeOx is evident in the diffraction pattern. This suggests that there is a thick coating of  $\text{YVO}_4$  around the ferrofluid nanoparticles. In addition, the absence of peaks associated

with Eu suggests that it is well dispersed in the  $\text{YVO}_4$  lattice. A mean crystallite size of 23 nm was determined from the broadening of the diffraction peaks and using the Scherrer equation. This is in good agreement with the TEM micrograph in Figure 9.7 (c). While the XRF results confirm that the Eu doping was 5.1%, the percentage of Fe was lower than expected at 10.5%. Since XRF is considered a surface technique, this low value indicates that the magnetic core is well encased in a thick shell of  $\text{YVO}_4$ .

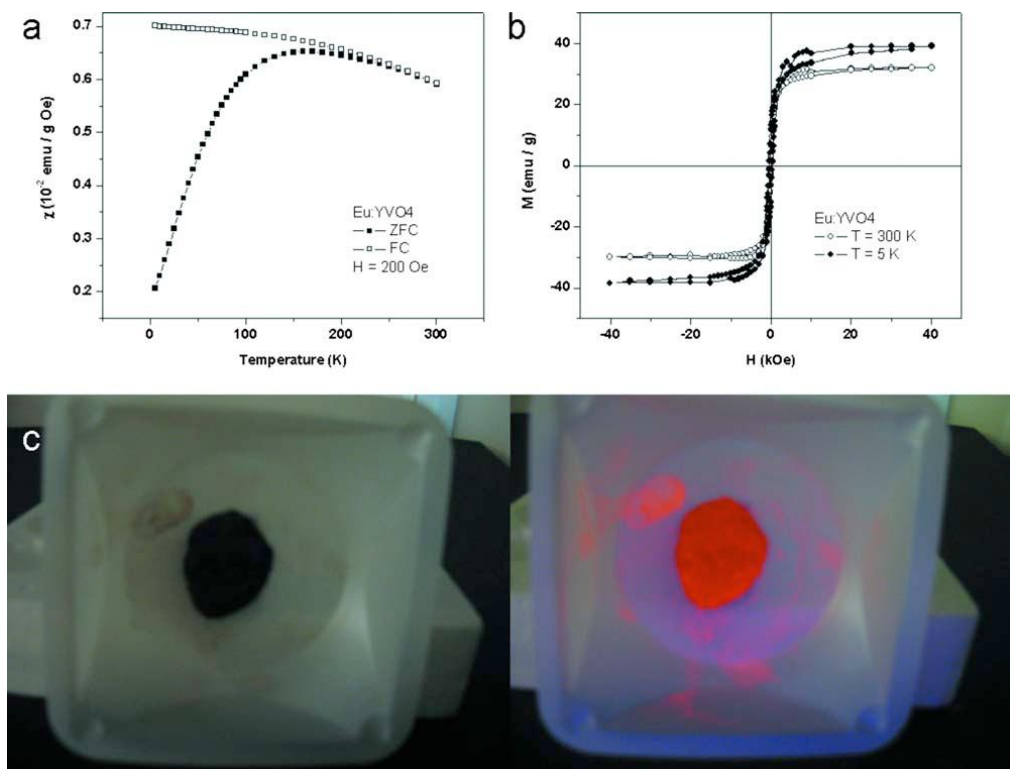


**Figure 9.8.** (a) Temperature dependence of the magnetic susceptibility  $\chi$ , (b)  $M$  vs  $H$  variations measured at 5 and 300 K for magnetic 5% Eu:YVO<sub>4</sub>, and (c) photograph indicative of the magnetic and luminescent properties of the as-prepared nanoparticles.

A FC/ZFC plot was used to determine the magnetic properties of the as-prepared magnetic/luminescent nanoparticles (Figure 9.8 (a)). It is evident from the graph that the sample displays an overall superparamagnetic character. The broad width of the blocking

temperature for the ZFC plot suggests that there is a large particle size distribution. In addition, the FC/ZFC plot suggests that there are interacting particles, due to the convergence of the FC and ZFC plot above the blocking temperature, which suggests that there are multiple magnetic particles within the core. This probably occurs during the precipitation of the Eu:YVO<sub>4</sub> and results in a cluster of Fe/FeOx nanoparticles situated in the core. The magnetization saturation of the magnetic/luminescent nanoparticles is about 41 emu/g, which is significantly lower than that of just the ferrofluid. This lower value is attributed to the addition of the diamagnetic contribution associated with the YVO<sub>4</sub> shell and is not unexpected since the saturation magnetization is mass dependent. While the thick shell may have decreased the overall saturation magnetization of the resulting particles, it is still significant enough to respond to an external magnetic field, as shown in Figure 9.8 (c).

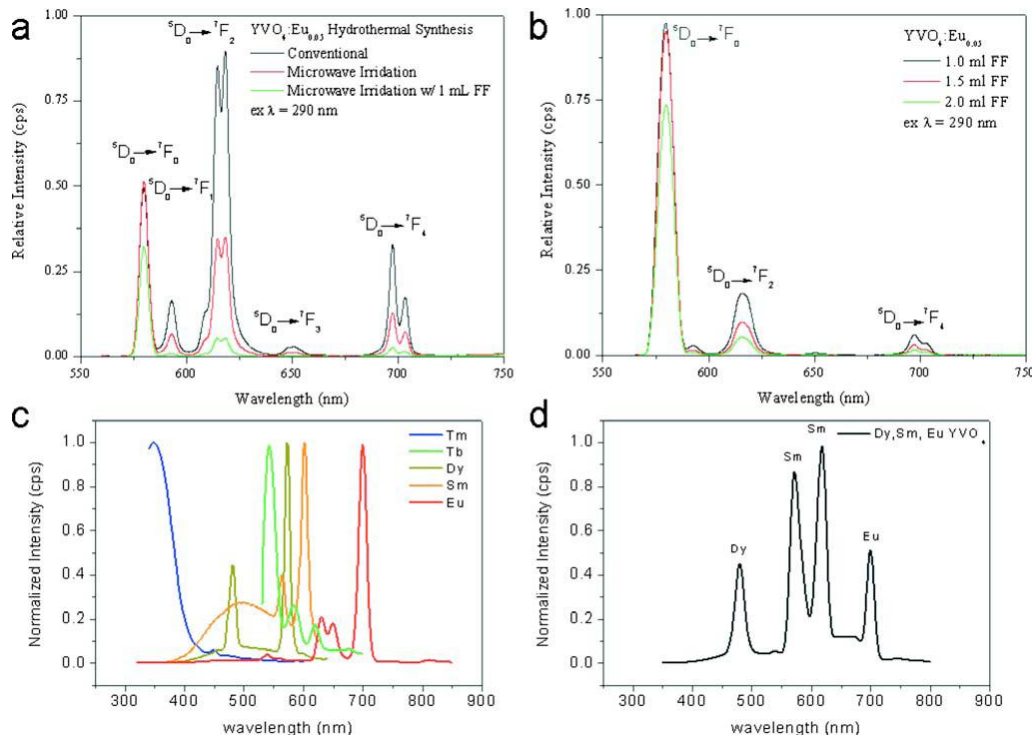


**Figure 9.9.** Emission spectra of (a) conventional and magnetic core luminescent nanoparticles prepared hydrothermally, (b) the effect of varying amounts of ferrofluid, (c) the effects of varying the RE dopants, and (d) the unique signatures can be created by combining various dopants.

The luminescent spectra of the magnetic 5% Eu doped  $\text{YVO}_4$  is shown in Figure 9.9(a). It has been well documented that strong luminescence occurs from efficient energy transfer from the  $\text{VO}_3^{3-}$  group to  $\text{Eu}^{3+}$ , specifically attributed to the charge transfer from the oxygen ligands to the central vanadium atom. This transition is known to occur at about 300 nm,<sup>312</sup> thus, we have chosen 290 nm as the excitation wavelength. It has also been shown that the quantum yield shows a maximum at 5% Eu doping and decreases as the Eu concentration increases. Figure 9.9(b) shows that the addition of ferrofluid is inversely proportional to the emission intensity. This can be explained by the addition of a strong magnetic dipole, which dominates over a forced electronic dipole when no

ferrofluid is present. We have also shown that the incorporation of other lanthanide ions in place of Eu leads to a variety of colors. It is significant to note that the doping concentration of the other lanthanide ions was kept at 5%. The primary emission peak of Sm occurs at 602 nm along with a secondary peak at 564nm. The magnetic 5% doped Sm YVO<sub>4</sub> gives rise to an orange emission. Doping with Dy gives rise to a yellow emission with the primary and secondary emission peak occurring at 573 nm and 482 nm, respectively. A green emission is seen when Tb is doped into the YVO<sub>4</sub> lattice and a primary emission peak occurs at 543 nm. Finally, Tm doping produces a blue emission with the peak at 349 nm. We have also shown that by codoping lanthanides into the YVO<sub>4</sub> lattice it is possible to create a unique emission spectra corresponding to the various dopants (Figure 9.9(d)).

To determine if the particles had the ability to be magnetically recollected after distribution, four different soil types were used with various moisture compositions. These soils were characterized as being sand, loamy sand, clay mixture, and loam. Six moistures were evaluated for each soil, including a dry variable. On the soil surface, 50 mg of particles were distributed as evenly as possible and allowed to interact for 2 hrs in a sealed container. After this time, the lid was removed and the samples were allowed to air dry for 24 hrs. Magnetic recollection was accomplished by holding a one-Tesla permanent magnet greater than 3 mm above the soil surface. Magnetic recollection was nearly 100% on all dry soil samples; however, on moist soil sample recollection, the density and moisture of the soil determined the recollection ability. Since the particles

adhere to the moist soil below, recollection was more successful on lower density soil (loam and clay mixture).

#### 9.4 Conclusions

In conclusion, an aqueous ferrofluid containing monodisperse  $\text{Fe}/\text{FeO}_x$  nanoparticles were produced using a modified one-pot polyol process. Controlling the reduction of the iron cations, along with the *in-situ* stabilization, results in particles with an enhanced magnetic moment due to the incorporation of metallic iron and iron oxide. The aqueous ferrofluid shows promise as an MRI contrast agent with enhanced  $T_2$  relaxivity. We have also shown that the ferrofluid can be used as a starting material for the heterogeneous nucleation and growth of a luminescent shell to create magnetic core nanoparticles with a spectrally tunable shell for the detection of environmental threats. These materials also have many promising aspects in biological applications and if linked with a biomolecule, could serve as promising magnetic carriers/labels for efficient bio-separation, drug delivery, and diagnostic applications.

## **Chapter 10: Design of Cobalt Carbide Nanoparticles**

## 10.1 Introduction

Permanent magnets are used for numerous applications including their use in electronics, automobiles, communication, and information technologies. High performance permanent magnets can be classified into three categories: 1) rare-earth-3d transition metal intermetallics (NdFeB, SmCo), 2) AlNiCo, and 3) ceramic magnets (hexaferrites). To rate the efficiency of a permanent magnet, researchers typically present the magnetic energy density or the maximum energy product ( $BH_{max}$ ). In the above mentioned applications, when the  $BH_{max}$  increases, so does the efficiency of the device. For example, in MRI devices, the high  $BH_{max}$  of a permanent magnet material is much more efficient than alternatives such as energy consuming electromagnets. To date, many of the permanent magnets contain rare earth elements and provide the highest  $BH_{max}$ . However, these materials are expensive to manufacture and are prone to corrosion. Cost is also increased by supply chain limitations, as the majority of the rare earth elements are mined in foreign countries such as China. As a cost effective and relatively available alternative, AlNiCo and ceramic magnets have been designed; however, these have a much lower  $BH_{max}$ . Despite their substantially lower energy product, these materials have grown as viable global permanent magnet materials. Since the 1980s, very few advances have been made for creating magnets that are more efficient. In addition, the need for the design of 3d-transition metal permanent magnets without the dependences on rare earth elements has increased due to current unwanted reliance on foreign resources. This chapter discusses a ferromagnetic material based upon nanoscale cobalt carbide particles that provides a rare earth free alternative to high performance permanent magnets.

As explained in the previous chapters, the polyol process has been extensively used to prepare an assortment of nanoparticles for a wide range of applications. Here we were able to extend the process to the design of permanent magnets. These particles show promise in the field of magnets with a room temperature coercivity of 3.4 kOe and a room temperature saturation magnetization of up to 73 emu/g. Figure 10.1 shows how these particles compare to the conventionally used permanent magnets.

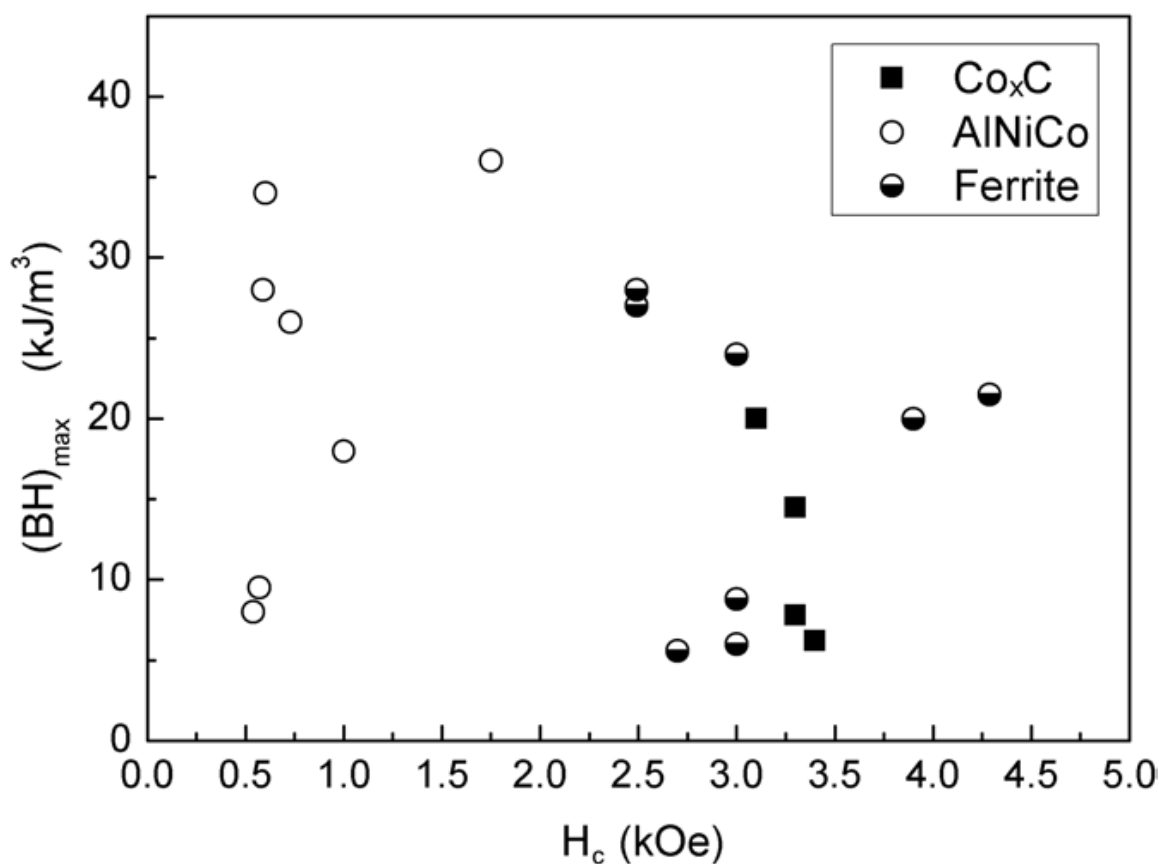


**Figure 10.1.** Energy products versus coercivity of cobalt carbide nanoparticle powders compared with powders of AlNiCo and ceramic ferrites systems.

## 10.2 Synthesis Techniques

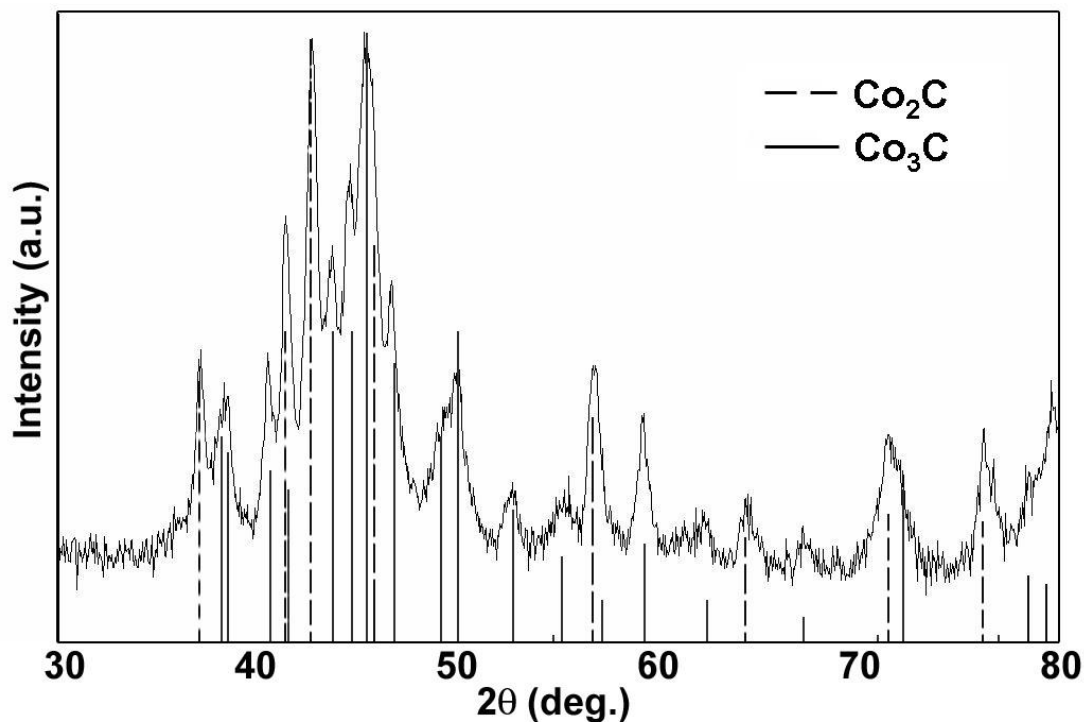
The chemical synthesis methods employed here to produce size-, shape-, composition- and phase-controlled, highly-coercive cobalt carbide nanoparticles are

based upon reduction of metallic salts in a liquid polyol medium that acts as both a solvent and a reducing agent. The reduction reaction kinetics of the process are enhanced by controlling the type, temperature, and concentration of the polyol medium and by adding appropriate surfactants that limit the oxidation of ions when reduced and regulate the growth of particles as the reaction progresses. In this study, several parameters were altered, such as the amount of NaOH, PVP, glycol, and temperature range. The typical chemical synthesis includes adding 0.1 M - 0.2 M concentration of Co (II) acetate to tetraethylene glycol. Poly-vinylpyrrolidone (PVP, MW~40,000) was introduced as a capping agent along with NaOH and Sm (III) acetate as catalysts. The solution was allowed to de-gas in N<sub>2</sub> gas (or in some instances Ar gas) for 10-15 minutes prior to the start of the reaction. The solution was then heated to the boiling point of tetraethylene glycol (~573K) for 1-2 hrs using a distillation apparatus with magnetic stirring. After the completion of the reaction, the solution was cooled to room temperature, magnetically separated several times using an external rare earth magnet, and rinsed repeatedly in methanol to remove un-reacted catalyst. The black precipitate was dried under vacuum at room temperature prior to characterization.

The resulting dried powders were characterized by XRD, TEM, and VSM for the determination of phase, morphology, and temperature dependent magnetic properties. XRD measurements were performed on a Rigaku-Ultima-III Bragg-Brentano diffractometer with Cu-K $\alpha$  radiation. Thermomagnetometry was performed using a Lakeshore Cryotonics Inc. Model 7400 VSM for temperature ranging from room temperature to 1000K. A Quantum Design physical property measurement system

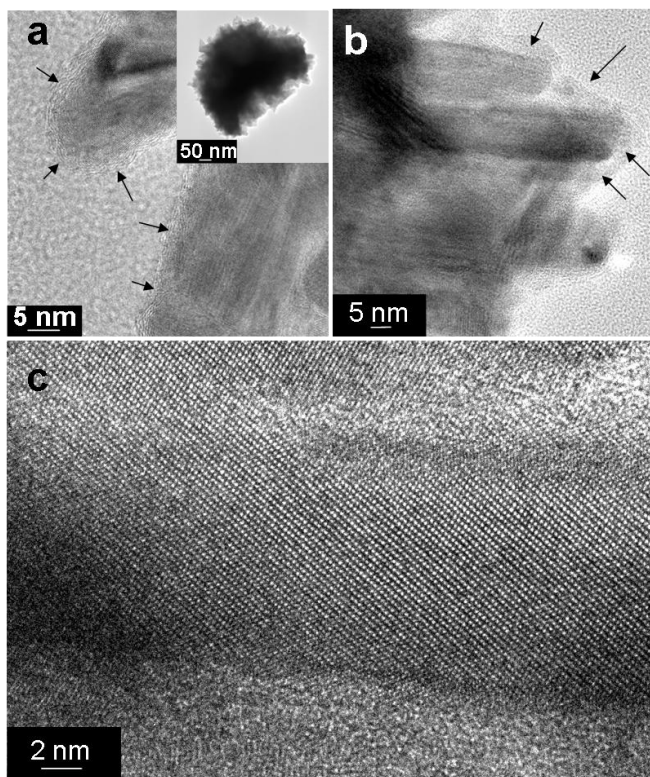
(PPMS) was employed to extend the temperature studies to 10K. The powder morphologies were characterized using a JEOL 2200-FX high-resolution transmission electron microscope with a 200 kV accelerating voltage. Samples for TEM were prepared by dispersing a drop of nanoparticle-loaded liquid suspension onto a carbon film supported by copper mesh followed by evaporation of the liquid. Fast Fourier transforms (FFTs) were obtained from experimental high resolution TEM images using the Digitalmicrograph software. EDXS was utilized to determine the composition of the individual powder particles.

### 10.3 Results and Discussion



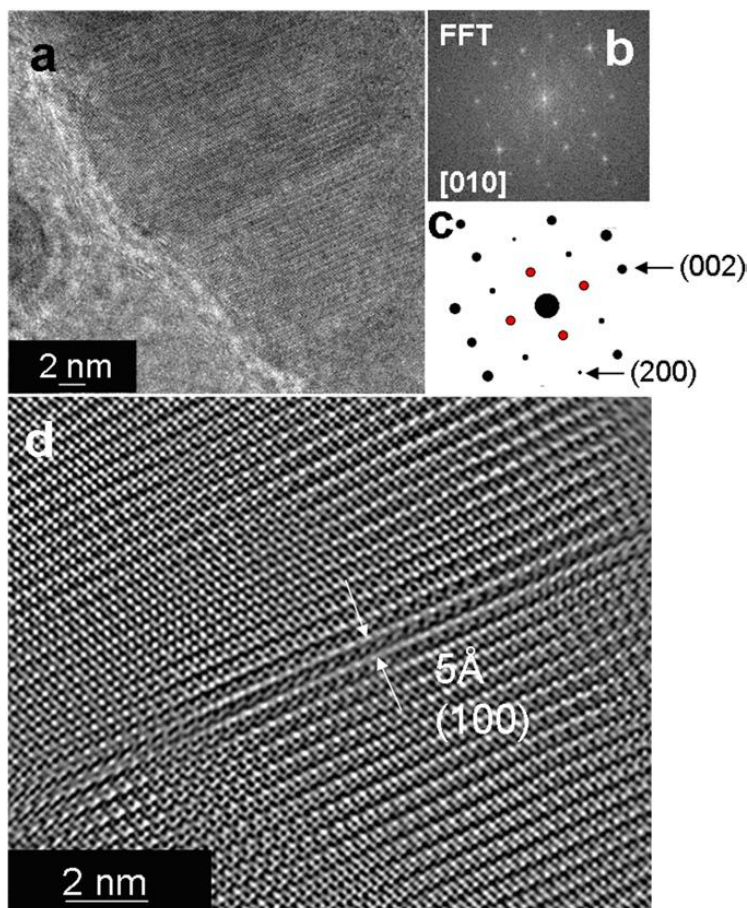
**Figure 10.2.** A representative XRD scan obtained from powders processed using the polyol reduction reaction. Vertical lines corresponding to the position and amplitude of diffraction peaks from JCPDS reference powder diffraction files  $\text{Co}_2\text{C}$  (65-1457) and  $\text{Co}_3\text{C}$  (26-0450) are also presented.

Figure 10.2 shows a representative XRD scan. The data was collected at room temperature and is depicted with an overlay of data from the JCPDS reference powder diffraction files of Co<sub>2</sub>C (65-1457) and Co<sub>3</sub>C (26-0450). The reference powder files are represented in the graph by vertical lines. From the data, you can see that all the main peaks can be indexed either to Co<sub>2</sub>C or Co<sub>3</sub>C suggesting that they are the dominant phases present in the material.



**Figures 10.3.** (A-C). High-resolution transmission electron microscopy images of a representative cobalt carbide sample. The insert to (A) shows an agglomerated particle cluster about 300-500 nm in diameter. Panels (A) and (B) are TEM images of rod-like Co-carbide crystals surrounded by a thin 1 to 4 nm graphite-like layer (denoted by arrows). (C) is an HRTEM image of a rod-like Co-carbide nanoparticle with an aspect ratio near 5:1.

Figures 10.3 (A-C) depict high-resolution TEM data images. An observation of the TEM shows that the particles are highly agglomerated clusters of about 300-500 nm in diameter. They consist of nanocrystalline Co-carbide particles with a rod-like morphology having an aspect ratio of approximately 2:1. It is hypothesized that the ferromagnetic behavior of the nanoparticles was the driving force for agglomeration. Figures 10.2 (A) and (B) are TEM images of the rod-like Co-carbide nanoparticles. The nanoparticles are surrounded by a thin, 1-4 nm graphitic layer, denoted by the arrows. This graphitic layer has been previously reported as an onion-like structure in other carbide nanoparticles.<sup>313</sup> We suspect that this carbon layer is formed during the synthesis and could occur from the reduction of precursors and surfactants, which may also act as a barrier that impedes further crystal growth. This result is the formation of acicular rod-like morphologies. To determine the crystal structure and preferred growth direction, FFTs were obtained from HRTEM images of individual nanoparticles. Figure 10.4 (A) is a HRTEM image of a representative Co-carbide nanoparticle consisting of mainly  $\text{Co}_3\text{C}$  with orientation close to the [010] zone axis. The FFT seen in figure 10.4 (B) was obtained from part of the nanoparticle and indexed to the  $\text{Co}_3\text{C}$  phase (space group: *Pnma*  $a = 5.03 \text{ \AA}$ ,  $b = 6.73 \text{ \AA}$ , and  $c = 4.48 \text{ \AA}$ ). A simulated diffraction pattern of  $\text{Co}_3\text{C}$  along the same zone axis is provided for comparison (Figure 10.4 (C)).



**Figure 10.4.** (A-C) HRTEM image of  $\text{Co}_3\text{C}$  nanoparticles with orientation close to the [010] zone axis. The FFT was indexed to the  $\text{Co}_3\text{C}$  phase. A simulated diffraction pattern of  $\text{Co}_3\text{C}$  along the same zone axis is provided for comparison.

For comparison, another area on the TEM grid was analyzed. This area had a majority phase of  $\text{Co}_2\text{C}$ . Figure 10.5 shows a HRTEM image of  $\text{Co}_2\text{C}$  nanoparticles (space group:  $Pnnm$  with  $a = 4.45 \text{ \AA}$ ,  $b = 4.37 \text{ \AA}$ , and  $c = 2.90 \text{ \AA}$ ) close to the [001] zone axis. The FFT from a portion of the crystal shows a near square pattern indicative of an axis in which the  $a$  and  $b$  lattice parameters are almost equal. The presented HRTEM analyses confirm the presence of both  $\text{Co}_2\text{C}$  and  $\text{Co}_3\text{C}$  phases in the nanoparticle clusters

along with a graphitic shell layer. The nanoparticle morphology seems to rod-like in nature.

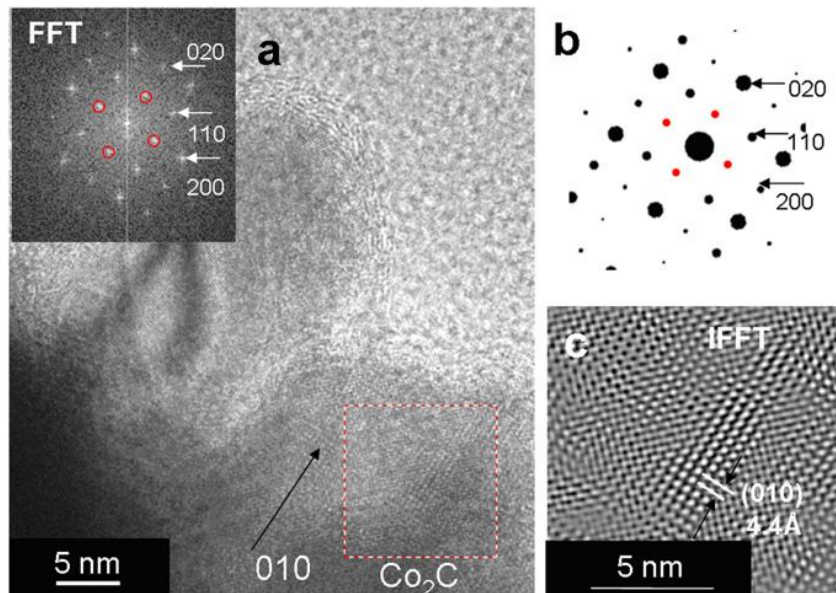


**Figure 10.5.** (A-C) HRTEM images of a  $\text{Co}_2\text{C}$  rich area of a nanoparticle. The FFT and a simulated FFT  $\text{Co}_2\text{C}$  images are shown for comparison.

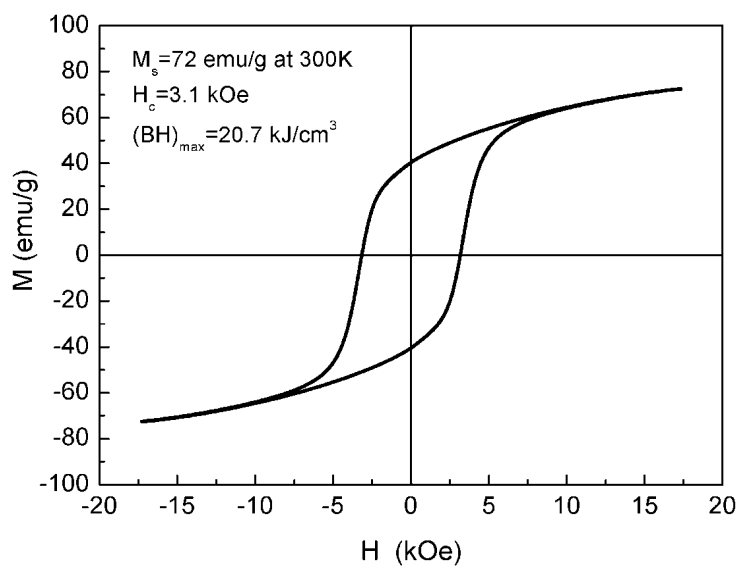


**Figure 10.6.** Room temperature hysteresis loop of representative sample having  $M_s$  of 73 emu/g and an  $H_c$  of 3.1 kOe. The  $(\text{BH})_{\text{max}}$  is  $20.7 \text{ kJ/m}^3$ .

Figure 10.6 is a room temperature hysteresis loop curve of a representative cobalt carbide nanoparticle. For this sample, the room temperature magnetization is about 74 emu/g with a coercivity of about 3.1 kOe. The room temperature  $BH_{max}$  for this sample was calculated to be 20.7 kJ/m<sup>3</sup>. It is noteworthy to discuss that the magnetization values of all the samples were corrected for the presence of the nonmagnetic graphitic layer seen on the nanoparticles. The correction was accomplished by calculating the surface volume fraction based on the thickness of the carbon layer seen in the HRTEM images. Figure 10.7 shows various values and volume ratios obtained by different samples. From this it can be seen that there are several variations in the volume ratio of the two types of carbide formed. There seems to be a trade off between the saturation magnetization and coercivity of the materials. However, we have been able to control the magnetic properties by carefully selecting the processing parameters during the synthesis of the nanoparticles.

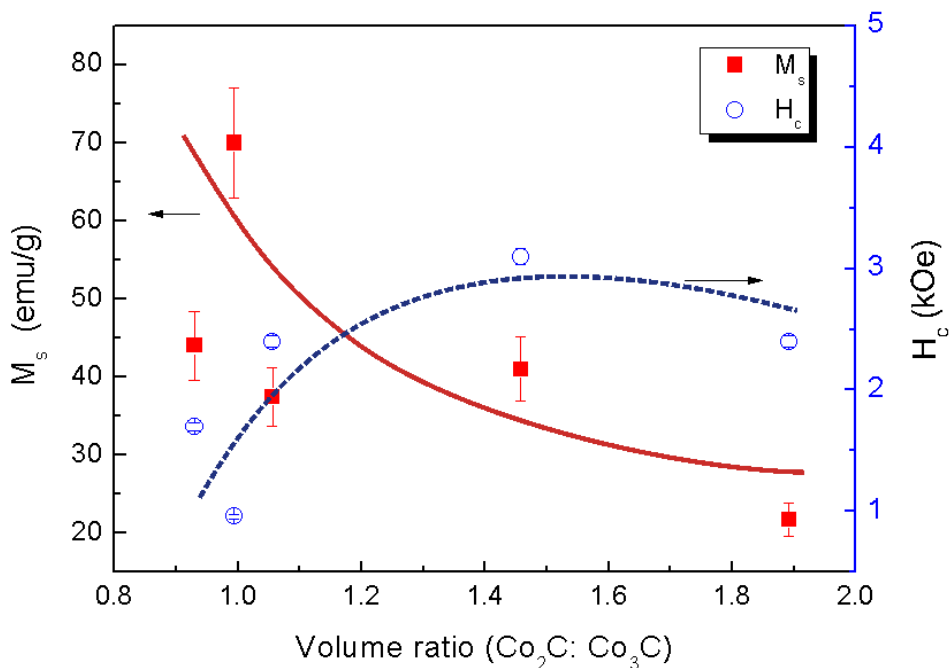


**Figure 10.7.** A plot of magnetic properties versus the phase volume ratio illustrating the interrelationship between saturation magnetization and coercivity to the volume fraction of Co<sub>2</sub>C to Co<sub>3</sub>C measured by X-ray diffraction. The plotted lines are intended as a guide to the eye. Error bars reflect the uncertainty in measured values.

#### 10.4 Conclusions

In summary, this chapter has highlighted the synthesis and characterization of cobalt carbide nanoparticles synthesized by a modified polyol process. The resulting nanoparticles have a rod-like morphology and are seen as clusters of Co<sub>3</sub>C and Co<sub>2</sub>C with room temperature coercivities reaching 3.4 kOe. These nanoparticles present an alternative route to producing rare earth element free high performance permanent magnets with a BH<sub>max</sub> greater 20 kJ/m<sup>3</sup>.

## **Chapter 11: Summary**

The goal of this dissertation is to improve the understanding of the physical and chemical properties in the nanoscale regime. As discussed in this dissertation, this goal is accomplished by specifically focusing on the investigation of the synthesis and characterization of metallic and bimetallic core/shell nanoparticles. A summary of some of the main conclusions in this dissertation work is presented below.

1) Effective synthetic methods and strategies for the design of functional metal and core/shell nanoparticles have been developed. Several new routes allowed us to synthesize Fe/Ag, Fe/SiO<sub>2</sub>/Au, Cu/Ni, Fe/FeO<sub>x</sub>, Fe/FeO<sub>x</sub>/Eu:YVO<sub>4</sub>, and Co/C core/shell nanoparticles with monodispersed sizes, controlled shapes, and tunable surfaces, which are some of the parameters that determine the unique nanoscale properties. For example, in one of our studies we investigated a route for the synthesis of various core/shell morphologies of Fe and Ag by manipulating the reaction parameters. We have found that by varying the addition time of AgNO<sub>3</sub>, we could form Ag/Fe and Fe/Ag core/shell nanoparticles. Core/shell morphology was achieved by the reduction of the core first, which acted as a seed for the heterogeneous nucleation and growth of the shell.

2) We have carried out both experimental measurements and computational modeling to gain insight into the mechanism of the polyol method. For example, our experimental work on the formation of copper and nickel metal using a variety of polyols allowed for an elucidation that in ethylene glycol, nickel chloride will only form a nickel hydroxyl salt under refluxing conditions. This is most likely due to the enhanced stability of the Ni(EG)<sub>3</sub> hydrated intermediate complex. When the reaction is switched to distillation, where water is evaporated out of the system, the formation of elemental

nickel is possible. In contrast, the Cu(EG)<sub>2</sub> hydrated intermediate complex was less stable, and the formation of elemental copper could be achieved under both refluxing and distillation conditions. This led us to create a novel one-pot synthesis of Cu/Ni core/shell nanoparticles by first refluxing the solution to produce Cu nanoparticles. The Cu nanoparticles were seeds for the growth of Ni shells once the system was set to distill off the water. The intermediate metal-glycolate has been proposed several times by others, but our work provides the first crystal structure of the trapped Cu-glycolate intermediate. This work allowed us to more reliably use computational modeling to determine the metal-glycolate stability for both Cu and Ni complexes. We have found, according to the modeled incremental binding energies, that the Cu(EG)<sub>2</sub> complex is the most stable glycolated species for Cu. In contrast, the Ni(EG)<sub>3</sub> complex is the most stable form for glycolated Ni. By understanding the stability of these intermediate complexes, we were able to form a reaction pathway for the reduction of elemental Cu and Ni.

3) We have also been able to manipulate a one-pot polyol reaction for the design of Fe/FeOx nanoparticles. This process enabled the liquid polyol to act not only as a solvent, but also as a mild reducing agent and a surfactant for the stabilization of the nanoparticles in aqueous media; this created a novel high magnetization aqueous ferrofluid. The ferrofluid was then investigated *in vitro* by magnetic relaxivity measurements and *in vivo* for its application in MRI. Also, by using the ferrofluid as a precursor media we were able to prepare magnetic/luminescent core/shell nanoparticles, where the shell was a RE luminescent Eu:YVO<sub>4</sub>.

4) Lastly, we were able to extend the polyol process to design a novel permanent magnet material with the absence of RE elements. The design of permanent magnets, which do not rely on RE elements, is extremely important if we are to produce efficient renewable energy materials and storage devices. Applications such as hybrid electric vehicles and Maglev trains of the future will depend on our success in producing cost efficient permanent magnets. Our work on the design and characterization of Co/C nanoparticles provides a RE-free alternative to high performance permanent magnets. These particles show promise in the field of magnets with a room temperature coercivity of 3.4 kOe and a room temperature saturation magnetization of up to 73 em/g. A further understanding of the reaction processes and synthetic parameters governing the growth of these particles may enable us to produce more efficient high performance magnets in the future.

Overall, these results have provided new insight into the fundamental factors governing the physical and chemical properties of the synthesis of metal and core/shell nanoparticles. While this work has added much to the understanding of bimetallic core/shell nanoparticles, part of our ongoing work includes a study of the chemical sensing, magnetic, and catalytic properties of these particles. Future work in this field will be useful for the design of advanced functional nanomaterials.

## **References**

## References

- (1) Huber, D. L. *small* **2005**, *1*, 482.
- (2) Burda, C.; Chen, X.; Narayanan, R.; El-Sayed, M. A. *Chemical Review* **2005**, *105*, 1025.
- (3) Srivastava, C.; Nikles, D. E.; Thompson, G. B. *Journal of Applied Physics* **2008**, *104*, 104314.
- (4) Cullity, B. D.; Graham, C. D. *Introduction to Magnetic Materials*; 2 ed.; John Wiley & Sons: Hoboken, New Jersey, 2009.
- (5) Easom, K. A.; Klabunde, K. J.; Sorensen, C. M.; Hadjipanayis, G. C. *Polyhedron* **1994**, *13*, 1197.
- (6) Gangopadhyay, S.; Hadjipanayis, G. C.; Dale, B.; Sorensen, C. M.; Klabunde, K. J.; Papaefthymiou, V.; Kostikas, A. *Physical Review B* **1992**, *45*, 9778.
- (7) Yiping, L.; Hadjipanayis, G. C.; Sorensen, C. M.; Klabunde, K. J. *J. Appl. Phys.* **1994**, *75*, 5885.
- (8) Wang, Y.; Herron, N. *Physical Review B* **1990**, *42*, 7253.
- (9) Johansson, K. P.; McLendon, G.; Marchetti, A. P. *Chem. Phys. Lett.* **1991**, *179*, 321.
- (10) Rossetti, R.; Hull, R.; Gibson, J. M.; Brus, L. E. *The Journal of Chemical Physics* **1985**, *83*, 1406.
- (11) Dannhauser, T.; O'Neil, M.; Johansson, K.; Whitten, D.; McLendon, G. *The Journal of Physical Chemistry* **1986**, *90*, 6074.

- (12) Lin, S. T.; Franklin, M. T.; Klabunde, K. J. *Langmuir* **1986**, *2*, 259.
- (13) Glaspell, G. P.; Zuo, C.; Jagodzinski, P. W. *Journal of Cluster Science* **2005**, *16*, 39.
- (14) Jun, B.-H.; Noh, M. S.; Kim, J.; Kim, G.; Kang, H.; Kim, M.-S.; Seo, Y.-T.; Baek, J.; Kim, J.-H.; Park, J.; Kim, S.; Kim, Y.-K.; Hyeon, T.; Cho, M.-H.; Jeong, D. H.; Lee, Y.-S. *Small* **2009**, *9999*, NA.
- (15) Kim, K.; Jang, H. J.; Shin, K. S. *Analyst* **2009**, *134*, 308.
- (16) Kneipp, K.; Kneipp, H.; Manoharan, R.; Hanlon, E. B.; Itzkan, I.; Dasari, R. R.; Feld, M. S. *Appl. Spectrosc.* **1998**, *52*, 1493.
- (17) Kneipp, K.; Kneipp, H.; Manoharan, R.; Itzkan, I.; Dasari, R. R.; Feld, M. S. *J. Raman Spectrosc.* **1998**, *29*, 743.
- (18) Li, X.; Zhang, J.; Xu, W.; Jia, H.; Wang, X.; Yang, B.; Zhao, B.; Li, B.; Ozaki, Y. *Langmuir* **2003**, *19*, 4285.
- (19) Michaels, A. M.; Jiang, J.; Brus, L. *J. Phys. Chem. B* **2000**, *104*, 11965.
- (20) Noh, M. S.; Jun, B.-H.; Kim, S.; Kang, H.; Woo, M.-A.; Minai-Tehrani, A.; Kim, J.-E.; Kim, J.; Park, J.; Lim, H.-T.; Park, S.-C.; Hyeon, T.; Kim, Y.-K.; Jeong, D. H.; Lee, Y.-S.; Cho, M.-H. *Biomaterials* **2009**, *30*, 3915.
- (21) Sato-Bertru, R.; Redon, R.; Vaquez-Olmos, A.; Saniger, J. M. *J. Raman Spectrosc.* **2009**, *40*, 376.
- (22) Sevilla, P.; Garcia-Blanco, F.; Garcia-Ramos, J. V.; Sanchez-Cortes, S. *Phys. Chem. Chem. Phys.* **2009**, *11*, 8342.
- (23) Shkilnyy, A.; Souce, M.; Dubois, P.; Warmont, F.; Saboungi, M. L.; Chourpa, I. *Analyst* **2009**, *134*, 1868.

- (24) Torreggiani, A.; Jurasekova, Z.; D'Angelantonio, M.; Tamba, M.; Garcia-Ramos, J. V.; Sanchez-Cortes, S. *Colloids and Surfaces a-Physicochemical and Engineering Aspects* **2009**, 339, 60.
- (25) Xu, H. X.; Aizpurua, J.; Kall, M.; Apell, P. *Physical Review E* **2000**, 62, 4318.
- (26) Steigerwald, M. L.; Brus, L. E. *Acc. Chem. Res.* **1990**, 23, 183.
- (27) Martin, T. P.; Naher, U.; Schaber, H.; Zimmermann, U. *The Journal of Chemical Physics* **1994**, 100, 2322.
- (28) Buffat, P.; Borel, J. P. *Phys. Rev. A* **1976**, 13, 2287.
- (29) Honeycutt, J. D.; Andersen, H. C. *The Journal of Physical Chemistry* **1987**, 91, 4950.
- (30) Solliard, C.; Flueli, M. *Surf. Sci.* **1985**, 156, 487.
- (31) Goldstein, A. N.; Echer, C. M.; Alivisatos, A. P. *Science* **1992**, 256, 1425.
- (32) Koper, O.; Li, Y. X.; Klabunde, K. J. *Chem. Mater.* **1993**, 5, 500.
- (33) Stark, J. V.; Klabunde, K. J. *Chem. Mater.* **1996**, 8, 1913.
- (34) Itoh, H.; Utamapanya, S.; Stark, J. V.; Klabunde, K. J.; Schlup, J. R. *Chem. Mater.* **1993**, 5, 71.
- (35) Zhao, J.; Peng, X.; Wang, F. *Mater. Res. Bull.* **2010**, 45, 420.
- (36) Cedeno-Mattei, Y.; Perales-Perez, O. *Microelectronics Journal* **2009**, 40, 673.
- (37) Guo, Q. B.; Rong, M. Z.; Jia, G. L.; Lau, K. T.; Zhang, M. Q. *Wear* **2009**, 266, 658.
- (38) Harrison, M. R.; Edwards, P. P. In *The Metallic and Nonmetallic State of Matter*; Rao, C. N. R., Taylor, E., Eds.; Francis Publishing: London, 1985, p 389.
- (39) Klabunde, K. J.; Stark, J.; Koper, O.; Mohs, C.; Park, D. G.; Decker, S.; Jiang, Y.; Lagadic, I.; Zhang, D. *The Journal of Physical Chemistry* **1996**, 100, 12142.

- (40) Lalena, J. N.; Cleary, D. A.; Carpenter, E. E.; Dean, N. F. *Inorganic Materials Synthesis and Fabrication*; John Wiley & Sons: New Jersey, 2008.
- (41) LaMer, V. *Ind. Eng. Chem. Res.* **1952**, *44*, 1270.
- (42) Alivisatos, A. P. *Science* **1996**, *271*, 933.
- (43) Hu, C. H.; Jiang, J. F.; Cai, Q. Y. *Supercond. Sci. Technol.* **2002**, *15*, 330.
- (44) Hua, Q.; et al. *Nanotechnology* **2010**, *21*, 215706.
- (45) Kastner, M. A. *Reviews of Modern Physics* **1992**, *64*, 849.
- (46) Dabbousi, B. O.; RodriguezViejo, J.; Mikulec, F. V.; Heine, J. R.; Mattoussi, H.; Ober, R.; Jensen, K. F.; Bawendi, M. G. *J. Phys. Chem. B* **1997**, *101*, 9463.
- (47) Freestone, I.; Meeks, N.; Sax, M.; Higgitt, C. *Gold Bulletin* **2007**, *40*, 270.
- (48) Gao, X. H.; Chan, W. C. W.; Nie, S. M. *Journal of Biomedical Optics* **2002**, *7*, 532.
- (49) Zhao, Y.; Cui, G. R.; Wang, J. J.; Fan, M. H. *Inorg. Chem.* **2009**, *48*, 10435.
- (50) Xie, W.; Su, L.; Donfack, P.; Shen, A. G.; Zhou, X. D.; Sackmann, M.; Materny, A.; Hu, J. M. *Chemical Communications* **2009**, 5263.
- (51) Ratyakshi; Chauhan, R. P. *Asian J. Chem.* **2009**, *21*, 113.
- (52) Kim, K.; Jing Jan, H.; Shin Soo, K. *Analyst* **2009**, *134*, 208.
- (53) Cho, S. J.; Idrobo, J. C.; Olamit, J.; Liu, K.; Browning, N. D.; Kauzlarich, S. M. *Chem. Mater.* **2005**, *17*, 3181.
- (54) Xu, X. H. N.; Huang, S.; Brownlow, W.; Salatia, K.; Jeffers, R. J. *J. Phys. Chem. B* **2004**, *108*, 15543.
- (55) Xu, X. H. N.; Brownlow, W. J.; Kyriacou, S. V.; Wan, Q.; Viola, J. J. *Biochemistry* **2004**, *43*, 10400.

- (56) Bai, X.; Son, S. J.; Zhang, S. X.; Liu, W.; Jordan, E. K.; Frank, J. A.; Venkatesan, T.; Lee, S. B. *Nanomedicine* **2008**, *3*, 163.
- (57) Gupta, A. K.; Gupta, M. *Biomaterials* **2005**, *26*, 3995.
- (58) Maurer, T.; Ott, F.; Chaboussant, G.; Soumire, Y.; Piquemal, J. Y.; Viau, G. *Appl. Phys. Lett.* **2007**, *91*.
- (59) Yan, J.-M.; Zhang, X.-B.; Akita, T.; Haruta, M.; Xu, Q. *J. Am. Chem. Soc.* **2010**.
- (60) Ponec, V.; Bond, G. C. *Catalysis by Metals and Alloys*; Elsevier, 1995
- 
- (61) Toshima, N.; Lu, P. *Chem. Lett.* **1996**, 729.
- (62) Sales, E. A.; Benhamida, B.; Caizergues, V.; Lagier, J. P.; Fievet, F.; Bozon-Verduraz, F. *Applied Catalysis a-General* **1998**, *172*, 273.
- (63) Lu, P.; Teranishi, T.; Asakura, K.; Miyake, M.; Toshima, N. *J. Phys. Chem. B* **1999**, *103*, 9673.
- (64) Spencer, M. S. *Catal. Lett.* **1999**, *60*, 45.
- (65) Lu, P.; Toshima, N. *Bull. Chem. Soc. Jpn.* **2000**, *73*, 751.
- (66) Boudjahem, A. G.; Monteverdi, S.; Mercy, M.; Bettahar, M. M. *J. Catal.* **2004**, *221*, 325.
- (67) Tang, X. L.; Zhang, B. C.; Li, Y.; Xu, Y. D.; Xin, Q.; Shen, W. *J. Catal. Lett.* **2004**, *97*, 163.
- (68) Zhong, C. J.; Luo, J. S.; Maye, M. M.; Kariuki, N. N. *Nanotechnology in Catalysis*; Kluwer Academic/Plenum Publishers, 2004; Vol. 1.
- (69) Hyeon, T.; Lee, S. S.; Park, J.; Chung, Y.; Na, H. B. *J. Am. Chem. Soc.* **2001**, *123*, 12798.
- (70) Sun, S.; Zeng, H.; Robinson, D. B.; Raoux, S.; Rice, P. M.; Wang, S. X.; Li, G. *J. Am. Chem. Soc.* **2003**, *126*, 273.
- (71) Sun, S.; Murray, C. B.; 8 ed.; AIP: 1999; Vol. 85, p 4325.

- (72) Hyeon, T. *Chemical Communications* **2003**, 927.
- (73) Joo, J.; Yu, T.; Kim, Y. W.; Park, H. M.; Wu, F.; Zhang, J. Z.; Hyeon, T. *J. Am. Chem. Soc.* **2003**, 125, 6553.
- (74) Park, J.; An, K. J.; Hwang, Y. S.; Park, J. G.; Noh, H. J.; Kim, J. Y.; Park, J. H.; Hwang, N. M.; Hyeon, T. *Nat. Mater.* **2004**, 3, 891.
- (75) Sun, S.; Murray, C. B.; Weller, D.; Folks, L.; Moser, A. *Science* **2000**, 287, 1989.
- (76) Glavee, G. N.; Jackelen, A. M. L.; Fox, N. M. *Abstracts of Papers of the American Chemical Society* **1999**, 218, 477.
- (77) Glavee, G. N.; Klabunde, K. J.; Sorensen, C. M.; Hadjipanayis, G. C. *Langmuir* **1992**, 8, 771.
- (78) Glavee, G. N.; Klabunde, K. J.; Sorensen, C. M.; Hadjipanayis, G. C. *Inorg. Chem.* **1993**, 32, 474.
- (79) Glavee, G. N.; Klabunde, K. J.; Sorensen, C. M.; Hadjipanayis, G. C. *Langmuir* **1994**, 10, 4726.
- (80) Glavee, G. N.; Klabunde, K. J.; Sorensen, C. M.; Hadjipanayis, G. C. *Inorg. Chem.* **1995**, 34, 28.
- (81) Glavee, G. N.; Klabunde, K. J.; Sorensen, C. M.; Hadjipanayis, G. C.; Tang, Z. X.; Yiping, L. *Nanostructured Materials* **1993**, 3, 391.
- (82) Jackelen, A. M. L.; Jungbauer, M.; Glavee, G. N. *Langmuir* **1999**, 15, 2322.
- (83) Klabunde, K. J.; Zhang, D.; Glavee, G. N.; Sorensen, C. M.; Hadjipanayis, G. C. *Chem. Mater.* **1994**, 6, 784.
- (84) Ekeirt, T. F., University of Delaware, 2010.

- (85) Lin, J.; Zhou, W.; Kumbhar, A.; Wiemann, J.; Fang, J.; Carpenter, E. E.; O'Connor, C. J. *J. Solid State Chem.* **2001**, *159*, 26.
- (86) Xu, Z.; Hou, Y.; Sun, S. *J. Am. Chem. Soc.* **2007**, *129*, 8698.
- (87) Hu, H.; Wang, Z.; Pan, L.; Zhao, S.; Zhu, S. *The Journal of Physical Chemistry C* **2010**.
- (88) Zhang, H.; Ding, J.; Chow, G.; Ran, M.; Yi, J. *Chem. Mater.* **2009**, *21*, 5222.
- (89) Andreeva, D. *Gold Bulletin* **2002**, *35*, 82.
- (90) Wan, J.; Cai, W.; Meng, X.; Liu, E. *Chemical Communications* **2007**, 5004.
- (91) V.K., P.; P.Y., Z. *Fundamentals of Powder Diffraction and Structural Characterization of Materials*; 2 ed.; Springer: New York, 2009.
- (92) Barrie, A. *Instrumentation for electron Spectroscopy*; Heyden and Sons LTD: London, 1977.
- (93) Briggs, D.; Seah, M. P. *Practical Surface Analysis by Auger and X-ray Photoelectron Spectroscopy*; Second ed.; John Wiley and Sons Ltd: Chichester, UK, 1990.
- (94) Stern, E. A. *Phys. Rev. B: Condens. Matter Mater. Phys.* **1974**, *10*, 3027.
- (95) Blazek, A. *Thermal Analysis*; Van Nostrand Reinhold Company LTD: London, 1972.
- (96) Anker, J. N.; Hall, W. P.; Lyandres, O.; Shah, N. C.; Zhao, J.; Van Duyne, R. P. *Nat. Mater.* **2008**, *7*, 442.
- (97) Cho, U.; Lee, Y.; Kumar, S.; Lee, C.; Koo, B. *Science in China Series E: Technological Sciences* **2009**, *52*, 19.
- (98) Keng, P. Y.; Shim, I.; Korth, B. D.; Douglas, J. F.; Pyun, J. *ACS Nano* **2007**, *1*, 279.
- (99) Shulika, V.; Potapov, A.; Noskova, N. *The Physics of Metals and Metallography* **2007**, *104*, 228.

- (100) Sudfeld, D.; Wojczykowski, K.; Hachmann, W.; Heitmann, S.; Rott, K.; Hempel, T.; Kammerer, S.; Jutzi, P.; Hutten, A.; Reiss, G. *Magnetics, IEEE Transactions on* **2002**, *38*, 2601.
- (101) Thomas, J. R. *J. Appl. Phys.* **1966**, *37*, 2914.
- (102) Grinstaff, M. W.; Salamon, M. B.; Suslick, K. S. *Physical Review B* **1993**, *48*, 269.
- (103) Kopcewicz, M. *Struct. Chem.* **1991**, *2*, (105)313.
- (104) Kwapulinski, P.; Stoklosa, Z.; Rasek, J.; Badura, G.; Haneczok, G.; Pajak, L.; Lelatko, L. J. *Magn. Magn. Mater.* **2008**, *320*, e778.
- (105) Zhang, L.; Manthiram, A. *J. Appl. Phys.* **1996**, *80*, 4534.
- (106) Repetsky, S. P.; Melnyk, I. M.; Tatarenko, V. A.; Len, E. G.; Vyshivanaya, I. G. *J. Alloys Compd.* **2009**, *480*, 13.
- (107) Moulas, G.; Lehnert, A.; Rusponi, S.; Zabloudil, J.; Etz, C.; Ouazi, S.; Etzkorn, M.; Bencok, P.; Gambardella, P.; Weinberger, P.; Brune, H. *Physical Review B (Condensed Matter and Materials Physics)* **2008**, *78*, 214424.
- (108) Chaubey, G. S.; Barcena, C.; Poudyal, N.; Rong, C.; Gao, J.; Sun, S.; Liu, J. P. *J. Am. Chem. Soc.* **2007**, *129*, 7214.
- (109) Kuhrt, C.; Schultz, L. *J. Appl. Phys.* **1992**, *71*, 1896.
- (110) Shin, S. J.; Kim, Y. H.; Kim, C. W.; Cha, H. G.; Kim, Y. J.; Kang, Y. S. *Current Applied Physics* **2007**, *7*, 404.
- (111) Glavee, G. N.; Klabunde, K. J.; Sorensen, C. M.; Hadjipanayis, G. C. *Langmuir* **1993**, *9*, 162.
- (112) Li, X.-q.; Zhang, W.-x. *The Journal of Physical Chemistry C* **2007**, *111*, 6939.

- (113) Mandale, A. B.; Badrinarayanan, S.; Date, S. K.; Sinha, A. P. B. *J. Electron Spectrosc. Relat. Phenom.* **1984**, *33*, 61.
- (114) Chuang, T. J.; Brundle, C. R.; Rice, D. W. *Surf. Sci.* **1976**, *59*, 413.
- (115) Park, H.-Y.; Schadt, M. J.; Wang; Lim, I. I. S.; Njoki, P. N.; Kim, S. H.; Jang, M.-Y.; Luo, J.; Zhong, C.-J. *Langmuir* **2007**, *23*, 9050.
- (116) Lee, I. S.; Lee, N.; Park, J.; Kim, B. H.; Yi, Y.-W.; Kim, T.; Kim, T. K.; Lee, I. H.; Paik, S. R.; Hyeon, T. *J. Am. Chem. Soc.* **2006**, *128*, 10658.
- (117) Radwan, F. R.; Carroll, K. J.; Carpenter, E. E. *J. Appl. Phys.* **2009**, *in press*.
- (118) Kim, J.-H.; Kim, J.-S.; Choi, H.; Lee, S.-M.; Jun, B.-H.; Yu, K.-N.; Kuk, E.; Kim, Y.-K.; Jeong, D. H.; Cho, M.-H.; Lee, Y.-S. *Anal. Chem.* **2006**, *78*, 6967.
- (119) Bala, T.; Bhame, S. D.; Joy, P. A.; Prasad, B. L. V.; Sastry, M. *J. Mater. Chem.* **2004**, *14*, 2941.
- (120) Kinoshita, T.; Seino, S.; Mizukoshi, Y.; Otome, Y.; Nakagawa, T.; Okitsu, K.; Yamamoto, T. *A. J. Magn. Magn. Mater.* **2005**, *293*, 106.
- (121) Zhang, J.; Post, M.; Veres, T.; Jakubek, Z. J.; Guan, J.; Wang, D.; Normandin, F.; Deslandes, Y.; Simard, B. *J. Phys. Chem. B* **2006**, *110*, 7122.
- (122) Mandal, M.; Kundu, S.; Ghosh, S. K.; Panigrahi, S.; Sau, T. K.; Yusuf, S. M.; Pal, T. *J. Colloid Interface Sci.* **2005**, *286*, 187.
- (123) Stoeva, S. I.; Huo, F.; Lee, J.-S.; Mirkin, C. A. *J. Am. Chem. Soc.* **2005**, *127*, 15362.
- (124) Wang, L.; Luo, J.; Fan, Q.; Suzuki, M.; Suzuki, I. S.; Engelhard, M. H.; Lin, Y.; Kim, N.; Wang, J. Q.; Zhong, C.-J. *J. Phys. Chem. B* **2005**, *109*, 21593.
- (125) Cho, S. J.; Jarrett, B. R.; Louie, A. Y.; Kauzlarich, S. M. *Nanotechnology* **2006**, *17*, 640.

- (126) Cho, S. J.; Kauzlarich, S. M.; Olamit, J.; Liu, K.; Grandjean, F.; Rebbouh, L.; Long, G. J. *J. Appl. Phys.* **2004**, *95*, 6804.
- (127) Cho, S. J.; Shahin, A. M.; Long, G. J.; Davies, J. E.; Liu, K.; Grandjean, F.; Kauzlarich, S. M. *Chem. Mater.* **2006**, *18*, 960.
- (128) Lin, J.; Zhou, W. L.; Kumbhar, A.; Wiemann, J.; Fang, J. Y.; Carpenter, E. E.; O'Connor, C. J. *J. Solid State Chem.* **2001**, *159*, 26.
- (129) Srikanth, H.; Carpenter, E. E.; Spinu, L.; Wiggins, J.; Zhou, W. L.; O'Connor, C. J. *Mater. Sci. Eng., A* **2001**, *304*, 901.
- (130) Wiggins, J.; Carpenter, E. E.; O'Connor, C. J. *J. Appl. Phys.* **2000**, *87*, 5651.
- (131) Zhou, W. L.; Carpenter, E. E.; Lin, J.; Kumbhar, A.; Sims, J.; O'Connor, C. J. *Eur. Phys. J. D* **2001**, *16*, 289.
- (132) Gole, A.; Stone, J. W.; Gemmill, W. R.; zur Loye, H.-C.; Murphy, C. J. *Langmuir* **2008**, *24*, 6232.
- (133) Lee, K. J.; Nallathamby, P. D.; Browning, L. M.; Osgood, C. J.; Xu, X.-H. N. *ACS Nano* **2007**, *1*, 133.
- (134) Levin, C. S.; Hofmann, C.; Ali, T. A.; Kelly, A. T.; Morosan, E.; Nordlander, P.; Whitmire, K. H.; Halas, N. J. *ACS Nano* **2009**, *3*, 1379.
- (135) Carroll, K. J.; Pitts, J. A.; Zhang, K.; Pradhan, A. K.; Carpenter, E. E. *J. Appl. Phys.* **2010**, *107*, *in press*.
- (136) Carroll, K. J.; Hudgins, D. M.; Brown, L. W.; Yoon, S. D.; Heiman, D.; Harris, V. G.; Carpenter, E. E. *J. Appl. Phys.* **2010**, *107*, *in press*.
- (137) Qadri, S. B.; Dinderman, M. A.; Dressick, W. J.; Schoen, P. E.; Lubitz, P.; He, J. H.; Tonucci, R. J.; Cross, J. *Appl. Phys. A: Mater. Sci. Process.* **2007**, *89*, 493.

- (138) Kapfenberger, C.; Albert, B.; Pottgen, R.; Huppertz, H. *Zeitschrift Fur Kristallographie* **2006**, *221*, 477.
- (139) Nurmi, J. T.; Tratnyek, P. G.; Sarathy, V.; Baer, D. R.; Amonette, J. E.; Pecher, K.; Wang, C. M.; Linehan, J. C.; Matson, D. W.; Penn, R. L.; Driessen, M. D. *Environ. Sci. Technol.* **2005**, *39*, 1221.
- (140) Joyner, D. J.; Johnson, O.; Hercules, D. M. *J. Am. Chem. Soc.* **1980**, *102*, 1910.
- (141) Grosvenor, A. P.; Kobe, B. A.; Biesinger, M. C.; McIntyre, N. S. *Surf. Interface Anal.* **2004**, *36*, 1564.
- (142) Johnson, O.; Joyner, D. J.; Hercules, D. M. *J. Phys. Chem.* **1980**, *84*, 542.
- (143) Joyner, D. J.; Hercules, D. M. *J. Chem. Phys.* **1980**, *72*, 1095.
- (144) Joyner, D. J.; Johnson, O.; Hercules, D. M. *J. Am. Chem. Soc.* **1980**, *102*, 1910.
- (145) Joyner, D. J.; Johnson, O.; Hercules, D. M. *Journal of Physics F-Metal Physics* **1980**, *10*, 169.
- (146) Joyner, D. J.; Johnson, O.; Hercules, D. M.; Bullett, D. W.; Weaver, J. H. *Physical Review B* **1981**, *24*, 3122.
- (147) Joyner, D. J.; Willis, R. F. *Philosophical Magazine a-Physics of Condensed Matter Structure Defects and Mechanical Properties* **1981**, *43*, 815.
- (148) Medina-Ramirez, I.; Bashir, S.; Luo, Z. P.; Liu, J. L. *Colloids and Surfaces B-Biointerfaces* **2009**, *73*, 185.
- (149) Prema, P.; Raju, R. *Biotechnol. Bioprocess Eng.* **2009**, *14*, 842.
- (150) Alvarez-Puebla, R. A.; Aroca, R. F. *Anal. Chem.* **2009**, *81*, 2280.
- (151) Blanco, M. C.; Meira, A.; Baldomir, D.; Rivas, J.; Lopezquintela, M. A. *IEEE Trans. Magn.* **1994**, *30*, 739.

- (152) Dong, X. Y.; Ji, X. H.; Wu, H. L.; Zhao, L. L.; Li, J.; Yang, W. S. *J. Phys. Chem. C* **2009**, *113*, 6573.
- (153) Wiley, B.; Sun, Y.; Xia, Y. *Acc. Chem. Res.* **2007**, *40*, 1067.
- (154) Machulek Junior, A.; de Oliveira, H. P.; Gehlen, M. H. *Photochem. Photobiol. Sci.* **2003**, *2*, 921.
- (155) Van Hyning, D. L.; Zukoski, C. F. *Langmuir* **1998**, *14*, 7034.
- (156) Calvin, S.; Carpenter, E. E.; Harris, V. G. *Phys. Rev. B: Condens. Matter Mater. Phys.* **2003**, *68*, 033411/1.
- (157) Carpenter, E. E.; Calvin, S.; Stroud, R. M.; Harris, V. G. *Chem. Mater.* **2003**, *15*, 3245.
- (158) Carroll, K. J.; Pitts, J. A.; Zhang, K.; Pradhan, A. K.; Carpenter, E. E. *J. Appl. Phys.* **2010**, accepted.
- (159) McDowall, N. B.; Wilkins, J. R.; Carroll, K. J.; Edwards, J. D.; Nelson, J. D.; Carpenter, E. E.; Glaspell, G. P. *J. Appl. Phys.* **2010**, *107*, In press.
- (160) Kneipp, K.; Kneipp, H.; Itzkan, I.; Dasari, R. R.; Feld, M. S. *Chem. Phys.* **1999**, *247*, 155.
- (161) Emory, S. R.; Nie, S. M. *Anal. Chem.* **1997**, *69*, 2631.
- (162) Nie, S.; Emory, S. R. *Science* **1997**, *275*, 1102.
- (163) Hulteen, J. C.; Treichel, D. A.; Smith, M. T.; Duval, M. L.; Jensen, T. R.; Van Duyne, R. P. *J. Phys. Chem. B* **1999**, *103*, 3854.
- (164) Jensen, T. R.; Duval, M. L.; Kelly, K. L.; Lazarides, A. A.; Schatz, G. C.; Van Duyne, R. P. *J. Phys. Chem. B* **1999**, *103*, 9846.
- (165) Malinsky, M. D.; Kelly, K. L.; Schatz, G. C.; Van Duyne, R. P. *J. Phys. Chem. B* **2001**, *105*, 2343.

- (166) Ammar, S.; Helfen, A.; Jouini, N.; Fievet, F.; Rosenman, I.; Villain, F.; Molinie, P.; Danot, M. *J. Mater. Chem.* **2001**, *11*, 186.
- (167) Ammar, S.; Hlfen, A.; Jouini, N.; Fievet, F.; Rosenman, I.; Villian, F.; Molinie, P.; Danot, M. *Journal of Material Chemistry* **2001**, *11*, 186.
- (168) Ammar, S.; Jouini, N.; Fievet, F.; Beji, Z.; Smiri, L.; Moline, P.; Danot, M.; Greneche, J. M. *Journal of Physics-Condensed Matter* **2006**, *18*, 9055.
- (169) Ammar, S.; Jouini, N.; Fievet, F.; Stephan, O.; Marhic, C.; Richard, M.; Villain, F.; Moulin, C. C. D.; Brice, S.; Sainctavit, P. *Journal of Non-Crystalline Solids* **2004**, *345-46*, 658.
- (170) Beji, Z.; Ben Chaabane, T.; Smiri, L. S.; Ammar, S.; Fievet, F.; Jouini, N.; Greneche, J. M. *Physica Status Solidi a-Applications and Materials Science* **2006**, *203*, 504.
- (171) Blin, B.; Fievet, F.; Beaupere, D.; Figlarz, M. *New Journal of Chemistry* **1989**, *13*, 67.
- (172) Blin, B.; Fievet, F.; Lagier, J. P.; Beaudoin, B.; Figlarz, M. *Journal De Chimie Physique Et De Physico-Chimie Biologique* **1987**, *84*, R15.
- (173) Brayner, R.; Coradin, T.; Fievet-Vincent, F.; Livage, J.; Fievet, F. *New Journal of Chemistry* **2005**, *29*, 681.
- (174) Brayner, R.; Coradin, T.; Vaulay, M. J.; Mangeney, C.; Livage, J.; Fievet, F. *Colloids and Surfaces a-Physicochemical and Engineering Aspects* **2005**, *256*, 191.
- (175) Chakroune, N.; Viau, G.; Ammar, S.; Jouini, N.; Gredin, P.; Vaulay, M. J.; Fievet, F. *New Journal of Chemistry* **2005**, *29*, 355.
- (176) Chakroune, N.; Viau, G.; Ammar, S.; Jouini, N.; Gredin, P.; Voulay, M. J.; Fievet, F. *New J. Chem* **2005**, *29*.
- (177) Chakroune, N.; Viau, G.; Ammar, S.; Poul, L.; Veautier, D.; Chehimi, M. M.; Mangeney, C.; Villain, F.; Fievet, F. *Langmuir* **2005**, *21*, 6788.

- (178) Chakroune, N.; Viau, G.; Ricolleau, C.; Fievet-Vincent, F.; Fievet, F. *Journal of Materials Chemistry* **2003**, *13*, 312.
- (179) Deschamps, A.; Lagier, J. P.; Fievet, F.; Aeiyach, S.; Lacaze, P. C. *Journal of Materials Chemistry* **1992**, *2*, 1213.
- (180) Fievet, F. *Surfactant Science Series* **2000**, *92*, 460.
- (181) Fievet, F.; Fievet, F. V.; Lagier, J. P.; Dumont, B.; Figlarz, M. *J. Mater. Chem.* **1993**, *3*, 627.
- (182) Fievet, F.; Fievet vincent, F.; Lagier, J. P.; Beaudoin, B.; Figlarz, M. *Journal De Physique IV* **1992**, *2*, 91.
- (183) Fievet, F.; Lagier, J. P.; Beaudoin, B.; Figlarz, M. *Solid State Ionics* **1988**, *26*, 154.
- (184) Fievet, F.; Lagier, J. P.; Blin, B. *Solid State Ionics* **1989**, *32/33*, 198.
- (185) Fievet, F.; Lagier, J. P.; Blin, B.; Beaudoin, B.; Figlarz, M. *Solid State Ionics* **1989**, *32-3*, 198.
- (186) Jezequel, D.; Guenot, J.; Jouini, N.; Fievet, F. *Journal of Materials Research* **1995**, *10*, 77.
- (187) Jouini, N.; Poul, L.; Fievet, F.; Robert, F. *European Journal of Solid State and Inorganic Chemistry* **1995**, *32*, 1129.
- (188) Matrab, T.; Yassar, A.; Viau, G.; Chakroune, N.; Fievet, F.; Lacaze, P. C. *Journal of Colloid and Interface Science* **2006**, *296*, 95.
- (189) Matrab, T.; Yassar, A.; Viau, G.; Chakroune, N.; Fievet, F.; Lacaze, P. C. *Materials Letters* **2006**, *60*, 698.
- (190) Mercier, D.; Levy, J. C. S.; Viau, G.; Fievet-Vincent, F.; Fievet, F.; Toneguzzo, P.; Acher, O. *Physical Review B* **2000**, *62*, 532.
- (191) Piquemal, J. Y.; Viau, G.; Beaunier, P.; Bozon-Verduraz, F.; Fievet, F. *Materials Research Bulletin* **2003**, *38*, 389.

- (192) Poul, L.; Ammar, S.; Jouini, N.; Fievet, F.; Villain, F. *Solid State Sciences* **2001**, *3*, 31.
- (193) Poul, L.; Ammar, S.; Jouini, N.; Fievet, F.; Villain, F. *Journal of Sol-Gel Science and Technology* **2003**, *26*, 261.
- (194) Poul, L.; Jouini, N.; Fievet **1998**, *213*, 416.
- (195) Poul, L.; Jouini, N.; Fievet, F. *Chem. Mater.* **2000**, *12*, 3123.
- (196) Poul, L.; Jouini, N.; Fievet, F. *Chemistry of Materials* **2000**, *12*, 3123.
- (197) Poul, L.; Jouini, N.; Fievet, F.; Herson, P. *Zeitschrift Fur Kristallographie* **1998**, *213*, 416.
- (198) Taibi, M.; Ammar, S.; Jouini, N.; Fievet, F. *Journal of Physics and Chemistry of Solids* **2006**, *67*, 932.
- (199) Toneguzzo, P.; Acher, O.; Viau, G.; Fievet-Vincent, F.; Fievet, F. *Journal of Applied Physics* **1997**, *81*, 5546.
- (200) Toneguzzo, P.; Acher, O.; Viau, G.; Pierrard, A.; Fievet-Vincent, F.; Fievet, F.; Rosenman, I. *Ieee Transactions on Magnetics* **1999**, *35*, 3469.
- (201) Toneguzzo, P.; Viau, G.; Acher, O.; Fievet-Vincent, F.; Fievet, F. *Advanced Materials* **1998**, *10*, 1032.
- (202) Ung, D.; Soumara, Y.; Chakroune, N.; Viau, G.; Vaulay, M. J.; Richard, V.; Fievet, F. *Chem. Mater.* **2007**, *19*, 2084.
- (203) Ung, D.; Soumara, Y.; Chakroune, N.; Viau, G.; Vaulay, M. J.; Richard, V.; Fievet, F. *Chemistry of Materials* **2007**, *19*, 2084.
- (204) Ung, D.; Viau, G.; Fievet-Vincent, F.; Herbst, F.; Richard, V.; Fievet, F. *Progress in Solid State Chemistry* **2005**, *33*, 137.
- (205) Viau, G.; Brayner, R.; Poul, L.; Chakroune, N.; Lacaze, E.; Fievet-Vincent, F.; Fievet, F. *Chemistry of Materials* **2003**, *15*, 486.

- (206) Viau, G.; FievetVincent, F.; Fievet, F. *Solid State Ionics* **1996**, *84*, 259.
- (207) Viau, G.; FievetVincent, F.; Fievet, F. *Journal of Materials Chemistry* **1996**, *6*, 1047.
- (208) Viau, G.; FievetVincent, F.; Fievet, F.; Toneguzzo, P.; Ravel, F.; Acher, O. *Journal of Applied Physics* **1997**, *81*, 2749.
- (209) Viau, G.; Piquemal, J. Y.; Esparrica, M.; Ung, D.; Chakroune, N.; Warmont, F.; Fievet, F. *Chemical Communications* **2003**, 2216.
- (210) Viau, G.; Ravel, F.; Acher, O.; Fievetvincent, F.; Fievet, F. *Journal of Magnetism and Magnetic Materials* **1995**, *140*, 377.
- (211) Viau, G.; Toneguzzo, P.; Pierrard, A.; Acher, O.; Fievet-Vincent, F.; Fievet, F. *Scripta Materialia* **2001**, *44*, 2263.
- (212) Anzlovar, A.; Orel, Z. C.; Zigon, M. *J. Nanosci. Nanotechnol.* **2008**, *8*, 3516.
- (213) Hou, Y.; Kondoh, H.; Ohta, T.; Gao, S. *Appl. Surf. Sci.* **2005**, *241*, 218.
- (214) Bonet, F.; Guery, C.; Guyomard, D.; Urbina, R. H.; Tekaia-Elhsissen, K.; Tarascon, J. M. *International Journal of Inorganic Materials* **1999**, *1*, 47.
- (215) Bonet, F.; Guery, C.; Guyomard, D.; Urbina, R. H.; Tekaia-Elhsissen, K.; Tarascon, J. M. *Solid State Ionics* **1999**, *126*, 337.
- (216) Harpeness, R.; Gedanken, A. *J. Mater. Chem.* **2005**, *15*, 698.
- (217) Johnson, R. *CrystEngComm* **2007**, *9*, T82.
- (218) Ammar, S.; Jouini, N.; Fievet, F.; Beji, Z.; Smiri, L.; Moline, P.; Danot, M.; Greneche, J.-M. *J. Phys.: Condens. Matter* **FIELD Full Journal Title:Journal of Physics: Condensed Matter** **2006**, *18*, 9055.
- (219) Carroll, K. J.; Calvin, S.; Ekiert, T. F.; Unruh, K. M.; Carpenter, E. E. *Chem. Mater.* **2010**.

- (220) Harris, V. G.; Chen, Y.; Yang, A.; Yoon, S.; Chen, Z.; Geiler, A.; Chinnasamy, C. N.; Lewis, L. H.; Vittoria, C.; Carpenter, E. E.; Carroll, K. J.; Goswami, R.; Willard, M. A.; Kurihara, L.; Gjoka, M.; Kalogirou, O. 2009.
- (221) Sun, K.; Fan, B. H.; Ouyang, J. Y. *J. Phys. Chem. C* **2010**, *114*, 4237.
- (222) Skupien, K.; Putyra, P.; Walter, J.; Kozlowski, R. H.; Khelashvili, G.; Hinsch, A.; Wurfel, U. *Progress in Photovoltaics* **2009**, *17*, 67.
- (223) Khelashvili, G.; Behrens, S.; Weidenthaler, C.; Vetter, C.; Hinsch, A.; Kern, R.; Skupien, K.; Dinjus, E.; Bonnemann, H. 2006, p 342.
- (224) Carroll, K. J.; Shultz, M. D.; Fatouros, P. P.; Carpenter, E. E. *J. Appl. Phys.* **2010**, *107*.
- (225) Larcher, D.; Patrice, R. *J. Solid State Chem.* **2000**, *154*, 405.
- (226) Fievet, F.; Lagier, J. P.; Blin, B.; Beaudoin, B.; Figlarz, M. *Solid State Ionics*, *32-33*, 198.
- (227) Silvert, P. Y.; Tekaiaelhsissen, K. *Solid State Ionics* **1995**, *82*.
- (228) Herricks, T.; Chen, J. Y.; Xia, T. N. *Nano Lett.* **2004**, *4*.
- (229) Sra, A. K.; Ewers, T. D.; Schaak, R. E. *Chem. Mater.* **2005**, *17*.
- (230) Perdew, J. P.; Burke, K.; Wang, Y. *Physical Review B* **1996**, *54*, 16533.
- (231) Koster, A. M.; Calaminici, P.; Casida, M. E.; Flores-Moreno, R.; Geudtner, G.; Goursot, A.; Heine, T.; Ipatov, A.; Janetzko, F.; Del Campo, J. M.; Patchkovskii, S.; Reveles, J. U.; Salahub, D. R.; Vela, A.; Developers, T. d., Ed. Cinvestav, Mexico, 2010.
- (232) Mintmire, J. W.; Dunlap, B. I. *Phys. Rev. A* **1982**, *25*, 88.
- (233) Koster, A. M.; Reveles, J. U.; del Campo, J. M. *J. Chem. Phys.* **2004**, *121*, 3417.
- (234) Calaminici, P.; Janetzko, F.; Koster, A. M.; Mejia-Olvera, R.; Zuniga-Gutierrez, B. *J. Chem. Phys.* **2007**, *126*.

- (235) Godbout, N.; Salahub, D. R.; Andzelm, J.; Wimmer, E. *Canadian Journal of Chemistry-Revue Canadienne De Chimie* **1992**, *70*, 560.
- (236) Reveles, J. U.; Koster, A. M. *J. Comput. Chem.* **2004**, *25*, 1109.
- (237) Bonet, F.; Grugeon, S.; Dupont, L.; Urbina, R. H.; Guery, C.; Tarascon, J. M. *J. Solid State Chem.* **2003**, *172*, 111.
- (238) Park, B. K.; Jeong, S.; Kim, D.; Moon, J.; Lim, S.; Kim, J. S. *J. Colloid Interface Sci.* **2007**, *311*, 417.
- (239) Sun, J.; Jing, Y.; Jia, Y.; Tillard, M.; Belin, C. *Mater. Lett.* **2005**, *59*, 3933.
- (240) Rivers, J. H.; Carroll, K. J.; Jones, R. A.; Carpenter, E. E. *Acta Crystallographica Section C* **2010**, *66*, m83.
- (241) Ying, Z.; Shengming, J.; Guanzhou, Q.; Min, Y. *Materials Science and Engineering: B* **2005**, *122*, 222.
- (242) Hinotsu, T.; Jeyadevan, B.; Chinnasamy, C. N.; Shinoda, K.; Tohji, K.; 11 ed.; AIP: 2004; Vol. 95, p 7477.
- (243) Tzitzios, V.; Basina, G.; Gjoka, M.; Alexandrakis, V.; Georgakilas, V.; Niarchos, D.; Boukos, N.; Petridis, D. *Nanotechnology* **2006**, *17*, 3750.
- (244) Gong, J.; Liu, Y.; Wang, L. L.; Yang, H.; Zong, Z. G. *Chem. J. Chin. Univ.-Chin.* **2007**, *28*, 1232.
- (245) Poul, L.; Jouini, N.; Fievet, F. *Chem. Mater.* **2000**, *12*, 3123.
- (246) Ung, D.; Soumare, Y.; Chakroune, N.; Viau, G.; Vaulay, M. J.; Richard, V.; Fievet, F. *Chem. Mater.* **2007**, *19*, 2084.
- (247) Lond, P. B.; Salmon, P. S.; Champeney, D. C. *J. Am. Chem. Soc.* **1991**, *113*, 6420.

- (248) Fievet, F.; Fievetvincent, F.; Lagier, J. P.; Dumont, B.; Figlarz, M. *J. Mater. Chem.* **1993**, *3*, 627.
- (249) Sun, Y. G.; Mayers, B.; Herricks, T.; Xia, Y. N. *Nano Lett.* **2003**, *3*, 955.
- (250) Bonet, F.; Tekaia-Elhsissen, K.; Sarathy, K. V. *Bull. Mater. Sci.* **2000**, *23*, 165.
- (251) Pasquarello, A.; Petri, I.; Salmon, P. S.; Parisel, O.; Car, R.; Toth, E.; Powell, D. H.; Fischer, H. E.; Helm, L.; Merbach, A. E. *Science* **2001**, *291*, 856.
- (252) Salmon, P. S.; Lond, P. B. *J. Phys.: Condens. Matter* **1992**, *4*, 5249.
- (253) Pico, A. R.; Houk, C. S.; Weakley, T. J. R.; Page, C. J. *Inorg. Chim. Acta* **1997**, *258*, 155.
- (254) Habermann, N.; Jung, G.; Klaassen, M.; Klufers, P. *Chemische Berichte-Recueil* **1992**, *125*, 809.
- (255) Love, C. P.; Torardi, C. C.; Page, C. J. *Inorg. Chem.* **1992**, *31*, 1784.
- (256) Allen, F. H. *Acta Crystallographica Section B-Structural Science* **2002**, *58*, 380.
- (257) Yao, J. W.; Cole, J. C.; Pidcock, E.; Allen, F. H.; Howard, J. A. K.; Motherwell, W. D. S. *Acta Crystallographica Section B-Structural Science* **2002**, *58*, 640.
- (258) Schubert, U.; Mereiter, K.; Elhofer, I. *Monatshefte Fur Chemie* **2000**, *131*, 931.
- (259) Cozzoli, P. D.; Pellegrino, T.; Manna, L. *Chem. Soc. Rev.* **2006**, *35*, 1195.
- (260) Salgueiriño-Macereira, V.; Correa-Duarte, M. A. *Advanced Materials* **2007**, *19*, 4131.
- (261) Sastry, M.; Swami, A.; Mandal, S.; Selvakannan, P. R. *J. Mater. Chem.* **2005**, *15*, 3161.
- (262) Willard, M. A.; Kurihara, L. K.; Carpenter, E. E.; Calvin, S.; Harris, V. G. *Int. Mater. Rev.* **2004**, *49*, 125.
- (263) Chatterjee, J.; Bettege, M.; Haik, Y.; Jen Chen, C. *J. Magn. Magn. Mater.* **2005**, *293*, 303.

- (264) Kuznetsov, A. A.; Leontiev, V. G.; Brukvin, V. A.; Vorozhtsov, G. N.; Kogan, B. Y.; Shlyakhtin, O. A.; Yunin, A. M.; Tsybin, O. I.; Kuznetsov, O. A. *J. Magn. Magn. Mater.* **2007**, *311*, 197.
- (265) Li, P.; Liu, J.; Nag, N.; Crozier, P. A. *J. Catal.* **2009**, *262*, 73.
- (266) Bonet, F.; Grugeon, S.; Tarascon, J. M. *J. Solid State Chem.* **2003**, *172*, 111.
- (267) Chinnasamy, C. N.; Jeyadevan, B.; Shinoda, K.; Tohji, K.; Narayanasamy, A.; Sato, K.; Hisano, S. In *49th Ann. Con. MMM*; 10 ed.; AIP: Jacksonville, Florida (USA), 2005; Vol. 97, p 10J309.
- (268) Park, B. K.; Jeong, S.; D.Kim; Moon, J.; Lim, S.; Kim, J. S. *J. Colloid Interface Sci.* **2007**, *311*, 417.
- (269) Shengming, J.; Liangsheng, Y.; Ying, Z.; Guanzhou, Q.; Cuifeng, W. *Mater. Res. Bull.* **2006**, *41*, 2130.
- (270) Zhang, X.; Yin, H.; Cheng, X.; Jiang, Z.; Zhao, X.; Wang, A. *Appl. Surf. Sci.* **2006**, *252*, 8067.
- (271) *Pearson's Handbook of Crystallographic Data for Intermetallic Phases*; American Society for Metals, Metals Park, 1989.
- (272) Jiao, J.; Seraphin, S.; Wang, X.; Withers, J. C. *J. Appl. Phys.* **1996**, *80*, 103.
- (273) Jeon, Y. T.; Moon, J. Y.; Lee, G. H.; Park, J.; Chang, Y. *J. Phys. Chem. B* **2005**, *110*, 1187.
- (274) Bhatt, R. K. *Indian J Eng Mater S* **1998**, *5*, 477.
- (275) Odenbach, S. *Ferrofluids*; Springer- Verlag: Bremen, Germany, 2002.
- (276) Odenbach, S. *Magnetoviscous Effects in Ferrofluids*; Springer-Verlag, 2002.
- (277) Shultz, M. D.; Calvin, S.; Fatouros, P. P.; Morrison, S. A.; Carpenter, E. E. *J. Magn. Magn. Mater.* **2007**, *311*, 464.
- (278) Badescu, V.; Badescu, R. *J Optoelectron Adv M* **2007**, *9*, 949.

- (279) Bozhko, A. A.; Putin, G. F.; Tynjaelae, T.; Sarkomaa, P. *J. Magn. Magn. Mater.* **2007**, *316*, 433.
- (280) Döbrich, F.; Michels, A.; Birringer, R. *J. Magn. Magn. Mater.* **2007**, *316*, e779.
- (281) Embs, J. P.; Wagner, C.; Knorr, K.; Lucke, M. *EPL (Europhysics Letters)* **2007**, *78*, 44003.
- (282) Ivanov, A. O.; Kantorovich, S. S.; Reznikov, E. N.; Holm, C.; Pshenichnikov, A. F.; Lebedev, A. V.; Chremos, A.; Camp, P. *J. Phys. Rev. E: Stat., Nonlinear, Soft Matter Phys.* **2007**, *75*, 061405/1.
- (283) Kuncser, V.; Schintele, G.; Sahoo, B.; Keune, W.; Bica, D.; Vekas, L.; Filoti, G. *J. Phys.: Condens. Matter* **2007**, *19*, 016205/1.
- (284) Larachi, F.; Desvigne, D. *Particuology* **2007**, *5*, 50.
- (285) Lee, C.-F.; Chou, Y.-H.; Chiu, W.-Y. *J. Polym. Sci., Part A: Polym. Chem.* **2007**, *45*, 3062.
- (286) Racuciu, M.; Creanga, D. E.; Apetroaie, N.; Badescu, V. *Journal of Optoelectronic and Advanced Materials* **2007**, *9*, 1633.
- (287) Salgueirino-Maceira, V.; Liz-Marzan, L. M.; Farle, M. *Langmuir* **2004**, *20*, 6946.
- (288) Schnorr, J. D. V. M.; Wagner, S. D. V. M.; Abramjuk, C. D. V. M.; Wojner, I. D. V. M.; Schink, T. P.; Kroencke, T. J. M. D.; Schellenberger, E. M. D.; Hamm, B. M. D.; Pilgrimm, H. P.; Taupitz, M. M. D. *Invest Radiol* **2004**, *39*, 546.
- (289) Carlin, R. L. *Magnetochemistry*; Springer-Verlag, 1985.
- (290) Papell, S. U.S.Patent, 1965; Vol. 3, p 572.
- (291) Massart, R.; Dubois, E.; Cabuil, V.; Hasmonay, E. *J. Magn. Magn. Mater.* **1995**, *149*, 1.
- (292) *Structure and Reactivity in Reverse Micelles*; Pilani, M., Ed.; Elsevier: Amsterdam, 1989.
- (293) Pilani, M.; Zemb, T.; Petit, C. *Chem. Phys. Lett.* **1985**, *118*, 414.
- (294) Harada, S.; Ugaji, M. *IEE Trans. Mag.* **1972**, *mag-8*, 468.

- (295) Akashi, G. U.S. Patent, 1969; Vol. 3, p 218.
- (296) Shultz, M. D.; Braxton, W.; Taylor, C.; Carpenter, E. *E. J. Appl. Phys.* **2009**, *105*.
- (297) Briley-Saebo, K. C.; Mani, V.; Hyafil, F.; Cornily, J. C.; Fayad, Z. A. *Magn Reson Med* **2008**, *59*, 721.
- (298) Broaddus, W. C.; Prabhu, S. S.; Gillies, G. T.; Neal, J.; Conrad, W. S.; Chen, Z. J.; Fillmore, H.; Young, H. *F. J Neurosurg* **1998**, *88*, 734.
- (299) Chen, Z. J.; Gillies, G. T.; Broaddus, W. C.; Prabhu, S. S.; Fillmore, H.; Mitchell, R. M.; Corwin, F. D.; Fatouros, P. P. *J Neurosurg* **2004**, *101*, 314.
- (300) Prabhu, S. S.; Broaddus, W. C.; Gillies, G. T.; Loudon, W. G.; Chen, Z. J.; Smith, B. *Surg Neurol* **1998**, *50*, 367.
- (301) Chan, W. C.; Nie, S. *Science* **1998**, *281*, 2016.
- (302) Wang, L.; Li, Y. *Chem. Mater.* **2007**, *19*, 727.
- (303) Singh, L. R.; Ningthoujam, R. S. *J. Appl. Phys.* **2010**, *107*, 104304.
- (304) Gao, J.; Zhang, W.; Huang, P.; Zhang, B.; Zhang, X.; Xu, B. *J. Am. Chem. Soc.* **2008**, *130*, 3710.
- (305) Liu, L.; Li, B.; Qin, R.; Zhao, H.; Ren, X.; Su, Z. *Solid State Sci.* **2010**, *12*, 345.
- (306) Rolf, K.; Willem, J. M. M.; Matti, M. v. S.; Gustav, J. S.; Andries, M.; Klaas, N. *Wiley Interdisciplinary Reviews: Nanomedicine and Nanobiotechnology* **2009**, *1*, 475.
- (307) Al Terary, S.; Mangeney, C.; Brayner, R.; Antoun, T.; Fievet, F.; Yassar, A. 2008, p 511.
- (308) Qian, H. F.; Li, L.; Ren, J. C. *Mater. Res. Bull.* **2005**, *40*, 1726.
- (309) Balakrishnan, S.; Launikonis, A.; Osvath, P.; Swiegers, G. F.; Douvalis, A. P.; Wilson, G. J. *Mater. Chem. Phys.* **2010**, *120*, 649.

- (310) He, F.; Yang, P. P.; Niu, N.; Wang, W. X.; Gai, S. L.; Wang, D.; Lin, J. *J. Colloid Interface Sci.* **2010**, *343*, 71.
- (311) Wang, L.; Yang, Z.; Zhang, Y.; Wang, L. *The Journal of Physical Chemistry C* **2009**, *113*, 3955.
- (312) Huignard, A.; Buissette, V.; Franville, A.-C.; Gacoin, T.; Boilot, J.-P. *The Journal of Physical Chemistry B* **2003**, *107*, 6754.
- (313) Huh, S. H.; Nakajima, A. *J. Appl. Phys.* **2006**, *99*, 064302.

**Vita**

**Kyler James Carroll**

7584 Charmant Dr Apt #2121

San Diego, Ca 92122

(517) 749-3528

carrollkj@vcu.edu, Kyler.Carroll@gmail.com

**Personal Data:**

Date and Place of Birth: 7 January 1984; Grand Rapids, Mi

**Academic Training:****Undergraduate:** B.S. in chemistry, Aquinas College, Grand Rapids, Mi, 2007**Graduate:** Ph.D. in chemistry, Virginia Commonwealth University, May 2007-July 2010**Professional Experiences:**

<b>2009-Present</b>	PhD Research Fellowship, Virginia Commonwealth University, Altria(Formerly Philip Morris USA) PhD Candidate Fellowship Award.
<b>2008-2009</b>	Student Research Assistant of Instrumentation. Instruments include: XPS, HR-SEM, SEM, TEM, ICP-MS, XRD, TGA, DSC, VSM, DLS, AFM, and SQUID. Conduct routine maintenance and train new users on proper instrument techniques. <a href="http://www.nano.vcu.edu/">http://www.nano.vcu.edu/</a>
<b>2007-2008</b>	Teaching Assistant, Virginia Commonwealth University. Educated undergraduate students in general/inorganic chemistry.
<b>Summer 2007</b>	Research Assistant, Virginia Commonwealth University, Philip Morris First Year Research Scholarship
<b>2006-2007</b>	Undergraduate chemistry/physics/biology/math tutor, Aquinas College.

<b>2006-2007</b>	Senior Research Project, Aquinas College, designed and implemented new analytical GC techniques into undergraduate instrumental classes. Built and Characterized a chiral capillary column for enantioseparation.
<b>2006-2007</b>	Quality Assurance Technician, Surefil LLC, Grand Rapids, Mi, Ran quality control checks on hair and body products. Gained experience in: FTIR spectroscopy, HPLC, quaternary amine titration, and acid-side titration.
<b>Summer 2006</b>	Undergraduate Research, University of Toledo, solid-state synthesis of negative thermal expansion materials.

**Awards, Scholarships, Honors, Professional memberships :**

<b>2010-present</b>	Royal Society of Chemistry (RSC) membership
<b>2009-present</b>	American Association for the Advancement of Science (AAAS) Membership
<b>2009-present</b>	Materials Research Society (MRS) membership
<b>2009- present</b>	Altria (Formerly Philip Morris USA) Outstanding Student fellowship
<b>2009</b>	Carl Storm Underrepresented Minority Fellowship (GRC)
<b>2008- present</b>	Phi Kappa Phi Honor Society membership
<b>Summer 2008</b>	ACA Small Molecule X-ray Crystallography Scholarship
<b>Summer 2008</b>	Philip Morris First Year Research Scholarship
<b>2005-2007</b>	Dean's List
<b>2007-2008</b>	Poje Senior Undergraduate Chemistry Scholarship
<b>2005-present</b>	American Chemical Society (ACS) member
<b>2005-2007</b>	Senate Representative
<b>2002-2007</b>	Manager of Aquinas College Radio Station

<b>2002</b>	Michigan Competitive Scholarship
<b>2002</b>	MEAP scholarship

**Publications:**

- 2010**
- 20) Daniel Carl, **K.J. Carroll**, E.E. Carpenter, *Gadolinium in Human Serum Measured by ICP-MS*, Journal of Nephrology, **in-preparation**
  - 19) T. Ekiert, **K.J. Carroll**, K. Unruh, E.E. Carpenter, *Annealing effects of Cu/Ni core/shell nanoparticles*, **in preparation**
  - 18) **K.J. Carroll**, J. Reveles, M.D Shultz, L. Stolp, S. Khanna, E.E. Carpenter, *Theoretical Study of Polyol Mechanism of Copper and Nickel Chlorides*, **in-preparation**
  - 17) **K.J. Carroll**, S. Naik, E.E. Carpenter, *XPS study of passivation layers for the stability of Fe nanoparticles*, **in-preparation**
  - 16) C. Fell, **K.J. Carroll**, Y. Meng, “*Synthesis – Structure – Property Relations in Layered, “Li-excess” Oxides Electrode Materials Li[Li<sub>1/3</sub>-<sub>2x</sub>/3Ni<sub>x</sub>Mn<sub>2/3</sub>-<sub>x</sub>/3]O<sub>2</sub>*”, Journal of The Electrochemical Society, **2010**, **in-review**
  - 15) **K.J. Carroll**, Z. Huba, E.E. Carpenter, *Cu<sub>2</sub>O nanoparticles prepared by annealing Cu nanoparticles by the polyol method*, MRS, **2010**, **in review**
  - 14) **K.J. Carroll**, G. Glaspell, N. McDowell, E.E. Carpenter, *SERS enhancement with Fe@SiO<sub>2</sub>@Au nanoparticles*, Nanotech proceedings, **2010**
  - 13) **K.J. Carroll**, E.E. Carpenter, G.P. Glaspell, *Synthesis of Magnetic Core/shell nanoparticles of Ag@Fe for Surface Enhanced Raman Spectroscopy*, Chem. Mater., **in-review**
  - 12) F.R. Radwan, S.A. Wyatt, **K.J. Carroll**, T.R. Croley, E.E. Carpenter, *Functionalization of Iron Oxide Nanoparticles with 2-amino-1,3,-propane Diol*, Journal of colloid and interface science, **in-review**

- 11) F.R. Radawan, **K.J. Carroll**, E.E. Carpenter, *Prussian Blue Coated Nanoparticles for Biomedical Applications*, Journal of colloid and interface science, **in-review**
- 10) F.R. Radwan, **K.J. Carroll**, E.E. Carpenter, *Dual Mode Nanoparticles: CdS Coated Iron Oxide Nanoparticles*, *J. Appl. Phys.*, “in-press”, **April 2010**
- 9) **K.J. Carroll**, D.M. Hudgins, L. Brown, E.E. Carpenter, *Annealing studies of  $Fe_xCo_{100-x}$  Nanoparticles synthesized by aqueous reduction of Metal Salts.*, *J. Appl. Phys.*, **107**, 09A303, **2010** [doi:[10.1063/1.3334172](https://doi.org/10.1063/1.3334172)]
- 8) N. McDowell, J. Watkins, **K.J. Carroll**, E.E. Carpenter, G. Glaspey, *Magnetic Upconverters*, *J. Appl. Phys.*, “in-press”, **May 2010**
- 7) Lei Wang, Kaida Yang, Cesar Clavero, Andrew Nelson, **K.J. Carroll**, Everett Carpenter, Rosa Alejandra Lukaszew, *Localized Surface Plasmon Resonance Enhanced magneto-optical activity in Core-shell Ag-Fe Nanoparticles*, *J. Appl. Phys.*, “in-press”, **May 2010**
- 6) **K.J. Carroll**, Michael D. Shultz, Everett E. Carpenter, *High Magnetization Aqueous Ferrofluid: A Simple One-pot Synthesis*, *J. Appl. Phys.*, “in-press”, **May 2010**
- 5) **K.J. Carroll**, J.A. Pitts, E.E. Carpenter, K. Zhang, A.K. Pradhan, E.E. Carpenter, *Non-classical Crystallization of Amorphous Iron Nanoparticles by Radio Frequency Methods*, *J. Appl. Phys.*, **107**, 09A302, (**2010**), [doi:[10.1063/1.3334169](https://doi.org/10.1063/1.3334169)]
- 4) Y. Zheng, W. Zhang, M. Gupta, S. Kankanala, C. Marks, **K.J. Carroll**, E.E. Carpenter, K. Wynne, *Poly(bis-2,2,2-trifluoroethyl oxetane): Multiple Crystal Phases, Crystallization-Induced Surface Topological Complexity and Enhanced Hydrophobicity.*, *Journal of Polymer Science Part B: Polymer Physics*, Published online April, 7<sup>th</sup>, **2010** [DOI: [10.1002/polb.21991](https://doi.org/10.1002/polb.21991)]
- 3) V.G. Harris, Y. Chen, A. Yang, S. Yoon, Z. Chen, Anton Geiler, C.N. Chinnasamy, L.H. Lewis, C. Vittoria, E.E. Carpenter and **K.J. Carroll**, R. Goswami, M. A. Willard, L. Kurihara, M. Gjoka, O. Kalogirou, *High Coercivity Cobalt Carbide Nanoparticles processed*

*via Polyol Reaction: A New Permanent Magnet Material*, J. Phys. D: Appl. Phys. **43**, 165003, 2010 [doi:[10.1088/0022-3727/43/16/165003](https://doi.org/10.1088/0022-3727/43/16/165003)]

- 2) **K.J. Carroll**, T. Ekiert, K. M. Unruh, S. Calvin, E.E. Carpenter, *Selective Nucleation and Growth of Cu and Ni Core/Shell Nanoparticles*, Chem. Mater., **2010** [DOI:[10.1021/cm1004032](https://doi.org/10.1021/cm1004032)]
- 1) J. Rivers, **K.J. Carroll**, R.A. Jones E.E. Carpenter, *A copper-polyol complex:  $[Na_2(C_2H_6O_2)_6][Cu(C_2H_4O_2)_2]$* , Acta. Cryst.(2010). C66, m83-m85 [doi:[10.1107/S0108270110006311](https://doi.org/10.1107/S0108270110006311)]

### **Presentations:**

**2010** “High Energy Permanent Magnets for Hybrid Vehicles and Alternative Energy”, ARPA-E team project update, University of Delaware, **February 26<sup>th</sup> 2010**

F.R. Radawan, **K.J. Carroll**, E.E. Carpenter, *Prussian Blue Coated Nanoparticles for Biomedical Applications*, **11<sup>th</sup> Joint MMM-Intermag Conference, Poster Presentation, January 2010**

F.R. Radawan, **K.J. Carroll**, E.E. Carpenter, *Dual Mode Nanoparticles: CdS Coated Iron Oxide Nanoparticles*, **11<sup>th</sup> Joint MMM-Intermag Conference, Oral Presentation, January 2010**

**K.J. Carroll**, J.A. Pitts, E.E. Carpenter, K. Zhang, A.K. Pradhan, E.E. Carpenter, *Non-classical Crystallization of Amorphous Iron Nanoparticles by Radio Frequency Methods*, **11<sup>th</sup> Joint MMM-Intermag Conference, Poster Presentation, January 2010**

**K.J. Carroll**, Michael D. Shultz, Everett E. Carpenter, *High Magnetization Aqueous Ferrofluid: A Simple One-pot Synthesis*, **11<sup>th</sup> Joint MMM-Intermag Conference, Poster Presentation, January 2010**

**K.J. Carroll**, D.M. Hudgins, L. Brown, E.E. Carpenter, *Annealing studies of  $Fe_xCo_{100-x}$  Nanoparticles synthesized by aqueous reduction of Metal Salts.*, **11<sup>th</sup> Joint MMM-Intermag Conference, Poster Presentation, January 2010**

N. McDowell, J. Watkins, **K.J. Carroll**, E.E. Carpenter, G. Glaspel, *Magnetic Upconverters, 11<sup>th</sup> Joint MMM-Intermag Conference, Oral Presentation, January 2010*

Lei Wang, Kaida Yang, Cesar Clavero, Andrew Nelson, **K.J. Carroll**, Everett Carpenter, Rosa Alejandra Lukaszew, *Localized Surface Plasmon Resonance Enhanced magneto-optical activity in Core-shell Ag-Fe Nanoparticles, 11<sup>th</sup> Joint MMM-Intermag Conference, Oral Presentation, January 2010*

**2008** M.D. Shultz, J.R. Marin, S.H. Naik, **K.J. Carroll**, J. Wilkins, J.M Laza, L.M. Leon, E.E. Carpenter, *Poly(styrene-co-vinylbenzylchloride-co-divinylbenzene) coated Iron Oxide Synthesis and Effects on Size and Morphology*, Poster presentation at 53<sup>rd</sup> Annual Conference on Magnetism and Magnetic Materials, **November 2008**

M.D. Shultz, W. Braxton, **K.J. Carroll**, E.E. Carpenter, “*One Parameter Control of the Size of Iron Oxide Nanoparticles Synthesized in Reverse Micelles*”, Poster presentation at 53<sup>rd</sup> Annual Conference on Magnetism and Magnetic Materials, **November 2008**

**Kyler J. Carroll**, Thomas Ekeirt, Karl Unruh, Scott Calvin, “*Synthesis and Characterization of Cu-Ni and Ni-Cu Core-Shell Nanoparticles*,” poster presentation at Virginia Commonwealth University, **October 2008**

Non-Thesis Research Seminar presentation titled, “*Negative Thermal Expansion Materials*.” **September 2008**

**2007** Senior Research Seminar titled, “*Characterization and Implementation of Chiral Separations using Gas Chromatography*.” Aquinas College, **May 2007**

**2006** Inorganic poster presentation on coordination compounds, Aquinas College, **May 2006**

Presentation to University of Toledo faculty and graduate students on the topic of negative thermal expansion materials, **July 2006**

Undergraduate research paper on A<sub>2</sub>M<sub>3</sub>O<sub>12</sub>, university of Toledo,  
**May 2006**

### **Technical Skills:**

Extensive training on: X-ray diffraction, x-ray absorption spectroscopy, thermogravimetric analysis, vibrating sample magnetometry, inductively coupled plasma-mass spectroscopy, x-ray photoelectron spectroscopy, and differential scanning calorimetry.

Also have skills in: UV/VIS spectroscopy, IR spectroscopy, Raman spectroscopy, Atomic force microscopy, Scanning electron microscopy, transmission electron microscopy, x-ray fluorescence spectroscopy, SQUID magnetometry, and gas chromatography.

Experience with MS-DOS, several versions of MS-Windows, Macintosh. Limited programming with HTML also Word, Excel, PowerPoint, CorelDraw, Photoshop, Keynote,

Moderate experience with X-ray refinement programs such as: GSAS, EXPGUI, Artemis, and Athena.

### **Workshops:**

**2008**      Varian Inorganic Workshop, Raliegh, NC  
                ICP-MS, ICP-OES, AA Training

American Crystallographic Association workshop on X-ray Diffraction Workshop, Indiana, PA

**2007**      Brookhaven National Laboratory Workshop on Extended X-ray Absorption Fine Structure data analysis and acquisition,  
                Brookhaven, NY

### **Committees:**

**2008-2009**    Student Representative for Promotion and Tenure Committee.  
                Served as a student representative for the promotion and tenure of assistant faculty.